

# Polyelectrolyte behaviour in solution and at interfaces

Promotoren    prof. dr. M. A. Cohen Stuart  
                  hoogleraar fysische chemie  
                  met bijzondere aandacht voor de kolloïdchemie

                  prof. dr. W. H. van Riemsdijk  
                  hoogleraar in de bodemscheikunde  
                  en chemische bodemkwaliteit

Copromotor    dr. ir. L. K. Koopal  
                  universitair hoofddocent  
                  bij de leerstoelgroep fysische chemie en kolloïdkunde

#### Samenstelling promotiecommissie

Dr. O. V. Borisov	Russian Academy of Science, St. Petersburg (Russia) LRMP, Pau (France)
Prof. dr. A. J. Schouten	Rijksuniversiteit Groningen
Dr. G. Koper	Rijksuniversiteit Leiden
Prof. dr. E. van der Linden	Wageningen Universiteit

# Polyelectrolyte behaviour in solution and at interfaces

Joanne Klein Wolterink

Proefschrift  
ter verkrijging van de graad van doctor  
op gezag van de rector magnificus  
van Wageningen Universiteit  
prof. dr. ir. L. Speelman  
in het openbaar te verdedigen  
op vrijdag 6 juni 2003  
des namiddags te 13.30 in de Aula

ISBN 90-5808-839-1

# Contents

<b>1</b>	<b>Polyelectrolytes in solution and at interfaces</b>	<b>1</b>
1.1	Introduction . . . . .	2
1.2	Polyelectrolytes in solution . . . . .	3
1.2.1	Polyelectrolyte architecture . . . . .	3
1.2.2	Monomeric electrolytes . . . . .	3
1.2.3	Polyelectrolytes . . . . .	4
1.3	Polyelectrolytes at interfaces . . . . .	5
1.3.1	Solid interfaces . . . . .	5
1.3.2	Adsorption theories . . . . .	5
1.4	Self-consistent-field (SCF) theory . . . . .	6
1.4.1	SCF versus Flory–Huggins theory . . . . .	6
1.4.2	Approximations in the SCF theory . . . . .	7
1.4.3	Polyelectrolytes in the SF–SCF theory . . . . .	7
1.5	Outline of this thesis . . . . .	8
<b>2</b>	<b>Quenched star</b>	<b>10</b>
2.1	Introduction . . . . .	11
2.2	Cell model for a solution of polyelectrolyte stars . . . . .	13
2.2.1	Analytical model . . . . .	14
2.2.2	Numerical SCF model . . . . .	16
2.3	Dilute salt-free solution . . . . .	18
2.4	Dilute solution: screening by added salt . . . . .	26
2.5	Increasing the polyelectrolyte concentration . . . . .	29
2.6	Discussion and conclusions . . . . .	36
<b>3</b>	<b>Annealed star</b>	<b>40</b>
3.1	Introduction . . . . .	41
3.2	Analytical model . . . . .	42
3.2.1	Polyelectrolyte regime . . . . .	43
3.2.2	Osmotic regime . . . . .	44
3.2.3	Quasi-neutral regime . . . . .	48
3.3	Numerical Self-Consistent-Field model . . . . .	48
3.4	Results and Discussion . . . . .	52
3.4.1	Behaviour at low ionic strength . . . . .	52
3.4.2	Behaviour upon increasing the ionic strength . . . . .	63

## CONTENTS

3.4.3	Form factors . . . . .	66
3.5	Comparison with experiment . . . . .	70
3.6	Conclusion . . . . .	75
3.7	Acknowledgments . . . . .	76
<b>4</b>	<b>Adsorption of a quenched polyelectrolyte: SF–SCF model</b>	<b>77</b>
4.1	Introduction . . . . .	78
4.2	SCF model by Scheutjens and Fleer (SF–SCF model) . . . . .	79
4.3	System definition . . . . .	81
4.4	Results and Discussion . . . . .	84
4.4.1	Adsorption isotherms . . . . .	84
4.4.2	Surface charge adaptation upon adsorption . . . . .	89
4.4.3	Distribution of adsorbed polymer segments . . . . .	93
4.4.4	Comparison to scaling laws . . . . .	99
4.5	Conclusions . . . . .	101
<b>5</b>	<b>Adsorption of poly(styrene sulfonate) onto hematite</b>	<b>103</b>
5.1	Introduction . . . . .	104
5.2	Theoretical model and results . . . . .	105
5.2.1	SF–SCF model and choice of the parameters . . . . .	105
5.2.2	Results of the SF–SCF calculations . . . . .	107
5.3	Materials and Methods . . . . .	113
5.3.1	Materials . . . . .	113
5.3.2	Methods . . . . .	114
5.4	Results . . . . .	115
5.5	Discussion . . . . .	119
5.6	Acknowledgements . . . . .	123
5.A	Calculation of the surface charge from different experiments . .	124
<b>6</b>	<b>Evaluation of the mastercurve procedure</b>	<b>125</b>
6.1	Introduction . . . . .	127
6.2	Electrostatic models . . . . .	128
6.3	Method . . . . .	130
6.4	Mastercurve procedure . . . . .	131
6.5	Results . . . . .	133
6.6	Discussion . . . . .	141
6.7	Humic substances . . . . .	143
<b>A</b>	<b>Dependence of a reaction constant on the discretisation</b>	<b>148</b>
<b>B</b>	<b>The calculation of the charge distribution fraction</b>	<b>150</b>
	<b>Summary</b>	<b>166</b>
	<b>Samenvatting</b>	<b>173</b>

## CONTENTS

Dankwoord	182
Levensloop	184

## CONTENTS



# Chapter 1

## Polyelectrolytes in solution and at interfaces

## 1.1 Introduction

### 1.1 Introduction

**Motive** This thesis is about polyelectrolytes in solution and at interfaces. This work was inspired by possible analogies with humic acids in solution and at the interface of mineral particles. Humic acids and mineral particles are two major components present in soil systems. In this introduction we therefore first mention some general properties of soils. Then we proceed with a more fundamental introduction of polyelectrolytes in solution and at interfaces. Next, the numerical model that was used in this study is introduced. Lastly, an outline of the thesis is given.

**Polyelectrolytes in soils** A soil is a complex mixture of different components. These components can be subdivided into five different categories. Firstly, living organisms such as bacteria, earthworms, and plant roots. Secondly, the minerals like sand ( $\text{SiO}_2$ ), metal oxides and clay. Thirdly, organic matter, which results from the degradation of dead plants and other organisms. The before mentioned humic acids are part of this organic matter. The fourth category of soil components is the soil solution, which consists of water, ions, and dissolved organic molecules. Most transport of molecules takes place in the soil solution, it can be viewed upon as the transport highway of a soil. Lastly, there is also a gas phase.

From a fundamental point of view, a soil is a very complex mixture. No one has found a general way to describe this mixture of different components. However, many attempts were made to describe the interaction between the soil solution and the other soil components. The organic matter present in soil is one of these components that can be present in the soil solution, be attached to the soil minerals or even be part of the soil particles. The soil organic matter is divided in three fractions: material that is insoluble at all natural conditions is called humins, materials that is soluble in solution with a  $\text{pH}$  higher than 2, is called humic acids, and material that is even soluble at very low  $\text{pH}$ , is called fulvic acids. The mechanisms which lead to the formation of the various types of organic matter are highly dependent on the local situation within the soil. This means that the exact environment determines the characteristics of organic matter in a soil to a large extent.

Nevertheless each of the three classes of soil organic matter shows generic characteristics. Especially the fulvic and humic acids are often considered as oligomeric and polymeric materials. In literature, there is some debate whether the high molecular mass is due to aggregation of small units, as in micelles, or due to covalently bound units, as in polymers.<sup>1-4</sup> However, under most circumstances the organic matter does not fall apart into units, as small as water molecules so the polymer approach has enough appeal to be often used to gain a better understanding of humic and fulvic acid behaviour.

Another generic aspect of both humic and fulvic acids is their charge. The building units contain acidic groups that can ionize depending on the  $\text{pH}$  of the soil solution. Hence, if one approximates humic and fulvic acids as polymers, it

is appropriate to consider them as polyelectrolytes. If one accepts this approach further insight in the behaviour of humic and fulvic acids can be gained by studying the behaviour of more simple polyelectrolytes. In order to approach the complex structure of the humic and fulvic acids polyelectrolytes of different architectures can be studied.

As humic and fulvic acids can be present both in the soil solution and adsorbed to the soil mineral particles, the study of the more simple polyelectrolytes should concentrate on their behaviour in solution and at interfaces.

## 1.2 Polyelectrolytes in solution

### 1.2.1 Polyelectrolyte architecture

Polymers are chain-like molecules, which consist of monomers. In a polymer several monomers are linked together to form a chain, comparable to a necklace. These chains can be linear or branched. Two types of branching are relevant for this thesis: stars and dendrimers. Star polymers consist of several linear chains (arms) which are all linked to each other at one end, see fig 1.1b. Dendrimers (also called: starbursts) are stars where at the end of each arm several new arms are attached, see fig 1.1c.

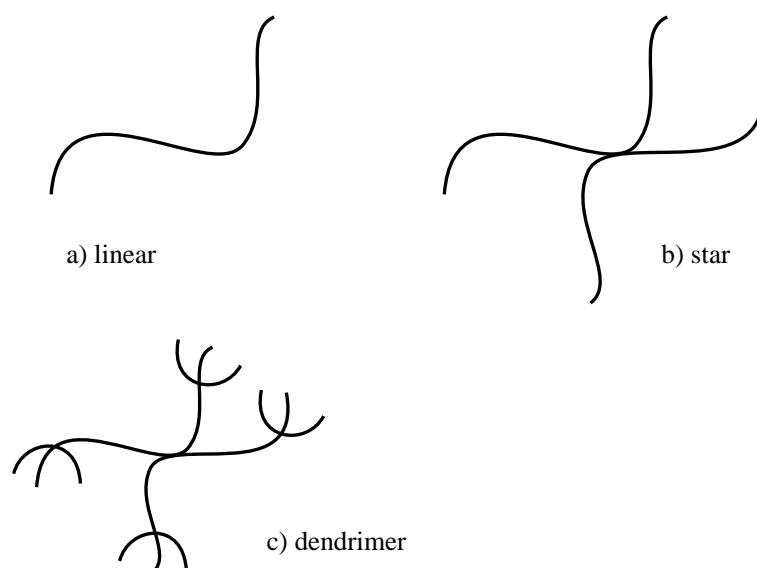


Figure 1.1: Molecules with different architecture.

### 1.2.2 Monomeric electrolytes

Before turning to the physical behaviour of polyelectrolytes in solution it is convenient to highlight some of the behaviour of monomeric electrolytes. It is common knowledge that table salt (NaCl) dissolves in water. The aqueous

## 1.2 Polyelectrolytes in solution

solution contains  $\text{Na}^+$  and  $\text{Cl}^-$  ions. However, it was already in the 1920's recognised that these ions do not distribute themselves evenly over the solution. The sodium  $\text{Na}^+$  and chloride  $\text{Cl}^-$  ions have a tendency to attract each other through Coulombic interactions. This leads to a certain ordering: around a cation there is on the average more negative charge than in the solution as a whole and the converse applies to an anion.<sup>5</sup> The famous Debye-Hückel theory takes this effect into account for dilute solutions of ions. It should be noted that the Debye-Hückel theory is not exact and several other approaches have been proposed.<sup>5</sup>

Additionally, the monomers may have acidic or basic properties. A monovalent acid HA may dissociate as



where all three forms (the acid HA, the proton  $\text{H}^+$ , and the base  $\text{A}^-$ ) are present in solution. An dissociation constant  $K$  is associated with the given equilibrium. The concentration of protons  $c_{\text{H}^+}$  influences the fraction of acid HA that is dissociated. The proton concentration is usually expressed as  $\text{pH}$ , which equals  $-\log(c_{\text{H}^+})$ . The case of dissociating monomers contrasts with strong electrolytes like the table salt, where *all* NaCl is dissociated into ions.

### 1.2.3 Polyelectrolytes

When a polyelectrolyte is dissolved in water, it may acquire a certain amount of charge. Like strong electrolytes, the monomers may be fully dissociated so that the charge on the polyelectrolyte is permanent. If all ionizable groups are fully dissociated we speak of a *quenched* polyelectrolyte. The ions that are released into the solution are called counterions. The ionizable groups may also be weak acids or bases. This results in a partially ionized polyelectrolyte. The fraction of ionized groups then depends on (among other aspects) the  $\text{pH}$ . This case is called an *annealed* polyelectrolyte. Of course, mixtures of different types of monomers may be present in polyelectrolytes. This is for example the case for humic and fulvic acids present in soils.

The theoretical description of polyelectrolytes in a dilute solution turns out to be non-trivial. This is due to the long range character of the charge interactions. Most interactions between two molecules are only noticeable when the two molecules touch each other. For electrostatic interaction the distance can be much larger, this means that a lot of molecules interact and not just two molecules. For a polyelectrolyte this means that the charges on the chain interact with each other, which causes a swelling, but due to the fact that they are linked together there is a finite extension of the chain. The counterions also interact with this chain and partly screen the repulsion between the charges on the polymer. A large number of molecules have therefore to be taken into account to describe the polyelectrolyte behaviour. Only fairly recently, successful theories in this area have been proposed. One such theory is known as the worm model.

## Polyelectrolytes in solution and at interfaces

The worm model assumes a polymer consisting of stiff segments. For these stiff segments the polymer configuration is taken to be fixed, which simplifies the description of the distribution of the counterions and the effective electrostatic potential. Because the main question is how the polyelectrolyte units distribute spatially, the stiff chains are used as building blocks of a larger polymer with a probability distribution between the angles of the different segments.<sup>6–9</sup>

Instead of looking at just one polyelectrolyte one can also approach the question how polyelectrolytes behave in solution using knowledge gained about the behaviour of a polyelectrolyte brush. In a polyelectrolyte brush, polyelectrolytes are attached to a surface. The polyelectrolytes influence each other in a way varying with the number of charges and of the grafting density: the amount of polyelectrolytes that are fixed to a surface.<sup>10,11</sup> What does this have to do with polyelectrolytes in solution? For star-shaped or dendrimeric molecules the interactions between the branches of those molecules is comparable to those between the polyelectrolytes in a brush. The main difference is that the ‘grafting density’ for such polyelectrolytes is not constant but varies within the molecule.

### 1.3 Polyelectrolytes at interfaces

#### 1.3.1 Solid interfaces

The interfaces that are discussed in this thesis are all solid-liquid interfaces. The boundary between a clay particle and the soil solution is an example of such a solid-liquid interface. Due to charges on the surface an environment is created that may attract or expel small ions and polyelectrolytes.

Two types of charged surfaces may be distinguished. Firstly, surfaces with a constant surface charge, which are also called *quenched* surfaces. Like the table salt, these surfaces carry groups which fully dissociate. An example of such a surface is the plate surface of a clay particle which has a charge due to isomorphic substitution. Secondly, there are surfaces with a variable surface charge. Like the annealed polyelectrolytes these surfaces carry groups that ionize depending on the  $pH$ , and they are called *annealed* surfaces. Examples of such surfaces are metal oxide surfaces. Variably charged mineral surfaces of iron and aluminum oxides can also be approximated as constant-potential surfaces. This is due to the high surface density of chargeable groups in combination with the ionization relation. In this thesis, we will also use the term constant-potential surface for such mineral oxide surfaces.

#### 1.3.2 Adsorption theories

The theories for describing the adsorption of polyelectrolytes can be split up in two classes, namely for the adsorption of one single polyelectrolyte chain and

## 1.4 Self-consistent-field (SCF) theory

for the adsorption of many chains.

For describing of the adsorption of a single polyelectrolyte to a surface, the attraction between the surface and the polyelectrolyte is a basic parameter. This attraction is counteracted by the loss of entropy of the chain due to adsorption. This means that stiff, rodlike chains will adsorb more easily than flexible coiled chains. The stiffness of a polyelectrolyte is not only governed by the molecular architecture but also by the degree of ionization.

The adsorption of many polyelectrolytes to a surface is mostly described using a mean-field theory. In a mean-field approximation the interactions of a given monomer with neighbouring units are not calculated explicitly. Instead, each monomer is supposed to experience a mean-field interaction potential that represents an average of the neighbour interactions. In the case of dense adsorbed layers the direct relation between the stiffness of a chain and the amount adsorbed is not so easily obtained as for the isolated chain. This is related to the fact that in a dense layer it is difficult for a stiff molecule to fit in. More details about these aspects can be found in a recent review by Netz and Andelman<sup>12</sup> about the adsorption of neutral and charged polyelectrolytes.

## 1.4 Self-consistent-field (SCF) theory

This thesis makes extensive use of a self-consistent-field (SCF) model to predict the behaviour of polyelectrolytes in solution and at interfaces. The SCF model as formulated by Scheutjens and Fleer is used (SF-SCF).<sup>13</sup> The foundation of this model was laid independently by Edwards<sup>14</sup> and Helfand.<sup>15</sup> The SF-SCF theory has been used successfully to describe the adsorption of homopolymers from solution, polymer and polyelectrolyte brushes, and the wetting behaviour of polymers.<sup>16</sup>

### 1.4.1 SCF versus Flory–Huggins theory

The SF-SCF model is a generalization of the classical Flory-Huggins theory. The Flory-Huggins theory is able to predict the phase behaviour of mixtures of (uncharged) polymers. This means that it is able to predict whether a given mixture of polymers (with or without solvent) remains fully mixed or separates in different phases. For example, oil and water do not mix but form two different phases: one water phase and an oil phase. These phases are not pure substances: a tiny fraction of oil is present in the water phase. Likewise, some water is present in the oil phase. Using relatively simple molecular parameters, the Flory-Huggins theory gives a prediction of the amount of water in oil and oil in water.

Whereas Flory-Huggins theory deals with homogeneous phases, the SF-SCF model deals with inhomogeneous systems. To illustrate the difference between a homogeneous and an inhomogeneous phase, we can again use the oil and water phases as an example. To the naked eye, the interface between oil

and water may seem infinitely sharp. In reality, there is a smooth transition between oil and water. Within the interface the concentration of water changes gradually from very low (in the oil phase) to very high (in the water phase). This occurs over distances comparable to molecular sizes. Flory-Huggins theory is able to predict the concentration of water in oil and oil in water (homogeneous phases). In addition, the SF-SCF model is also able to predict the transition in concentration within the interface (an inhomogeneous system). The SF-SCF theory gives detailed information on the chain conformations of polymers in these interfaces and in the bulk solution.

Using relatively simple molecular parameters like the chain length, the solvent strength, and the adsorption energy, the SF-SCF theory leads to the volume fraction profiles of adsorbed polymers or the surface tension of interfaces. The equations of the SF-SCF theory cannot be solved analytically, therefore a dedicated software package has been used: `sfbox`.<sup>17</sup>

### 1.4.2 Approximations in the SCF theory

As explained in the previous paragraph, the SF-SCF model can be viewed as a generalization of the classical Flory-Huggins theory. As such, in both theories the same approximations are made. The main approximation is the use of a mean field. The same approximation is, for instance, present in the above mentioned adsorption theories and in the Debye-Hückel and Poisson-Boltzmann theories. Indeed, when applied to classical electric double layers, the SF-SCF theory recovers the Poisson-Boltzmann results.

Another approximation is the use of random walk chain statistics. One may look upon the conformation of an individual chain in solution as a walk through space. When walking from one end of the chain to the other, one never passes the same position twice. This reflects the fact that the monomers of a given polymer may not occupy the same position in space, which seems obvious. However, in calculations this restriction complicates calculations considerably. Therefore, the chains are described as random walks: when walking from one end of the chain to the other, we do not remember where we have been before. This approximation works rather well for very concentrated solutions of polymers or dilute solutions of uncharged polymers, but not so well for dilute solutions of polyelectrolytes.

### 1.4.3 Polyelectrolytes in the SF-SCF theory

The swelling behaviour of polyelectrolytes in solution can be calculated within the SF-SCF theory by considering one individual chain. Space is divided into spherical shells and within each shell the mean-field approximation is applied. One segment of the chain is fixed in the centre of the spherical geometry. Mean-field theories are not suitable to describe the behaviour of linear polyelectrolytes. However, for more dense polyelectrolyte architectures, the mean-field approximation does yield satisfactory results.

## 1.5 Outline of this thesis

The description of the adsorption of polyelectrolytes is rather problematic in the standard SF–SCF theory. The main problem is again the mean-field approximation, which not only breaks down for linear polyelectrolytes, but even, and severely, for dense polyelectrolyte architectures. The main reason for this break-down is the treatment of chains in solution. Only one molecular field is employed for both adsorbing and bulk chains. This molecular field is taken to be homogeneous in the bulk phase. Effectively, this means that the swelling of bulk chains is completely neglected: they are treated as random walks. This leads to a large overestimation of the conformational entropy of the bulk chains. In contrast, a varying molecular field is present near the surface, which leads to swelling of the adsorbed chains. As a result, the adsorbed amount is underestimated in the standard SF–SCF theory.

A rather nice aspect of the standard SF–SCF theory is that it can describe charged surfaces rather well. The full Poisson–Boltzmann equation is solved numerically. This means that neither a constant-potential surface nor a constant-charge surface have to be assumed. For instance, mineral oxide surfaces are surfaces which can be either an almost constant-charge surface or a constant-potential surface depending on the solution conditions and the type of mineral oxide. With the SF–SCF model it is possible to treat also intermediate cases, in between these two extreme situations.

## 1.5 Outline of this thesis

Chapters 2 and 3 deal with polyelectrolyte stars in solution. In chapter 2 the properties of quenched (a fixed charge per monomer) polyelectrolyte stars are investigated using the SF–SCF theory. The results are compared to an existing analytical theory. In chapter 3 the same is done for annealed (monomers with a  $pH$ -dependent charge) polyelectrolyte stars. The existing analytical theory describes the swelling of polyelectrolyte stars as a function of the molecular architecture (the amount of charges on the arms, the length, and the number of arms). Depending on these conditions, one may distinguish different regimes of behaviour, where one force, responsible for swelling, dominates over the others. This contrasts with the SF–SCF theory that uses the same fundamental approximations but all swelling forces are treated simultaneously. Therefore, it is of interest to compare the scaling predictions for the swelling behaviour from the analytical theory with the results obtained from the numerical SCF results. This is done in chapters 2 and 3.

In chapter 4 the adsorption of quenched polyelectrolytes on charged surfaces is theoretically investigated using the SF–SCF theory. Two types of surfaces are considered: quenched and annealed surfaces. In the latter case, the surface charge depends on both the  $pH$  and the amount of adsorbed polyelectrolyte. As explained in section 1.4.3, polyelectrolytes adsorbing onto the surface feel a mean-field potential in the standard SF–SCF theory. In contrast, the bulk chains experience no field at all and are treated as random walks. In chapters 2



## Polyelectrolytes in solution and at interfaces

and 3, it is shown that this approximation does not hold at all for bulk chains. Therefore, also a new variant of the SF–SCF theory is introduced in which the equilibrium adsorption is calculated from two separate calculations. The first calculation considers the bulk solution, where an individual chain swells due to its own charges. The second calculation is at the surface, where the adsorbed chains swell due to the accumulation of charges at the surface. The equilibrium adsorbed amount is then calculated by equating the chemical potentials of the polyelectrolyte resulting from both separate calculations. The results for this new method are compared to the results obtained from the standard SF–SCF calculations for polyelectrolytes with the molecular architectures depicted in fig 1.1.

Now that several theoretical approaches to polyelectrolyte adsorption have been discussed, it is time to turn to experiments. Chapter 5 shows results obtained from proton titration experiments done on hematite in the presence of adsorbing poly(styrene sulfonate). Hematite is an iron oxide mineral with a  $pH$ -dependent surface charge. At  $pH$ 's lower than 9, the surface charge is positive. Poly(styrene sulfonate) is a linear polymer with a constant negative charge. Special attention is given to the surface charge behaviour of hematite upon adsorption of poly(styrene sulfonate). The measured adsorption and surface charge behaviour are compared to SF–SCF calculations.

Finally in chapter 6, the numerical SCF calculations are used to determine the  $pH$ -dependent charging of stars and dendrimers in solution. The results obtained, are analysed with two simple electrostatic models, to see whether such a simple approximation can lead to a reasonable description of the intrinsic charging behaviour. The two simple models are (i) a Donnan and (ii) a hard-sphere model. A crucial parameter in these models is the assumed radius of the particles. In the analysis the results of different choices for the radius are compared. A main incentive for this investigation is that such simple models are frequently used to describe the electrostatic interactions of humic and fulvic acids.

## Chapter 2

# Screening in Solutions of Star-Branched Polyelectrolytes\*

### Abstract

Equilibrium conformations of star-branched polyelectrolytes in dilute solutions are studied on the basis of a numerical Self-Consistent-Field (SCF) approach and analytical theories. It is shown that even in a dilute salt-free solution the intramolecular Coulombic repulsion in many-armed stars is strongly screened by counterions which are localised preferentially in the intra-star space. As a result the dependence of the star size on the number of branches levels off for many-armed stars. Addition of salt results in additional screening and in contraction of the stars. The scaling prediction  $R \sim c_s^{-1/5}$  for the star size as a function of the salt concentration  $c_s$  is well confirmed by SCF-calculations. A decrease in the star size can also be induced by an increase in the concentration of the polyelectrolyte in the solution. We have observed significant contraction of the stars with increasing concentration below the overlap threshold, i.e. in dilute solutions. The latter effect is more pronounced for stars with a small number of branches. The screening of the intramolecular Coulombic repulsion due to added salt is compared with that occurring upon increasing the concentration of the polyelectrolyte.

---

\*published in *Macromolecules*, 1999, 32; 2365–2377

## 2.1 Introduction

Even though the properties of solutions of linear chain polyelectrolytes are not completely understood,<sup>8,18</sup> charged polymers of more complex architecture, such as randomly or regularly branched polyelectrolytes or polyelectrolyte gels, attract strong attention.

Partially this is because of their relevance for practical applications, such as colloid stabilization.<sup>19</sup> Polyelectrolyte stars can be considered as models of micelles formed by hydrophobically modified polyelectrolytes in aqueous solutions,<sup>20–24</sup> and for more complex practical systems like humic acids.<sup>25</sup>

The behaviour of charged polymers in the solution is determined by the interplay of long-range Coulombic interactions and effects of chain connectivity. From a theoretical point of view, the most important feature that makes polyelectrolyte solutions differ from those of ordinary low-molecular-weight electrolytes is essentially the non-linear character of the screening of the Coulombic interactions. In other words, the linear Debye–Hückel (DH) approximation fails to describe the equilibrium properties of polyelectrolyte solutions, especially at low polyelectrolyte concentration and at low ionic strength of the solution.

The importance of non-linear screening effects in polyelectrolyte solutions has been understood early. The Manning counterion condensation concept is the first example in this direction.<sup>26</sup> We note that this type of condensation occurs only for strongly charged and stiff chains which retain local cylindrical symmetry on a large scale, exceeding the electrostatic screening length. In addition, non-linear screening effects are also important for flexible polyelectrolytes in dilute solutions, even when they are only weakly charged. (In this paper we discuss only quenched polyelectrolytes; the term weak refers to a small fraction of charged monomers).

Several approaches have been used to describe screening in dilute and semi-dilute solutions of weakly charged linear polyelectrolytes.<sup>27–30</sup> They all are based on certain heuristic ideas which can not be proved rigorously. Most of these theories predict that screening of intra- and inter-chain Coulombic interactions in dilute polyelectrolyte solutions is stronger than follows from the linear DH approximation.<sup>28–30</sup> Clearly, the most important question is what happens in the dilute solution. When the cross-over concentration is defined, the properties in the semi-dilute regime can then be obtained from scaling arguments.

The essential feature of dilute solutions is the inhomogeneous distribution of counterions. Counterions are preferentially localised in the proximity of the polyions. The inhomogeneous distribution of counterions is also confirmed by simulations.<sup>31–33</sup> Therefore, for weakly charged linear chains a scaling analysis, which can deal only with power law dependencies, is hardly feasible, even when the chains are very long.

The origin of the inhomogeneous distribution of counterions in dilute solutions is, of course, the strong Coulombic attraction between the counterions and the polyion, which carries a large net charge. The equilibrium distribution

## 2.1 Introduction

is determined by the competition between this attraction and the translational entropy of the counterions.

One can expect that this inhomogeneity is even stronger for branched polyions, where a comparatively large charge is immobilised in a small volume. This charge concentration must result in stronger attraction and less freedom for the counterions than in a solution of linear polyelectrolytes.

For strongly branched polyelectrolytes the effect of the localization of counterions in the intramolecular volume appears to be strong enough to be treated on the level of a scaling approximation.<sup>34–36</sup> It was shown that even in a very dilute solution the high concentration of counterions inside the branched polyelectrolyte provides strong screening of Coulombic repulsion between charged monomers.

There are two important consequences from this trapping of counterions by strongly branched polyelectrolytes. First, the conformations of branched chains are less sensitive to the addition of salt, because intramolecular repulsion is already screened. An increase in the salt concentration leads to additional screening and contraction of the branched polyelectrolyte only when this concentration exceeds the intrinsic concentration of counterions in the intramolecular space. Second, the effect of an increasing polymer concentration (in the dilute range) is expected to be weak in comparison to that in linear or weakly branched polyelectrolytes. This is because branched polyions release only a small fraction of their counterions into the intermolecular space. Hence, in a wide range the intramolecular concentration of counterions (and the intramolecular screening) depends only weakly on the overall polyelectrolyte concentration.

Up to now these effects in branched polyelectrolytes have been considered only on the basis of the scaling approximation.<sup>34,35</sup> From these predictions the main power law dependencies for the structural properties of branched polyions are known. But this approximation can not account for weaker non-power dependencies. The latter are expected to be rather important especially when the number of charges per branch is relatively low.

The aim of the present paper is to go beyond the scaling approximation and to analyse the screening effects in branched polyelectrolytes in dilute solution on the basis of a Self-Consistent-Field (SCF) numerical approach, which on the mean-field level gives exact results, in combination with a strongly simplified analytical mean-field model. The results of the SCF-calculations are compared to earlier scaling predictions, which serve as a guide-line for a more elaborated analysis. We show that scaling gives a qualitatively correct description of the main trends in the behaviour of branched polyelectrolytes in solution. For our analysis we have chosen the simplest, but most instructive type of branched polyelectrolytes, the star-branched polyelectrolyte. The degree of branching in this case is simply determined by the number of branches joined in one junction point.

After the description of our model in section 2.2, we consider the intramolecular screening by counterions in the dilute limit as manifested in the depen-

dence of the star size on the number of branches (section 2.3). The screening by added salt and the dependence of the star conformation on the salt concentration is analysed in section 2.4. In section 2.5 we consider the concentration effects in a salt-free solution of stars and we discuss the overlap threshold. Our conclusions are summarized in section 2.6.

## 2.2 Cell model for a solution of polyelectrolyte stars

We envisage a dilute solution of star-branched polyelectrolytes as an ensemble of spherical cells (analogous to Wigner–Seitz cell) each containing one polyelectrolyte star molecule localised at the center, fig 2.1.<sup>37</sup> The cell radius  $D$

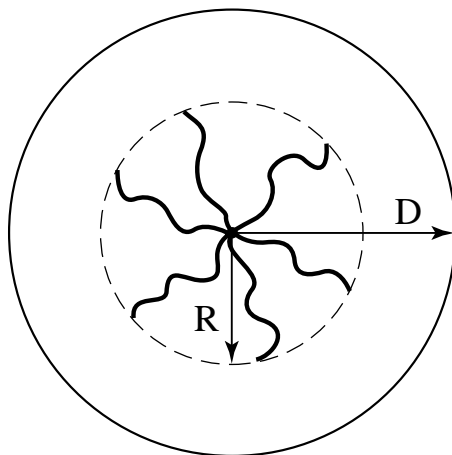


Figure 2.1: Polyelectrolyte star in a spherical cell. The star has  $f$  branches of  $N$  monomer units each. The cell radius is  $D$ , and the star occupies the central region within radius  $R$ .

equals half the average distance between the centers of neighbouring stars, i.e.  $D \sim c_P^{-1/3}$ . Here and below the polyelectrolyte concentration  $c_P$  is assumed to be below the overlap concentration. The star-shaped polyion (with a bare charge  $eQ$ ) occupies the central region,  $r < R$ , of each cell. Here,  $r$  is the distance from the centre of the cell and  $R$  is the average extension of branches. The periphery of the cell,  $R < r < D$ , corresponds to the inter-star space in the solution.

The strength of the electrostatic field (and as a result the derivatives of the concentration profiles of all types of small ions) vanishes at the edge of the cell, at  $r = D$ . Polymer concentration effects in the dilute range are modelled by varying  $D$ .

The main molecular parameters of the polyelectrolyte star are the number of branches  $f$ , the number of monomers per branch  $N$ , and the fraction of charged monomers  $m^{-1}$ . Here,  $m - 1$  is the number of uncharged monomers

## 2.2 Cell model for a solution of polyelectrolyte stars

between two neighbouring charges along the chain. The overall charge  $eQ$  of the star is then equal to  $eQ = efN/m$ , where  $e$  is the elementary charge.

The fraction  $m^{-1}$  of charged monomer units in the chain is assumed to be small. The Bjerrum length  $l_B = e^2/k_B T \varepsilon$  is of the order of a monomer size which is taken as the unit length. Here,  $\varepsilon$  is the permittivity of the solvent,  $T$  is the temperature, and  $k_B$  is the Boltzmann constant. The star branches are intrinsically flexible, i.e. the Kuhn segment length is also of order unity.

Because of the electroneutrality of the solution as a whole, the cell contains  $Q$  monovalent counterions. When salt is added, co- and counterions of the salt are also added in equal amounts.

### 2.2.1 Analytical model

In the following, we will use a mean-field Flory-type approach for the analysis of the large-scale properties of a dilute salt-free solution of polyelectrolyte stars. The free energy can be split up into various contributions

$$F = F_{Coulombic} + F_{ions} + F_{conf} + F_{conc} \quad (2.1)$$

describing the Coulombic interactions between all charges (charged monomers and counterions), the translational entropy of counterions, the conformational entropy of the extended branches of the star, and the concentrational (osmotic) part describing short-range interactions between uncharged monomers, respectively. We remark that within the accuracy of excluded volume terms this mean-field model is equivalent to that used earlier.<sup>34</sup> A similar mean-field cell model has also been applied for ionic microgels by Kramarenko et al.<sup>38</sup>

The free energy given by eq 2.1 is a functional of the monomer and counterion density distributions. However, in order to analyse the dependence of the average star size  $R$  on parameters such as the number of branches  $f$ , the length of the branches  $N$ , the fraction of charged monomers  $m^{-1}$ , and the cell radius  $D$ , we neglect spatial variations of these densities within the central region  $r < R$  and in the peripheric region  $R < r < D$ . In other words we define the free energy eq 2.1 as a function of two variables: the radius of the star  $R$  and the actual (uncompensated) charge in this central region  $Q^*$ . Hence we assume that  $Q - Q^*$  counterions are retained by Coulombic attractions in this central region  $r \leq R$ , whereas the remainder of the counterions  $Q^*$  are distributed evenly in the region  $R < r < D$ .

As we assume the density of counterions (and the electrostatic potential) to have constant (but different) values inside and outside the star, the Coulombic term equals<sup>†</sup>

---

<sup>†</sup>The Coulombic contribution to the free energy of the cell can be obtained as  $F_{Coulombic} = (\epsilon/2) \int_0^D (d\psi(r)/dr)^2 r^2 dr$  where the strength of the electrostatic field is given by  $-d\psi(r)/dr = (4\pi/\epsilon r^2) \int_0^r r'^2 q(r') dr'$  and the local charge density (in the frame of our uniform approximation) is equal to  $q(r) = 3Q^*/4\pi R^3$  at  $r \leq R$  and  $q(r) = -3Q^*/4\pi(D^3 - R^3)$  at  $R \leq r \leq D$ , respectively.

$$F_{Coulombic}/k_B T = l_B \frac{Q^{*2}}{R} \vartheta\left(\frac{R}{D}\right) \quad (2.2)$$

where the function  $\vartheta(x)$  is given by

$$\vartheta(x) = \frac{1}{10} \left[ 1 + \frac{5 - 9x + 5x^3 - x^6}{(1 - x^3)^2} \right]$$

The translational entropy term, giving the contributions of the translational entropy of ions inside and outside the star equals

$$F_{ions}/k_B T = (Q - Q^*) \ln \frac{Q - Q^*}{V(R)} + Q^* \ln \frac{Q^*}{V(D) - V(R)} \quad (2.3)$$

where  $V(r) = (4\pi/3)r^3$ .

The conformational entropy of the extended branches of the star can, in the Gaussian approximation, be written as

$$F_{conf}/k_B T = \frac{3fR^2}{2N} \quad (2.4)$$

For the non-electrostatic osmotic contribution we use the virial expansion

$$F_{conc}/k_B T = \frac{1}{2} v f N \varphi_P + \frac{1}{6} w f N \varphi_P^2 \quad (2.5)$$

where  $\varphi_P = 3fN/4\pi R^3$ , which is the volume fraction of polymer segments within the star volume and  $v$  and  $w$  are the dimensionless second and third virial coefficients, respectively. The former is related to the Flory–Huggins  $\chi$  parameter as  $v = 1 - 2\chi$ . In a  $\theta$ -solvent the binary attraction of monomers compensates their excluded volume so that  $v = 0$ . Whereas linear polymers under  $\theta$ -conditions exhibit Gaussian statistics, in strongly branched polymers the ternary repulsive interactions appear to be strong enough to induce swelling of the star even when  $v = 0$ .<sup>39–42</sup>

The values of  $Q^*$  and  $R$  are found from minimization of the free energy:

$$\left( \frac{\partial F(Q^*, R)}{\partial Q^*} \right)_R = 0 \quad (2.6)$$

$$\left( \frac{\partial F(Q^*, R)}{\partial R} \right)_{Q^*} = 0 \quad (2.7)$$

The result is:

$$Q^* = \frac{R}{l_B} \frac{1}{2\vartheta(R/D)} \ln \left[ \left( \frac{Q}{Q^*} - 1 \right) \left( \frac{D^3}{R^3} - 1 \right) \right] \quad (2.8)$$

$$R^3 = \frac{N}{3f} \left\{ l_B Q^{*2} \left[ \vartheta(R/D) - \frac{R}{D} \vartheta'(R/D) \right] + 3R \left[ Q - \frac{Q^*}{1 - (R/D)^3} \right] - \frac{9f^2 N^2}{8\pi R^2} \left( v + \frac{fN}{2\pi R^3} w \right) \right\} \quad (2.9)$$

## 2.2 Cell model for a solution of polyelectrolyte stars

where  $\vartheta'(x) \equiv d\vartheta/dx$ .

These two equations describe both the star size  $R$  and the uncompensated charge  $Q^*$  inside  $R$  as a function of the bare charge  $Q$ , the number of branches  $f$ , the branch length  $N$ , and the cell size  $D$ .

### 2.2.2 Numerical SCF model

The numerical SCF-approach is based on the Scheutjens–Fleer (SF) algorithm proposed earlier for neutral polymers at interfaces<sup>13,16</sup> and extended to account for the electrostatics on a Poisson–Boltzmann level.<sup>43</sup> Some information on the method is given below, for full details one should consult the original literature.

The SF–SCF approach uses a lattice which facilitates to account for the volume of all molecular components. A lattice cell with the size of the Bjerrum length can be occupied either by a solvent molecule  $S$ , a polymer segment  $P$  or by a mobile ion. We assume that there are two types of ions in the system: co-ions,  $Cl^-$ , and counterions,  $Na^+$  (polymer segments are assumed to be negatively charged). The lattice cells are arranged in an array of concentric spherical shells (or “layers”) numbered as  $z = 1, \dots, M$ ; the outer surface of the  $z$ -th layer is at the distance  $r = zl_B$  from the center. The total cell radius is given by  $D = Ml_B$ . The volume of the system within the shell number  $z$  is given by  $V(z) = 4\pi z^3 l_B^3/3$  and a layer at co-ordinate  $z$  contains  $L(z) = (V(z) - V(z-1))/l_B^3 = 4\pi(z^2 - z + 1/3)$  lattice sites. The dimensionless inner area  $a_i$  and outer area  $a_0$  of a lattice site in layer  $z$  are given by  $a_i(z) = 4\pi(z-1)^2/L(z)$  and  $a_0(z) = 4\pi z^2/L(z)$ , respectively. These quantities determine the so-called a priori step probabilities,  $\lambda(z, z')$ , for steps from layer  $z$  to  $z'$ , where  $z'$  takes the values  $z-1$  (to the inner layer),  $z+1$  (to the outer layer), or  $z$  (within the same layer). The step probabilities are given by  $\lambda(z, z-1) = a_i(z)/6$ ,  $\lambda(z, z+1) = a_0(z)/6$  and  $\lambda(z, z) = 1 - \lambda(z, z+1) - \lambda(z, z-1)$ , respectively.

The SCF formalism features the particle potentials  $u_x(z)$  which are conjugated to the volume fractions  $\varphi_x(z)$ . These volume fractions are related to the local concentrations as  $\varphi_x(z) = c_x(z)l_B^3$ . Subscript  $x$  is used to refer to the various types of particles  $x = S, P, Na^+, Cl^-$ . The functionals  $u_x(z)$  and  $\varphi_x(z)$  are mutually dependent and are, for a given particle type, only functions of the  $z$  co-ordinate. Hence all the local properties of the system are pre-averaged over the angular co-ordinates (the spherical approximation). The total potential of a particle of type  $x$  comprises three terms:

$$u_x(z) = u'(z) + k_B T \sum_y \chi_{xy} (\langle \varphi_y(z) \rangle - \varphi_y^b) + \nu_x e \psi(z) \quad (2.10)$$

The first term is coupled to the incompressibility constraint  $\sum_x \varphi_x(z) = 1$ . The second term gives the short-range interactions, parameterized by Flory–Huggins interaction parameters  $\chi_{xy}$  between particle types  $x$  and  $y$ ; this interaction term depends on the volume fraction of the components. The term



$\langle \varphi_y(z) \rangle$  is the site average volume fraction, which is equal to  $\lambda(z, z-1)\varphi_y(z-1) + \lambda(z, z)\varphi_y(z) + \lambda(z, z+1)\varphi_y(z+1)$  (note that the site fraction causes the potential to be non-local and geometry dependent). The quantity  $\varphi_y^b$  in eq 2.10 is the concentration of monomers of type  $y$  in the bulk. The third term accounts for the electrostatic contributions. The local charge  $q(z)$  per lattice layer is given by  $q(z) = e \sum_x \nu_x \varphi_x(z)$ , where  $e$  is the elementary charge and  $\nu_x$  the valence of the particle of type  $x$ . The local electrostatic potential,  $\psi(z)$ , is related to the local charge density,  $q(z)$ , via the Poisson equation.

In order to obtain the density profiles  $\varphi_x(z)$  from the segment potentials  $u_x(z)$  one has to evaluate all possible and allowed conformations of the molecules in the potential field. In the special case of a polymeric star one has to consider the grafting constraint present on the first segments of each arm. In a first-order Markov approximation, one can compare the chain conformations of one arm of the star with segments  $s = 1, \dots, N$  with the path of a diffusing particle in an external field that starts in (or near) the center of the co-ordinate system and ends up somewhere in the system at a time  $t$  ( $= N$ ). The corresponding diffusion equation features end-point distribution functions  $G_P(z, s|z^*, 1)$  for the statistical weight of finding a chain fragment that starts with segment  $s = 1$  at  $z^*$  (grafting point) and ends in layer  $z$  with segment  $s$ , and correspondingly  $G_P(z, s|N)$  for the statistical weights of all possible and allowed conformations, with the specification that segment  $s = N$  can be anywhere in the system and again segment  $s$  is at co-ordinate  $z$ . Hence,  $G_P(z, s|N)$  is the sum of  $G_P(z, s|z', N)$  over all  $z'$ . The end point distribution functions obey, as already mentioned, the diffusion equation which, in discrete notation, can be written as:

$$\begin{aligned} G_P(z, s|z^*, 1) &= G_P(z) \langle G_P(z, s-1|z^*, 1) \rangle \\ G_P(z, s|N) &= G_P(z) \langle G_P(z, s+1|N) \rangle \end{aligned} \quad (2.11)$$

These propagator relations are started by the condition that a “walk” of one segment long should be weighted by the free segment distribution function:  $G_P(z, N|N) = G_P(z)$  for all  $z$  and  $G_P(z^*, 1|z^*, 1) = G_P(z^*)$  (grafting condition). The segmental weighting factor  $G_P(z)$  is defined as  $\exp(-u_P(z)/k_B T)$ . The segment densities follow from the composition law:

$$\varphi_P(z, s) = C_P \frac{G_P(z, s|z^*, 1) G_P(z, s|N)}{G_P(z)} \quad (2.12)$$

Here, the factor  $G_P(z)$  in the denominator corrects for the double counting of the Boltzmann weight for segment  $s$  in the nominator. The normalization factor  $C_P$  is fixed by the number of arms  $f$  in the system:

$$C_P = \frac{f \cdot N}{\sum_{z=1}^M L(z) G_P(z, N|z^*, 1)} \quad (2.13)$$

### 2.3 Dilute salt-free solution

The grafting co-ordinate of the arms of the star,  $z^*$ , is chosen such that  $L(z^* - 1) < f < L(z^*)$ . The density distributions of all monomeric components  $x \in \{S, Na^+, Cl^-\}$  follow directly from the above formalism; eq 2.12 now reduces to  $\varphi_x(z) = \varphi_x^b G_x(z)$ . Note that  $\varphi_{Na^+}^b = \varphi_{Cl^-}^b$  as the electrostatic potential vanishes in the bulk of the solution.

The set of equations as presented in this section is closed, but should be complemented by boundary conditions. As the cell is electroneutral as a whole, we set the “reflecting” boundary conditions at  $z = M$  which guarantees that there are no gradients present in the  $z$  direction between  $z = M$  and  $z = M + 1$ : i.e.,  $\psi(M + 1) = \psi(M)$ ,  $u_x(M + 1) = u_x(M)$ , etc.

The above set of equations are solved iteratively by a Newton-like method. This results in radial distributions of overall monomer densities,  $P$ ,  $S$ ,  $Na^+$ ,  $Cl^-$  as well as, e.g., the densities of end segments and all the interior segments, the segment potentials, and the electrostatic potential. It is also easy to obtain measures for the size of the star, such as the first moment of the distribution of end segments:

$$R = \frac{\sum_{z=z^*}^M L(z) \cdot (z - z^*) \cdot \varphi_P(z, N)}{\sum_{z=z^*}^M L(z) \varphi_P(z, N)} \quad (2.14)$$

Parameters are taken as simple as possible:  $\chi_{xy} = 0$  when both  $x$  and  $y$  are not  $P$ , in a good solvent  $\chi_{Py} = 0$  and under  $\theta$ -conditions  $\chi_{Py} = 0.5$ . The valences are defined as follows  $\nu_S = 0$ ,  $\nu_{Na^+} = 1$ ,  $\nu_{Cl^-} = -1$ , and  $\nu_P = m^{-1}$ . The last statement means that every monomer has the same charge, which is between 0 and  $-1$ .

### 2.3 Dilute salt-free solution: charge renormalization and intrinsic screening

We start with the analysis of the conformation of a polyelectrolyte star in a dilute, salt-free solution. The value of  $R$  and  $Q^*$  follow from solving the two implicit eqs 2.8 and 2.9 simultaneously. Previously, scaling relations for the star size as a function of the number of branches, the fraction of charged monomers, and the branch length have been derived.<sup>34</sup> In this section we compare these scaling predictions to the analytical model as described in the previous section and to the numerical SCF-results.

As follows from eq 2.8, in the dilute limit  $D \gg R$ , the distribution of counterions in the solution strongly depends on the ratio between the bare star charge  $eQ$  and the star radius  $R$ .

At  $Q \ll R/l_B$  the Coulombic attraction of counterions to the star is relatively weak and the translational entropy favours a uniform distribution in the whole available space of the solution. This means that at  $D \gg R$  (dilute limit) the average fraction of counterions localised in the volume occupied by

the star is small and charged branches interact by unscreened Coulombic repulsion. This is the case for stars with a small number of branches,  $f \ll f^*$ , where  $f^*$  corresponds to the crossover between the unscreened and the intrinsically screened stars (see below). As has been shown in literature  $f^* \cong m^{1/2} l_B^{-1}$ .<sup>34,35</sup> The stars with  $f \ll f^*$  shall be referred to as “unscreened stars”. The asymptotic expression for the dimensions of the unscreened star can be obtained from eqs 2.8 and 2.9 if the last two terms in eq 2.9 describing the contribution of the excluded volume interactions are negligibly small compared to the other terms and  $f \ll f^*$ . Balancing then the unscreened Coulombic repulsion, so  $Q^* = Q$ , with the conformational entropy losses in extended branches, gives that the star size grows with increasing number of branches as<sup>34</sup>

$$R \cong N m^{-2/3} l_B^{1/3} f^{1/3} \quad (2.15)$$

As soon as the excluded volume interactions play an important role, the effective exponent for the  $f$ -dependence of the star size is somewhat smaller. We remark that the size of a neutral star grows due to intra-branch steric repulsion with increasing number of branches as  $R \sim f^{1/5}$  or  $R \sim f^{1/4}$  under good or  $\theta$ -solvent conditions, respectively, instead of  $R \sim f^{1/3}$  as for polyelectrolyte stars.<sup>39–42</sup>

In the opposite limit,  $Q \gg R/l_B$  (corresponding to the screened stars), the Coulombic attraction becomes strong enough to win the competition with the translational entropy so that the distribution of counterions in the solution becomes strongly non-uniform. Most of the counterions remain in the volume occupied by the star, their concentration is much larger there than the average concentration in the solution, while the concentration of “free” counterions in the inter-star volume is much smaller than this average value.

The average number of “free” counterions, given by the uncompensated charge  $Q^*$  in the volume occupied by the star, is determined by eq 2.8 and presented in fig 2.2 as a function of the bare charge  $Q$ .

As follows from the fig 2.2,  $Q^*$  equals  $Q$  for small values of  $Q$ , whereas at large values of the bare charge the effective uncompensated charge  $Q^*$  grows only logarithmically with increasing  $Q$ , so that the dependence of  $Q^*$  on  $Q$  levels off. In the range of large bare charges,  $Q \gg R/l_B$ , the uncompensated charge within the volume of the star remains proportional to  $R/l_B$  (i.e., it is much smaller than the bare charge  $Q$ ). This means, in turn, that most of counterions remain effectively trapped in the interior of the star by the Coulombic attraction and only a small fraction of them is released into the bulk of the solution. This concept is known as charge renormalization and has been first proposed by Alexander et al.<sup>44</sup> for salt-free solutions of charged colloidal particles, and later by Pincus<sup>45,46</sup> for polyelectrolyte brushes.

The physical meaning of the charge renormalization threshold,  $Q^* \cong R/l_B$ , is transparent: the counterions are pulled inside the star by the Coulombic force and compensate the charge of the star unless the energy of the Coulombic attraction  $e^2 Q^* / \varepsilon R$  is smaller than the thermal energy  $k_B T$ .

### 2.3 Dilute salt-free solution

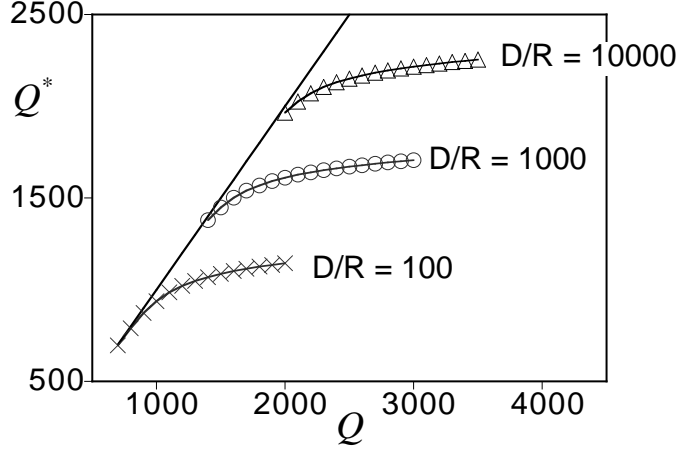


Figure 2.2: Charge renormalisation effect: an effective (uncompensated) charge  $Q^*$  within the radius  $R$  as a function of the bare (immobilised) charge  $Q$  calculated from eq 2.8 for different values of the cell size:  $D/R = 10^2, 10^3, 10^4$ , and  $R = 100$ .

With increasing number of branches,  $f$ , the Coulombic interactions get stronger, because the size of the star in the unscreened regime grows as  $\sim f^{1/3}$ , according to eq 2.15, whereas the bare charge of the star grows as  $\sim f$ . For stars with a large number of branches,  $f \gg f^*$ ,  $Q$  is no longer much smaller than  $R/l_B$ , and most of the counterions are retained in the interior of the star. These counterions ensure partial screening of the Coulombic repulsion between charged branches. In the limit  $f \gg f^*$  the terms  $\sim Q^*$  in the right-hand side of eq 2.9 are negligibly small. If we ignore the non-electrostatic (excluded volume) interactions, we derive from eq 2.9 the dependence of the size of the star as a function of the number of arms in the screened regime:

$$R(f) \cong Nm^{-1/2} \quad (2.16)$$

which indicates that the size of the many-armed star becomes independent of the number of branches. Eq 2.16 does not take into account the incomplete compensation of the star charge by counterions trapped in the intra-star space, i.e. the presence of small fraction of counterions in the inter-star space of the solution. If the latter is taken into account, a weak (logarithmical) growth instead of a plateau in the  $R(f)$  curve is expected. This regime for  $Q \gg R/l_B$  is called the osmotic regime. The reason is that eq 2.16 can be obtained also on the basis of "osmotic" arguments:<sup>34,45,46</sup> the extensional Coulombic force applied to the branches of the star is proportional to the excess osmotic pressure due to counterions trapped inside the star by the attractive Coulombic force. The balance between this osmotic pressure and the conformational free energy penalty for the extension of branches, eq 2.4, results in eq 2.16.

The alternative set of arguments leading to eq 2.16 is based on the concept

of intrinsic screening length. We introduce the Debye screening length,  $\kappa^{-1}$  as

$$\kappa^{-1} \cong (l_B c)^{-1/2}, \quad (2.17)$$

where  $c$  is the concentration of mobile ions. In this paper we use two different Debye screening lengths, the intrinsic screening length,  $\kappa_i^{-1}$ , and the screening length caused by added salt,  $\kappa_s^{-1}$ .  $\kappa_i^{-1}$  is defined as  $(l_B c_i)^{-1/2}$ , where  $c_i$  is the concentration of counterions in the intra-star space. It is easy to prove, that  $\kappa_i^{-1} \ll R$ , i.e. Coulombic interactions inside the star are screened on a scale much smaller than the star radius if the condition  $f \gg f^*$  applies. This is the basis of the local electroneutrality approximation, according to which there is a local compensation of the immobilised charge on the branches by counterions on the scales larger than  $\kappa_i^{-1}$ .

The effect of the screened Coulombic repulsion of the charged monomers on the large scale conformational properties of the star polymer is equivalent to that of the short-range binary repulsion (excluded volume interactions) and can be formally described using the effective (electrostatic) second virial coefficient<sup>‡</sup>

$$v_{eff} \cong l_B \kappa^{-2} m^{-2}, \quad (2.18)$$

The factor  $m^{-2}$  reflects the fact, that only a fraction  $m^{-1}$  of monomers is charged. The size of the star, which is dominated by short-range binary repulsive interaction between monomers (good solvent conditions), is given by

$$R \cong N^{3/5} f^{1/5} v^{1/5} \quad (2.19)$$

Taking into account the definition of  $\kappa_i^{-1}$ , and the local electroneutrality condition  $c_i \cong c_P/m$  we arrive to the known result eq 2.16.

According to eq 2.16 the star size is expected to be virtually independent of the number of branches in a certain range of  $f$ . Therefore with increasing number of branches the monomer concentration and, as a result, the relative importance of the non-electrostatic interactions between uncharged monomers increases. At very large number of branches,  $f \gg (N/m)^2$ , these non-electrostatic interactions become dominant.<sup>34</sup> Obviously, this regime is attainable only for very weakly charged,  $m \gg 1$ , stars.

If the concentrational contribution described by the last term in eq 2.9 is neglected, then eqs 2.8 and 2.9 interpolate between two asymptotic limits given by eq 2.15 and 2.16 which give the radius  $R$  for a star with small and large number of arms, respectively.

The dependencies of the star size  $R$  on the number of branches  $f$  have been calculated with the numerical SCF-model at low ionic strength of the solution,  $\varphi_{Na^+}^b = \varphi_{Cl^-}^b = 10^{-7}$ , and by simultaneous solution of eqs 2.8 and 2.9 of the analytical model. The results are shown in fig 2.3.

---

<sup>‡</sup>The second virial coefficient of two elementary charged monomers interacting via DH-potential  $u_{DH}(r)/k_B T = l_B \exp(-\kappa r)/r$  is proportional to  $\int (1 - \exp(-u_{DH}(r)/k_B T)) r^2 dr$ . The latter integral is dominated by large  $r$  that results in eq 2.18.

### 2.3 Dilute salt-free solution

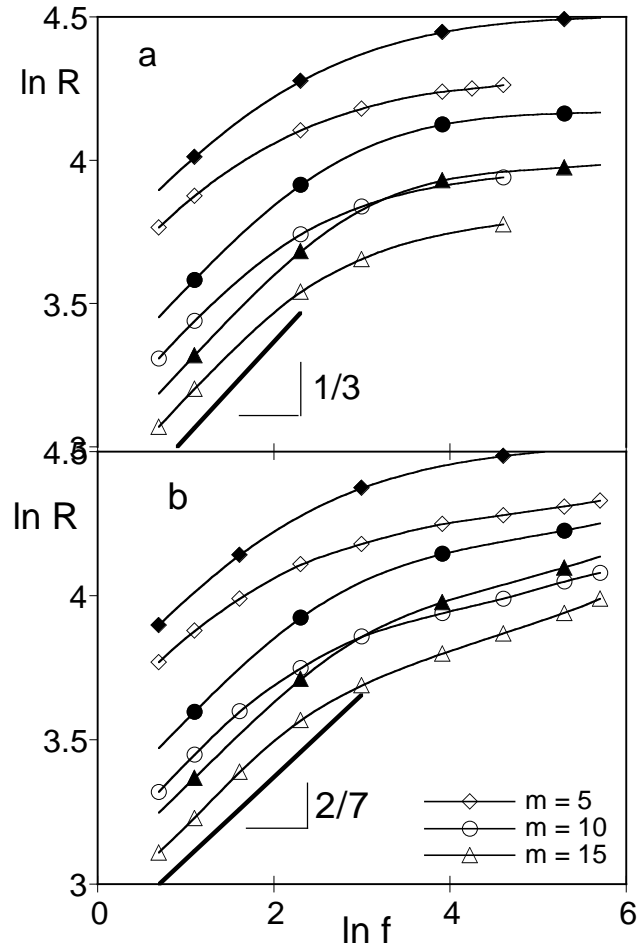


Figure 2.3: The star size  $R$  as a function of the number of branches  $f$  (in double-log co-ordinates) in a salt-free solution under  $\theta$ -(a) and good (b) solvent conditions for  $N = 200$  and for  $m = 5$ (diamonds),  $10$ (circels), and  $15$ (triangles). The curves with the filled symbols correspond to the solution of eqs 2.8, 2.9, while the lines with the open symbols correspond to results of SCF-calculation at  $\phi_s^b = 10^{-7}$  and  $D = 150$ . The bold lines show the slopes predicted by scaling.

As expected from eqs 2.15 and 2.16,  $\ln R$ , increases linearly with  $\ln f$  for the star with small number of branches and levels off for the many-armed stars. The remaining growth is mainly due to the increasingly importance of the non-electrostatic interactions of uncharged monomers and is more pronounced in a good solvent (fig 2.3b) than in a  $\theta$  solvent (fig 2.3a).

The initial slope of  $\ln R$  vs.  $\ln f$  curves is close to  $1/3$  (eq 2.15) in a  $\theta$  solvent ( $m = 5, 10, 15$ ) and is close to  $2/7$  in a good solvent, as predicted earlier.<sup>34</sup> For  $m = 2$  (not shown in fig 2.3) the initial slope is significantly smaller because the fraction of charged monomers is large enough to induce intrinsic screening by counterions even at small values of  $f$  ( $f^* \sim m^{1/2} \sim 1$  in this case).

The two methods of calculation give the same trends, although the analytical approach gives systematically a larger star radius than the SCF-calculations. This difference is not surprising in view of the uniform charge density approximation used in our analytical model. The latter approximation becomes especially poor in the inter-star region where the actual distribution of counterions is strongly non-uniform. This non-uniform distribution is fully taken into account in the SCF-calculations.

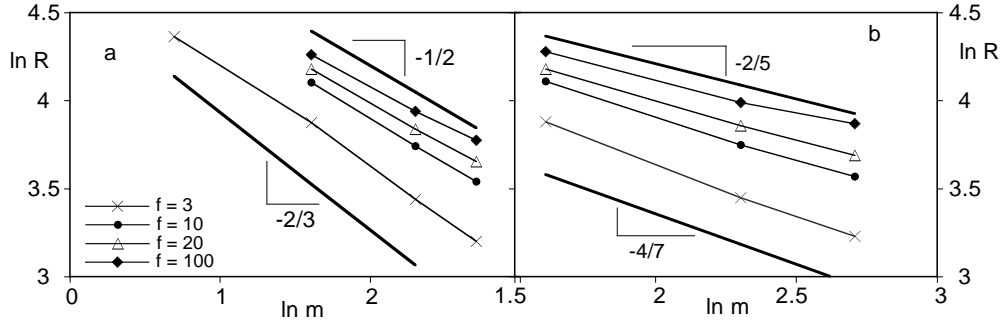


Figure 2.4: The star size  $R$  as a function of  $m$  (in double-log co-ordinates) for  $f = 3$ (crosses), 10(dots), 20(triangles), and 100(diamonds), under  $\theta$ - (a) and good (b) solvent conditions.  $N = 200$ ,  $D = 150$ , and  $\phi_s^b = 10^{-7}$ . The bold lines show the slopes predicted by scaling.<sup>34</sup>

It is instructive to analyse the  $m$ -dependence of the size of stars for different values of  $f$ . Fig 2.4 shows a double-logarithmic plot of  $R$  as a function of  $m$ . We see that with increasing  $f$  the absolute value of the slope of  $\ln R$  vs.  $\ln m$  curves systematically decreases from  $\cong 0.66$  to  $\cong 0.5$  in a  $\theta$  solvent and from  $\cong 0.57$  to  $\cong 0.4$  in a good solvent, which is in accordance with the prediction of eqs 2.15, 2.16 and the results of the scaling analysis.<sup>34</sup> This gives thus an indication that the (asymptotic) unscreened and osmotic regimes at small and large  $f$ , respectively, really exists.

The SCF-method allows us to get a better insight in the intrinsic structure of the star through the analysis of radial distribution of the monomer and

### 2.3 Dilute salt-free solution

counterions densities. Fig 2.5 shows the radial decay of the monomer density

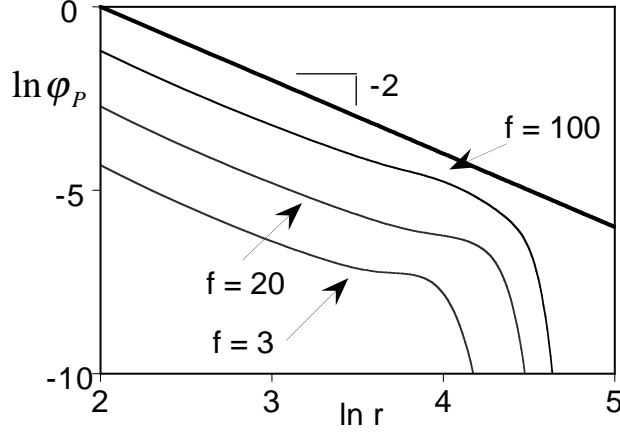


Figure 2.5: The monomer density profile  $\varphi_P(r)$  (in double-log co-ordinates) for stars with a different number of branches  $f$  ( $\theta$ -solvent conditions,  $N = 200$ ,  $m = 5$ ,  $D = 150$ , and  $\phi_s^b = 10^{-7}$ ). The bold line indicates the slope -2 corresponding to a uniform extension of the branches.

in log-log co-ordinates for stars with a different number of branches ( $f = 3, 20, 100$ ). We see that in a wide range of  $r$ , corresponding to the internal region  $r < R$ , the slope is close to -2, which indicates a uniform extension of the branches. This is expected because  $R \sim N$ , according to eqs 2.15 and 2.16, both for unscreened and osmotic stars.<sup>35</sup>

The extension vanishes (i.e. the local tension vanishes) at the free ends of branches. Fig 2.6 presents the radial distribution of the free chain ends, normalised for one branch, in stars with a different number of branches.<sup>§</sup> The free ends are localised in a relatively narrow range near the edge of the star. The fluctuations in the overall extension of branches are nearly Gaussian in stars with a relatively small number of branches ( $f \leq 50$ , see fig 2.6). With increasing number of branches the position of the maximum of the distribution shifts to larger  $r$ , which reflects an increase in the overall extension. However, as we have discussed above, for many-armed stars the average star size (i.e. the position of the maximum in the  $\varphi_e(r)$  curve) is virtually independent of the number of branches. This feature is clearly demonstrated in fig 2.6. It is important to note that the distribution of the free ends is wide for large  $f$ ; its shape becomes asymmetric and is reminiscent of the distribution of free chain ends in a planar polyelectrolyte brush.<sup>11,47</sup> In other words, near the edge of a many-armed star the effect of curvature is weak and the structure of the peripheric region of the star resembles with that of a planar polyelectrolyte

<sup>§</sup>The normalised to one branch end segment distribution has been calculated as  $\varphi_e(z) = L(z)\varphi(z|N)/f$ .



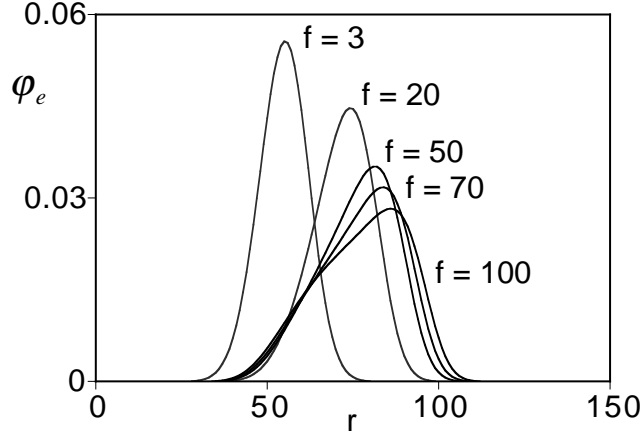


Figure 2.6: The radial distribution  $\varphi_e(r)$  of the end monomers of the star (normalised for one branch) for stars with a different number of branches  $f$  ( $\theta$ -solvent conditions,  $N = 200$ ,  $m = 5$ ,  $D = 150$ , and  $\phi_s^b = 10^{-7}$ ).

brush. As a rough estimate for the onset of the developing of the asymmetry of the  $\varphi_e(r)$  distribution, we can use the condition  $\kappa_i^{-1} \leq N^{1/2}$ , which implies that the electrostatic field gets screened on the lengths smaller than the range of the Gaussian fluctuations of extended branches of the star. This condition results in  $f \geq f^* N/m$ . For the set of parameters used in fig 2.6 we calculate that the number of arms should be larger than 40, which agrees with the observation noted earlier. At larger  $f$  the intrinsic screening length  $\kappa_i^{-1}$  at the edge of the star is smaller than the range of Gaussian fluctuations of the extension of branches and we expect quasi-planar behaviour of the periphery of the star. We mention the direct analogy between this observation and that in the literature,<sup>48</sup> where the intrinsic structure of neutral polymer stars was studied by the numerical SCF-method.

Fig 2.7 gives an illustration of the distribution of counterions inside the star and in the bulk of the solution around the star. In order to illustrate the degree of localisation of counterions in many-armed stars, we present both the counterion and the polymer densities (the latter is divided by  $m$ ). Both densities are normalised for one branch. As follows from fig 2.7, at small  $f$  the counterions spread fairly uniformly over the cell volume. With increasing  $f$  the counterions become more and more localised inside the star. At large  $f$  the radial profile of counterions and charged monomers inside the star approach each other, which illustrates the local electroneutrality in the many-armed stars. The deviation from local electroneutrality becomes significant in the peripheric regions close to the edge of the star, see insert in fig 2.7. The local concentration of monomers (and of counterions) there is such that the local screening length becomes comparable to the total star size.<sup>35</sup>

Fig 2.8 presents the fraction of “trapped” counterions (localised at  $r \leq R$ ,

## 2.4 Dilute solution: screening by added salt

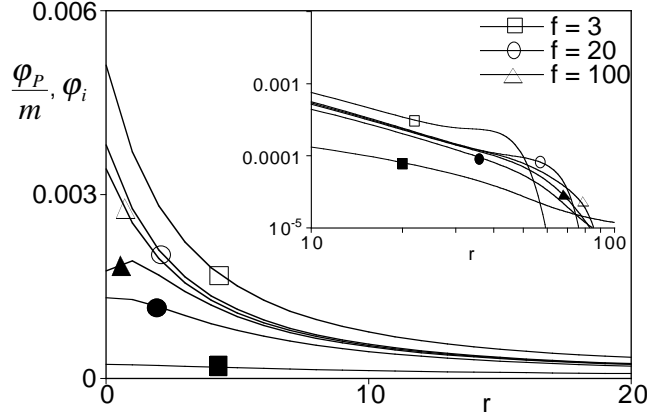


Figure 2.7: The radial distribution of charged monomers and counterions (normalised for one branch) in stars with a different number of branches  $f$ . The curves with the filled marks correspond to the distribution of counterions  $\varphi_i$ , those with the open symbols give the monomer distribution  $\varphi_P/m$ . ( $\theta$ -solvent conditions,  $N = 200$ ,  $m = 5$ ,  $D = 150$ , and  $\phi_s^b = 10^{-7}$ ).

where  $R$  is the average end position) as a function of  $f$ . With increasing  $f$  the fraction of trapped counterions systematically increases and it tends to 1 for large  $f$ . This constitutes a direct proof of the localisation of counterions in many-armed stars, i.e. the existence of the osmotic regime.

## 2.4 Dilute solution: screening by added salt

The addition of low-molecular-weight salt to a solution of branched polyelectrolytes results in additional screening of the Coulombic repulsion between charged branches of the stars and in a de-swelling with increasing salt concentration.

As we have demonstrated in the previous section, the intramolecular Coulombic repulsion in many-armed stars is already partially screened in the salt-free solution by counterions localised preferentially in the intra-star space. The degree of localisation of counterions and the effect of intrinsic screening depends strongly on the number of branches. Hence the effect of additional screening by salt is expected also to be strongly dependent on the number of branches in the star.

As was discussed earlier,<sup>35</sup> the larger the number of branches, the higher is the salt concentration required to affect the conformation of the star. In other words, the salt concentration in the bulk of the solution  $c_s^b$  must exceed significantly the intrinsic concentration of counterions  $c_i \cong c_P/m$  in order to affect the star conformation (i.e., to induce de-swelling of branches). So at small salt concentration,  $c_s^b \ll c_i$ , the intramolecular screening is dominated by

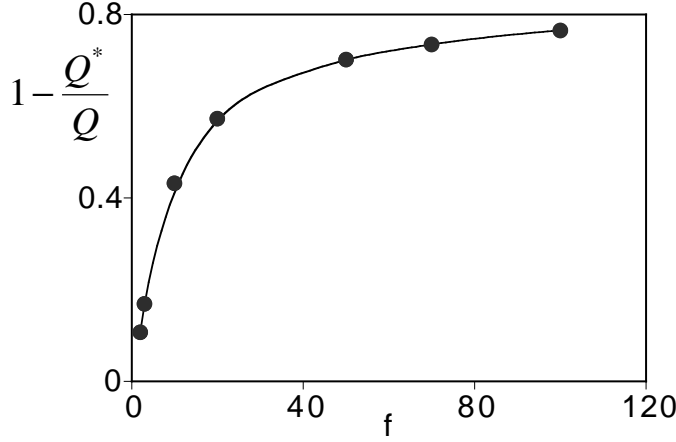


Figure 2.8: The fraction of counterions localised inside the star (at  $r < R$ ) as a function of the number of branches  $f$  ( $\theta$ -solvent,  $N = 200$ ,  $m = 5$ ,  $D = 150$ , and  $\phi_s^b = 10^{-7}$ ).

counterions, while in the limit of high salt,  $c_s^b \gg c_i$ , both co- and counterions contribute significantly to the screening of the intra-star Coulombic repulsion.

The size of the star in the salt-dominance regime can be derived using the same mean-field arguments as used for the star screened by counterions only. The effective (electrostatic) second virial coefficient,  $v_{eff} \cong l_B \kappa^{-2} m^{-2}$ , is determined by the bulk screening length,  $\kappa_s^{-1} \cong (l_B c_s^b)^{-1/2}$  and substitution into eq 2.19 gives

$$R \cong N^{3/5} f^{1/5} m^{-2/5} (c_s^b)^{-1/5} \quad (2.20)$$

The same result has been obtained in the literature on the basis of osmotic arguments by balancing elasticity of the branches with the differential (excess) osmotic pressure of all types of mobile ions inside and outside the star.<sup>35</sup>

Fig 2.9 presents the results of SCF-calculations for the star size  $R$  as a function of the bulk volume fraction of salt  $\varphi_s^b \equiv \varphi_{Na^+}^b \equiv \varphi_{Cl^-}^b$  in the range of  $\varphi_s^b$  from  $10^{-7}$  to  $10^{-1}$  corresponding to the variation of the Debye screening length (measured in the monomer lengths) from approximately 200 to unity. The number of monomers per branch is equal to  $N = 200$ , the fraction of charged monomers is set equal to 0.2 (i.e.  $m = 5$ ). Different curves correspond to a different number of branches  $f$ , which number is varied over a wide range,  $3 < f < 200$ .

All the curves in fig 2.9a are normalised to the value at “low” salt (at  $\varphi_s^b = 10^{-7}$  in our calculations). At large  $f$  there is a well-developed plateau at small salt concentration where  $R = R_{low}$ , corresponding to a predominance of counterions in the intramolecular screening. With increasing salt concentration the salt starts to contribute to the screening and gradual de-swelling of stars occurs. The larger the number of branches  $f$  in the star, the higher is the salt

## 2.4 Dilute solution: screening by added salt

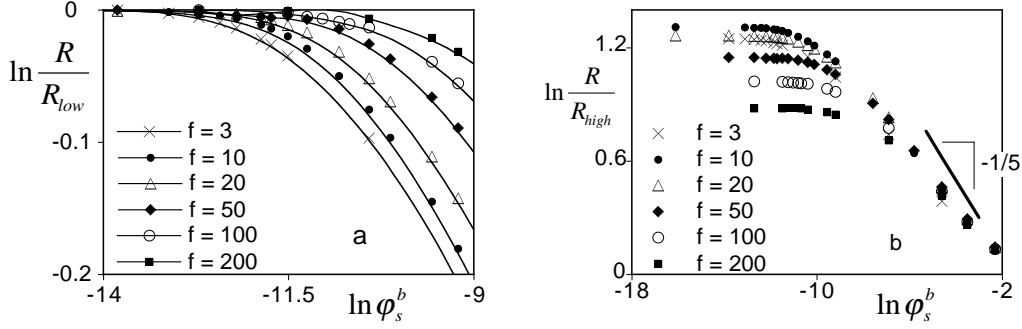


Figure 2.9: The star size  $R$  as a function of the volume fraction of salt in the bulk  $\phi_s^b$  (in double-log co-ordinates) for stars with a different number of branches  $f$  under  $\theta$ -solvent conditions;  $N = 200$ ,  $m = 5$ . In fig 2.9a the star size  $R$  is normalised to its value at  $\phi_s^b = 10^{-7}$ ,  $R_{low}$ , while in fig 2.9b it is normalised to its value at  $\phi_s^b = 10^{-1}$ ,  $R_{high}$ . The bold line shows the slope predicted by scaling.<sup>35</sup>

concentration where the onset of this de-swelling is found.

In the limit of large salt concentration (the salt-dominance regime)  $\ln R$  decreases almost linearly with  $\ln \phi_s^b$ , as demonstrated in fig 2.9b, where the size of the stars is normalised to their values at “high” salt concentration  $\phi_s^b = 10^{-1}$ . The slope is found to be close to  $-1/5$  as predicted by eq 2.20.

Fig 2.10 presents the evolution of the monomer density profile (in log-log co-ordinates) for a star with  $f = 20$  at several ionic strengths. The slope of  $\ln \varphi_P(r)$  vs.  $\ln r$  curves in central part of the star progressively decreases from around  $-2$  in the salt-free regime to around  $-4/3$  at high salt concentration. The power law  $\varphi_P \sim r^{-4/3}$  for the radial decay of the monomer density is typical for a star swollen by short-range binary repulsive interaction between the monomers<sup>¶</sup> and has been predicted for the salt-dominance regime.<sup>35</sup>

Fig 2.11 shows the relative volume fractions of co- and counterions inside the star as a function of  $\phi_s^b$  for different values of  $f$ . For a star with a small number of arms and low  $\phi_s^b$  the concentration of ions inside the star is relatively close to the bulk value. For large  $f$  the concentration of counterions inside the star is much bigger than the bulk volume fraction  $\phi_s^b$  but the difference becomes smaller as  $\phi_s^b$  increases and the salt dominance regime is approached.

<sup>¶</sup>The exponent  $-4/3$  for the density profile directly follows from the exponent  $3/5$  for the molecular weight dependence of the overall star size, see eq 2.20.

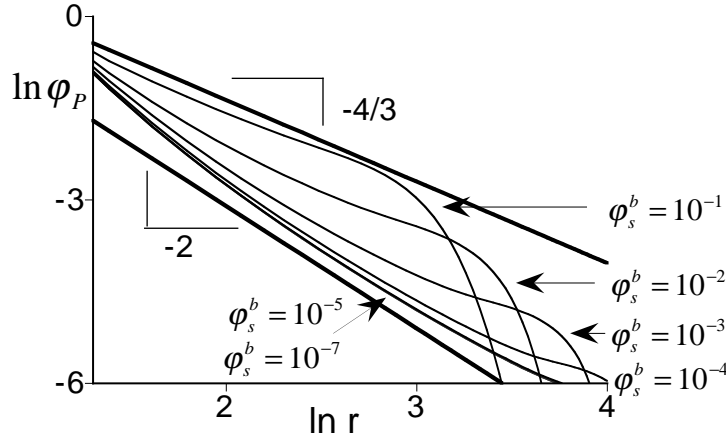


Figure 2.10: The monomer density profile (in double-log co-ordinates) of a star with  $f = 20$  branches under  $\theta$ -solvent conditions at different salt concentrations (shown in the figure);  $N = 200$ ,  $m = 5$ ,  $D = 150$ . The bold lines show the slopes predicted by scaling.<sup>35</sup>

## 2.5 Concentrational effects in dilute solution: the star contraction and the overlap threshold

The behaviour of charged macromolecules with increasing concentration in the solution is qualitatively different from that of neutral ones, because of the long-range character of intramolecular Coulombic interaction and the screening effect of counterions. This difference is most pronounced in a salt-free case. In the high-salt-concentration regime strongly screened Coulombic interactions are equivalent to short-range excluded volume interactions. In the latter case, charged polymers behave like neutral ones under good solvent conditions (see previous section).

In dilute solutions (and in a good solvent) neutral polymers are swollen due to short-range intramolecular excluded volume repulsion of monomers. This swelling is the same (with the accuracy of weak concentrational effects) in the whole range of dilute solutions, i.e. at all concentrations below the overlapping threshold  $c^*$ . At concentrations above  $c^*$  the intramolecular excluded volume repulsion gets partially screened due to other polymers. This screening becomes stronger and, correspondingly, the polymer de-swells, as the concentration of the solution increases. The chains approach their Gaussian (ideal) dimensions as the volume fraction (the concentration of polymer in the solution) approaches unity. For neutral polymers screening of intramolecular interactions occurs only above  $c^*$ , i.e. in the semi-dilute regime. The overlap threshold is thus determined by the polymer size  $R$  in the dilute solution as

## 2.5 Increasing the polyelectrolyte concentration

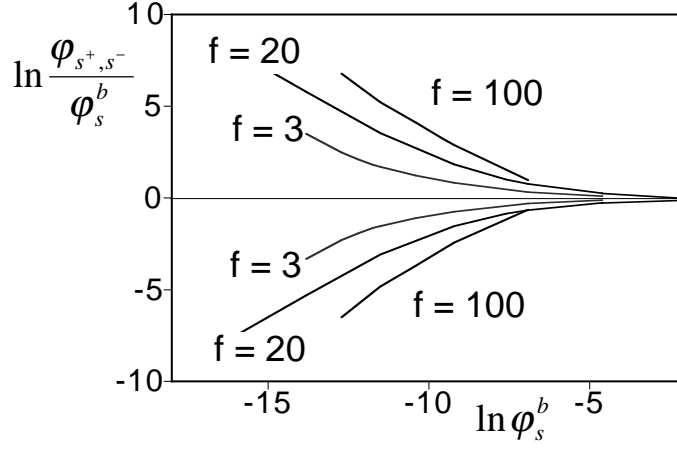


Figure 2.11: The ratios of the average concentrations of co- and counterions inside the star to the bulk value as a function of the volume fraction of salt in the bulk  $\phi_s^b$  (in double-log co-ordinates), for stars with a different number of branches  $f$  under  $\theta$ -solvent conditions;  $N = 200$ ,  $m = 5$ , and  $D = 150$ .

$c^* \cong N/R^3$ .<sup>49</sup> Concentrational effects in solution of neutral polymer stars have already been extensively discussed.<sup>39,41,42</sup>

The swelling of charged polymers in dilute solution is determined by the intramolecular Coulombic repulsion. Due to the presence of counterions, which are spread all over the volume of the solution because of entropic reasons, this intramolecular repulsive interaction gets progressively screened with increasing solution concentration even below the geometrical overlapping threshold for polyions. With increasing concentration of polyelectrolytes (and of the counterions) in the solution the corresponding screening length becomes progressively smaller. The intra-chain repulsion becomes weaker and, as a result, de-swelling of polyelectrolytes occurs.

As discussed in Section 2.3, the distribution of counterions in dilute solutions of branched polyelectrolytes is strongly inhomogeneous: the local density of counterions in the intramolecular space is larger than the average in the solution. This inhomogeneity gets more pronounced with increasing degree of branching and becomes extreme (trapping of most of counterions) in solution of many-armed stars. Hence, one can expect that

- i. Polyelectrolyte molecules in a salt-free solution exhibit considerable de-swelling with increasing concentration of polyelectrolytes below the overlapping threshold.
- ii. The overlapping threshold is determined not by the polyelectrolyte size in the highly dilute limit, but by the actual (much smaller) size which polyelectrolytes attain at the crossover between dilute and semi-dilute regimes.

- iii. The de-swelling induced by an increase of the solution concentration in the dilute regime is more pronounced for weakly branched polyelectrolytes; strongly branched ones are less sensitive to the solution concentration below the overlap threshold.

The last statement is the most important for us and is based on the fact that the concentration of counterions in the intermolecular space in a dilute solution of strongly branched polyelectrolytes is low in comparison to their intramolecular concentration.

In order to check these predictions we have performed SCF-calculations for the stars with different numbers of branches in a cell with a variable radius  $D$ .

The polymer density and the free-end distributions as well as the counterions distributions were calculated in order to get insight in the conformational changes which occur in a polyelectrolyte star with increasing concentration of the solution in the dilute regime (below the overlap threshold).

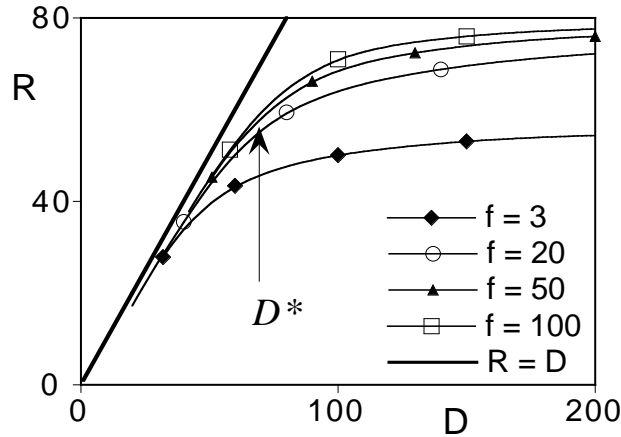


Figure 2.12: The star size  $R$  as a function of the cell radius  $D$  for different number of branches  $f$  ( $\theta$ -solvent conditions,  $N = 200$ ,  $m = 5$ ,  $\phi_s^b = 10^{-7}$ ). The "confinement" line  $R = D$  is shown for comparison.

Fig 2.12 presents the average star size as a function of the cell radius  $D$  for different values of  $f = 3, 20, 50, 100$  and  $N = 200, m = 5$ . The bold line  $R = D$  indicates the regime of "geometrical confinement" of the star in a cell corresponding to the close packing of stars in the solution. All the stars exhibit a significant decrease in size with decreasing  $D$  (increasing concentration) in the range  $R \leq D$ , i.e.  $D \geq D^*$ . Here we define the cell size  $D^*$  in analogy to the overlapping concentration of the solution  $c^*$ , this means that for  $D^*$  the star size  $R$  is the same as the shell size  $D^*$ ,  $R(D^*) \cong D^*$ . In order to get a better estimate for  $D^*$ , we have to analyse the evolution of the star intrinsic conformational structure with increasing solution concentration (decreasing  $D$ ). From fig 2.13, presenting the radial distribution of the free ends of a star,

## 2.5 Increasing the polyelectrolyte concentration

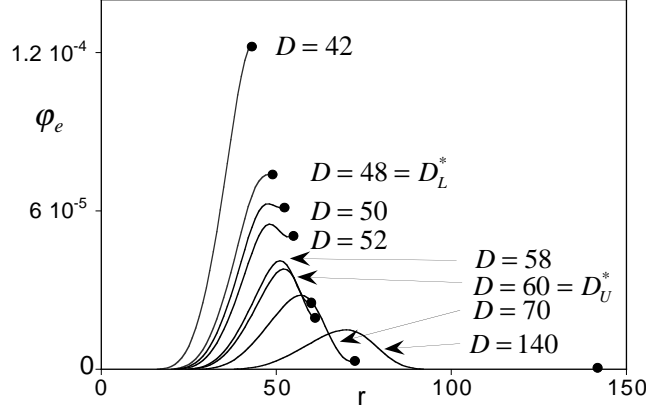


Figure 2.13: An example of the radial distribution of the end monomers  $\varphi_e(r)$  for a star with  $f = 20$ ,  $N = 200$ ,  $m = 5$ ,  $\phi_s^b = 10^{-7}$ , and  $\theta$ -solvent conditions, at different cell sizes  $D$ . The dots denote the end of the cell.

it follows that roughly three stages of the star contraction with decreasing  $D$  can be distinguished.

The first stage,  $D \gg R$ , the star size decreases due to enhanced screening of intra-star repulsion by counterions which are progressively pushed into the intra-star volume as the overall available volume of the cell decreases. The maximum of the end-segments density distribution gets progressively displaced to smaller  $r$ , but retains its symmetrical (Gaussian) shape. In fig 2.13 this is the case for  $D \geq 70$ .

However, the star size decreases with decreasing  $D$  not as rapidly as the cell radius and at sufficiently small  $D$  the right wing of the end-monomers distribution becomes truncated at the cell edge,  $r = D$ , and the distribution loses its symmetry. In fact, this marks the beginning of overlapping of stars in the solution and corresponds to the crossover between dilute and semi-dilute regimes. With decreasing  $D$  the right wing of the distribution becomes more and more narrow and the maximum of the distribution becomes higher and approaches the cell edge.

Finally, upon decreasing  $D$  even further the maximum (and the right wing) in the distribution disappears and the density of end segments becomes a monotonically increasing function from the centre of the cell to the periphery (this is the case for  $D \leq 48$  in fig 2.13). This last regime corresponds obviously to the geometrical confinement of the star in the cell.

It is natural to associate the second stage of contraction, when the symmetry of the free ends distribution is already perturbed by the presence of the cell wall at  $r = D$ , but the maximum of the distribution is still localised at  $r < D$ , with the crossover region between dilute and semi-dilute solution. For the conditions of fig 2.13, this is the case for  $50 \leq D \leq 60$ . Hence we can estimate  $D^*$



from above using the condition  $D^* - R(D^*) \cong \Delta$ , where  $\Delta$  is the width of the free ends distribution. The lower estimate for  $D^*$  is given by the condition of the disappearance of the maximum in the free ends distribution. The upper estimate for  $D^*$  is given by the condition that the volume fraction of the end segments at  $D$  is half the value of the maximum, i.e.  $\varphi_{e,max} = 2\varphi_e(D)$ . The upper and the lower estimates for  $D^*$  are referred as  $D_U^*$  and  $D_L^*$ , respectively, both are indicated in fig 2.13.

Of course this difference is only important for finite  $N$ . For sufficiently long branches the width,  $D_U^* - D_L^*$ , of this crossover regime is relatively small (in comparison to the overall star size or to  $D^*$ ) and the difference between lower and upper estimates for  $D^*$  becomes irrelevant.

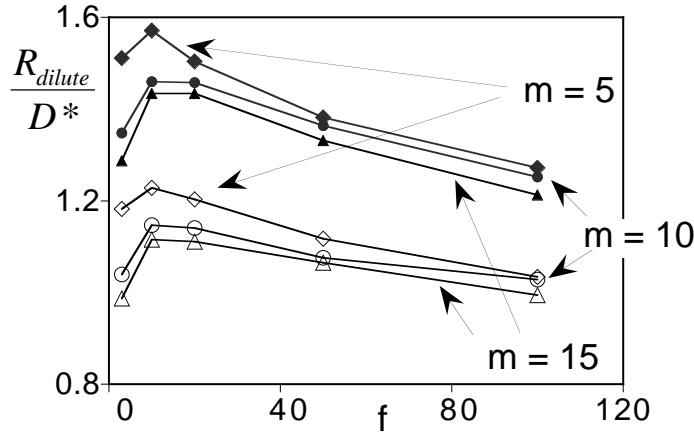


Figure 2.14: The relative magnitude of the maximal star contraction in the dilute regime,  $R_{dilute}/D^*$  as a function of the number of branches  $f$  for different  $m$ , which are indicated in the graph ( $\theta$  solvent,  $N = 200$ , and symbols refer to  $D_U^*$  and the filled symbols to  $D_L^*$ ).

Fig 2.14 presents the ratio  $R_{dilute}/D^*$ , where  $R_{dilute}$  is the star size at infinite dilution, so for  $D = \infty$ .  $R_{dilute}/D^*$  characterises the magnitude of contraction of the star in the dilute regime as a function of the number of branches in the star  $f$ . In the calculations, it is not possible to take  $D$  infinitely high so  $D$  is taken 200. In accordance to our expectations for many-armed stars, the larger the number of branches in the star, the less sensitive is the polyelectrolyte star size to the concentration increase in the dilute regime. For a many-armed star the magnitude of this contraction is not large. We expect that in the limit  $f = \infty$  the  $D^*$  tends to the star size in a highly dilute solution. An opposite trend, i.e. an increase of the ratio  $R_{dilute}/D^*$  for the stars with small number of branches is remarkable.

In order to analyse the dependence of  $D^*$  on the star parameters, we can use the following arguments. Near the overlap threshold,  $R \cong D$ , the concentration

## 2.5 Increasing the polyelectrolyte concentration

of counterions is almost uniform throughout the solution, i.e.  $Q^*/Q \leq (1 - (R/D)^3)$ . Under these conditions the second, osmotic, term in the right-hand-side of eq 2.9 predominates over other terms. Expanding the right-hand-side of eq 2.8 in powers of  $(1 - (R/D)^3)$  and substituting the result in eq 2.9 we obtain (neglecting the excluded volume interactions)

$$D^* \cong R^* \cong (l_B N^3)^{1/4} \Delta^{1/4} (f/m^2)^{1/4} \quad (2.21)$$

We expect that the above equation is valid in a wide range of  $f$  including  $f \geq f^*$  provided  $\Delta$  is larger than the intrinsic screening length near the edge of the star. In fig 2.15 calculated values of  $D^*$  are plotted vs.  $f/m^2$  on a double

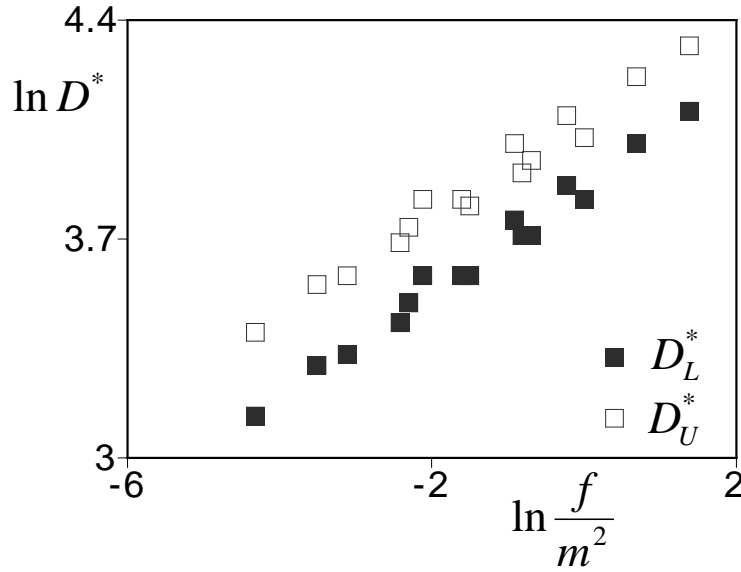


Figure 2.15: The parameter  $D^*$  as a function of  $f/m^2$  for different  $f$  and  $m$ . The open symbols refer to  $D_U^*$  and the filled symbols to  $D_L^*$ .

logarithmic scale. The observed dependence is close to a linear one that is expected from the scaling arguments presented above. The slope is smaller than it follows from eq 2.21 under the assumption of Gaussian fluctuations of the extension of branches, i.e.  $\Delta \sim N^{1/2}$ . This difference can be explained by non-negligible contribution of other interaction terms in eq 2.9.

Comparing eq 2.21 to eqs 2.15 and 2.16 we find, that the ratio  $R_{dilute}/D^*$  is expected to vary non-monotonically with increases in  $f$ , i.e. weakly increase for small  $f \leq f^*$  and decrease for large  $f$ . This conclusion is in qualitative agreement with fig 2.14.

It is instructive to compare the conformational changes in the star induced by an increase of the salt concentration (at small and constant concentration of polyelectrolytes in the solution) or by an increase of the polyelectrolyte concentration at low and constant concentration of salt. In the latter case the screening of intramolecular Coulombic repulsion is provided by counterions, while in the former case both co- and counterions contribute to screening.

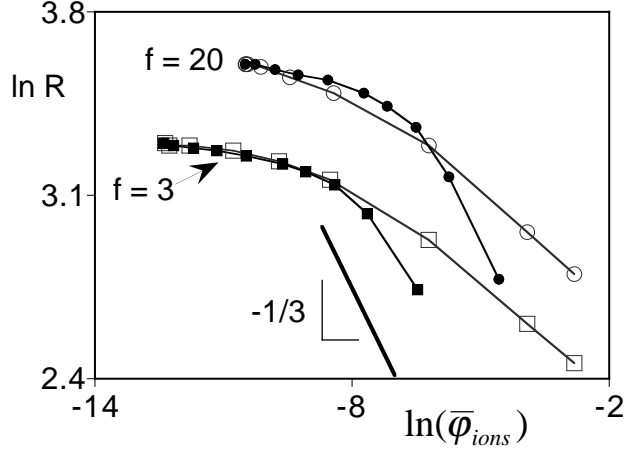


Figure 2.16: The star size  $R$  as a function of the average volume fraction of mobile ions  $\bar{\phi}_{ions}$  in the cell (in double-log co-ordinates);  $f = 3$  and  $20$ ; ( $\theta$  solvent,  $N = 100$ ,  $m = 5$ ). The open symbols refer to the case where the salt concentration is varied and  $D = \text{const} = 200$ . The filled symbols correspond to the calculations where  $\phi_s^b = \text{const} = 10^{-7}$  and  $D$  is varied.

In fig 2.16 the star size is plotted as a function of average volume fraction of the mobile ions  $\bar{\phi}_{ions}$  in the cell. Open points correspond to a salt-induced de-swelling of the star, whereas filled points show the decrease in the star size with decreasing cell size (equivalent to the increase in the concentration of stars in the solution). The "initial" points of both curves correspond to the star in the cell of radius  $D = 200$  and bulk value of the salt concentration  $\phi_s^b = 10^{-7}$  and, obviously, coincide.

At high salt concentration the star size  $R$  decreases as  $R \sim (\phi_s^b)^{-1/5}$ , which corresponds to linear the part of the curve describing screening by salt; the slope is close to predicted value of  $-1/5$ . For the salt-free case large values of  $\bar{\phi}_{ions}$  correspond to a small cell size  $D$  when geometrical confinement of the star in a cell occurs,  $D < D^*$ . Therefore, the  $\ln R$  vs.  $\ln \bar{\phi}_{ions}$  curve tends to become linear with a slope  $-1/3$ ,<sup>||</sup> thus going below the curve of screening by added salt.

The relative strength of intra-star screening (manifested in the star size) due to added salt or due to increased polyelectrolyte concentration in the intermediate range depends on the degree of branching.

For  $f = 3$  the distribution of counterions between inter- and intra-star space is in a salt-free case almost uniform even in dilute solution (see fig 2.7) and becomes more uniform with increasing concentration of the solution. As a result, the enhanced screening effect of polyelectrolyte concentration appears

<sup>||</sup>The slope  $-1/3$  follows directly from the condition that the  $\bar{\phi}_{ions} \sim D^{-3}$  and in the confinement regime  $R \sim D$ .

## 2.6 Discussion and conclusions

to be almost the same as that of the salt concentration in a wide range of concentrations below  $c^*$  (corresponding to the overlap of the stars in a salt-free solution).

The situation is different in the solution of many-armed stars,  $f = 20$ , where the distribution of counterions (in the absence of salt) at small concentrations of polyelectrolytes is strongly non-uniform (see again fig 2.7). At concentrations far below the overlap threshold  $c^*$  a decrease of inter-star distance (decrease in  $D$ ) does not affect significantly the intra-star screening and star conformation, because intra-star space contains only a small fraction of all counterions. As a result, the star remains more swollen than in the salt-added solution with the same average concentration of mobile ions. The star size starts to decrease rapidly (as  $R \sim c^{-1/3}$ ) as the overlap threshold is approached and the confinement of the stars comes into play. This behaviour is consistent with earlier scaling prediction for the many-armed polyelectrolyte stars.<sup>34</sup> We remark that for many-armed stars the regime of close packing without considerable interpenetration is expected to occur in a wide range of concentrations above the overlap threshold,  $c > c^*$ , i.e. in a semi-dilute solution. Therefore we expect that our cell model provides a correct description of the cross-over between dilute and semi-dilute regimes, although it loses its applicability above the overlap threshold  $c^*$ .

The concentrational effects in the regime of dilute solution become less pronounced as salt is added to the solution of star polyelectrolytes. The salt concentration imposes the bulk screening length,  $\kappa_s^{-1} \cong l_B(\varphi_s^b)^{-1/2}$ . We expect that the concentrational effects are negligible unless the inter-star distance,  $D$ , is smaller than  $\kappa_s^{-1}$ . On the other hand, the intramolecular screening turns to be dominated by salt when the bulk screening length  $\kappa_s^{-1}$  becomes smaller than the intrinsic screening length  $\kappa_i^{-1}$ , which, for many-armed stars is much smaller than the overall star size  $R$ .

In figs 2.17 and 2.18 we give some additional information on the behaviour of  $D^*$  as a function of the bulk volume fraction of salt  $\varphi_s^b$ . Fig 2.17 shows that for high salt concentration  $D^*$  becomes close to  $R_{dilute}$ . In this regime the charge is almost completely screened and the polyelectrolyte star behaves like a neutral one. In fig 2.18, it is shown that  $D^*$  depends in the same way as  $R$  on  $\varphi_s^b$ , see also eq 2.19.

## 2.6 Discussion and conclusions

On the basis of the numerical SCF-approach we have analysed the conformational structure of star-branched polyelectrolytes in dilute solution. The effect of the degree of branching and the salt and polyelectrolyte concentrations on the screening of intramolecular Coulombic repulsion was studied systematically. The SCF-results confirm the general trends predicted earlier on the basis of scaling approach and give a better insight in the behaviour in the cross-over regions, where non-power dependencies of large-scale and local conformational

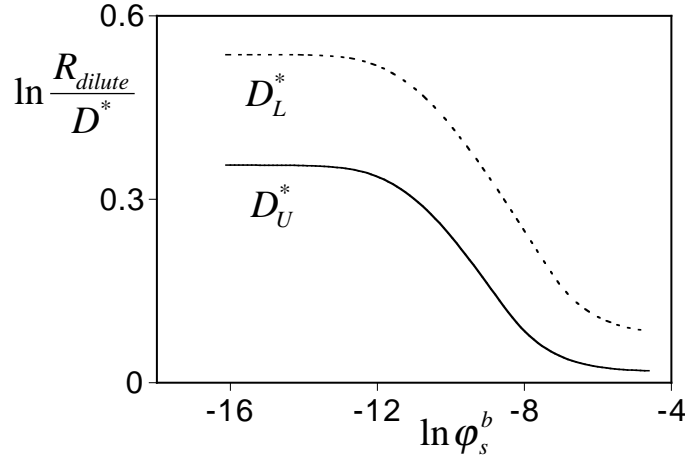


Figure 2.17: The relative magnitude of the maximal star contraction in the dilute regime,  $R_{dilute}/D^*$  as a function of the volume fraction of salt in the bulk  $\phi_s^b$  (in double log scale). The solid curve corresponds to  $D_U^*$  and the dotted curve to  $D_L^*$  ( $\theta$ -solvent conditions,  $N = 200$ ,  $m = 5$ ,  $f = 20$ ).

properties on the molecular and solution parameters play an important role.

It is shown, that in dilute salt-free solutions the distribution of counterions is strongly inhomogeneous: their local concentration is much higher in the intra-star space and rapidly decreases in the bulk of the solution. The effect of localisation of the counterions in the intra-star space becomes stronger with an increasing number of branches  $f$  in the star. As a result, the intramolecular Coulombic repulsion in many-armed stars is strongly screened. This is manifested in a levelling off of the  $f$ -dependence on the star size at large  $f$ .

We remark that the mean-field approach used in the present paper does not allow to take into account the fluctuation-induced attractive electrostatic forces between the star branches. These forces arise due to strong local fluctuations of the concentration of counterions near strongly charged polyions and become important at sufficiently large values of the Bjerrum length. One can expect that this effect is stronger for highly branched polyions in comparison to that for linear ones because of larger concentration of counterions in the intra-star space. However, the analysis of this phenomenon leads beyond the Poisson–Boltzmann approximation used in the present paper.

With increasing concentration of polyelectrolytes, the decrease in the translational entropy of counterions results in their progressive re-distribution from the bulk of the solution to the intra-star space and in additional screening of the Coulombic repulsion between charged monomers. Therefore the star size decreases. Significant star contraction is observed with increasing concentration of polyelectrolytes in the regime of dilute solution, i.e. below the overlap threshold for branched polyions. The effect is less pronounced in a solution of many-armed stars which retain most of the counterions in the intra-star space

## 2.6 Discussion and conclusions

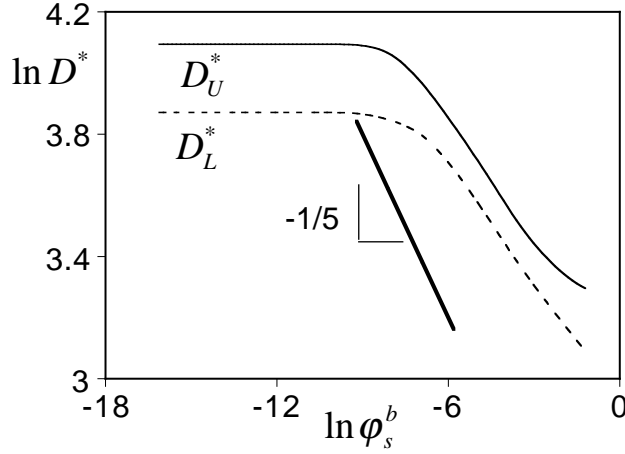


Figure 2.18: The parameter  $D^*$  as a function of the volume fraction of salt in the bulk  $\phi_s^b$  (in double log scale). The solid curve corresponds to  $D_U^*$  and the dotted curve to  $D_L^*$  ( $\theta$  solvent,  $N = 200$ ,  $m = 5$ ,  $f = 20$ ).

even in the dilute regime. In this case an increase in the average solution concentration does not affect the local (intramolecular) counterion concentration and, as a result, the intramolecular screening is not changed. Hence, screening of intramolecular Coulombic repulsion is determined not only by the average solution concentration, but depends strongly on the molecular architecture.

We have analysed the structural changes in the polyelectrolyte star induced by increasing the concentration of the solution and identified the cross-over concentration  $c^*$ . This concentration corresponds to close packing of stars which are already partially de-swollen in the dilute regime due to enhanced intramolecular screening. At concentrations above  $c^*$  our cell model describes the geometrical confinement of the star. If this model is mapped to a (star)polyelectrolyte solution, then  $c^*$  corresponds to the cross-over to the semi-dilute regime. With increasing concentration above  $c^*$  overlapping and partial interpenetration of the stars in solution occurs. However, in analogy to semi-dilute solutions of neutral stars we expect that for many-armed stars there is a wide concentration range where star contraction occurs with increasing concentration according to the power law  $R \sim c^{-1/3}$ , i.e. without significant interpenetration. The reason is, obviously, the remaining extension of the star branches with respect to the dimension of an individual polymer chain in the semi-dilute solution of the same concentration. Only at concentrations considerably above the overlap threshold,  $c \gg c^*$ , such interpenetration becomes significant and the structure of the solution becomes the same as that of the solution of individual linear chains of length  $N$ .

Our analysis of the effect of added salt on the polyelectrolyte star conformation in the dilute regime shows that the star size is virtually independent of the salt concentration over a wide range because of intrinsic screening by counter-

ions. The onset of salt-induced star contraction corresponding to a cross-over to the dominance of salt in the intramolecular screening is shifted to higher salt concentration as the number of branches in the star increases. This prediction is in a good agreement with experimental results demonstrating low sensitivity of polyelectrolyte stars to added salt in comparison to their linear analogues.<sup>50</sup> In the salt-dominance regime the star size decreases as  $R \sim (\varphi_s^b)^{-1/5}$  according to earlier scaling predictions.<sup>35</sup>

The comparison of the effect of added salt and that of increasing polyelectrolyte concentration on the star conformation shows that in the dilute regime the star size is less sensitive to increase of polyelectrolyte concentration than to addition of salt. This effect is due to the strongly inhomogeneous distribution of counterions in a salt-free dilute solution of many-armed stars. The difference between the two mechanisms of screening becomes less significant as the number of arms in the stars decreases: for stars with a small number of branches it is the average concentration of mobile ions that determines intramolecular screening.

## Chapter 3

# Annealed Star-Branched Polyelectrolytes in Solution\*

### Abstract

Equilibrium conformations of annealed star-branched polyelectrolytes (polyacids) are calculated with a numerical Self-Consistent-Field (SCF) model. From the calculations we obtain also the size and charge of annealed polyelectrolyte stars as a function of the number of arms,  $pH$ , and the ionic strength. The results are compared with predictions from analytical theory.

Upon varying the number of branches or the ionic strength of the solution, the star-size changes non-monotonically, which is in agreement with the analytical predictions. The salt concentration at this maximum is directly related to the charge density of the star. The internal structural properties of the star corona (the polymer density, the ionisation profiles, and the distribution of the end points) are analysed. The shape of the density profiles indicates increasing local stretching of the branches as a function of the distance from the star centre. Analytical theory predicts a decrease of the polymer density with distance as a power law an exponent of  $-\frac{8}{3}$ . This exponent can only be found for a narrow range of  $pH$  values and number of arms.

Furthermore a bimodal end-point distribution is found and interpreted in analogy to that predicted earlier by analytical SCF-theory for planar polyelectrolyte brushes.

Results of recent experiments with annealed star-shaped micelles are discussed on the basis of our numerical model calculations.

---

\*published in *Macromolecules*, 2002, 35; 9176–9190



### 3.1 Introduction

Weakly dissociating polyelectrolytes play an important role in stabilizing colloids and in buffering environments.<sup>51</sup> An example is the buffer capacity of soils: weak acidic polyelectrolytes, i.e. humic acids, regulate a change in the  $pH$  and/or the (heavy) metal ion concentration. Micelles with a polyelectrolyte corona have practical relevance in drug- and pesticide delivery systems.<sup>52</sup>

Solutions of polyelectrolytes, in general, still remain one of the under-explored fields in polymer science since the conventional linear Debye–Hückel approximation usually fails to describe structural properties of the solutions of highly charged polyions. Even though the properties of solutions of linear chain polyelectrolytes are not completely understood, charged polymers of more complex architecture, such as randomly<sup>36</sup> or regularly<sup>34,35,53–55</sup> branched polyelectrolytes have attracted considerable attention.

Polyelectrolyte stars, comprising a relatively small core region and an extended charged corona, resemble polymeric micelles<sup>23,24,56–62</sup> or small colloidal particles stabilised by grafted polyelectrolytes. Furthermore, a star-like architecture provides the simplest model of branching and is useful for getting an insight in the behaviour of branched polyelectrolytes with more complex architecture.

Two types of polyelectrolytes can be distinguished: quenched (or strong) and annealed (or weak). The dissociation constant for a monomer of a quenched polyelectrolyte is so high, that the actual degree of ionisation is constant, irrespective of the local electrostatic potential. Poly(styrene sulphonate), PSS, serves as a typical example of a quenched polyelectrolyte. On the other hand, the degree of ionisation of an annealed polyelectrolyte depends strongly on the local electrostatic potential because the ionisation constant of the monomer is low. Poly(acrylic acid) is a well known example of an annealed polyelectrolyte.

In our present study we focus on the conformational properties of a weak star-branched poly-acid. Making the choice of  $pK = 5$  for the acidic monomer and assuming a given fraction of acidic monomers in the branches, we thus mimic, e.g., a star-shaped partially hydrolysed poly(acryl amide) or a star-shaped poly(acrylic acid).

The poly-acid stars do not only respond on the variation in salt concentration, as in case of quenched polyelectrolytes, but also to the  $pH$  of the solution. The reaction with hydrogen ions is specific and therefore more sensitive to small changes in the concentration of these ions than to the change in concentration of indifferent salt ions.

The most spectacular trends in the large-scale behaviour of annealed star-branched poly-acids, (e.g. the non-monotonic dependence of the gyration radius upon the number of branches or ionic strength of the solution), were treated earlier on the basis of a scaling approach.<sup>35</sup> In this scaling analysis the Local–Electroneutrality–Approximation (LEA) is utilised. LEA assumes accumulation of the majority of counterions in the interior of the many-arm

### 3.2 Analytical model

polyelectrolyte stars. However, for real polyelectrolyte stars, both simple theoretical estimates and numerical solution of the Poisson–Boltzmann (PB) equation for the distribution of counterions show that a non-negligible fraction of counterions is released from the corona of the polyelectrolyte. Therefore, in order to find out whether LEA is justified, a more accurate approach based on the numerical solution of the PB equation is required.

We analyse in a systematic way the effects of branching (number of arms in the star), ionic strength, and  $pH$  of the solution on the conformational properties of the annealed star-branched polyelectrolyte. The numerical SCF theory that will be applied here is based on the Scheutjens–Fleer (SF–SCF) algorithm.<sup>13</sup> It is a powerful method for getting an insight into the radial distributions of the polymer and the counterion density in stars or micellar coronae. No *a priori* assumptions, other than the mean-field approximation and Gaussian chain statistics, are made about the conformations of the polyelectrolyte stars or about the distribution of counterions. Also, a quantitative prediction concerning their scattering behaviour can be made. The latter will be compared to recent SANS experiments, which probed the internal structure of the corona of star-like polyelectrolyte micelles.<sup>61</sup>

The paper is organised as follows: In section 3.2 we present an overview of the results of the analytical theory concerning the behaviour of annealed star-branched polyelectrolytes in dilute solutions.<sup>35</sup> This work is extended for the case of arbitrary  $pH$  of the solution. In section 3.3 we give the most important features of the numerical SCF model. Results and discussion are given in section 3.4. We end up with the comparison of our calculations with a recent experiment (section 3.5) and with the conclusions in section 3.6.

## 3.2 Analytical model

The analytical model considers a star-branched polyelectrolyte comprising  $f$  branches (arms), attached with one end onto an impermeable core of size  $R_{\text{core}}$  (fig 3.1). The size of the core is assumed to be small with respect to that of the arms and it will be neglected in the analytical model. Each arm is a linear, intrinsically flexible polymer chain comprising  $N$  monomers. The star consists of  $fN$  monomers. Each  $m$ th monomer ( $m=1,2,\dots$ ) is capable of ionisation via dissociation of a hydrogen ion  $H^+$ . The fraction of ionised acidic monomers at place  $r$  is denoted as  $\alpha(r)$  and depends on the local proton volume fraction  $\varphi_{H^+}(r)$  as<sup>63</sup>

$$\frac{\alpha(r)}{1 - \alpha(r)} = \frac{K}{\varphi_{H^+}(r)} \quad (3.1)$$

where  $K$  is the dissociation constant. By using the local proton volume fraction we assume in eq 3.1 that the activity coefficient is 1. The overall charge  $Q$  of the star-branched poly ion is given by  $Q = \alpha f N e / m$ , where  $e$  is the elementary charge.

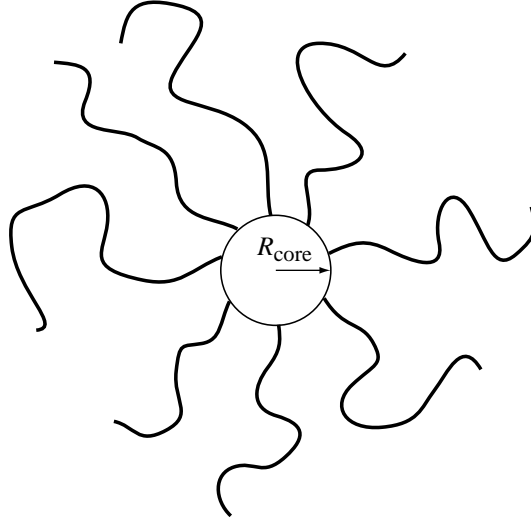


Figure 3.1: Schematic picture of a star-shaped polyelectrolyte with an impenetrable core.

In experimentally relevant situations water is a marginally good solvent for the uncharged monomers. In our analysis we therefore assume  $\theta$ -solvent conditions for the uncharged monomers.

The properties of polyelectrolyte stars in a dilute salt-free solution depend on the number of branches. Three regimes can be distinguished:<sup>34,35</sup>

**The polyelectrolyte regime** occurs for stars with a small number of branches. In this case most of the counterions are released into the bulk of the solution. The star size is determined by the interplay between electrostatic repulsion and a conformational entropy penalty for the extension of the branches (conformational elasticity).

**The osmotic regime** occurs for stars with a larger number of branches, which retain most of the counterions in the intra-star space. The size is determined by the interplay between osmotic pressure of counterions and conformational elasticity of the branches.

**The quasi-neutral regime** appears if the number of branches is further increased. This regime is *not* dominated by the charge of the polyelectrolyte but by the steric interactions. The size is determined by the interplay between steric repulsion between the monomers and conformational elasticity of the branches.

### 3.2.1 Polyelectrolyte regime

For stars with a small number of arms, counterions spread uniformly over the solution. The dissociation of a monomer, which is part of the polyelectrolyte star, is then approximately equal to the dissociation of a monomer in the bulk:  $\alpha \approx \alpha_b$ . The degree of ionisation  $\alpha_b$  at zero electrostatic potential obeys the

### 3.2 Analytical model

equation

$$\frac{\alpha_b}{1 - \alpha_b} = \frac{K}{\varphi_{bH^+}} \quad (3.2)$$

where  $\varphi_{bH^+}$  is the concentration of hydrogen ions in the bulk of the solution. Eq 3.2 is a limiting value of eq 3.1. This means that in the polyelectrolyte regime annealed polyelectrolytes at a given  $pH$  and quenched polyelectrolytes behave identically. At low salt concentration the star conformation is governed by non-screened Coulomb repulsion between the arms. The size  $R$  of the stars in this regime is given by:<sup>35</sup>

$$R \cong N f^{1/3} \left( \frac{\alpha_b}{m} \right)^{2/3} \left( \frac{l_B}{a} \right)^{1/3} a \quad (3.3)$$

where  $l_B = \frac{e^2}{\varepsilon k_B T}$  is the Bjerrum length ( $\varepsilon$  is the permittivity of the solvent,  $k_B$  is the Boltzmann constant and  $T$  the temperature). The size of the monomer is denoted by  $a$ . Because  $R \sim N$ , the extension of the branches is uniform. In a spherical geometry, this means that the radial distribution of polymer density  $\varphi(r)$  in the star is given by

$$\varphi(r) \sim r^{-2} \quad (3.4)$$

where  $r$  is the distance from the centre of the star. These relations hold for the case of low or no added salt.

For high salt concentration, i.e.  $\kappa R < 1$  where  $\kappa^{-1} = (l_B I_b)^{-1/2}$  is the Debye screening length and  $I_b$  is the ionic strength in the bulk and defined as:

$$I_b = \frac{1}{2} \sum_i \nu_i^2 \varphi_{bi} \quad (3.5)$$

where  $\nu_i$  is the valence, and  $\varphi_{bi}$  is the volume fraction of mobile ions of type  $i$  in the bulk. The screened Coulomb interactions inside the polyelectrolyte star can be taken into account via an effective second viral coefficient of monomer/monomer interactions,  $v_{\text{eff}} \sim \left( \frac{\alpha_b}{m} \right)^2 I_b^{-1}$ .

The star size and the polymer density distribution are now given by<sup>35</sup>

$$R \cong N^{3/5} f^{1/5} \left( \frac{\alpha_b}{m} \right)^{2/5} I_b^{-1/5} a \quad (3.6)$$

$$\varphi(r) \sim r^{-4/3} \quad (3.7)$$

These expressions for the properties of the polyelectrolyte star in solution with added salt are similar to those for a neutral star polymer in a good solvent.

#### 3.2.2 Osmotic regime

As the number of arms in the star increases, more and more counterions are attracted to the vicinity of the star. With increasing number of arms the

fraction of free counterions becomes asymptotically small.<sup>34,35</sup> For these stars the Local–Electroneutrality–Approximation (LEA) is applicable even when the solution contains no salt.<sup>34</sup> The LEA assumes local compensation of the immobilised charge on the branches by that of the counterions. In the general case, when in addition to  $H^+$  and  $OH^-$  ions, the solution contains also salt (e.g.  $NaCl$ ) the local electroneutrality condition assumes the form

$$\sum_{i^-} \varphi_{i^-}(r) + \alpha(r)\varphi(r)/m = \sum_{i^+} \varphi_{i^+}(r) \quad (3.8)$$

where  $\varphi(r)$  and  $\alpha(r)$  are the local volume fraction of the monomers and the local degree of ionisation inside the star corona ( $R_{\text{core}} \leq r \leq R$ ); the summation in the r.h.s. is running over all the cationic species (i.e. salt ions  $\varphi_{Na^+}(r)$  and hydrogen ions  $\varphi_{H^+}(r)$ ) while the summation in the l.h.s. is running over all the anionic species (i.e. salt ions  $\varphi_{Cl^-}(r)$  and hydroxide ions  $\varphi_{OH^-}(r)$ ). In order to find the local degree of ionisation  $\alpha(r)$  inside the star, eq 3.8 has to be combined with eq 3.1 and to the Donnan rule, which reflects the Boltzmann distribution of co- and counterions between the interior of the star and the bulk of the solution;

$$\varphi_{i^-}(r)/\varphi_{bi^-} = \varphi_{bi^+}/\varphi_{i^+}(r) \quad (3.9)$$

As a result, one gets an equation which couples the local degree of ionisation  $\alpha(r)$  to the local polymer concentration  $\varphi(r)$ :

$$\frac{\alpha(r)}{1 - \alpha(r)} \cdot \frac{1 - \alpha_b}{\alpha_b} = \sqrt{\left(\frac{\alpha(r)\varphi(r)}{m\Phi_b}\right)^2 + 1} - \frac{\alpha(r)\varphi(r)}{m\Phi_b} \quad (3.10)$$

where  $\Phi_b = \sum_i \varphi_{bi}$ , the total volume fraction of all mobile ions in the bulk of the solution; in the case when only monovalent ions are present in the system,  $\Phi_b = 2I_b$ . In the osmotic regime, the polymer density profile  $\varphi(r)$  can be determined by balancing the local osmotic force,  $4\pi r^2 \Delta\Pi(r)$ , with the elastic force. The elastic force is given by

$$\frac{\mathcal{F}_{\text{elas}}}{k_B T} = \frac{3f^2}{4\pi r^2 \varphi(r)} \quad (3.11)$$

This force is arising in the extended branches.<sup>35</sup> Eq 3.11 assumes Gaussian elasticity and equal stretching of all the branches. The excess osmotic pressure inside the star is given by

$$\Delta\Pi(r)/k_B T = \sum_i \varphi_i(r) - \Phi_b + \Delta\Pi_\theta(r)/k_B T \quad (3.12a)$$

$$= \sqrt{(\alpha(r)\varphi(r)/m)^2 + \Phi_b^2} - \Phi_b + \Delta\Pi_\theta(r)/k_B T \quad (3.12b)$$

where  $\Delta\Pi_\theta(r) \sim \varphi^3(r)$  is the contribution due to non-electrostatic (steric) repulsion between the monomers. The latter contribution dominates for the

### 3.2 Analytical model

stars with a sufficiently large number of arms and/or close to the centre of the star, i.e. when  $\varphi(r)$  is sufficiently large while  $\alpha(r)$  is small. For the stars that do not have a very large number of arms, the contribution of  $\Delta\Pi_\theta(r)$  can be neglected, except for the central region of the star. The behaviour of the central part of the star is the same as for a star in the quasi-neutral regime, this will be addressed in section 3.2.3.

Asymptotic expressions for the size and the polymer density profiles can be obtained in two opposite limits:  $\frac{\alpha(r)\varphi(r)}{m\Phi_b} \gg 1$  (osmotic annealing regime) and  $\frac{\alpha(r)\varphi(r)}{m\Phi_b} \ll 1$  (salt dominance regime), i.e. the ratio between the local concentration of counterions and the total concentration of mobile ions in the bulk of the solution serves as a natural parameter for expansion of eqs 3.10 and 3.12. We remind the reader that  $\Phi_b$  does depend not only on the concentration of added salt, but also on the  $pH$  of the solution, which in turn determines  $\alpha_b$ .

**Osmotic annealing regime,**  $\alpha(r)\varphi(r)/m \gg \Phi_b$ . This regime occurs when the concentration of added salt is low and while the  $pH$  is sufficiently high to induce appreciable ionisation of the star arms. Then eq 3.10 assumes the form

$$\frac{\alpha(r)^2}{1 - \alpha(r)} \approx \frac{\alpha_b}{1 - \alpha_b} \frac{m\Phi_b}{2\varphi(r)} \quad (3.13)$$

As one can see from eq 3.13 the degree of ionisation of monomers in the branches  $\alpha(r)$  is at low salt concentration much smaller than that in the bulk of the solution  $\alpha_b$ , unless  $\alpha_b \rightarrow 1$ , i.e. unless the  $pH \gg pK$ .

For this low salt regime, the excess osmotic pressure reduces to

$$\Delta\Pi(r)/k_B T \approx \alpha(r)\varphi(r)/m \quad (3.14)$$

i.e. it is dominated by the osmotic pressure of counterions, which are accumulated inside the star volume. From eqs 3.11 and 3.14 we obtain the relation between the radial profiles of the polymer density and the degree of ionisation.

$$\varphi(r) \approx f r^{-2} \sqrt{m/\alpha(r)} \quad (3.15)$$

For  $\alpha \ll 1$ , the combination of eqs 3.13 and 3.15 gives the radial profile of the degree of dissociation and of the polymer density:

$$\alpha(r) \approx \left( \frac{\alpha_b}{1 - \alpha_b} \frac{m^{1/2}\Phi_b}{f} \right)^{2/3} r^{4/3} \quad (3.16)$$

$$\varphi(r) \approx f^{4/3} r^{-8/3} \left( \frac{1 - \alpha_b}{\alpha_b} \frac{m}{\Phi_b} \right)^{1/3} \quad (3.17)$$

For the case of  $pH \gg pK$ ,  $\alpha(r) \rightarrow 1$ , eq 3.15 reduces to

$$\varphi(r) \approx \frac{f m^{1/2}}{r^2} \quad (3.18)$$

Subsequent integration of the density profile,  $4\pi \int_{R_{\text{core}}}^R \varphi(r) r^2 dr = fN$  provides an equation for the overall star size  $R$  as a function of structural parameters  $(f, N)$ , salt concentration and  $\text{pH}$  of the solution. The size  $R$  is given by:

$$R \approx \begin{cases} \frac{\alpha_b}{1-\alpha_b} N^3 f^{-1} m^{-1} \Phi_b a & \text{for } \alpha_b/(1-\alpha_b) \sim 1 \\ Nm^{-1/2} a & \text{for } \alpha_b \rightarrow 1 \end{cases} \quad (3.19)$$

where we have neglected the size of the core,  $R_{\text{core}}$ . The remarkable consequence of eq 3.19 is that the size *decreases* as a function of the number of arms and *increases* as a function of  $\Phi_b$  for  $\text{pH}$  values around the  $\text{pK}$ . This is analogous to the behaviour of the weak planar polyelectrolyte brush upon increasing the grafting density and/or the salt concentration in the osmotic regime.<sup>10,64–66</sup> The physical explanations of these effects are that:

- upon an increase in the number of arms the number of charged monomers is decreased because more and more counterions, i.e. protons, are retained within the star volume, thus reducing the degree of dissociation and the concomitant swelling.
- upon an increase in the salt concentration hydrogen ions inside the star corona are substituted by sodium ions. The decrease of the local proton concentration promotes ionisation.

**Salt dominance regime**,  $\alpha(r)\varphi(r)/m \ll \Phi_b$ . This regime applies when the salt concentration in the bulk becomes larger than the concentration of mobile ions in the interior of the star. The asymptotics of eq 3.10 and of eq 3.12 for high salt concentrations are given by

$$\frac{\alpha(r)}{1-\alpha(r)} \cdot \frac{1-\alpha_b}{\alpha_b} \approx 1 - \frac{\alpha(r)\varphi(r)}{m\Phi_b} \quad (3.20)$$

$$\Delta\Pi(r)/k_B T \approx \alpha^2(r)\varphi^2(r)/2m^2\Phi_b \quad (3.21)$$

For high salt concentrations the degree of dissociation of the monomers in the star branches is the same as in the bulk. The polymer density distribution is found by using eqs 3.21 and 3.11:

$$\varphi(r) \approx f^{2/3} r^{-4/3} \left( \frac{m}{\alpha_b} \right)^{2/3} \Phi_b^{1/3} \quad (3.22)$$

The size of the star is therefore given by

$$R \approx N^{3/5} f^{1/5} \left( \frac{\alpha_b}{m} \right)^{2/5} \Phi_b^{-1/5} a \quad (3.23)$$

As follows from eq 3.19 and eq 3.23, the size of a star at low  $\text{pH}$  passes through a maximum as a function of the ionic strength. The ionic strength  $\Phi_b^*$  at which this maximum occurs, is found by equating eqs 3.23 and 3.19 and is given by

$$\Phi_b^* \approx m^{1/2} \alpha_b^{-1/2} (1-\alpha_b)^{5/6} f N^{-2} a^{-3} \quad (3.24)$$

### 3.3 Numerical Self-Consistent-Field model

#### 3.2.3 Quasi-neutral regime

The quasi-neutral regime occurs when steric (non-electrostatic) interactions between the arms dominate over the electrostatic ones, i.e.  $\Delta\Pi_\theta(r)$  is the dominant term in eq 3.12. Close to the centre of the star, this is for all regimes the case. On the scale of the star as a whole, the quasi-neutral regime occurs either at low  $pH$  (when ionisation of arms is small) or at sufficiently large number of arms. (Upon an increase in the number of arms, the ionisation of the arms is progressively suppressed, while the steric interactions get stronger.) In the quasi-neutral regime, the size of the star depends not on its charge but on the solvent quality. The size of the star scales therefore in the same way as for a neutral star. For a  $\theta$ -solvent it is given by:<sup>39–41</sup>

$$R \sim N^{1/2} f^{1/4} a \quad (3.25)$$

and the monomer density profile decays as

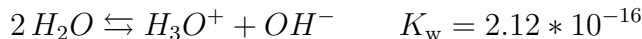
$$\varphi \sim r^{-1} \quad (3.26)$$

### 3.3 Numerical Self-Consistent-Field model

The numerical SCF-approach is based on the Scheutjens–Fleer (SF) algorithm. This algorithm was first proposed for neutral polymers at interfaces<sup>13,16</sup> and extended to account for electrostatics on a Poisson–Boltzmann level<sup>43</sup> and later generalised by Van Male<sup>67</sup> for spherical geometry and for calculating chemical reactions. All the calculations were done with the software package **sfbox**.<sup>17</sup> Some information on the SF–SCF model is given below, for full details the reader should consult the literature references quoted above.

The SF–SCF model is a self-consistent-field model, this means that from a given distribution  $\varphi_x(r)$  of all the particles in the system, a potential field  $u_x(r)$ , is calculated. From this field, which acts on the particles  $x$ , a new distribution is recalculated and this is repeated until  $u_x(r)$  and  $\varphi_x(r)$  of all the particles are consistent. The subscript  $x$  is used to refer to the various types of particles. First we explain the way to calculate the field,  $u_x(r)$ , from the distribution,  $\varphi_x(r)$ , after which we proceed to calculate  $\varphi_x(r)$  from  $u_x(r)$ .

The SF–SCF approach uses layers which are characterised by the (smeared out) volume fractions of the particles and by the total charge, i.e. a mean field approximation. The thickness  $a$  of a layer is 0.6 nm. Every layer is totally filled. In the calculations the following particles  $x$  are used: solvent molecules ( $H_2O$ ), salt ions ( $Na^+$  and  $Cl^-$ ), a non-ionizable polymer segment ( $P_u$ ), and a polymer segment with a  $pH$ -dependent charge ( $P_{pK}$ ). The last type of segment can either be neutral or negatively charged depending on the  $pH$ . There are two types of salt ions in the system: co-ions  $Cl^-$  and counterions  $Na^+$ . The solvent molecule, water, can dissociate according to the following reaction:





. A solvent molecule may take on 3 different *states*  $k$ , i.e.  $H_2O^0$ ,  $H_3O^+$ , and  $OH^-$ . The value of the equilibrium constant  $K_w$  is the dimensionless equivalent of the familiar water dissociation constant of  $10^{-14} \text{ mol}^2/\text{L}^2$ . The value of  $K_w$  depends on the thickness of the layer,<sup>67</sup> see also the appendix A. The reaction of the polymer segment  $P_{pK}$  with water is



This means that at a local concentration of  $H_3O^+$  of  $10^{-5} \text{ mol/L}$  half of the  $P_{pK}$  segments is dissociated. The polyelectrolyte stars are composed of three types of segments,  $P_u$ ,  $P_{pK}^-$  (the charged form) and  $P_{pK}^0$  (the non-charged form).

The lattice layers are arranged in an array of concentric spherical shells numbered as  $z = 1, 2, \dots, M$ ; the outer surface of the  $z$ -th layer is at the distance  $r = R_{\text{core}} + z * 0.6$ , in nm, from the centre, where  $R_{\text{core}}$  is the size of the core (see fig 3.1). In the article we will use  $r$  for continuously changing sizes and distances, as e.g. are used in the analytical theory and  $z$  for discrete steps in sizes or distances, e.g. in the numerical calculations. The dimensionless volume of layer  $z$  is  $L(z)$  which is given by  $4/3\pi(z^3 - (z-1)^3)$ .

The SCF formalism features the particle potentials of state  $k$   $u_{x,k}(z)$  which are conjugated to the volume fractions  $\varphi_{x,k}(z)$ . The functions  $u_{x,k}(z)$  and  $\varphi_{x,k}(z)$  for a given particle type in state  $k$  are only functions of the  $z$  co-ordinate. Hence, all the local properties of the system are pre-averaged over the angular co-ordinates (the spherical approximation). The total potential of a particle of type  $x$  in state  $k$  comprises three terms:

$$u_{x,k}(z) = u'(z) + k_B T \sum_{y,l} \chi_{x,k-y,l} (\langle \varphi_{y,l}(z) \rangle - \varphi_{b,y,l}) + \nu_{x,k} e \psi(z) \quad (3.28)$$

The first term is coupled to the incompressibility constraint  $\sum_{x,k} \varphi_{x,k}(z) = 1$ . The second term gives the short-range interactions, parameterized by Flory-Huggins interaction parameters  $\chi_{x,k-y,l}$  between particle types  $x$  with state  $k$  and  $y$  in state  $l$ . This interaction of particle of type  $x$  with state  $k$  in layer  $z$  with a particle of type  $y$  in state  $l$  depends on the volume fraction of a particle of type  $y$  in state  $l$  positioned in layers  $z-1$ ,  $z$ , and  $z+1$ . The site average volume fraction, denoted as  $\langle \varphi_{y,l}(z) \rangle$ , depends on  $\varphi_{y,l}(z-1)$ ,  $\varphi_{y,l}(z)$ , and  $\varphi_{y,l}(z+1)$  and is weighted by the geometry of the system.<sup>48</sup> The quantity  $\varphi_{b,y,l}$  in eq 3.28 is the volume fraction of particles of type  $y$  in state  $l$  in the bulk. The third term accounts for the electrostatic contributions. The local charge density per layer  $q(z)$  is given by  $q(z) = e \sum_{x,k} \nu_{x,k} \varphi_{x,k}(z)$ , where  $e$  is the elementary charge and  $\nu_{x,k}$  the valence of the particle of type  $x$  in state  $k$ . The local electrostatic potential  $\psi(z)$  is related to the local charge density  $q(z)$  via the Poisson equation.

The way to find  $u_{x,k}(z)$  from the volume fractions of all particles is given by eq 3.28. To calculate  $\varphi(z)$  of a polymer from  $u_{x,k}(z)$  one has to evaluate all possible and allowed conformations of the polymer in the potential field. The monomers in a polymer have a ranking number  $s$  which is ranging from 1 to

### 3.3 Numerical Self-Consistent-Field model

$N$ . In the case of a polymeric star one has to take into account the grafting constraint on the first segment. The chain statistics are treated in a first order Markov approximation. Using this, we calculate the end-point distribution function  $G(z, s|z^*, 1)$  for the statistical weight of finding a chain fragment that starts with segment  $s = 1$  at  $z^*$  (grafting point) and ends in layer  $z$  with segment  $s$ . Correspondingly,  $G(z, s|N)$  is the statistical weight of all possible and allowed conformations, with the specification that segment  $s = N$  can be anywhere in the system and segment  $s$  is again at co-ordinate  $z$ . Hence,  $G(z, s|N)$  is the sum of  $G(z, s|z', N)$  over all  $z'$ . The end-point distribution functions, in the approximation of first order Markov chain statistics, obey the diffusion equation which, in discrete notation, can be written as:

$$G(z, s|z^*, 1) = G(z, s)\langle G(z, s-1|z^*, 1) \rangle \quad (3.29a)$$

$$G(z, s|N) = G(z, s)\langle G(z, s+1|N) \rangle \quad (3.29b)$$

where  $G(z, s)$  is the segmental weighting function and defined as  $\sum_k \alpha_{b,k} G_k(z, s)$  with  $\alpha_{b,k}$  the fraction of the segment at ranking number  $s$  in state  $k$  in the bulk and  $G_k(z, s) = e^{u_{x,k}(z)/k_B T}$ , where  $x$  is the particle type at ranking number  $s$ .  $\langle G(z, s-1|z^*, 1) \rangle$  and  $\langle G(z, s+1|N) \rangle$  denote the site average endpoint distribution of segment  $s-1$  and  $s+1$ , respectively. The starting conditions for the propagators are  $G(z, N|N) = G(z, N)$  for all  $z$  and  $G(z^*, 1|z^*, 1) = G(z^*, 1)$  (grafting condition). The density of a monomer with ranking number  $s$  follows from the composition law:

$$\varphi(z, s) = C \frac{G(z, s|z^*, 1)G(z, s|N)}{G(z, s)} \quad (3.30)$$

Here, the factor  $G(z, s)$  in the denominator corrects for the double counting of the Boltzmann weight for segment  $s$  in the nominator. By summing eq 3.30 over  $s$  we get the polymer density profile

$$\varphi(z) = \sum_{s=1}^N \varphi(z, s) \quad (3.31)$$

The normalization factor  $C$  is fixed by the number of monomers belonging to the star molecule:

$$C = \frac{fN}{\sum_{z=1}^M L(z)G(z, N|z^*, 1)} \quad (3.32)$$

The grafting co-ordinate of the arms of the star  $z^*$  is chosen as close to the centre as possible, i.e.  $L(z^* - 1) < f \leq L(z^*)$ . Hence for  $f = 5$  we take  $z^* = 2$  and for  $f = 100$  we choose  $z^* = 4$ .

The set of equations as presented in this section is closed, but should be complemented by boundary conditions. As the cell is electroneutral as a whole, we set the “reflecting” boundary conditions at  $z = M$ , which guarantees that

there are no gradients present in the  $z$  direction between  $z = M$  and  $z = M + 1$ : i.e.  $\psi(M + 1) = \psi(M)$ ,  $u_x(M + 1) = u_x(M)$ , etc.

The above set of equations are solved iteratively by a Newton-like method. This results in the electrostatic potential profile and a distribution of number of charges per layer. Furthermore, the radial distributions of the salt ions, the polymer segments and also, for instance, the end points of the branches are calculated.

The solvent is chosen to be a  $\theta$ -solvent for the polymer, i.e.  $\chi = 0.5$  between the solvent molecules and the polymer monomers, see eq 3.28. Each polymer arm of the star has  $N$  monomers, every  $m$ -th monomer can dissociate. The average degree of dissociation per dissociating monomer  $\bar{\alpha}$  is defined as:

$$\bar{\alpha} = \frac{\sum_z \varphi_{P_{pK}^-}(z)L(z)}{\sum_z \varphi_{P_{pK}}(z)L(z)} \quad (3.33)$$

$P_{pK}^-$  denotes the charged form of the dissociating polymer segment and  $P_{pK}$  the total number of dissociable monomers, i.e.  $P_{pK} = P_{pK}^0 + P_{pK}^-$ . The volume fraction of the charged form of the  $P_{pK}$  monomer in a layer is coupled to the electrostatic potential in layer  $z$  through

$$\frac{\varphi_{P_{pK}^-}(z)}{\varphi_{P_{pK}}(z)} = \alpha(z) = \alpha_b e^{e\psi(z)/kT} \quad (3.34)$$

where  $\psi(z)$  is the electrostatic potential in layer  $z$ .

As a measure for the size, the following definition of  $R$  is used

$$R = \frac{\sum_{z=z^*}^M (z - z^*)\varphi(z, N)L(z)}{\sum_{z=z^*}^M \varphi(z, N)L(z)}, \quad (3.35)$$

i.e., the first moment of the radial distribution of the end segments  $\varphi(z, N)$ , starting from the grafting point. Because we want to compare star with different  $f$ , we have to use a size which is comparable for all the stars. Due to the fact that stars with large number of arms have a small core, we have chosen to neglect the inner-part and look upon the stretching from  $z^*$  on. The values of  $z^*$  are chosen to satisfy the volume requirements of a star.

To make a comparison with SANS experiments feasible, we need to calculate the scattering form factor from the radial distribution of the polymer segments. This is done through a Debye Transformation. The form factor  $P(q)$  for an object with a spherically symmetric density distribution is given by:<sup>61,68</sup>

$$P(q) = \frac{1}{(Nf)^2} F(q)^2 \quad (3.36)$$

where  $Nf$  is the number of scattering units and  $F(q)$  is form factor amplitude i.e.  $F(q) = \int \varphi(z)e^{-iqz}dz$ , the Fourier transform of the volume fraction profiles

### 3.4 Results and Discussion

of the scattering units. Eq 3.36 is not only valid for star-shaped objects but also for polymeric micelles and small spherical particles with polymeric chains grafted to a surface. In the latter two cases however, this validity applies only when the core is negligibly small or matched in scattering density with the solvent,<sup>68</sup> i.e. when the scattering is only due to the coronal chains. The scattering amplitude  $F(q)$  (in discrete notation) is given by

$$\begin{aligned}
 F(q) &= \sum_{z=1+Z_{\text{core}}}^{z=M+Z_{\text{core}}} \varphi(z) \int_{z-1}^z 4\pi z^2 \frac{\sin(qz)}{qz} dz \\
 &= \frac{4\pi}{q^2} \sum_{z=1+Z_{\text{core}}}^{z=M+Z_{\text{core}}} \varphi(z) ((z-1)\cos(q(z-1)) - z\cos(qz)) \quad (3.37) \\
 &\quad + \varphi(z) \left( \frac{\sin(qz)}{q} - \frac{\sin(q(z-1))}{q} \right)
 \end{aligned}$$

In this equation only the monomers of the polyelectrolyte scatter,  $z$  is the distance from the centre,  $Z_{\text{core}}$  is the number of layers which form the core to which the polyelectrolytes are grafted. In the second equation of eq 3.37 the integration over one layer has been performed. The scattering wave vector  $q$  is limited by the number of layers used:  $\frac{\pi}{M} \leq q \leq \pi$ , because distances smaller than one layer or larger than  $M$  layers have no meaning. The factor  $\pi$  stems from  $2\pi$  in the Fourier argument of the sin-function, multiplied by the Nyquist critical frequency,  $\frac{1}{2}$ .<sup>69</sup> The step in  $q$  is  $\frac{\pi}{M}$ .

## 3.4 Results and Discussion

We will first show some overall features of the star molecule. Most calculations are done for  $N = 200$ , but in order to investigate finite size effects, some calculations were performed for  $N = 1600$ . The stars, calculated in this section, do not have a core, so if  $z^* > 1$  then the inner part is penetrable for the polyelectrolyte. The number of the segments which will indeed go into the inner-part is negligible small. This means that in practice the core is impenetrable. In section 3.4.1 the behaviour at a low salt concentration is given. In the section 3.4.2 the effects, induced by changing the salt concentration, are investigated.

### 3.4.1 Annealed polyelectrolyte stars in a solution with low ionic strength

First the size and the average degree of ionisation of a polyelectrolyte star on the  $pH$  will be shown. This will be followed by the evolution of the radial density profiles of the monomers and the radial profile of the degree of dissociation.

Changing the  $pH$  in experiments or in numerical calculations to obtain a desired dissociation, automatically affects the ionic strength  $I$ . The ionic

strength is defined as

$$I = A \frac{1}{2} \sum_i \nu_i^2 \varphi_{bi} = AI_b \quad (3.38)$$

Here,  $i$  denotes all small, mobile, ionic molecules,  $H_3O^+$ ,  $Na^+$ ,  $OH^-$ , and  $Cl^-$ ,  $\nu_i$  is the valence and  $\varphi_{bi}$  the volume fraction of molecule  $i$  in the bulk,  $A$  is a conversion factor needed to express the ionic strength in mol/L, see appendix A.

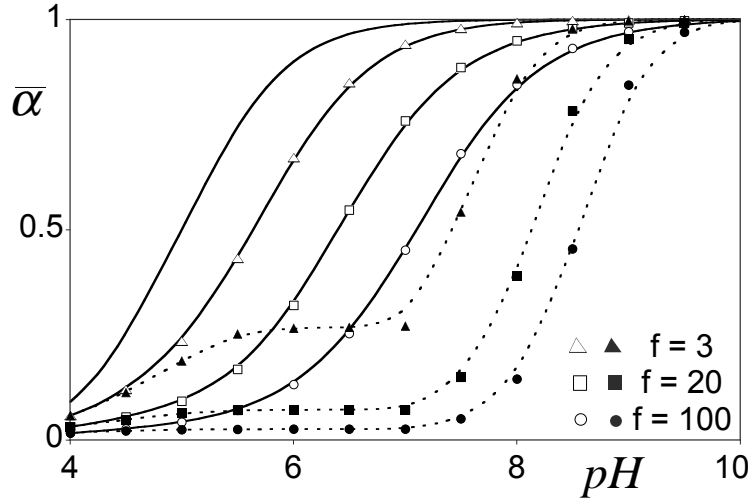


Figure 3.2: The average degree of dissociation as a function of the pH for different numbers of arms. Triangles denote  $f = 3$ , cubes  $f = 20$ , and circles  $f = 100$ . The filled symbols are the calculations without added salt and the open symbols the ionic strength is kept constant at  $10^{-4}$  mol/L, the curves through the points are a guide to the eye. The curve without symbols denotes an individual monomer in the bulk.

Fig 3.2 shows the titration curves ( $\bar{\alpha}$  vs pH) for the stars with different number of branches (for comparison the titration curve on an individual monomer in the bulk of the solution is plotted as well). The shift of the titration curve to higher pH with increasing number of branches is clearly observed. There is a remarkable difference between a titration curve calculated with a constant ionic strength and one calculated with no added salt, for stars with different number of branches  $f$ . For the titration curves with constant ionic strength salt is added to keep the ionic strength constant while for the case, when no salt is added, the pH is also a measure for the ionic strength. The titration of monomers in a polyelectrolyte star is influenced by their surrounding, for increasing number of branches the increase of the charge on the star is slower with increasing pH see fig 3.2. For  $f = 100$ ,  $\bar{\alpha} = 0.5$ ,  $pH = 7$ , and  $I = 10^{-4}$  mol/L, we see a shift of the apparent pK from 5 to 7. For the case of no added salt the shift is even larger. Furthermore, it can be seen from fig 3.2 that for the system with no added salt the dissociation does not increase with increasing pH from  $pH = 4$  until  $pH = 7$ . From  $pH = 4$  to  $pH = 7$  the

### 3.4 Results and Discussion

ionic strength decreases by a factor of 1000 and the low ionic strength prevents dissociation. Upon further increasing the  $pH$  the ionic strength increases again and the dissociation becomes possible. This rather special behaviour can only be measured if one starts with a salt-free solution at  $pH = 7$  and then goes to either  $pH = 4$  or  $pH = 10$ .

Further on in this section the ionic strength  $I$  is kept constant and low. For the highest acid or base concentration, i.e.  $pH = 4$  or  $pH = 10$  the ionic strength is  $10^{-4}$  mol/L, even if no extra salt is added. In order to keep the ionic strength in the bulk constant and equal to  $10^{-4}$  mol/L while varying  $pH$ , extra salt is added in the range of  $pH$ 's between 4 and 10.

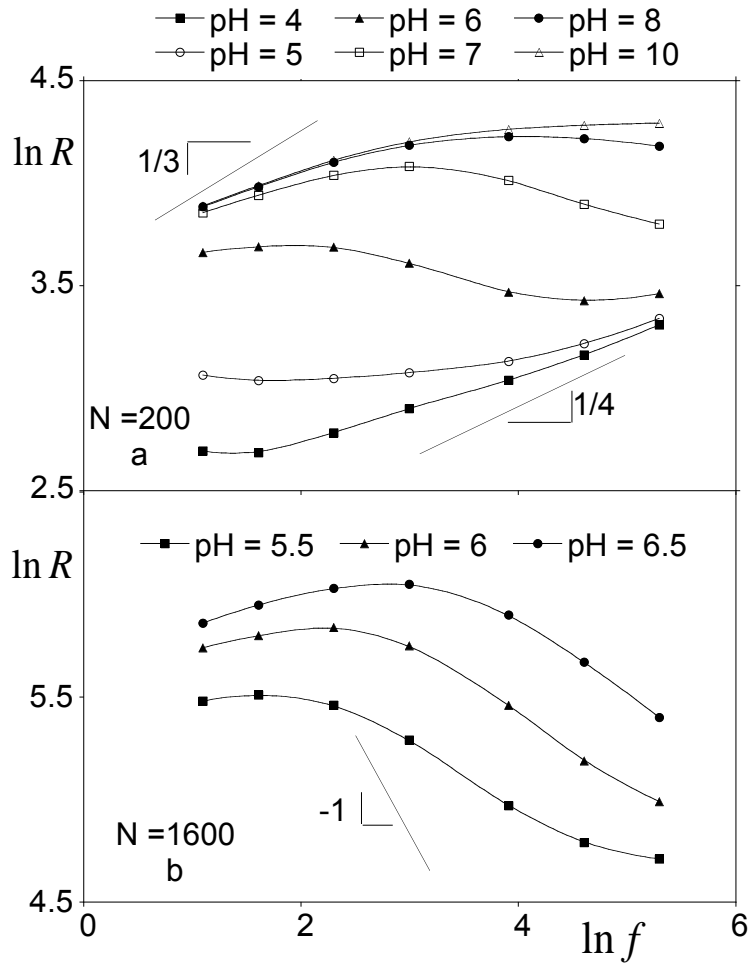


Figure 3.3: The size as a function of the number of arms  $f$  for  $I = 10^{-4}$  mol/L,  $m = 5$ ,  $pH$  as denoted in the graphs and  $N = 200$  (a) or  $N = 1600$  (b). Both graphs are in double logarithmic scale. The curves are a guide to the eye. The straight lines show the predicted scaling behaviour.

In fig 3.3 the size of a star is shown as a function of the number of arms  $f$ , for different values of  $pH$ , with  $m = 5$  and  $N = 200$  (fig 3.3a) or 1600 (fig 3.3b). It can be seen that for constant  $f$  the size increases with the  $pH$ ;

this is due to an increasing ionisation of the branches. At low  $pH$ , i.e. small  $\bar{\alpha}$ , in fig 3.3a the size increases monotonically with the number of arms due to an enhancement of the steric interactions. At  $pH = 4$  the slope of  $\ln R$  vs  $\ln f$  is close to  $1/4$  which is predicted for a neutral star in  $\theta$ -solvent, see eq 3.25. For high  $pH$  (i.e.  $pH \geq 8$ ) the star size grows for increasing  $f$  at small  $f$  and flattens off at larger  $f$ , just as for quenched polyelectrolyte stars.<sup>34,35,55</sup> The small increase with  $f$  means that the star is in the polyelectrolyte regime, see eq 3.3. The most interesting behaviour is found for intermediate  $pH$  i.e.  $pH \gtrsim pK$ . The size exhibits a maximum as a function of  $f$  for  $5.5 \leq pH < 8$ . The weak increase, because the star is still in the polyelectrolyte regime, is followed by a sharp decrease in size with increasing number of branches. This maximum is seen for  $pH$  6 and 7. As discussed in section 3.2.2, the decrease in the star size as a function of the number of branches is due to suppressed ionisation. In the osmotic annealing regime a power law exponent of  $-1$  is expected, see eq 3.19, the slopes found in fig 3.3 are smaller. This is due to increasing steric repulsion between the branches, which is not taken into account in eq 3.19. This decrease in size is more clearly seen in fig 3.3b, due to the less pronounced steric interactions for the star with longer branches. By comparing the stars with  $N = 200$  and  $N = 1600$ , it can be concluded that the finite size effects are small and the main features, which are analytically predicted, are already seen for  $N = 200$ .

In fig 3.4 the segment density is plotted as a function of the distance from the centre in double logarithmic co-ordinates, for a range of  $pH$  values, 3 different values of  $f$ , and  $N = 200$ . The volume fraction of the polymer segments decreases with distance from the centre. The decrease becomes steeper with increasing  $pH$ , due to the increasing number of charges on the chain. With increasing number of arms the susceptibility for changes to the  $pH$  decreases, compare the degree of dissociation for  $f = 3$  and  $f = 100$  in fig 3.2, the difference in  $R$  between  $pH$  4 and 6 for  $f$  is 3 and 100 in fig 3.3a. This is due to increasing importance of steric interactions. For low  $pH$  the slope of the  $\ln \varphi$  vs  $\ln z$  curve is close to  $-1$ , which is expected for uncharged stars, see eq 3.26.<sup>35</sup> For high  $pH$ , the situation is similar to that of quenched stars, the observed slope is close to  $-2$ , as expected for the case of uniformly extended branches according to eq 3.18. For intermediate  $pH$  a decrease faster than  $z^{-2}$ , is seen for  $f = 100$  at the periphery of the star. The extra extension is due to a gradient in the ionisation of the branches. The predicted decrease of  $-8/3$ , see eq 3.17, is not confirmed, however. This may be due to the limited size of the arms; therefore we turn to the results for  $N = 1600$ .

In fig 3.5 the volume fraction profiles of a star with 20 and 100 branches is shown, each branch has 1600 monomers. In fig 3.5a, where  $f = 20$ , a steep slope is observed at the periphery of the star. In fig 3.5b, for  $f = 100$ , this steep decrease of the volume fraction profiles with  $z$  is even better seen. In the region of this steep slope of  $\ln \varphi$  vs  $\ln z$ , the local tension of the arms is an increasing function of  $z$  due to increasing ionisation. The effect of increasing number of branches can be clearly seen: for  $f = 20$  at the periphery, a small

### 3.4 Results and Discussion

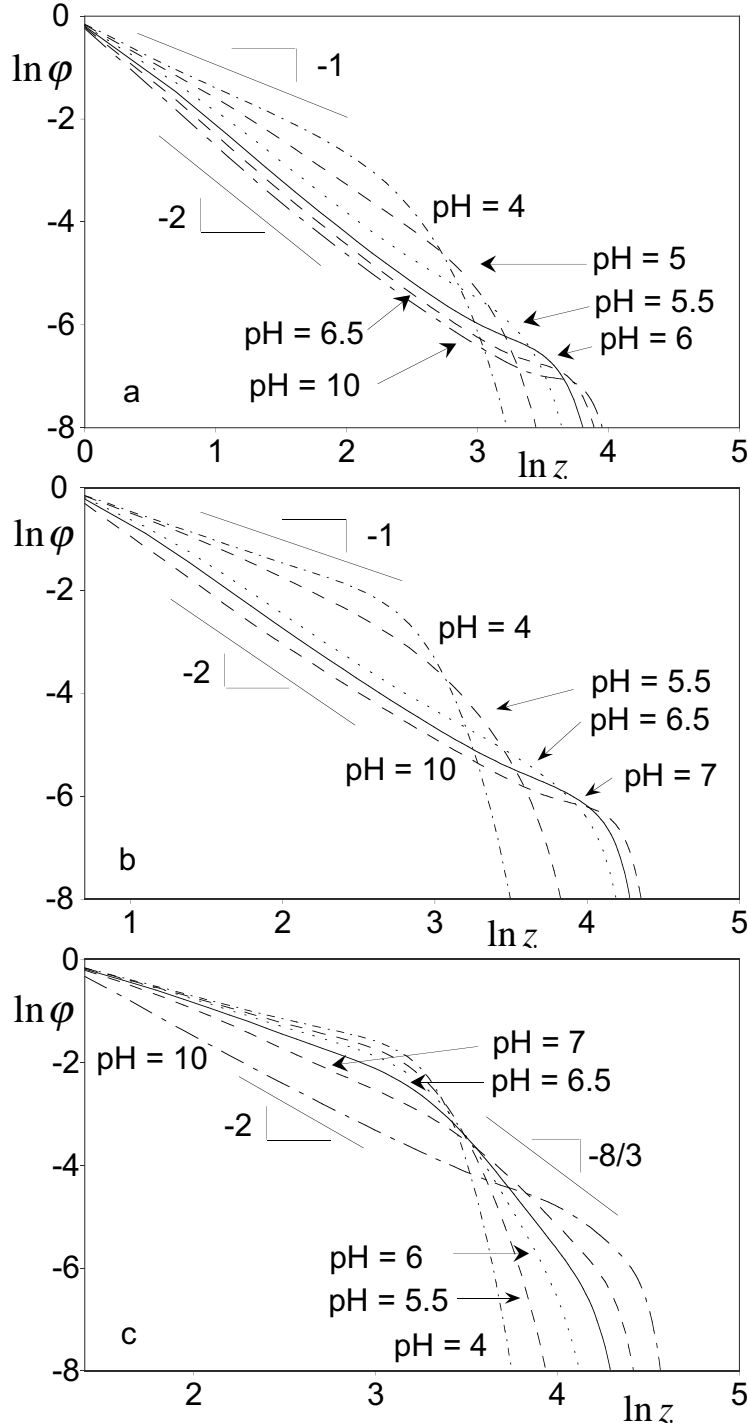


Figure 3.4: A double logarithmic plot of the volume fraction of the polyelectrolyte as a function of the distance from the centre  $z$  for  $I = 10^{-4}$  mol/L,  $m = 5$ ,  $pH$  as denoted in the graphs and  $N = 200$  for  $f = 3$  (a),  $f = 20$  (b), and  $f = 100$  (c).



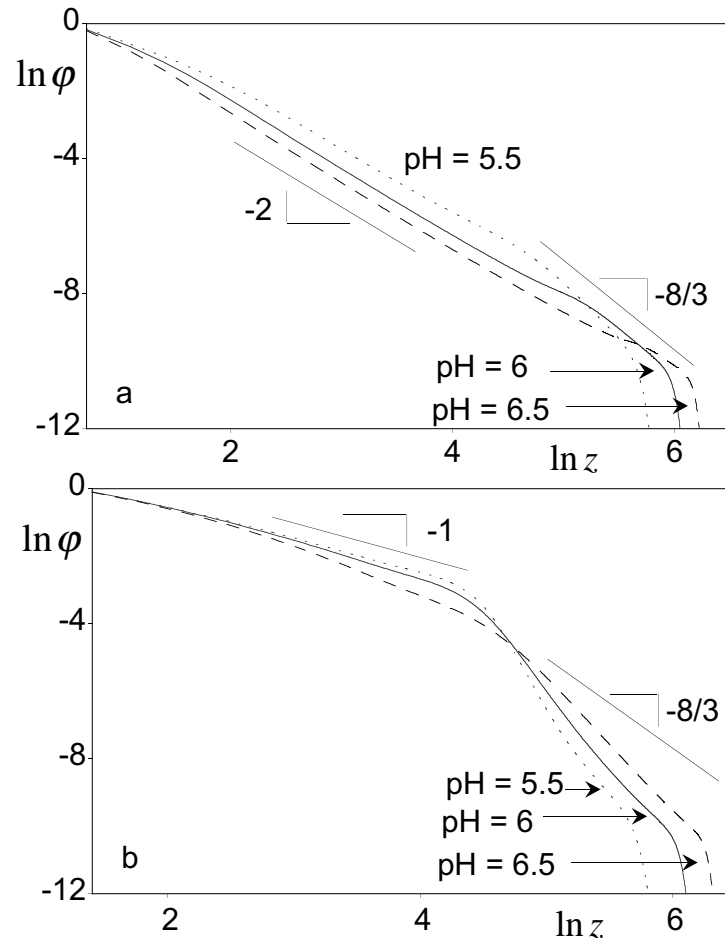


Figure 3.5: A double logarithmic plot of the volume fraction of the polyelectrolyte as a function of the distance from the centre  $z$  for  $I = 10^{-5.5}$  mol/L,  $m = 5$ ,  $N = 1600$ , and  $pH$  as denoted in the graphs. In fig (a)  $f = 20$  and (b)  $f = 100$ .

### 3.4 Results and Discussion

region  $\varphi(z) \sim z^p$ , with  $p < -2$  can be observed, and for  $f = 100$  this region occurs over a larger  $z$ -range. The power law exponent for  $f = 100$  is even more negative than the predicted  $-8/3$ , see eq 3.17.

The volume fraction decay of  $z^{-2}$  for  $f = 20$  in fig 3.5a, is larger than expected which is based on the charge of the star, see fig 3.6a. A  $z^{-2}$ -decay of the volume fraction is expected for a fully charged star. The expected decay for a non-charged star is  $\varphi(z) \sim z^{-1}$ . This fast decay is probably due to the pulling of the ends of the star branches, which like to stretch due to their charge.

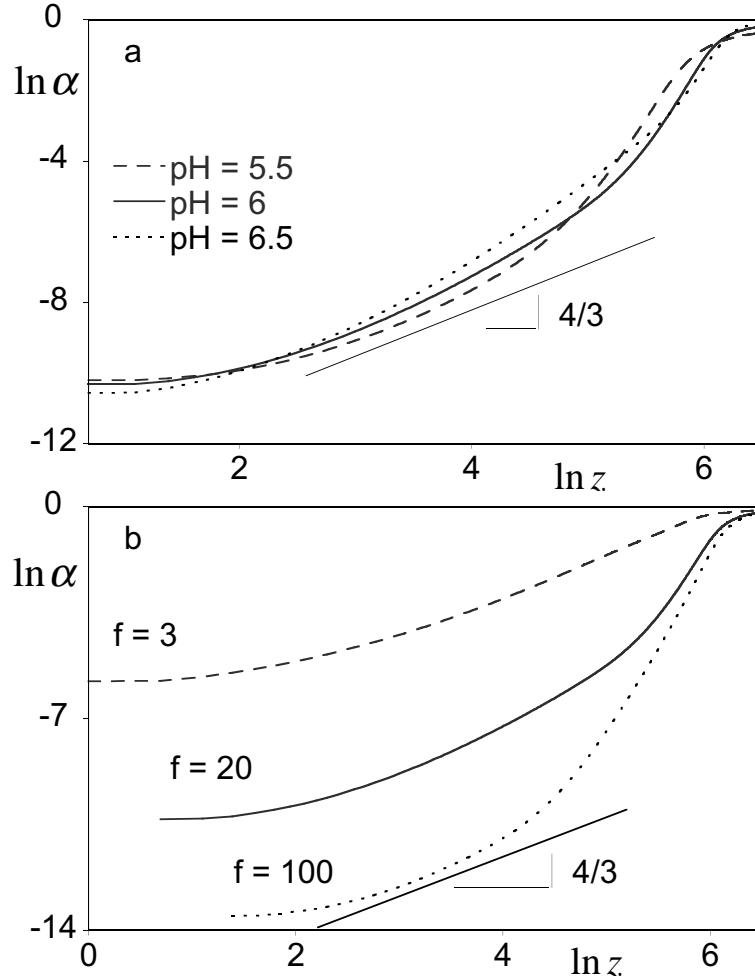


Figure 3.6: The degree of dissociation as a function of the distance from the centre  $z$  for  $I = 10^{-5.5}$  mol/L,  $m = 5$ , and  $N = 1600$ . In fig (a)  $f = 20$ , pH as denoted in the graph and in fig (b) the pH is 6 and  $f$  as denoted in the graph, both plots are in double logarithmic scale.

The decay of the volume fraction profiles faster than  $z^{-2}$ , indicates an increase in the ionisation of the arms, this is shown in fig 3.6. This figure shows clearly the large increase in ionisation of the branches with distance from the centre. The fraction of charged monomers increases towards the periphery of the star,  $\alpha \rightarrow \alpha_b$ . However, the expected power law dependence

for  $\alpha(r) \sim r^{4/3}$ , see eq 3.16, is observed at smaller  $z$ -values than the fast decay of the volume fraction profiles plotted in fig 3.5. The faster than predicted  $z^{4/3}$  increase of the ionisation at the periphery of the star is in agreement with the faster than predicted  $z^{-8/3}$  decrease of the volume fraction profiles in fig 3.5b. In fig 3.6b, the radial increase of the degree of dissociation from the centre to the periphery for  $f = 100$  is most pronounced, the dissociation is negligible in the inner region of the star, where the power law dependence of  $\varphi(z) \sim r^{-1}$  occurs, and it increases to  $\alpha_b$  at the end of the arms.

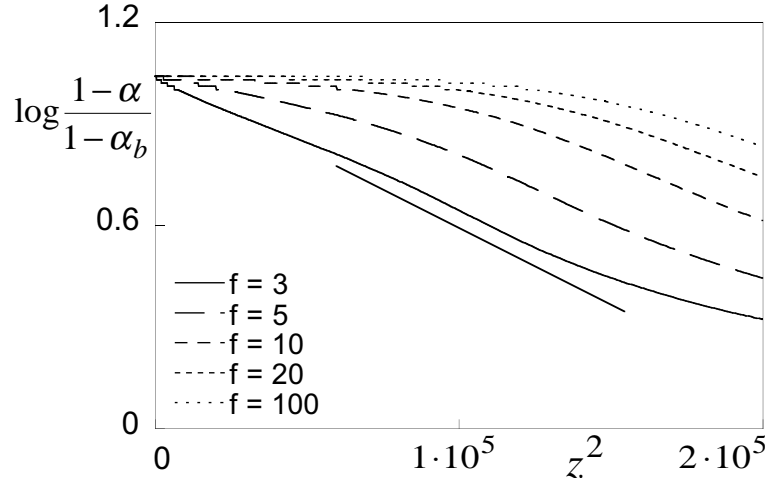


Figure 3.7:  $\text{Log}\left(\frac{1-\alpha}{1-\alpha_b}\right)$  as a function of  $z^2$  for  $I = 10^{-5.5}$  mol/L,  $m = 5$ , and  $N = 1600$ , and pH 6 for different number of arms.

The profiles of the degree of dissociation are represented in fig 3.7 and clearly demonstrate a linear dependence of  $\log(1-\alpha)$  vs  $z^2$  in the periphery of the star. This linear dependence was predicted by analytical SCF theory for annealed planar brushes.<sup>65</sup> Hence we find the structure of the annealed star at the outer edge is not depending on the curved geometry anymore and resembles that of a planar polyelectrolyte brush.

The distribution of end points is an interesting property which is easily obtained in the SCF-calculations but not from analytical theory. In fig 3.8 the volume fraction (fig (a)) and total number (fig (b)) of the end segments of the polyelectrolyte star per layer are shown. In order to facilitate a comparison between stars with different number of arms, the volume fraction and the total number are normalised with respect to the number of arms. (The total number of segments gives extra information especially because the lattice is spherical and the size  $R$ , defined in eq 3.35, is determined by the number of segments in a layer and not by the volume fraction.)

For stars with a small number of branches (the polyelectrolyte regime), e.g.  $f = 3$  in fig 3.8a we observe a “Gaussian” shape of the free end distribution function. It peaks close to the periphery of the corona and we find a wide zone, where no free ends occur, in the central region of the star (a dead zone). For  $f = 20$  the free ends distribution is much broader and skewed, see fig 3.8a.

### 3.4 Results and Discussion

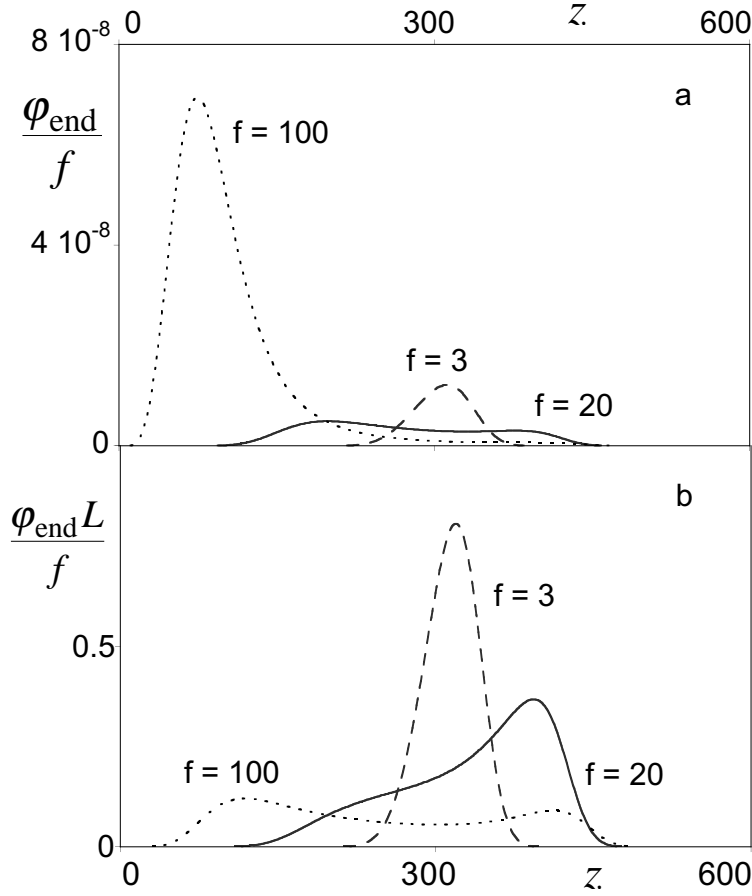


Figure 3.8: The volume fraction and the total number of the end segments as function of  $z$  in fig (a) and (b), respectively. Both the volume fraction profiles and the profiles of the total amount of end segments are normalised by  $f$ . The other parameters are  $m = 5$ ,  $\text{pH} = 6$ ,  $N = 1600$ ,  $I = 10^{-5.5}$  mol/L, and  $f$  as denoted in the graphs.

One maximum of the curve is shifted to lower  $z$  value, as compared to the ends distribution for the star with  $f = 3$  branches. This shift of the maximum is related to the suppressed ionisation upon an increase in the number of branches. The maximum at higher  $z$ -value is due to some star arms which are more charged and therefore more stretched. For  $f = 100$  the distribution exhibits a maximum and a long tail. The position of the maximum is shifted to even smaller  $z$ , as compared to the distribution of the ends in a star with  $f = 20$  branches. Due to the high local polymer density, the chains having ends close to the maximum of the distribution are weakly charged, while more strongly charged (and therefore stronger extended) chains contribute to the tail of the distribution.

Fig 3.8b, where the total amount of the end points per layer is given for  $N = 1600$ , shows for  $f = 100$  two maxima and for  $f = 20$  a very broad distribution with a shoulder. (For  $N = 200$  the end-point distribution is unimodal, but

exhibits a weak shoulder (not shown)). One can think that these two maxima indicate two populations of chains which stem a choice a chain can make: it can either dissociate weakly and remain weakly extended or it can dissociate substantially, resulting in strong electric repulsion and significant stretching. Fig 3.9a demonstrates the evolution of the end profiles as a function of the  $pH$ . With an increase in the  $pH$ , the two populations remain but the maxima of the distribution are shifted to higher  $z$ -value. Fig 3.9b shows the probability distribution of the number of charges on an arm. On the  $x$ -axis the number of dissociated segments on an arm is plotted, irrespective of the position of these dissociated segments on the arm. The way to calculate the probability of finding a branch with a certain amount of charges is described in appendix B. Fig 3.9b shows that there are two populations of arms with respect to their charge for  $pH$  5.5 and 6 but not for  $pH \geq 6.5$  even though at this  $pH$  the endpoint distribution is also bimodal.

Even though we see two populations of end points and at some  $pH$ 's also two populations of charged chains, we do not expect a “phase”-transition between branches which are hardly charged and ones which are more ionised. Because not in all cases where a bimodal distributions in end points is seen give a bimodal distribution in the fraction of charges per chain and a second reason is that the amount of charges varies gradually when changing the  $pH$ . Other reasons not to expect a phase-transition due to the amount of charges on a branch, is because the two maxima in the distribution of end points have also been found by SCF-calculations for quenched polyelectrolyte stars, although the second peak is very small. Furthermore analytical SCF-theory predicts this kind of bimodal planar quenched brushes as well.<sup>11,70</sup>

In the last part of this section, we discuss some special features of the segment density, which follow from the numerical calculations. In fig 3.10a the polymer density profiles of an annealed star with 3 arms,  $N = 200$ , and  $m = 1$  are presented. The difference between fig 3.4a and fig 3.10a is that the total number of charged monomers in the latter case can be higher, because every monomer is capable for ionisation, i.e.  $m = 1$  instead of  $m = 5$ . In this case the volume fraction of polymer segments exhibits a weak maximum at the edge of the star corona. This maximum is observed only for strongly charged stars,  $pH \gg pK$ ,  $m \approx 1$ , and small number of branches. (The maximum is not found for  $f = 20$  and 100, not shown.)

For comparison, also the polymer density profiles of a quenched polyelectrolyte star are shown in fig 3.10b; here an increase in  $\varphi(z)$  near the periphery of the star can be seen at low  $f$  as well. Hence, the appearance of the maximum in the polymer density profile is not related to the ionisation/recombination balance in the star branches.

We remind the reader, that polyelectrolyte stars with small number of branches release most of counterions in the outer space. In the interior of the star the branches are extended fairly uniformly and the polymer density decreases  $\sim r^{-2}$  due to geometric reasons. On the contrary, near the periphery of the corona the effect of curvature becomes irrelevant and it behaves as a planar

### 3.4 Results and Discussion

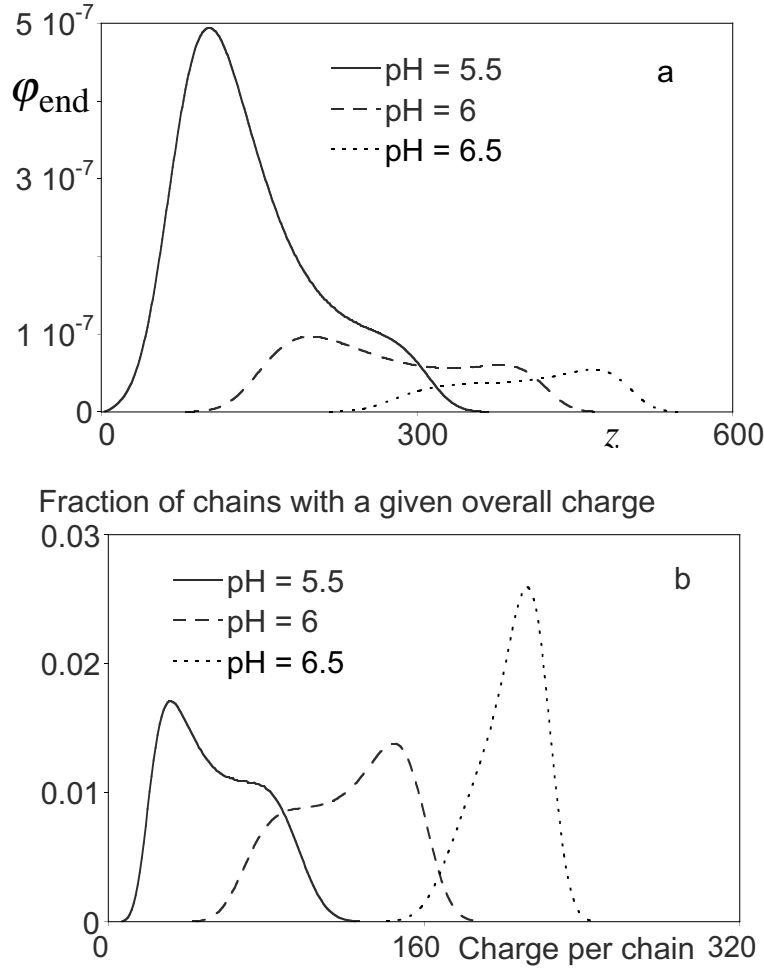


Figure 3.9: The end-point radial distribution profiles for different pH are shown in fig (a). In fig (b), the fraction of chains with a specific number of charges on the arm as a function of the number of dissociated groups on one arm is given. Other parameters of the star are  $N = 1600$ ,  $f = 20$ ,  $m = 5$  and  $I = 10^{-5.5}$  mol/L.

brush. For a planar brush, polymer density slightly increases before vanishing at the edge of the corona (cf. Borisov et al.<sup>71</sup>). This increase in the polymer density at the edge of the corona has been predicted by assuming both pure unscreened Coulomb repulsion and equal stretching of the branches.

As to why it is only visible for stars with small number of arms, those stars exhibit a narrow distribution of the end segments. Upon an increase in the number of arms, the end-segment distribution becomes broader. Due to this broad distribution of the end segments the edge maximum in the polymer density in many-arm stars is smeared out, see also fig 3.8a, and therefore not visible anymore.

On the other hand, the mean-field assumption becomes questionable for stars with long arms and low density because the volume fraction and the

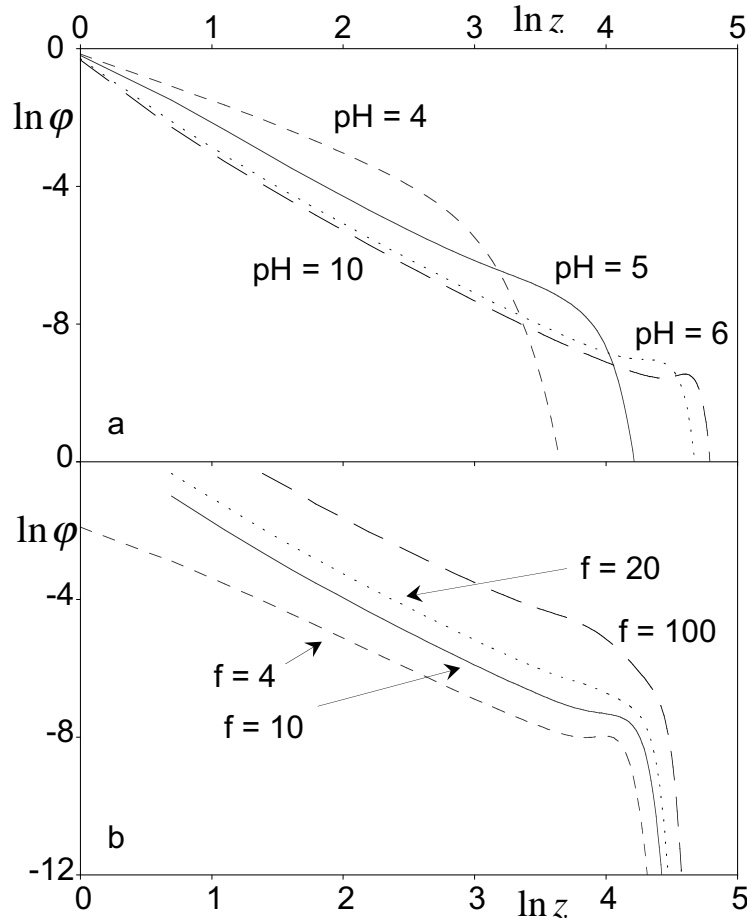


Figure 3.10: The volume fraction as function of the distance from the centre  $z$  in fig (a) an annealed polyelectrolyte star with  $I = 10^{-4}$  mol/L,  $m = 1$ ,  $f = 3$ ,  $N = 200$ , and pH as denoted in the graphs. Fig (b), a quenched star with  $\phi_s = 10^{-8}$  mol/L,  $m = 3$ ,  $N = 134$  and,  $f$  as denoted in the figure is shown. Both graphs are in double logarithmic scale

charge within one layer are smeared-out over the huge volume of one layer.

### 3.4.2 Behaviour of annealed polyelectrolyte stars upon changing the ionic strength

Increasing the salt concentration has two competing effects on the radius  $R$  of the star. The most common effect is the screening of the charges: with an increase in the salt concentration the electrostatic repulsion between the arms gets weaker. Therefore the size of the star decreases with increasing salt concentration namely (according to eq 3.23) as  $R \sim \Phi_b^{-1/5}$ , provided the salt concentration outside the star volume is larger than the concentration of counterions inside the star volume. The other effect is due to the fact that  $H^+$  and  $OH^-$  do not only contribute to the ionic strength but also participate in the

### 3.4 Results and Discussion

dissociation equilibrium, thereby determining the charge of the polyelectrolyte. At not too high  $pH$ , addition of salt in the bulk of the solution results in progressive substitution of  $H^+$  ions inside the star volume by  $Na^+$  ions and, hence, in an additional ionisation followed by an extension of the star arms. As long as the (simultaneously increasing) screening of the Coulomb interactions can be neglected, the scaling theory predicts a linear *increase* of the star size with increasing salt concentration:  $R \sim \Phi_b$  according to eq 3.19. The latter effect is only seen for low ionic strength. Altogether, the increase in the ionic strength will at first lead to an increase in the size, and when the ionic strength in the bulk solution becomes larger than that inside the star volume it causes a decrease in size, i.e. a maximum of the size as a function of salt concentration is expected.

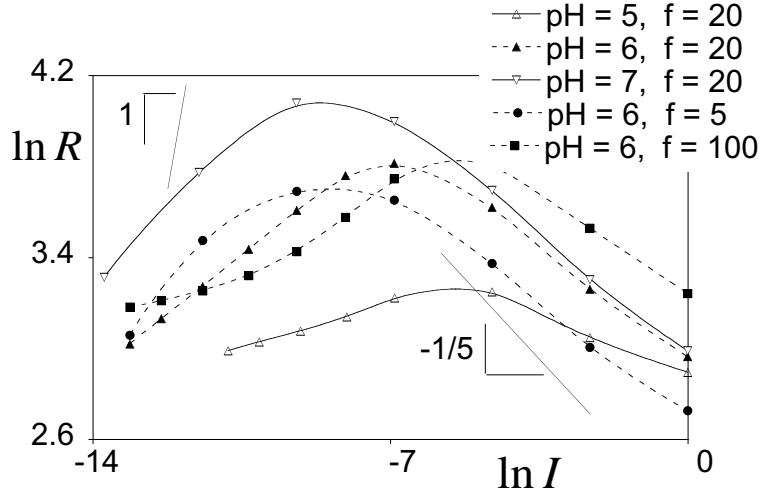


Figure 3.11: The size of an annealed star as a function of the ionic strength, for  $N = 200$ ,  $m = 5$ ,  $pH$  and number of arms  $f$  as denoted in the graph.

The size of the stars as a function of the ionic strength is shown in fig 3.11, a clear maximum is indeed observed in all cases. We observe, after the maximum, a slope slightly smaller than  $-1/5$ , due to the increasing importance of steric repulsion at large  $I$ . However, the power law dependence of  $R$  on  $\Phi_b$  in the annealed osmotic regime (low salt) is much weaker than  $R \sim \Phi_b$ , due to the fact that an increase in the salt concentration results simultaneously in stronger screening of the repulsion between ionised monomers. The maximum in size for an annealed star or curved brush is also found experimentally for some systems.<sup>72,73</sup>

The salt concentration  $\Phi_b^*$  at which the maximum in the star size is observed depends on  $f$  and  $\alpha_b$ , see eq 3.24. In fig 3.12 we see a linear increase of  $\Phi_b^*$  with the number of arms (fig 3.12a), and a maximum in  $\Phi_b^*$  with increasing bulk degree of dissociation  $\alpha_b$  (fig 3.12b and c). The proportionality between  $\Phi_b^*$  and  $f$ , predicted by eq 3.24, is nicely confirmed.

In fig 3.12b the dependence of  $\Phi_b^*$  on  $\alpha_b$  is shown. The exponent of the



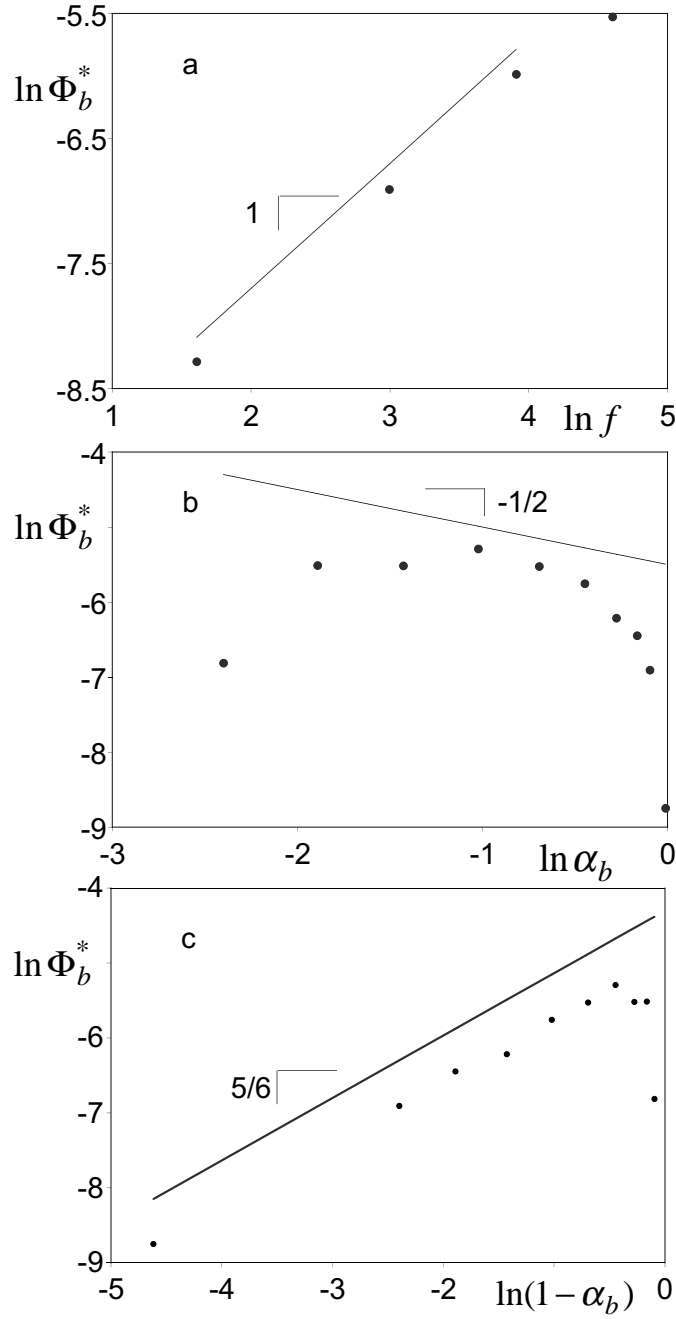


Figure 3.12: The dependence of the salt concentration  $\Phi_b^*$  at which the star size is maximal on the number of arms (a) and the degree of dissociation (b and c). The parameters are  $N = 200$ ,  $m = 5$ , in (a) the pH is 6, and in (b) and (c)  $f = 20$ .

### 3.4 Results and Discussion

powerlaw dependence, predicted as  $\alpha_b^{-1/2}$  (see eq 3.24), is not observed. To explain this, we have to make a distinction between the low degree of ionisation and the high degree of ionisation in the bulk. For the small  $\alpha_b$ , not only the electrostatic interactions determine the star conformation, but also steric interactions. Furthermore, the star size does not change dramatically with increasing ionic strength.

The reason, why for large  $\alpha_b$  the theoretical dependence of  $\Phi_b^*$  on  $\alpha_b$  is not observed, may be related to the underestimation of the screening of the electrostatic repulsion for  $\Phi_s < \Phi_s^*$ . This was also noted when we discussed fig 3.11. The dependence of  $R$  on the ionic strength is much weaker than the predicted linear dependence.

The dependence of  $\Phi_b^*$  on  $1 - \alpha_b$  is shown in fig 3.12c. The exponent of the power law dependence,  $\frac{5}{6}$ , is found.

The last part of this section, is addressed to the volume fraction profiles. For a star with 20 arms,  $m = 5$  or 1, at pH 5 or 6, and  $N = 200$ , the volume fraction profiles decay at low ionic strength as  $z^{-1}$ , as for neutral stars. An increase in the ionic strength induces ionisation and the polymer density profile decays as  $z^{-2}$ , a further increase in the ionic strength leads to screening of the charges on the arms. In this last regime the volume fraction profiles show a  $\varphi(z) \sim z^{-4/3}$  decay, see eq 3.22. Any new information is not gained from these volume fraction profiles and therefore they are not shown.

#### 3.4.3 Form factors of star shaped polyelectrolytes

A good technique to measure the internal structure and the size of a small object is SANS. The measurements give the scattering intensity as a function of the wave vector  $q$ . From the intensity the form factor  $P(q)$  can be obtained at sufficiently low concentration.<sup>†</sup> The form factor  $P(q)$  is directly related to the shape of the concentration profile by eq 3.36. So we explicitly calculate form factors from our volume fraction profiles. For comparison we also calculate  $P(q)$  for a single-power-law density profile,  $\varphi(z) \sim z^p$ . In figs 3.13 and 3.14, we present the form factors of a quenched and of an annealed polyelectrolyte star, respectively.

In fig 3.13a we see that upon increasing the charge on the branches the initial decay of  $P(q)$  gets faster, that indicates an increasing size of the star, as expected for quenched stars.<sup>55</sup> Simultaneously the first minimum in  $P(q)$  shifts to smaller  $q$ -value. The low  $q$  region for the non-charged star is nicely described by the form factor obtained with a volume fraction profile, decaying as  $z^{-1}$ , although volume fraction profiles with  $\varphi(z) \sim z^p$  in which  $p < -1$  fit the calculated form factor even better. The  $P(q)$  for the star with  $\alpha_q = 0.986$  is mimicked fairly well by a form factor resulting from  $\varphi(z) \sim z^{-2}$ . The  $P(q)$

---

<sup>†</sup>At the high  $q$  range not only the form factor contributes to the overall scattering intensity. An additional contribution is due to local fluctuations, and can therefore not be taken into account in our mean field model.

Table 3.1: Parameters used for fitting of the form factors of quenched and annealed stars, with a single-power-law decay.\*

System	$I$ in mol/L	$\varphi(z) \sim z^p$	$R_{star}$	$R_{core}$
neutral		$p = -1$	28	1
quenched, $\alpha_q = 0.014$	$10^{-4}$	$p = -1$	28	1
quenched, $\alpha_q = 0.339$	$10^{-4}$	$p = -2$	109	1
		$p = -2$	180	1
quenched, $\alpha_q = 0.986$	$10^{-4}$	$p = -2$	180	1
quenched, $\alpha_q = 0.339$	$10^{-4}$	$p = -2$	109	1
		$p = -2$	180	1
quenched, $\alpha_q = 0.339$	$10^{-2}$	$p = -4/3$	58	0
quenched, $\alpha_q = 0.339$	1	$p = -4/3$	31	1
annealed, pH= 6	$10^{-6}$	†		
annealed, pH= 6	$10^{-5}$	†		
annealed, pH= 6	$10^{-3}$	$p = -2$	180	1
annealed, pH= 6	$10^{-2}$	$p = -4/3$	81	0
annealed, pH= 6	1	$p = -4/3$	36	1
annealed, pH= 4	$10^{-4}$	$p = -1$	21	1
annealed, pH= 5.5	$10^{-4}$	$p = -8/3$	100	1.5
		$p = -2$	60	1.5
annealed, pH= 6	$10^{-4}$	$p = -2$	100	1.5
annealed, pH= 9	$10^{-4}$	$p = -2$	195	1

\*The core size for a star is  $(z^* - 1)$  layers large, where  $z^*$  is the layer where the arms are grafted. For a star with 20 arms, the grafting layer is 2 and therefore the core is 1 layer thick.

† can not be fitted with one exponent

### 3.4 Results and Discussion

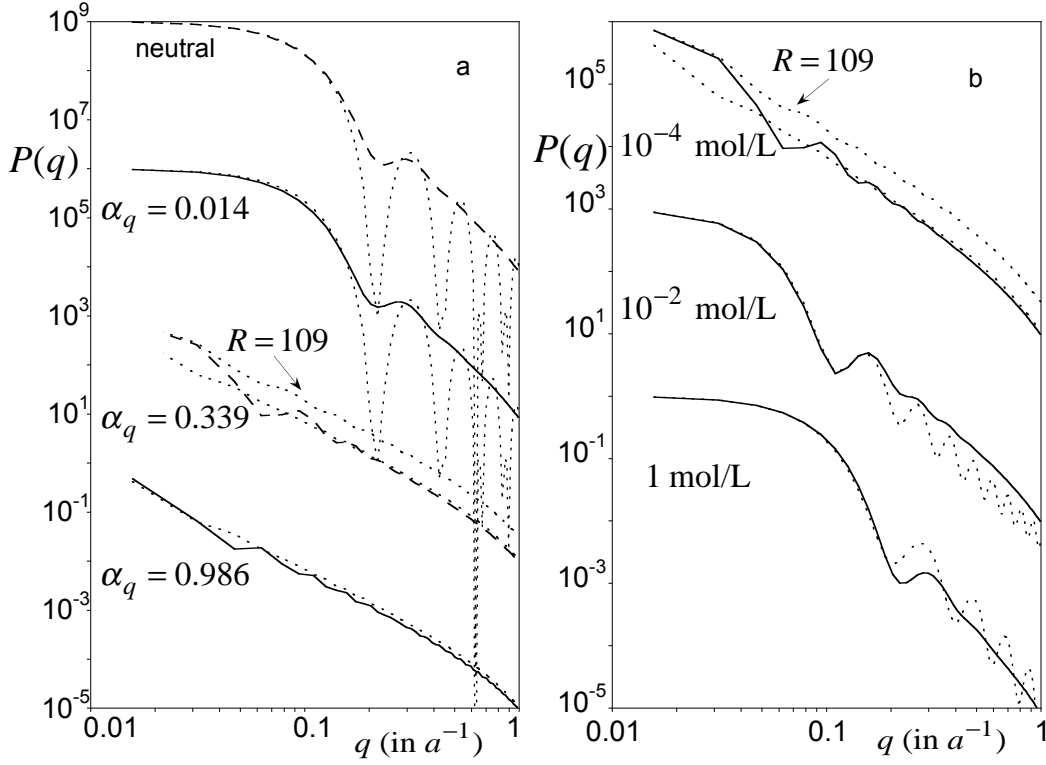


Figure 3.13: The form factor  $P(q)$  for a quenched star with  $N = 200$ ,  $m = 1$ , and  $f = 20$  in a  $\theta$ -solution. The dotted lines show the form factor for calculated volume fraction profiles with a single-power-law decay. In fig (a) the ionic strength is  $10^{-4}$  mol/L for a star with different number of charge per monomer  $\alpha_q$  (as indicated in the graph), in fig (b) a quenched star with  $\alpha_q = 0.339$  per monomer at different ionic strengths (concentrations are shown in the graph) is shown. The different calculations are shifted by multiplication factor of 1000. The parameters for the single exponential decay are denoted in table 3.1.

for the star with  $\alpha_q = 0.339$  can not be fitted using a single power law decay of the density profile; the low  $q$  region can be fitted with a  $P(q)$  obtained with a profile of  $\varphi(z) \sim z^{-2}$ , but  $P(q)$  at the high  $q$  range has the same shape as that of that of the star with a charge of  $\alpha_q = 0.986$ .

fig 3.13b shows the effect of varying the ionic strength. With decreasing ionic strength the star size grows. The star passes from the salt dominance regime,  $\varphi(z) \sim z^{-4/3}$ , to the osmotic regime,  $\varphi(z) \sim z^{-2}$ . The  $P(q)$  curves for the lowest salt concentrations ( $10^{-4}$ ,  $10^{-5}$ , and  $10^{-6}$  mol/L) have an identical shape (therefore the latter two are not shown).

The effect of different ionic strengths for an annealed polyelectrolyte is shown in fig 3.14a. The high salt concentrations give the same trends for annealed and quenched stars, i.e. the same exponent  $p = -4/3$  for the power law polymer density decay and a decreasing size with increasing the salt concentration. The salt ions only screen the charge but do not affect the degree of dissociation. In contrary for the low salt concentrations, i.e.  $10^{-5}$  and  $10^{-6}$

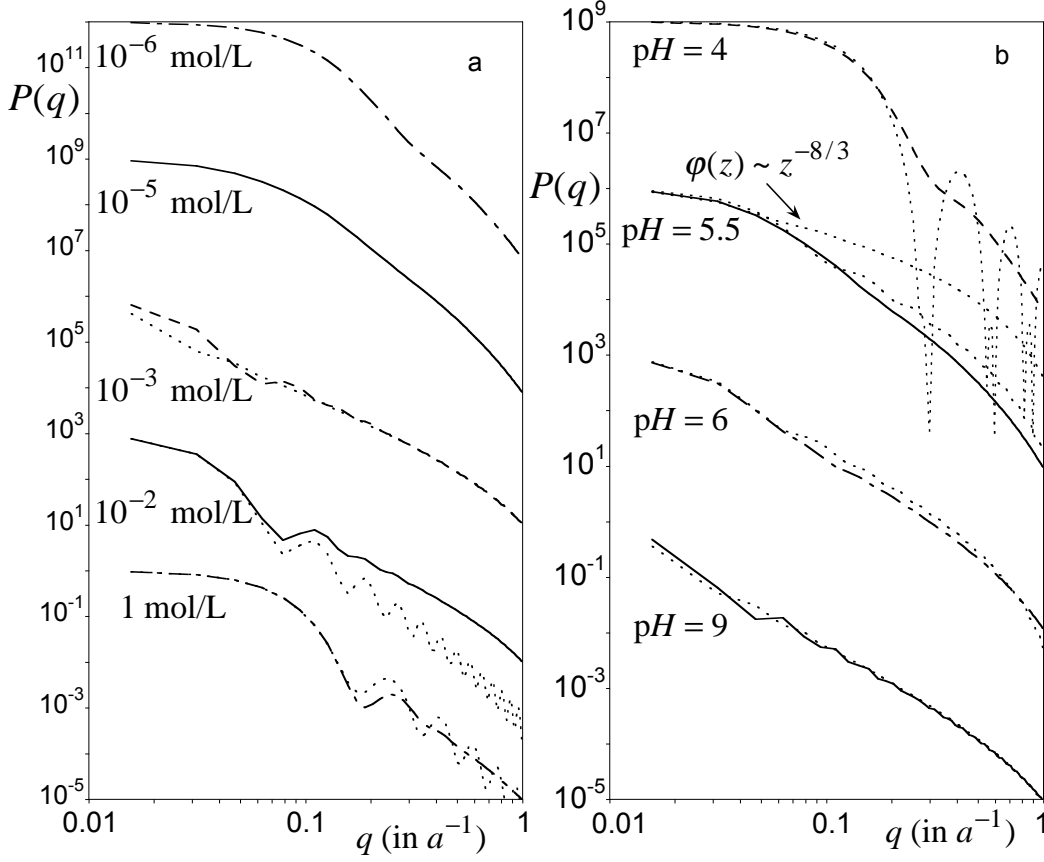


Figure 3.14: The form factor  $P(q)$  for an annealed star with  $N = 200$ ,  $m = 1$ , and  $f = 20$  in a  $\theta$ -solution. The dotted lines show the form factor calculated for volume fraction profiles with one-power-law decay. In fig (a) the  $\text{pH} = 6$  and the ionic strength is varied, in fig (b) the ionic strength is constant,  $I = 10^{-4} \text{ mol/L}$ , and the  $\text{pH}$  is changed. The different calculations are shifted by multiplication factor of 1000. The parameters for the one exponential decay are denoted in table 3.1.

mol/L, the shape of the form factors is totally different from those of the quenched star. The  $P(q)$  for these salt concentrations is smooth and can not be fitted with a single power law density decay. By changing the salt concentration from  $10^{-3}$  to  $10^{-6}$  mol/L, the initial decay of  $P(q)$  becomes smaller, and the oscillations disappear. The former indicates a decrease in size of star due to suppressed ionisation. This is expected because in fig 3.11 the star with  $f = 20$  and at  $\text{pH} 6$  has its maximum in size at  $\ln I = -7$ , i.e. at  $\approx I = 10^{-3} \text{ mol/L}$ . By comparing figs 3.13b and 3.14a the qualitative difference in the behaviour of the form factors of an annealed and a quenched star with changing the salt concentration is clearly seen. The  $P(q)$  of the annealed star loses most of its structure with decreasing the salt concentration while that for the quenched star exhibits pronounced oscillations in the whole range of salt concentrations.

In fig 3.14b the effect of increasing the  $\text{pH}$ , i.e. the amount of charges

### 3.5 Comparison with experiment

on the branches, at a constant ionic strength is shown. The form factors decrease faster as a function of  $q$  with increasing  $pH$ , that is an indication for an increasing size of the star. In fig 3.14b we see at  $pH$  4 and 9 the form factor has pronounced oscillations in contrast to  $pH$  5.5 and 6. The  $P(q)$  curve at  $pH$  4 resembles that for a neutral star and can be fitted with a density profile of  $\varphi(z) \sim z^{-1}$ . The  $P(q)$  at  $pH$  9 can be fitted by the  $\varphi(z) \sim z^{-2}$  decay just as for a fully charged star, compare fig 3.14a. At intermediate  $pH$  values, where the number of charges on the star branches is gradually increasing, the form factors can not be fitted by those calculated with one power law density decay. From the analytical theory one expects for these intermediate values of  $pH$  the combination of a  $\varphi(z) \sim z^{-1}$  and a  $\varphi(z) \sim z^{-8/3}$  density profile (in the central and in the peripheral region of the star corona, respectively). Therefore, the form factor calculated with the volume fraction profile with a single-power-law volume fraction profile of  $\varphi(z) \sim z^{-8/3}$  does not provide a good fit for the  $P(q)$  curves.

At the high  $q$  region, the  $P(q)$  is very sensitive to the size of the core, especially for the profiles with a strong decay, i.e.  $\varphi(z) \sim z^{-2}$  or  $z^{-8/3}$ .

### 3.5 Comparison with experiment

The calculated  $P(q)$  curves (figs 3.13 and 3.14) give the general trends for the expected behaviour of the form factors for star-shaped polyelectrolytes. Now we want to compare our calculations directly to a recent SANS-experiment with polymeric micelles with annealed polyelectrolytes as the coronal chains. Groenewegen et al.<sup>61</sup> used a diblock copolymer of polystyrene/poly(acrylic acid) (PS/PAA), which associate in aqueous solutions to form micelles. The core is formed by the PS-block and has an average size of 4.5 nm. The number of polymers associated in one micelle was about 100. This number was calculated from the core size, using the density of poly styrene and by normalizing the partial form factor of PS-PS. Groenewegen et al.<sup>61</sup> have fitted the measured form factors with those obtained from volume fraction profiles with a one power law decay, and found that  $\varphi(z) \sim z^p$  with  $p < -2$  provides the best fit for their experimental data at low degree of ionisation.

To compare the measured data, we use the parameters listed in table 3.2. For the polymeric micelles studied by Groenewegen et al.<sup>61</sup> it was shown that the variation of  $pH$  and/or salt concentration does not affect the aggregation number and therefore also not the core size. Therefore these micelles can be modeled like star polymers with fixed number of arms grafted to an impermeable core of a given size. The parameters used, are partially given by Groenewegen et al.<sup>61,62</sup>

Fig 3.15 shows the volume fraction profiles calculated for the above mentioned system. It is seen that for  $pH$  4 and 5 the volume fraction of the polymer segments decreases as  $z^{-1}$  and for  $pH$  8 and 9 as  $z^{-2}$ . Analytical theory predicts these decays for non-charged and fully charged stars, respectively.

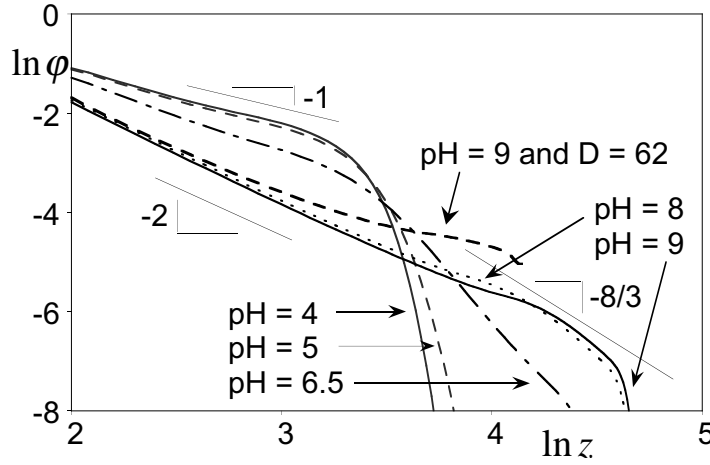


Figure 3.15: The volume fraction of the polyelectrolyte micelle as a function of the distance from the centre  $z$  in double logarithmic scale. The  $pH$  is denoted in the graphs. The parameters of the polyelectrolyte micelle are denoted in table 3.2.

At  $pH$  6.5 a transition between the fully charged and the non-charged state is seen. The volume fraction profiles show a wide range with a radial density decay, which is faster than  $z^{-2}$ .

The volume fraction profile for a smaller cell size is just shown for comparison. The size of the cell is related to the micellar concentration,  $D = 62$  is obtained from the given concentration of 0.093 mol PAA/l, the degree of polymerization (120) and the aggregation number of the micelle (100).<sup>‡</sup> Only at high  $pH$ , where the micelle is fully charged there is a difference between  $D = 62$  and  $D = 206$ . Further on we will use the data collected for a cell with 206 layers.

To be able to compare directly with the measured data of Groenewegen et al.<sup>61</sup>, we calculate the scattering form factor from the volume fraction profiles using eq 3.36. In fig 3.16 the calculated form factors are shown. With increasing  $pH$  the  $P(q)$  curves decrease faster, which indicates a larger size for the micelles. The first minimum in  $P(q)$  for  $pH$  4 and  $pH$  5 is at  $q = 0.37 \text{ nm}^{-1}$ , which is in good agreement with the experiment, see also fig 3.17. This minimum shifts to larger  $q$  with increasing  $pH$ . This shift of the minimum to higher  $q$  indicates a change in the shape of the density profile.

We have fitted our calculated form factors with form factors for a single-power-law decay. For  $pH$  4, 5, 8, and 9 this leads to good fits. As was already

<sup>‡</sup>The average distance between two polyelectrolyte micelles can be calculated from the concentration of hydrophobic PAA  $x$ , the aggregation number  $f$ , and the degree of polymerization  $N$ . Every polymer has a volume of  $\frac{N}{xN_{Av}}$  liter available, in which  $N_{Av}$  is Avagadros number. The volume occupied by one micelle is then  $\frac{Nf}{xN_{Av}}$ , from this volume one can easily calculated the average distance between two micelles and the dimensionless radius of the cell  $D$ .

### 3.5 Comparison with experiment

Table 3.2: Parameters\* used for the calculation of the polymeric micelles that can be compared with the experimental results of Groenewegen et al.<sup>61</sup>

Parameter	value
Number of monomers, $N$	120
Number of arms, $f$	100
$m$	1
Solvent quality	$\theta$
Ionic strength	$10^{-4}$ mol/L
$pK$	5
Permittivity of the core	$2\epsilon_0$
Radius of the core $R_{\text{core}}$	$6 * 0.6$ nm
Radius of the cell $D$	$206 * 0.6$ nm

\*The polystyrene core is known to be hydrophobic. In the numerical calculations it is possible to take this into account but it hardly effects the volume fraction profiles and even less the form factors. Therefore the results of these calculations are not shown.

Table 3.3: Parameters for the single-power-law decay of the volume fraction profiles used for the fit the calculated form factors in fig 3.16.

pH	$\varphi(z) \sim z^p$	$R_{\text{star}}$	$R_{\text{core}}$	
4	$p = -1$	18	6	dashed line
5	$p = -1$	18	6	dashed line
5	$p = -1$	19	6	dashed line
5	$p = -8/3$	35	10	dotted line
6.5	$p = -8/3$	50	8	dotted line
6.5	$p = -2$	40	6	dashed line
6.5	$p = -2$	40	6.5	dashed line
8	$p = -2$	95	6	dashed line
9	$p = -2$	100	6	dashed line



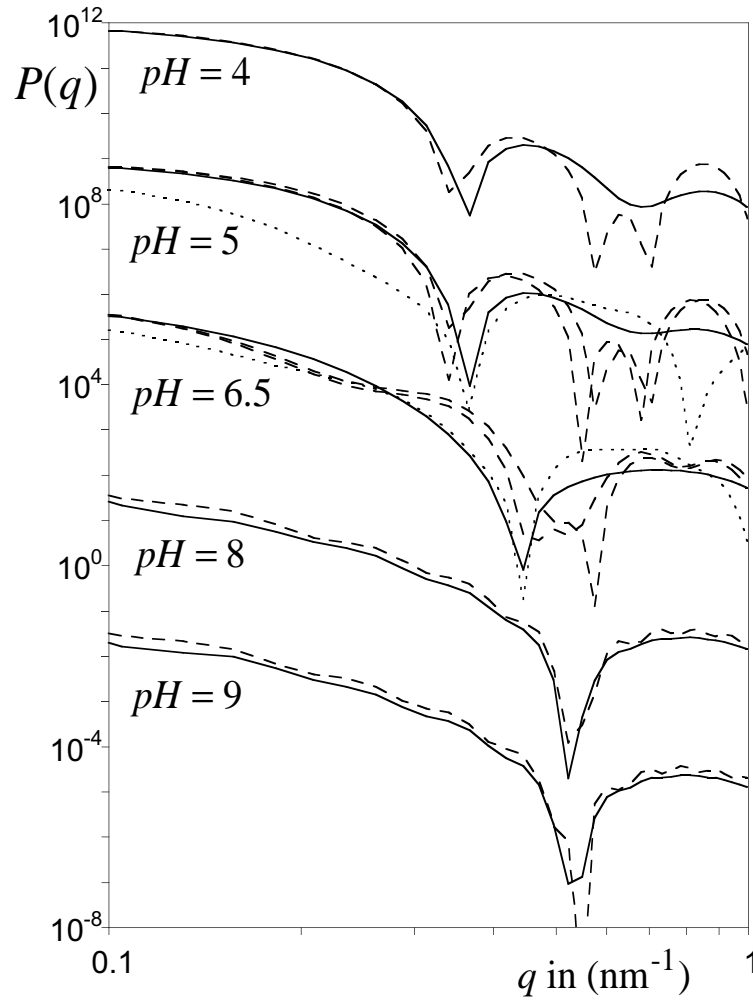


Figure 3.16: The calculated form factors of a polyelectrolyte micelle,  $I = 10^{-4}$  mol/L,  $D = 200$ , and the pH as denoted in the graph. The dashed and dotted lines are the calculated form factors for a single-power-law decay, the parameters are listed in table 3.3. The form factors for the different pH's are shifted along the y-axis by multiplication factor of 1000.

### 3.5 Comparison with experiment

mentioned for these  $pH$ 's the volume fraction profiles show just one regime with a clear power law behaviour ( $\varphi(z) \sim z^{-1}$  for  $pH$  4 and 5 and  $\varphi(z) \sim z^{-2}$  for  $pH$  8 and 9). At  $pH$  6.5 a good fit to the calculated form factors is hardly found, a volume fraction with a density decay as  $\varphi(z) \sim z^{-2}$  gives a form factor with a minimum at too high  $q$ . The density decay of  $z^{-8/3}$ , gives a the minimum at the right  $q$ -value but only if the size of the core is set larger than it was. Furthermore at low  $q$  this form factor of this single-power-law decay gives a lower value for  $P(q)$ .

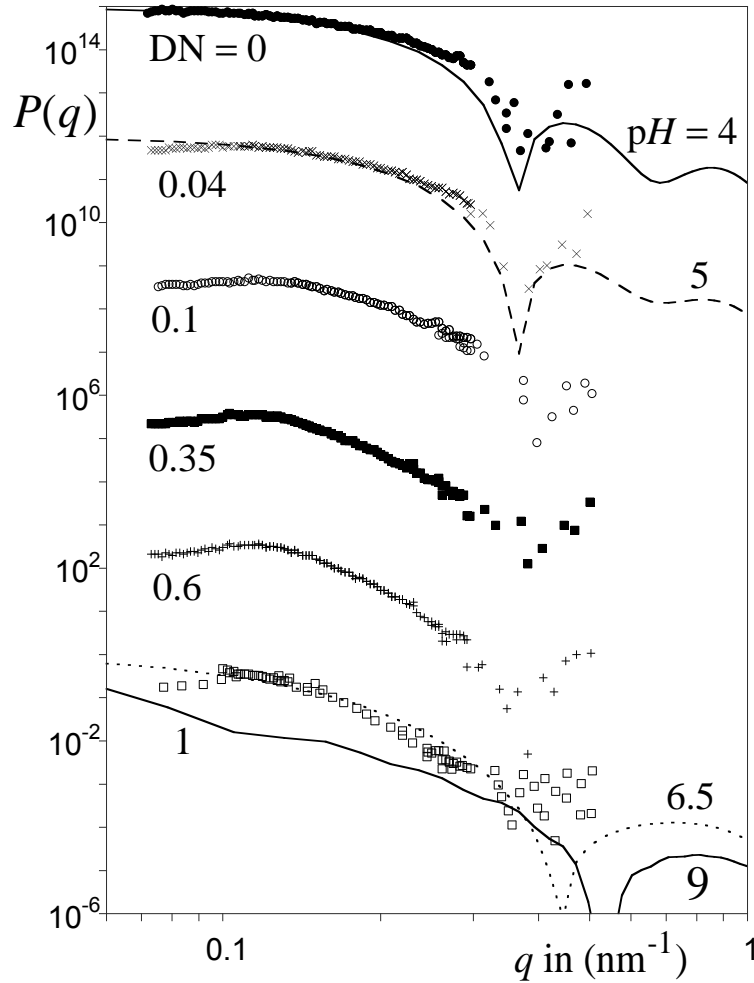


Figure 3.17: The data of Groenewegen et al.<sup>61</sup> (symbols) for different degree of neutralization (DN) compared with the calculated form factors of a polyelectrolyte micelle,  $I = 10^{-4}$  mol/L,  $D = 200$  (lines). The degree of neutralization is the ratio of added moles of base per monomers of acrylic acid present in the solution. The form factors for the different degrees of neutralization are shifted along the y-axis by a multiplication factor of 1000.

In fig 3.17 the numerical form factor is directly compared with the data given in fig 6 of Groenewegen et al..<sup>61</sup> The degree of neutralization is an easy experimental accessible parameter, which gives an indication of the change in

the degree of dissociation  $\alpha$ . The actual degree of dissociation depends for the same degree of neutralization on the concentration of the polyelectrolyte, we therefore used the  $pH$  which is directly related to the degree of dissociation, via eq 3.1.

From fig 3.17 it can be seen that the data of the DN of 0, 0.04 and 1 can be reasonably well be described by the calculated form factors of respectively  $pH$  4, 5 and 6.5. The form factors of the degree of neutralization in between 0.04 and 1 change gradually, the minimum shifts to larger  $q$  and the slope of  $P(q)$  gets steeper. These features are obtained also from the calculated form factors. The surprising part is that the high degree of neutralizations are not well described by the form factors of  $pH$  9 but by the form factor of  $pH$  6.5. Furthermore we conclude from the experimental and the numerical results that with increasing  $pH$ :

- Both calculated and measured formfactors exhibit faster initial decay.
- The first minimum in  $P(q)$  is shifted in the calculated curves to larger  $q$  while in the measured curves the minimum gets broader and also shifts to larger  $q$ .

### 3.6 Conclusion

We have investigated the conformational structure of annealed polyelectrolyte stars in dilute solutions as a function of the number of arms, the ionic strength, and the  $pH$  of the solution. This has be done by means of detailed numerical SCF-calculations, which complement the analytical scaling theory.<sup>35</sup> The calculations confirm the specific behaviour of annealed stars vs quenched stars and enable us also to

- study the intrinsic structure of an annealed star
- calculate measurable properties of an annealed star
- indicate the parameter range where the specific effects of annealed stars are expected in experiments

The decay of the polymer denstiy profiles in the osmotic annealing regime is predicted as  $\varphi(r) \sim r^{-8/3}$ . In the numerical results the exponent  $p$  of  $-8/3$  can only be found for a small range of  $pH$ 's and number of arms. Although a fast ( $p < -2$ ) decrease of the polymer density and a huge increase of the charge on the star with distance from the centre are seen, there does not seem to be a single scaling exponent for the osmotic annealing regime. There remains another small question with respect to the volume fraction profiles; in some calculations this fast decay of the volume fraction profile at the end of the star is preceded by a decay of  $z^{-2}$ . This decay is expected for fully charged stars, but this is not the case. This extra stretching of the inner part of the star can be due to pulling of the ends of the star branches, which are charged.

Furthermore our calculations show that at the periphery of the star corona, the effect of curvature on the conformations of the star branches is less important, i.e. the outermost regions of the star corona behaves similarly as a

### 3.7 Acknowledgments

planar annealed polyelectrolyte brush. This conclusion is supported by (i) a bimodal distribution of the end-segments and (ii) a quasi-linear dependence of  $\log(1 - \alpha)$  on  $z^2$ .

Where the star is not fully charged, the end-point distribution shows two maxima. This bimodal distribution is only clearly seen for stars with long branches and low salt concentration.

The analytical prediction of the maximum in the size with increasing number of arms or with increasing salt concentration is confirmed. The salt concentration at this maximum is directly related to the internal charge density,  $\Phi_b^* = \frac{\alpha_b f N/m}{4/3\pi R^3}$ . This means that by just measuring the size of a micelle or branched polyelectrolyte as a function of the ionic strength, an estimate of a charge density of the particle can be obtained. The maximum in size for a annealed star or curved brush is also found experimentally for some systems.  
72,73

The evolution of the form factor of a star as a function of the salt concentration is totally different for a quenched and an annealed star. With decreasing the salt concentration the quenched star shows always oscillations, pronounced minima, and an increase in the slope of the initial decay of the form factor. In contrast, for annealed stars the oscillations and the minima disappear with decreasing the salt concentrations and the slope of the initial decay gets weaker.

The form factors calculated from numerical volume fraction profiles can be well-mapped to the experimental form factors measured by Groenewegen et al.<sup>61</sup> for annealing star-shaped polyelectrolyte micelles. The fit of the form factors with volume fractions with a single exponential decay is feasible in the extreme states of the star, i.e. fully charged or neutral. In the intermediate range of pH's both  $\varphi(z) \sim z^{-1}$  and  $\varphi(z) \sim z^{-8/3}$  decay play a role in the volume fraction profiles and therefore a fit of the form factor decay with a one exponential decay is not feasible.

From this study, we got a detailed and consistent picture of the behaviour of annealed and quenched polyelectrolyte stars. Furthermore, we have demonstrated that the numerical method we used is flexible and can mimic well experimental systems.

### 3.7 Acknowledgments

F.A.M. Leermakers is acknowlegde for his enthousastic discussions.

## Chapter 4

# Adsorption of a quenched polyelectrolyte: SF–SCF model calculations

### Abstract

The adsorption of polyelectrolytes on a charged surface is calculated with a numerical self-consistent-mean-field model. Only electrostatic interactions between the polyelectrolyte and the surface are taken into account, specific or chemical interactions are neglected. The adsorbed amount is calculated without and with taking into account the swelling in the bulk due to electrostatic repulsion. The latter is done by adsorbing the polyelectrolyte until it has the same chemical potential as a polyelectrolyte with excluded volume interaction in the bulk.

The adsorption is higher when the swelling in the bulk is taken into account. Furthermore, due to the fact that in the new way of calculating the polyelectrolyte in solution is surrounded by an electric field, adsorption of the polyelectrolyte can overcompensate the charge on the surface, even though there is no specific interaction with the surface.

The difference between a surface with quenched (fixed) charges and a surface with annealed (regulating) charges is studied. The annealed surface has almost a constant surface potential. The amount of adsorbed polyelectrolytes on a quenched surface is lower than that on an annealed surface, if the initial surface charge is the same. On an annealed surface, the adsorption of a polyelectrolyte induces extra charges and this increases the adsorption. For the same reason, it is harder to overcompensate the charge on an annealed surface than on a quenched surface.

To study the influence of the molecular architecture of a polyelectrolyte on the adsorption, we compare a linear chain, a star-shaped polymer, and a dendrimer. The more densely branched polyelectrolytes have a higher adsorbed amount than linear polyelectrolytes.

## 4.1 Introduction

### 4.1 Introduction

A lot of work has been done on the adsorption of polyelectrolytes onto charged and uncharged surfaces. Most theoretical work has been devoted to the adsorption on neutral surfaces or to surfaces with a quenched charge.<sup>74–79</sup> Muthukumar dealt with the question at which salt concentration or temperature the adsorption starts, and he calculated the layer thicknesses and the stretching of the adsorbed polyelectrolyte in Monte Carlo simulations. Andelman and Joanny,<sup>80</sup> and Borukov et al.<sup>81</sup> studied the adsorption of a polyelectrolyte on a surface with a constant potential. A surface with annealed charges can in practice be seen as a surface with a constant potential.

Annealed charged surfaces, i.e. oxide surfaces, have a large relevance for catalysis,<sup>82</sup> soil chemistry,<sup>83–85</sup> and paint chemistry.<sup>86</sup> This is due to their high reactivity and large abundance. These surfaces adjust their charge to the local concentration of, e.g., hydrogen ions and are called variably charged, annealed, or constant-potential surfaces.

Adsorption of small ions on annealed surfaces has been studied extensively. The experiments are normally interpreted by site binding models.<sup>87,88</sup> The MUSIC model presents a detailed description of the surface and its charge, together with an electrostatic model for the solution side of the interface.<sup>88</sup> The conformational entropy of the adsorbed species is not taken into account because for small molecules this is not important. The surface charge density is affected by both the adsorption of protons and of salt ions. The electrostatic interaction is mostly done on a mean-field base. Borkovec has shown that in practice this approximation suffices.<sup>89</sup>

In this article we study theoretically the adsorption of polyelectrolytes onto surfaces with either quenched or annealed charges with a self-consistent-mean-field model (SF–SCF model). The basis of this theory has been developed by Scheutjens and Fleer<sup>13,16</sup> for the adsorption of neutral polymers on a surface. The effect of charge has been incorporated by Van der Schee.<sup>74</sup> Böhmer et al.<sup>90</sup> have made a start with incorporating charges which depend on the  $pH$ . Israëls et al.<sup>43</sup> have improved the description of annealed charges. The reaction of segments with protons was extended to the reaction with different molecules by Van Male.<sup>67</sup> Vermeer et al.<sup>91</sup> were the first who calculated polyelectrolyte adsorption on an annealed surface with this model.

In comparison to other theoretical calculations,<sup>80,81</sup> the SF–SCF calculations do not assume that the surface has a constant potential, but the potential follows self-consistently from the surface reaction with protons and can be influenced by adsorption of salt ions and polymers.

Yet, the standard SF–SCF model is not well suited to describe the adsorption of polyelectrolytes. The main reason is the neglect of swelling of polyelectrolytes in the bulk solution. In the standard SF–SCF model the chains in the bulk are described as ideal random walks, irrespective of solvent strength, bulk volume fraction or charge on the chains. This results in a systematic over-estimation of the entropy of polyelectrolytes in solution. In contrast, the

## Adsorption of a quenched polyelectrolyte: SF–SCF model

chains at the surface do experience swelling due to the accumulation of mass and charge. This means that in classical mean-field models the adsorption of polyelectrolytes is always under-estimated. In this article a novel way is used to calculate the adsorption of polyelectrolytes.<sup>67,92</sup> In the new method, the chemical potential of a polyelectrolyte in solution is calculated separately; the calculation is done in such a way that the polyelectrolyte feels its own charge. When the adsorption of this polyelectrolyte is calculated we use this chemical potential together with the standard equilibrium criterion of equal chemical potential. While we do not claim that this trick overcomes all well-known deficiencies of mean-field models for polyelectrolyte adsorption, we do expect a significant improvement over the classical SF–SCF method

The adsorption of polyelectrolytes is studied for the case in which only electrostatic interactions are present. Other interactions like Van der Waals forces may play a role in the adsorption too but in most cases the electrostatic interactions will be dominant. Two types of surfaces will be distinguished. Firstly, surface with a fixed charge density (a quenched surface) representing, for instance, a latex particle with sulfonate groups at the surface. Secondly, a surface which adjusts its charge by proton exchange as polyelectrolytes adsorb onto it (an annealed surface) representing, for example, a metal-oxide surface. Additionally, the effect of different chain architectures of the polyelectrolyte is studied. To this end we have chosen to study linear, star-shaped, and starburst (dendrimeric) polyelectrolytes.

First, we will explain the new theory for polyelectrolyte adsorption in a mean-field model. This is followed by the results of the adsorption of quenched polyelectrolytes of different shapes on a quenched surface, and on an annealed surface. The results of the new model are compared with the classical model. The extent of the charge adjustment of the annealed surface and the volume fraction profiles of adsorbed polyelectrolytes are presented and discussed in the context of current theoretical treatments.

## 4.2 SCF model by Scheutjens and Fler (SF–SCF model)

The numerical SCF-approach used is based on the Scheutjens–Fler (SF) algorithm. All the calculations in this article were done with the software package `sfbox`.<sup>17</sup> Some information on the SF–SCF model is given below, for full details the reader should consult the references quoted in the previous section.

The SF–SCF model is a self-consistent-field model. The distribution of molecules in the system, i.e. the volume fraction profiles  $\varphi(z)$ , are generated using spatially varying fields  $u(z)$ . In turn, these fields are a function of the volume fractions. The fields contain various specific interactions as well as an excluded volume parameter, which results from an incompressibility constraint. At the start of the calculation, initial fields are assumed and the resulting

## 4.2 SCF model by Scheutjens and Fler (SF–SCF model)

volume fractions are calculated. Then the incompressibility constraint is tested and the fields are adjusted until fields and volume fraction profiles are mutually self-consistent.

To facilitate the calculation of the distribution of molecules, space is divided into layers (flat geometry) or shells (spherical or cylindrical space). Within each layer or shell, local differences are smeared out, i.e. a mean-field model in one dimension results. The maximum number of layers or shells is denoted as  $M$ .

Electrostatic interactions are taken into account by a multi-Stern-layer model, the charge planes are placed in the middle of each layer. The capacity of the layer is determined by the permittivities of the segments and the solvent in that layer and the thickness of the layer  $a$ . This thickness is in this article chosen to be 0.3 nm, which is about equal to the edge of a cube with the volume of one water molecule. This ensures that in a liter 55 moles of monomers are present, see also appendix A.

In earlier calculations<sup>91,93,94</sup> the polyelectrolyte molecules in bulk solution behaved as if they were neutral, i.e. they did not feel their own charge or potential. As a consequence they did not swell. Therefore, their entropy was over-estimated and their chemical potential was too low compared to that of a real polyelectrolyte. At the same time, it was assumed that the chains, at the surface the chains *do* swell to some extent due to the accumulation of charge. As a result the adsorbed amount was too small, in the earlier SF–SCF calculations.

In the present paper, we try to overcome this deficiency of the standard method by performing two separate calculations: one in the bulk solution and one at the surface. In the bulk calculation, one polyelectrolyte molecule is pinned in space and surrounded by the electrolyte solution, which contains salt and other (freely translating) polyelectrolyte molecules. The restricted polyelectrolyte is forced to have at least one segment in the centre of a spherical calculation box, i.e. the polyelectrolyte is “pinned”. The chemical potential  $\mu_{p, c}$  of the pinned polyelectrolyte can now be defined as<sup>67</sup>

$$\mu_{p, c} = F - \sum_{i \neq p, c} n_i \mu_i^{\text{FH}} + k_B T \ln \varphi_b \quad (4.1)$$

where  $F$  is the Helmholtz energy of the system,  $n_i$  is the total number of molecules of component  $i$ , and  $\mu_i^{\text{FH}}$  is the Flory–Huggins expression for the chemical potential of component  $i$ . In the second term on the right hand side,  $k_B$  is the Boltzmann constant,  $T$  the temperature, and  $\varphi_b$  the volume fraction of the polyelectrolyte in solution. The sum runs over all molecules in the system, except for the pinned molecule. Since the position of the restricted molecule is fixed, the translational entropy should be added separately; this justifies the last term.

Now that we have an expression for the chemical potential of a swollen chain in the bulk phase (eq 4.1), we turn our attention to the surface. Here, the adsorbed amount is *a priori* unknown. We vary the adsorbed amount until



## Adsorption of a quenched polyelectrolyte: SF–SCF model

the chemical potential is equal to that resulting from the bulk calculation. Just as the pinned polymer in the bulk calculation, also the adsorbed polymer is not in equilibrium with its bulk (which is a neutral, non-swollen, gaussian chain in the mean-field calculations). The chemical potential  $\mu_{p, \text{ ads}}$  of the adsorbed polymer is given as<sup>67</sup>

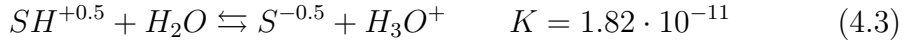
$$\mu_{p, \text{ ads}} = \frac{\partial \left( F - \sum_{i \neq p, \text{ ads}} n_i \mu_i^{\text{FH}} \right)}{\partial n_{p, \text{ ads}}} \quad (4.2)$$

where the sum runs over all molecules, except those that are adsorbed to the surface. The differentiation is performed using a constant surface area, volume, temperature, and chemical potential of all components included in the sum. Eq 4.2 reproduces the standard SF–SCF result for the chemical potential when the adsorbed amount is taken equal to that resulting from a standard SF–SCF calculation. \*

### 4.3 System definition

**Surface** In the calculations we use two kinds of surfaces namely with a quenched and with an annealed surface charge density.

The annealed surface is chosen as a model for an oxide surface.<sup>95–97</sup> For describing the pH-effect on the surface charge density, the so called 1-pK model is used.<sup>98</sup> In this model the surface consists of monomers which can dissociate according to the following reaction:



The point of zero charge (pzc) of the surface is fixed by the proton dissociation constant  $K$ .  $K$  is the dimensionless value of a dissociation constant, i.e. the concentrations of both  $H_2O$  and  $H_3O^+$  are used in the definition of  $K$ . The pzc is taken to be at pH 9, this corresponds with the  $K$ -value in eq 4.3. The permittivity of the surface segment is  $40\epsilon_0$  in which  $\epsilon_0$  is the permittivity of vacuum. Every site is  $(0.3 \text{ nm})^2$  small, i.e.  $\approx 11$  sites per  $\text{nm}^2$ , therefore the maximal surface charge is  $0.5e/(0.3 \text{ nm})^2 = 0.889 \text{ C/m}^2$ .

In fig 4.1a the surface potential of the annealed surface is shown. There is hardly any difference between the different salt concentrations. The solid line denotes the surface potential if the surface behaved as a Nernstian surface, for which the potential is directly proportional to  $(\text{pH}_{\text{pzc}} - \text{pH})$ . It follows from fig 4.1a that the surface is pseudo-Nernstian.

In fig 4.1b the surface charge density  $\sigma_s$  of the annealed surface is shown, the point of zero charge (pzc) is at pH 9. The surface charge density decreases

---

\*Eq 4.2 represents a numerical differentiation to obtain  $\mu_{p, \text{ ads}}$ . An explicit expression is available

### 4.3 System definition

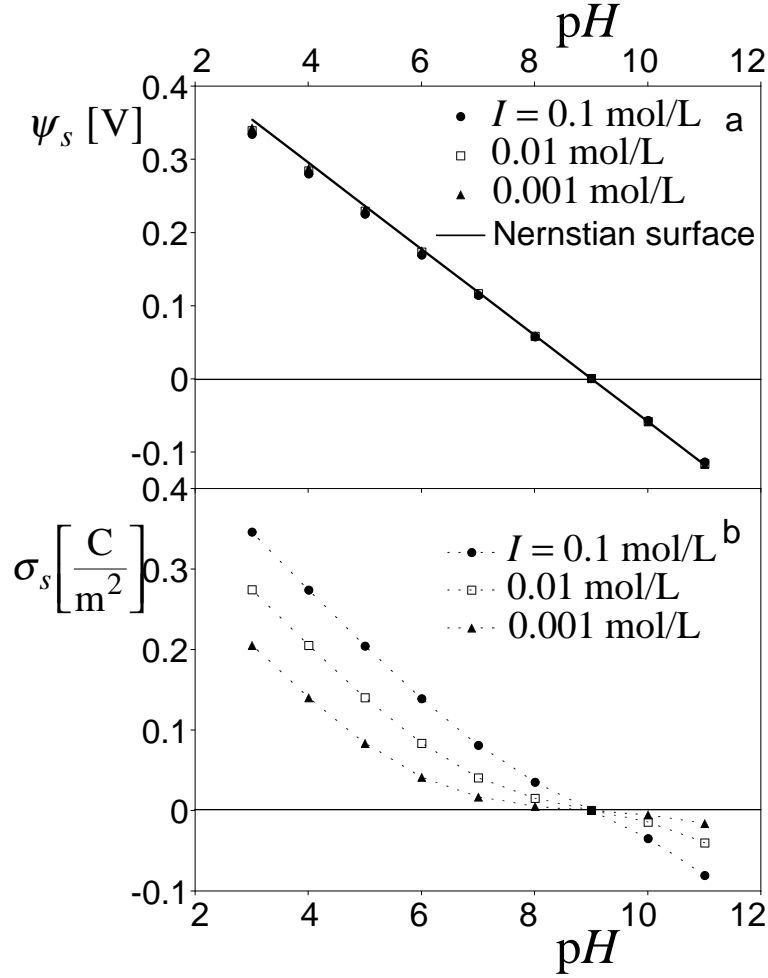


Figure 4.1: Characteristics of the calculated annealed surface as a function of the pH for different ionic strengths  $I$ , (a) the surface potential  $\psi_s$  and (b) the surface charge density  $\sigma_s$ .

with increasing pH and decreasing salt concentration. Typically, this behaviour corresponds to iron oxides such as goethite and hematite.<sup>95,96,99</sup>

The quenched surface is chosen to have a charge density  $\sigma_s = 1.7 \cdot 10^{-2}$  C/m², which is the same as that of an annealed surface at pH 7 and at an ionic strength of 0.001 mol/L.

**Polyelectrolytes** The polyelectrolytes are homopolymers, i.e. every monomer has the same charge and chemistry. The Flory–Huggins parameter  $\chi_{FH} = 0$ , which indicates that the solvent quality is good. All the molecules have 201 monomers and every monomer has a fractional charge of  $\frac{1}{m}$ .

Three polyelectrolyte molecules with different architecture are studied in this article: a linear chain, a star-shaped molecule, and a dendrimer, see also fig 4.2.

## Adsorption of a quenched polyelectrolyte: SF–SCF model

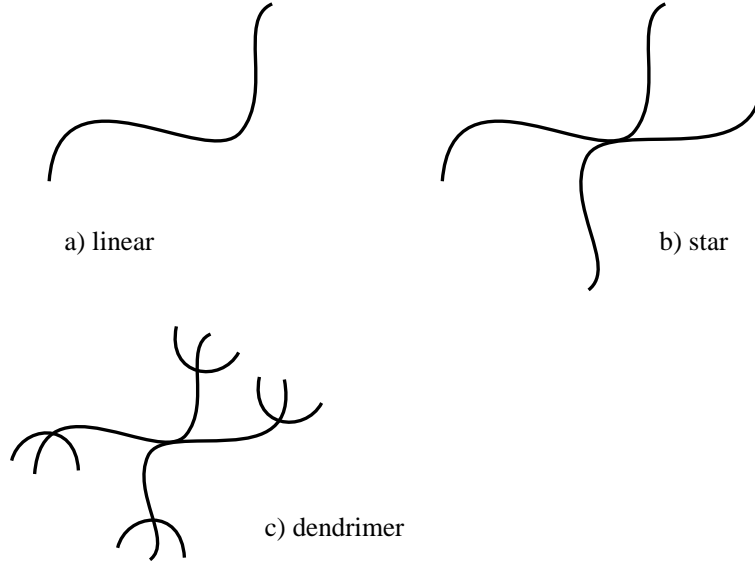


Figure 4.2: Molecules with different architecture.

**Adsorbed amount** The adsorbed amount  $\theta_{exc}$  of the polymer is calculated as the excess amount, i.e.

$$\theta_{exc} = \sum_1^M (\varphi(z) - \varphi_b) \quad (4.4)$$

In eq 4.4  $\varphi(z)$  is the volume fraction of the polymer in layer  $z$  and  $\varphi_b$  is the volume fraction of the polymer in the bulk solution. Negative values of  $\theta_{exc}$  are also possible, namely when the polymer is depleted from the surface. A  $\theta_{exc}$  of 1 means that one lattice layer is totally filled. The definition of the adsorbed amount as given in eq 4.4 loses its relevance if the bulk volume fraction of the polymer is high ( $\varphi_b \geq 10^{-2}$ ), or if the polymer adsorbs with most of its segments protruding into the solution.

The adsorbed amount is calculated as a function of the volume fraction of the polymer  $\varphi_b$ , the ionic strength  $I$ , and for the annealed surface also as a function of the  $pH$ . Both the polymer concentration and the  $pH$  can influence the ionic strength. Therefore the amount of added salt is different for different  $pH$ 's and volume fractions of the polyelectrolyte. Furthermore, the ionic strength determines the upper limit of the the polymer concentration in the bulk. The ionic strength of 0.001 mol/L means a volume fraction of  $10^{-3}/55$ , to have approximately a constant ionic strength the counterions of the polymer should not add more than 10% to the ionic strength  $I$ , i.e.  $\frac{\varphi_b}{m} < 0.1 \frac{I}{55}$ . For a polyelectrolyte with  $m = 10$  the maximal volume fraction is  $10^{-5}$  at  $I = 0.001$  mol/L.

**Overcompensation of the surface charge** In this article the term overcompensation will be used when the number of charges on the adsorbed polyelectrolyte per unit area is larger than the surface charge density. This is

## 4.4 Results and Discussion

somewhat arbitrary, different choices can be made, such as that overcompensation occurs if the electrostatic potential has a minimum, if the surface charge is positive, or a maximum, when the surface charge density is negative, see for instance Andelman and Joanny.<sup>80</sup> In the latter definition the counterions of the surface also are included in the number of charges which contribute to the compensation of the surface charge and therefore overcompensation is reached at lower  $\varphi_b$  of the adsorbing polymer.

In experiments the two different definitions are used, too. In depletion experiments, the amount of charges can be calculated and therefore the former definition of overcompensation will be used. When the  $\zeta$ -potentials are measured, the latter definition of overcompensation is the logical one to be used.

## 4.4 Results and Discussion

In this section, the adsorption isotherms of the polyelectrolytes will first be presented. This is followed by the description of the response of the annealed surface charge to adsorption. Then the volume fraction profiles of the polyelectrolytes will be shown. In the last part of this section the results of the numerical SCF model will be compared to scaling results.

### 4.4.1 Adsorption isotherms

We begin by considering the effect of the new calculation method on the adsorption. For this we consider the simple situation of a linear quenched polyelectrolyte adsorbing on a quenched surface.

Fig 4.3 shows several adsorption isotherms on a semi-log scale. The adsorption isotherms at 0.001 and 0.01 mol/L are high affinity isotherms. Although high-affinity adsorption isotherms are also observed for uncharged polymers, there is an important difference. With adsorbed polyelectrolytes the high affinity is mainly due to the increase of the entropy of the small ions released from the polyelectrolyte and from the double layer of the surface, whereas for uncharged polymers it is due to the segment-surface attraction. As a result, the adsorption isotherm at  $I = 0.1$  mol/L is no longer of the high affinity type: at low polyelectrolyte concentrations the adsorption is zero or small. In the range of the volume fractions shown the adsorption does not overcompensate the surface charge.

The fact that the adsorption decreases with increasing salt concentration is due competition between the small salt ions and the polyelectrolyte. The small ions gain less entropy in a solution with a higher salt concentration. For 0.1 mol/L, this competition is so efficient that a polymer volume fraction above  $10^{-3}$  is required to replace the small ions.

The adsorbed amount  $\theta_{\text{exc}}$  for the polyelectrolyte calculated with the new method (the filled symbols in fig 4.3) is higher then the adsorption calculated

### Adsorption of a quenched polyelectrolyte: SF-SCF model

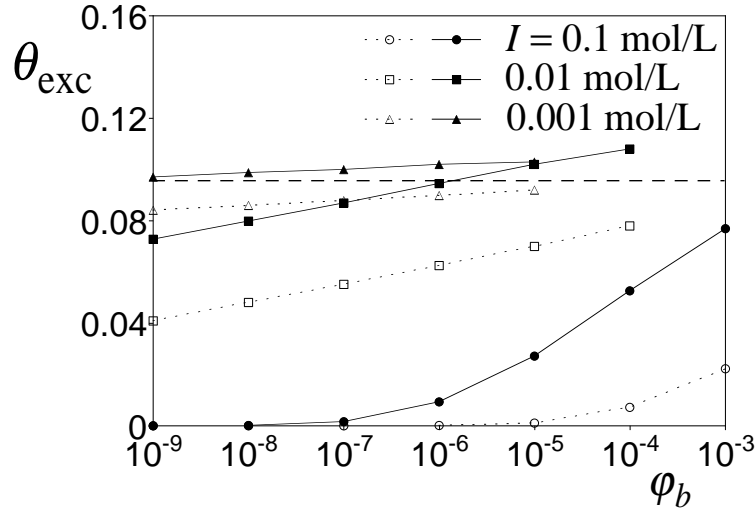


Figure 4.3: The adsorption isotherm of a linear polyelectrolyte on a quenched surface for different ionic strengths as denoted in the graph. The open symbols are the calculations with the old method and the filled symbols those with the new method.  $\sigma_s = +0.017$  C/m<sup>2</sup>, and every monomer has a charge of  $-0.1e$ , i.e.  $m = 10$ . The dashed line denotes surface charge compensation by the adsorbed polyelectrolyte.

with the old method (the open symbols in fig 4.3). This is due to the fact that in the new method the polyelectrolytes in the bulk have a higher free energy than a neutral polymer and must have this higher free energy in the adsorbed state. The increase in adsorbed amount due to the new calculation method is huge.

If one compares  $\theta_{\text{exc}}$  at a given volume fraction in the bulk of the polymer  $\varphi_b$ , the difference between the old en new method increases with increasing salt concentration. The difference for the polyelectrolyte in a solution with high ionic strength is larger than that for the polyelectrolyte in a solution with a low ionic strength. This is due to the fact that the adsorption at higher salt concentrations is lower and can therefore more easily increase than at a higher adsorbed amount. At high salt concentrations the adsorbed amount increases with a factor of 3 to 4 between the old en new method of calculation. For the low ionic strength the difference is small.

If one compares at constant excess amount, the difference in volume fraction is a measure of the extra driving force for adsorption. At  $I = 0.01$  mol/L, the adsorbed amount reached at  $\varphi_b = 10^{-4}$  for the old method, is with the new method already reached at  $\varphi_b = 10^{-9}$ . This is a shift of five decades. For 0.1 mol/L, the  $\theta_{\text{exc}}$  of 0.01 corresponds to a  $\varphi_b$  of  $10^{-4}$  and  $10^{-6}$  for the old calculation method and the new one, respectively. The difference is two decades. For 0.001 mol/L the difference is larger than five decades. This means that the new calculation method has more influence if the salt concentration is low, which is due to less screening in the bulk at low ionic strength. The effects

## 4.4 Results and Discussion

at high salt concentration seem more spectacular, just because the polymer starts to adsorb.

Another important difference is the overcompensation of the surface charge, see fig 4.3. Overcompensation could not occur with the old calculation method. Furthermore, as the charge of the surface is overcompensated by the charge of the adsorbed polyelectrolyte, the effect of the salt concentration is inverted, i.e. the adsorption *increases* with increasing salt concentration. The adsorbed amount curves at the 0.01 mol/L and the 0.001 mol/L in fig 4.3 crosses at a volume fraction of polyelectrolyte in the bulk  $\varphi_b$  of  $10^{-5}$ . This is due to the fact that as soon as the charge of the polyelectrolyte overcompensates the surface charge then the adsorption is halted because the monomers repel each other. This repulsion is better screened by a higher salt concentration than by a lower salt concentration.

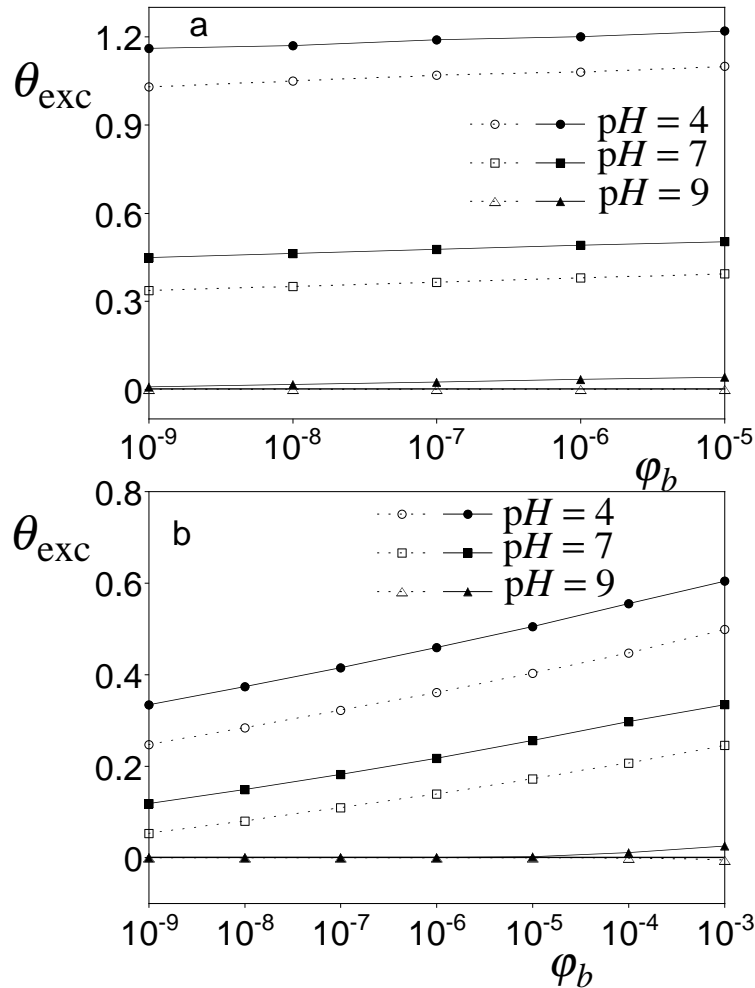


Figure 4.4: The adsorption isotherm of a linear polyelectrolyte ( $m = 10$ ) on an annealed surface for different pH's as denoted in the figure. In fig (a) the ionic strength is 0.001 mol/L and in (b) 0.1 mol/L. The open symbols are the results from the old method and the filled symbols from the new method.

## Adsorption of a quenched polyelectrolyte: SF–SCF model

Let us now consider the adsorption of a linear polyelectrolyte on an annealed surface. In fig 4.4 the adsorption isotherms for different  $pH$ 's and salt concentrations are shown. The adsorption increases with decreasing  $pH$ , as expected, because the surface charge becomes more positive and the adsorbing polyelectrolyte has a constant negative charge. Furthermore, with increasing salt concentration the adsorption decreases, compare fig 4.4a and b. This was also seen for the adsorption on a surface with quenched charges.

The adsorption at low salt concentration is almost independent of the volume fraction of polymer, i.e. the adsorption plateau is reached (see fig 4.4a). In fig 4.4b the adsorption isotherms at 0.1 mol/L salt is shown. It is clearly seen that at  $pH$  4 and 7 the adsorption is increasing with increasing volume fraction of polymer and the adsorption is *not* zero for small  $\varphi_b$  as was the case for the adsorption on a quenched surface. However, the small ions still compete effectively with the polymer, just as was seen for the adsorption on a surface with quenched charges.

At  $pH$  9 the bare surface charge is zero: therefore the polyelectrolyte does not adsorb with the old calculation method for any ionic strength. Yet, for the new method we see some adsorption. Also for the  $pH$  4 and 7 the adsorbed amount increases, when the new method of calculations is used, i.e. compare the filled symbols with the open symbols.

The excess amount of adsorbed polyelectrolyte on the annealed surface is considerably larger than on a quenched surface, compare the results shown in fig 4.3 at 0.001 mol/L with those at  $pH$  7 in fig 4.4a. The surface charge used for the quenched surface is the same as the bare surface charge of the annealed surface at  $pH$  7 and the ionic strength of 0.001 mol/L, see also fig 4.1. The large increase in the adsorbed amount is due to the increase in the surface charge due to adsorption. This increase in  $\sigma_s$  will be further discussed in section 4.4.2.

The effects of salt concentration and  $pH$  on the adsorption have been discussed, now we turn to the effect of the molecular architecture of the polymer. First the results for the adsorption on a quenched surface are shown, followed by those on an annealed surface.

In fig 4.5 adsorption isotherms of polyelectrolytes with different architectures on a surface with quenched charges at  $I = 0.01$  mol/L are shown, for the two calculation methods. Again, the adsorption calculated with the new method is higher than that with the old method. Furthermore, the adsorbed charges found with the new method overcompensates the surface charge at high volume fractions of the polymer in solution.

With the old method the adsorption isotherms for the different architectures are found to be the same, because the molecules behave as uncharged objects in the bulk, and the only reason for adsorption is the charge of the molecules. Furthermore, the equality of the excess amount means that the polymer density in the adsorbed layer is low. If this was not the case, there would be a difference in adsorption of the different molecules just due to their shape.

For the new method of calculation the most densely packed molecule, i.e. the dendrimer, has the highest adsorbed amount. This molecule has the highest

#### 4.4 Results and Discussion

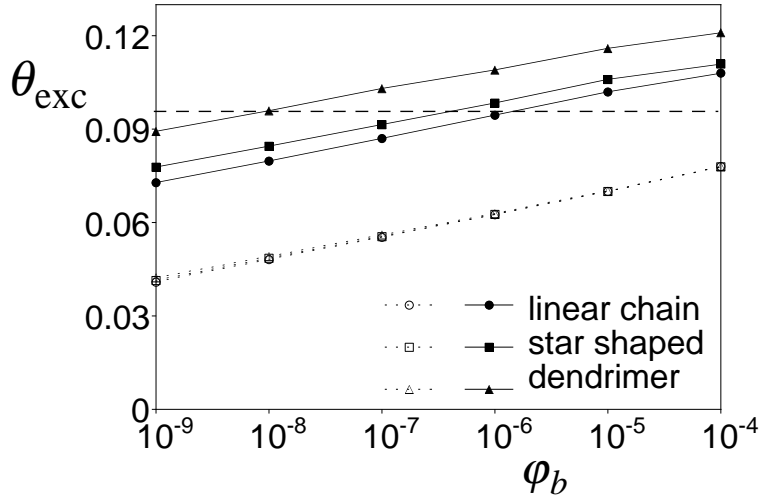


Figure 4.5: The adsorption isotherm of polyelectrolytes with different architecture on a quenched surface for the two different methods of calculation at an ionic strength of 0.01 mol/L. Other parameters are the same as in fig 4.3.

bulk free energy, due to the more densely packed charges. As a result, it can adsorb until the free energy of the adsorbed molecule is higher.

Leermakers et al.<sup>92</sup> also found overcompensation of the surface charge by an adsorbing star-shaped polyelectrolyte. These authors used the same method, but with gradients in two dimensions. Their result is comparable to what we find here.

In fig 4.6 the adsorption isotherms of molecules with different architecture on an annealed surface, at pH 7 and for two ionic strengths, are shown. The lines without symbols denote the old calculation method. It can be seen that with the new calculation method the adsorbed amount of polyelectrolytes increases considerably. Furthermore, the adsorbed amount of the dendrimer is the highest. Both effects were also seen for the adsorption on a quenched surface.

With increasing salt concentration the difference in adsorbed amount between polyelectrolytes of different architecture becomes smaller, because salt ions screen the effect of electrostatic repulsion in the bulk. This can be seen by comparing the volume fraction of polymer in the bulk which leads to the same adsorbed amount for the old and the new method of calculation. For  $I = 0.1$  mol/L and a linear polymer the same adsorbed amount is reached at a bulk volume fraction one to two decades higher than that of the dendrimer, and for 0.001 mol/L the bulk volume fraction differ by four decades.

There will be differences between calculations done before with SF-SCF models<sup>93,94,100,101</sup> but if a non-electrostatic adsorption energy for the surface had been introduced smaller differences between the old and new calculation method would have been found. The older calculations would have given smaller adsorbed amounts.



## Adsorption of a quenched polyelectrolyte: SF-SCF model

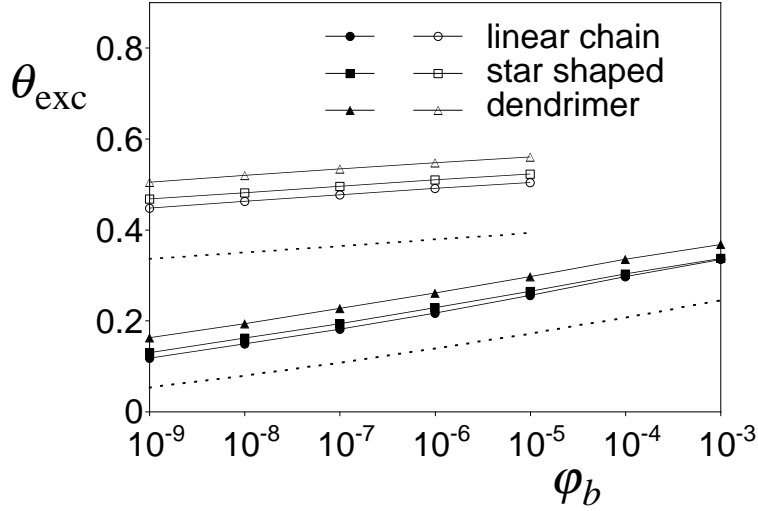


Figure 4.6: The adsorption isotherm of polyelectrolytes with different architecture on an annealed surface at pH 7 for two different ionic strengths. The filled symbols denote the calculations at a ionic strength of 0.1 mol/L and the open symbols at 0.001 mol/L. The dotted lines without symbols denote the results of the calculations with the old method at 0.1 and 0.001 mol/L.

### 4.4.2 Surface charge adaptation upon adsorption

The effect of the adaptation of the surface charge density of the annealed surface upon polyelectrolyte adsorption will be discussed in this paragraph. First the surface charge adaptation will be shown and then the effect of overcompensation of the surface charge by the adsorbed polyelectrolyte.

In fig 4.7 the surface charge of the annealed surface for different volume fractions of polymer in the bulk, pH's, and ionic strength is shown. The surface charge increases with a decreasing pH, just as for the bare surface, see fig 4.1. Due to the adsorption the surface charge increases further, the increase is larger for systems with a low ionic strength, compare fig 4.7a and b.

In fig 4.7a the surface charge density is larger for the new method as compared to the old method, see the filled symbols and the open symbols respectively. This was also the case for the adsorbed amount, see fig 4.4a. For the calculations with the new method, the surface is slightly charged in the presence of polyelectrolyte at pH 9, the pzc of the bare surface. The absolute increase of the surface charge due to the new method of calculation is from these three pH's the largest for pH 7. However, the absolute increase in the adsorbed amount due to the new method increased with decreasing pH (see fig 4.4a), this means that the adsorbed polyelectrolytes at pH 7 has a larger influence on the surface charge than at pH 4 and 9. This is probably caused by the fact that at pH 4 the surface charge is higher and therefore less easy to increase.

At high salt concentration, fig 4.7b, the surface charge is for the old and new calculation method almost the same, even though the adsorption is larger

#### 4.4 Results and Discussion

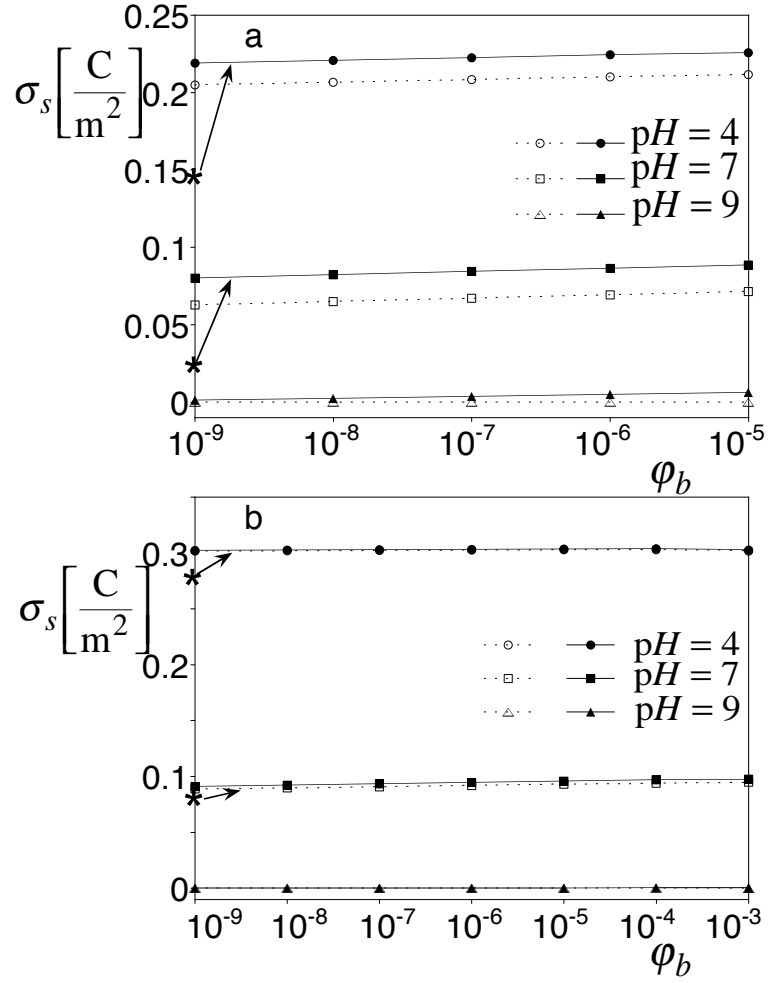


Figure 4.7: The surface charge density  $\sigma_s$  as a function of the volume fraction  $\phi_b$  of the linear polymer ( $m = 10$ ) in the bulk for different pH. The asterisks on the Y-axis denote the bare surface charge. In fig (a) the ionic strength is 0.001 mol/L and in fig (b) 0.1 mol/L. The parameters and the symbols are the same as for fig 4.4 and explained there.

## Adsorption of a quenched polyelectrolyte: SF-SCF model

in the new calculation method, see fig 4.4b. Apparently, the higher adsorbed amount can not induce extra charges on the surface. We will come back to this issue later.

In the remaining part of this article, the new method for calculating the adsorbed amount will be used. We will now discuss the charging up of the surface and overcompensation of the surface charge by the charge of the adsorbed polyelectrolyte. To be able to compare easily we introduce the charge density of the adsorbed polymer  $\sigma_p$ , it is given by

$$\sigma_p = -\theta_{\text{exc}}e/(ma^2)$$

in which  $e$  is the elementary charge,  $m^{-1}$  the fraction of charged monomers on the polymer and  $a$  the thickness of a lattice layer. The minus sign is due to the negative charge on the polyelectrolyte.

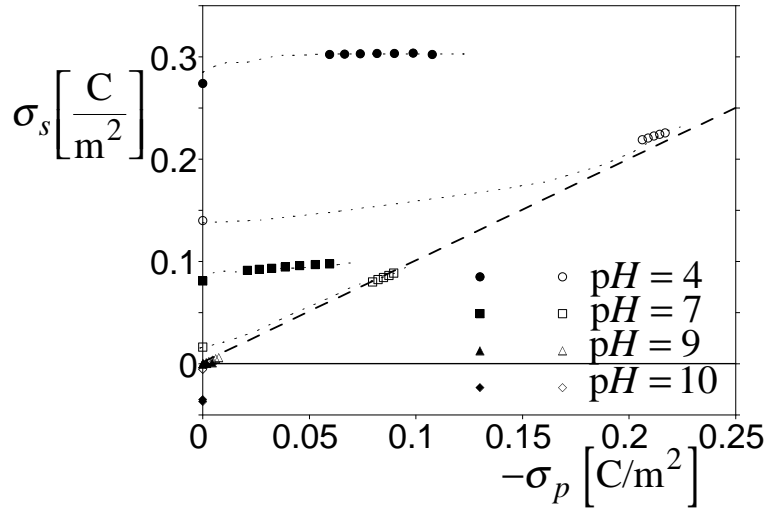


Figure 4.8: The surface charge density  $\sigma_s$  as a function of the charge of the adsorbed polyelectrolyte  $\sigma_p$ . The adsorbed polymer is a linear chain and  $m = 10$ . Results are shown for four different  $\text{pH}$ -values as denoted in the graph and for two ionic strengths. The open symbols are 0.001 mol/L salt and the filled ones are 0.1 mol/L. The dashed line denotes compensation of the surface charge by the charge of the adsorbed polyelectrolyte. The thin dotted lines are merely guides to the eye.

In fig 4.8 the surface charge density  $\sigma_s$  is shown as a function of the adsorbed charge density  $\sigma_p$ . This representation immediately reveals to what extent the surface charge of an annealed surface is (over)compensated by the charge of the adsorbed polyelectrolytes.

From fig 4.8 it can be seen that with increasing  $\text{pH}$ , the amount adsorbed decreases as does the surface charge. At  $\text{pH} 10$ , nothing is adsorbed so that also the surface charge is unchanged. The points for  $\text{pH} 9$  cluster around zero charge and zero adsorption, the surface charge is for both ionic strength just overcompensated and this prohibits the adsorption to increase much further.

#### 4.4 Results and Discussion

For pH 4 and 7, and low ionic strength the surface charge follows the diagonal line of charge compensation (open symbols). For the same pH's at high ionic strength (filled symbols) the surface charge is larger than a bare surface, i.e. at  $-\sigma_p = 0$ , and increases slowly with increasing adsorption.

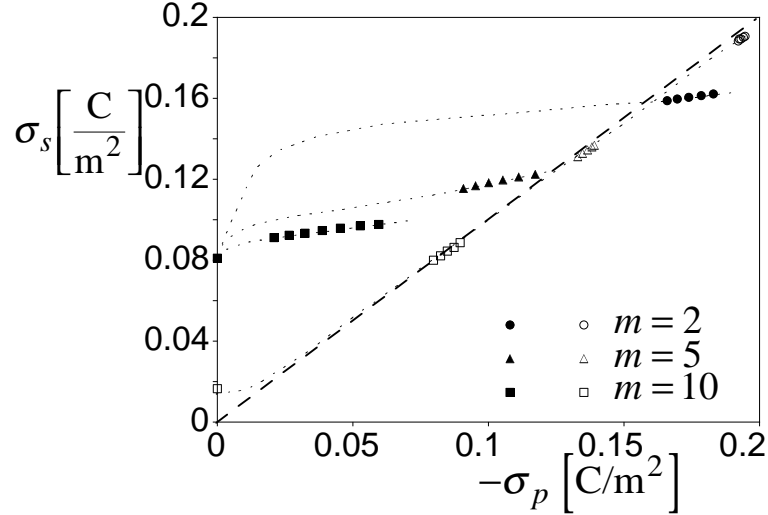


Figure 4.9: The surface charge density  $\sigma_s$  as a function of the charge of the adsorbed linear polyelectrolyte  $\sigma_p$  for three different  $m$  as denoted in the graph, at pH 7, and for two different ionic strengths. The open symbols are 0.001 mol/L salt and the filled ones are 0.1 mol/L. The dashed line denotes charge compensation of the surface charge by the charge of the adsorbed polyelectrolyte. The thin dotted lines are merely guides to the eye.

The effect of the amount of charges on the chain on the surface charge at pH 7 is indicated in fig 4.9. With increasing the charges on the polyelectrolyte, i.e. decreasing  $m$ , the adsorbed charge density is increasing and also the surface charge density is increasing.

In fig 4.9 a similar difference between the two ionic strength values is observed as in fig 4.8, i.e. the low ionic strength gives a slight overcompensation of the surface charge and the surface charge increases strongly with the adsorbed charges.

Table 4.1: Increase of the surface charge due to adsorption

system	Slope $-\frac{\partial \sigma_s}{\partial \sigma_p}$	
	$I = 0.1 \text{ mol/L}$	$I = 0.001 \text{ mol/L}$
pH 4, $m = 10$	0.04	0.64
pH 7, $m = 10$	0.17	0.88
pH 7, $m = 5$	0.26	0.96
pH 7, $m = 2$	0.19	0.84
pH 9, $m = 10$	0.16	0.82

## Adsorption of a quenched polyelectrolyte: SF–SCF model

In table 4.1 the average slopes of figs 4.8 and 4.9 are summarized. The large difference between the two ionic strengths is immediately seen. A slope of 1 would mean that only the polyelectrolytes are screening the surface charge. If the surface charge density would have been plotted versus all the excess charges in the solution, the slope resulting from that plot is always 1. The surface-charge increase for 0.001 mol/L almost follows the charge of the adsorbed polymer. This means that the surface charge is almost solely screened by the polyelectrolyte, due to the fact that the polyelectrolytes in 0.001 mol/L salt are more effective in screening the surface charge than the small ions. The surface charge screening is done by the small salt ions which are located at a distance smaller than the Debye length from the surface. The polyelectrolyte has more charged segments closer to the surface and can therefore compensate the surface charge better. We will illustrate the layer structure in section 4.4.3.

The effect of the number of charges on the chain is not straightforward. With increasing number of charges on a polyelectrolyte (i.e. with decreasing  $m$ ), the screening of the surface is better, so an increase in the slope would be expected. However, going from  $m = 5$  to  $m = 2$  a decrease is seen in table 4.1. This is due to surface charge overcompensation by the polyelectrolyte with  $m = 2$  and also due to the fact that the charge of the surface is higher and therefore less susceptible to adapt its surface charge to a new situation, see also the very low slope for  $pH\ 4$ .

Dobrynin<sup>102</sup> derives the adsorption of polyelectrolytes for various solvent qualities on a surface with a constant charge. His results show that there is always overcompensation of the surface charge for a good or a  $\theta$  solvent. The calculations presented here were all done in good solvent and the results show that overcompensation of the surface charge depends on the salt concentration, the concentration of the polymer in the bulk, the surface charge, and the charge of the monomers.

### 4.4.3 Distribution of adsorbed polymer segments

The volume fraction profiles of the adsorbed polyelectrolytes are easily obtained in SF–SCF calculations. They give information on the conformations of the adsorbed molecules.

In fig 4.10 the volume fraction profiles of linear polyelectrolytes near a quenched surface at 0.01 mol/L salt are shown. In fig 4.3 it was shown that the adsorbed amount with the new calculation method was higher than with the classical method. The volume fraction profiles in fig 4.10 show that not only the amount per layer is higher, but also the adsorbed layer is thicker. The small inset, (semi-log scale), shows that up to  $z = 30$  the amount per layer with the new method is higher. At  $z > 30$  the volume fraction profile goes through a minimum, this is due to the fact that the charge of the adsorbed polymer overcompensates the surface charge (see fig 4.3), so that free chains are repelled.

In comparison to volume fraction profiles of neutral polymers on a neutral

#### 4.4 Results and Discussion

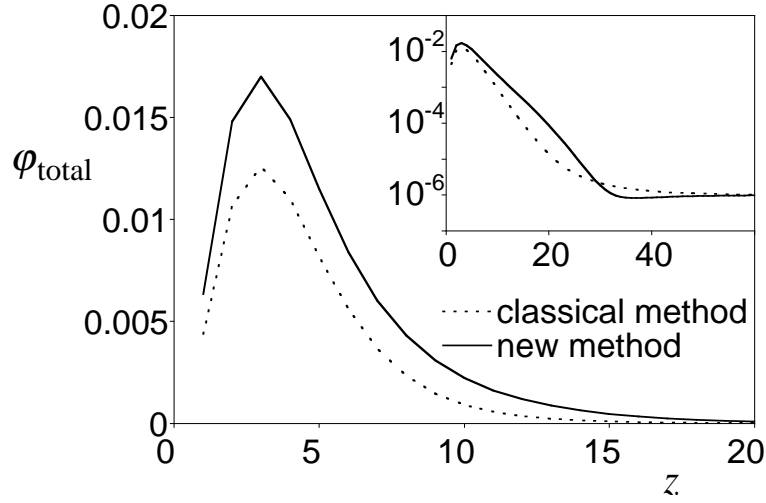


Figure 4.10: The volume fraction profiles of linear polyelectrolytes ( $m = 10$ ) on a quenched surface,  $\varphi_b = 10^{-6}$  and the ionic strength is 0.01 mol/L.

surface, the maximum in the volume fraction profiles is not located immediately at the wall (see Fleer et al.<sup>16</sup>). The adsorbing polyelectrolyte feels the attraction of the charged surface also at some distance from the surface.

From this point on the volume fraction profiles obtained by the new calculation method will be shown. First, the differences due to different molecular architectures of the polyelectrolytes will be considered. Then the effect of different charge densities on the polyelectrolyte chain will be discussed.

In fig 4.11 the volume fraction profiles of polyelectrolytes with different architectures, adsorbed on a quenched surface, are shown in a solution with an ionic strength of 0.01 mol/L. The differences between the volume fraction profiles for the different architectures are small. The dendrimer adsorbs to somewhat higher density and slightly more closely to the surface than the linear polyelectrolyte does. This is expected because of the smaller entropy loss incurred by a linear chain which can adsorb with long tails.

The minimum in the volume fraction profile, which is shown in fig 4.11b, is due to electrostatic repulsion. The charge of the surface is overcompensated by the charge of the adsorbed dendrimer and of the adsorbed star-shaped polyelectrolyte, see fig 4.5. Therefore, the electrostatic potential becomes negative inside the adsorbed layer and the free polyelectrolytes are expelled from the surface.

In fig 4.12 the volume fraction profiles of polyelectrolytes that do not touch the surface are shown. The volume fraction of the polymers in the bulk is  $10^{-9}$  and the salt concentration is the same (0.01 mol/L) as in fig 4.11. Although these molecules do not touch the surface, they do accumulate near the surface because the electrostatic potential is positive, which is the case for the low  $\varphi_b$ . However, the dendrimer is depleted from the surface although the surface charge is not yet overcompensated, see fig 4.5. The electrostatic potential in

## Adsorption of a quenched polyelectrolyte: SF-SCF model

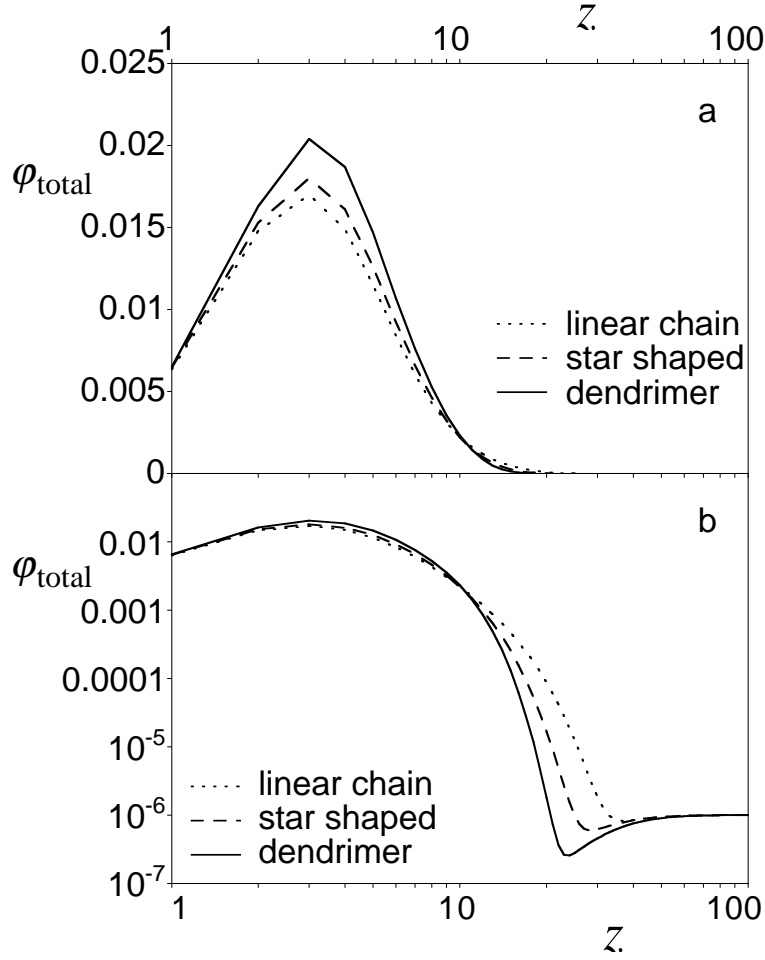


Figure 4.11: The volume fraction profile of polyelectrolytes ( $m = 10$ ) with different architecture on a quenched surface,  $\varphi_b = 10^{-6}$ , and at the ionic strength of 0.01 mol/L. Fig (a) is in semi-log scale, and (b) in double-log scale.

the adsorbed layer is negative, this is not the case for the linear and star-shaped polyelectrolyte.

The depletion of dendrimer can also be due to its own dense structure. However, this is highly unlikely because the amount adsorbed is low, less than 10% of one layer is filled. The linear and star shaped molecule can penetrate into the adsorbed layer, but the amounts are small and only visible for small concentrations of polyelectrolyte.

In fig 4.13 the volume fraction profiles of linear polyelectrolytes adsorbed at pH 7 on an annealed surface are shown for different ionic strengths. The corresponding adsorption isotherm of the polyelectrolyte with  $m = 10$  was shown in fig 4.4 and the surface charge as a function of the adsorbed charges of both polyelectrolytes was shown in fig 4.9.

The shapes of the volume fraction profiles of the polyelectrolytes, which have the same amount of charge, are rather similar. The volume fraction profiles of the polyelectrolyte with  $m = 2$  start at the wall with a higher concentra-

#### 4.4 Results and Discussion

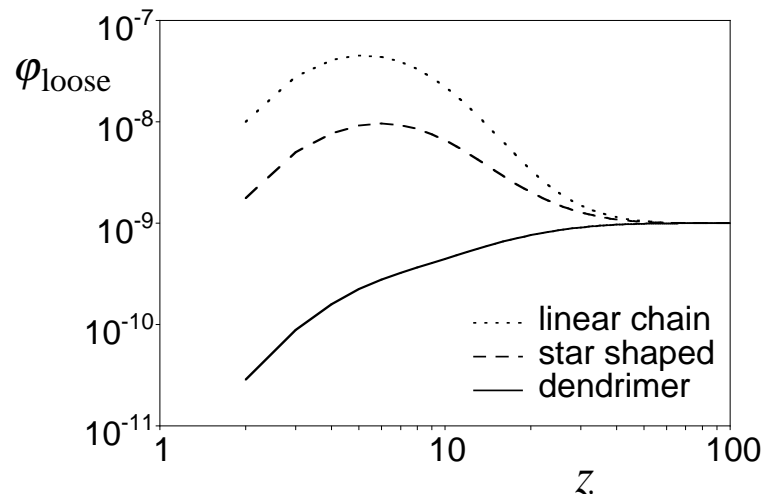


Figure 4.12: The volume fraction profiles of "loose" polyelectrolytes ( $m = 10$ ) with different architecture on a quenched surface in double-logarithmic scale. The ionic strength is 0.01 mol/L and  $\varphi_b = 10^{-9}$ .



# Adsorption of a quenched polyelectrolyte: SF-SCF model

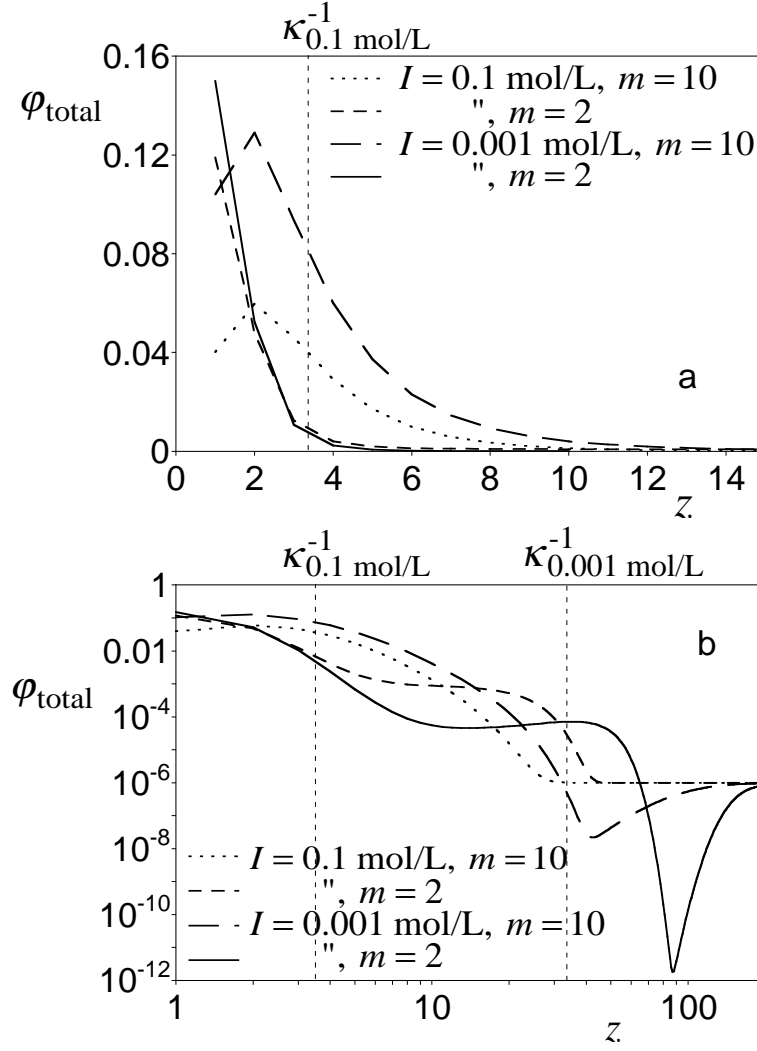


Figure 4.13: The volume fraction profiles of linear polyelectrolytes with different charge density on the chain adsorbed to an annealed surface. The salt concentration and the amount of charges on the polyelectrolyte are denoted in the graph. The pH is 7 and  $\phi_b$  is  $10^{-6}$ . The horizontal dashed lines denote the Debye length. In fig (a) both axis are in linear scale, in fig (b) in log scale.

## 4.4 Results and Discussion

tion than those of the polyelectrolyte with  $m = 10$ . The polyelectrolyte with a high charge density, i.e.  $m = 2$ , adsorbs flat on the surface in comparison with the polyelectrolyte with less charges. In log-scale another feature of the adsorbed layer can be seen, fig 4.13b. After a steep decrease the volume fraction shows a “plateau”, which is not present for the curves of the polyelectrolyte with  $m = 10$ .

The horizontal lines in fig 4.13 indicate the Debye lengths  $\kappa^{-1}$  0.001 mol/L salt concentration, respectively. As can be clearly seen, all segments of the polyelectrolyte lie within  $\kappa^{-1}$  from the surface implying that the polyelectrolyte screens the surface charge more effectively than the small salt ions at 0.001 mol/L salt so that it will easily induce new surface charges due to adsorption.

The curves for the low salt concentration have a clear minimum in the profile as also seen in the previous figures. This is due to a negative (i.e. repulsive for the polyelectrolytes) electrostatic potential. This can be expected because the surface charge was overcompensated by the adsorbed charges, see fig 4.9. However, this is not the whole story, because for the case of high ionic strength, the surface charge is also overcompensated by the charge of the adsorbed polyelectrolyte with  $m = 2$ , but in the corresponding volume fraction profile in fig 4.13 we do not see a minimum in the volume fraction profiles. Clearly, the electrostatic potential is effectively screened by the salt concentration.

The minima in the volume fraction profiles in figs 4.11 and 4.13 may also be an artifact because the adsorbed polyelectrolytes are allowed to have a higher free energy (because of the new method of calculating polyelectrolyte adsorption). The polyelectrolytes in the bulk of the adsorption-calculation still feel a zero electrostatic field and have therefore a lower free energy. This could mean that the density minimum in the depleted zone is too deep and perhaps even not always real. On the other hand, Monte Carlo simulations of adsorbing polyampholytes by Broukhno et al.<sup>103</sup> also show a minimum in the volume fraction profiles for an adsorbing polyampholyte on a quenched surface.

Another distinct feature in fig 4.13 is the strong stretching of the polyelectrolytes with a high charge. This strong stretching results in a “plateau value” for the volume fraction profile between layers 6 and 30, for the low ionic strength even a bit further into the solution. The large amount of charges on the polyelectrolyte chain results in a strong repulsion between the charges.

This “plateau” value in the volume fraction profile is also seen in the electrostatic potential; the increase in the electrostatic potential to zero, after the minimum (due to overcompensation) is for polymer with  $m = 10$  best described with a exponential increase to zero with  $\kappa^{-1}$  as the critical distance. This means that the polyelectrolyte with  $m = 10$  acts like a small salt ion. However, for the polyelectrolyte with  $m = 2$  the electrostatic potential increases very slowly to zero. On a semi-log scale, i.e.  $\ln \psi$  as a function of  $z$ , the potential is approximately constant (Figures not shown). The charges on the adsorbed polyelectrolyte chain keep the electrostatic potential low.

#### 4.4.4 Comparison to scaling laws

Andelman and Joanny<sup>80</sup> put forward relations between the layer thickness  $D$  and the adsorbed amount  $\theta_{\text{exc}}$  as a function of the fractional charge of a polyelectrolyte  $m$ , for a surface with a constant potential  $\psi_s$ . Our model surface acts as a surface with a roughly constant potential, see fig 4.1a. The relations for low salt concentration, i.e.  $D \ll \kappa^{-1}$ , are  $D \sim m^{1/2}\psi_s^{-1/2}$  and  $\theta_{\text{exc}} \sim m^{1/2}\psi_s^{3/2} \sim \sigma_s m$ , the last term denotes charge compensation. The relations for high ionic strength are  $D \sim \kappa m \psi_s^{-1} \sim \kappa^2 m \sigma_s^{-1}$  and  $\theta_{\text{exc}} \sim \kappa m \psi_s \sim \sigma_s m$ .

In fig 4.14 the adsorbed amount of a linear polyelectrolyte on an annealed surface is shown as a function of the charge on the polyelectrolyte. The ad-

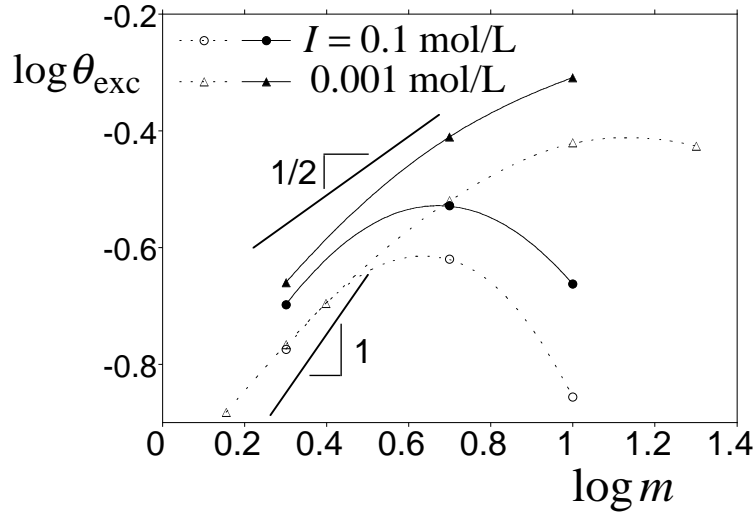


Figure 4.14: The adsorbed amount  $\theta_{\text{exc}}$  as a function of the charge of a monomer  $m$  in double-log plot. The linear polymer is adsorbed on an annealed surface, the  $\text{pH} = 7$ ,  $\varphi_b = 10^{-6}$ , and the ionic strength as denoted in the graph. The open symbols denote the old calculation method and the filled symbols the new calculation method. The lines are guides for the eye.

sorption increases with increasing  $m$  for low ionic strength and has a maximum for the high ionic strength. The decrease in adsorbed amount after the maximum is due to competition with salt ions. The curves for the new calculation method have approximately the same shape (in a double-logarithmic figure) as those for the old calculation method. Only the adsorbed amount is higher for the new calculation method.

For  $I = 0.001$  mol/L the Debye length is about 10 nm, which is  $10/0.3$  lattice layers,  $z = 33$ , for 0.1 mol/L,  $\kappa^{-1} = 1$  nm i.e.  $z = 3.3$ . As can be seen in fig 4.13a, most of the adsorbed amount is located within distances smaller than  $z = 15$ . The polymer with a high charge density even resides within three lattice layers. This means that for the 0.001 mol/L salt, the low salt approximation, i.e.  $\theta_{\text{exc}} \sim m^{1/2}m$  should hold and for  $m = 10$  at 0.1 mol/L the high salt approximation ( $\theta_{\text{exc}} \sim m$ ). For the polymer with  $m = 2$  at 0.1

#### 4.4 Results and Discussion

mol/L, the Debye length and the layer thickness are approximately equal so it does not fall easily in one of the regimes as denoted by Andelman and Joanny. According to fig 4.14, none of the regimes is found, the increase of  $\theta_{\text{exc}}$  with  $m$  has an exponent larger than  $1/2$  but smaller than 1.

Furthermore, the relation which they derive for higher salt concentrations, predicts only an increase in adsorbed amount with increasing  $m$ . However, in fig 4.14 we clearly find a maximum for high salt concentration.

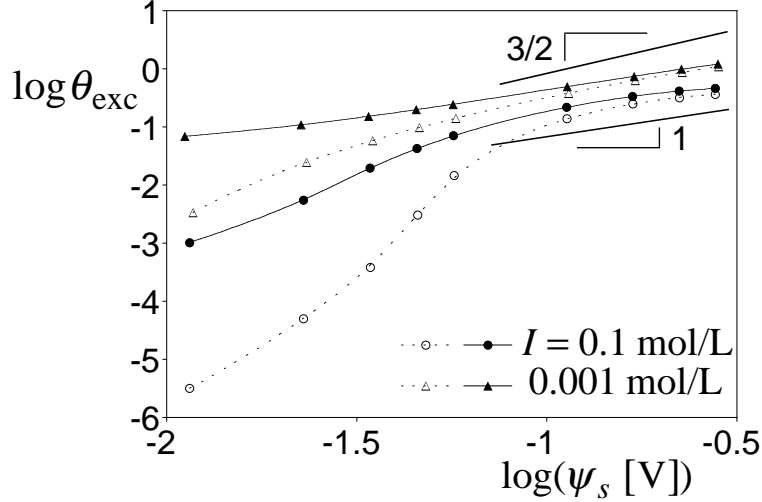


Figure 4.15: The adsorbed amount  $\theta_{\text{exc}}$  of a linear polyelectrolyte ( $m = 10$ ) adsorbed to an annealed surface at different surface potentials  $\psi_s$ , i.e. at different pH-values, in double-log plot. The salt concentration is denoted in the graph. The  $\varphi_b$  of the polymer in the bulk is  $10^{-6}$ . The open symbols denote calculations with the old method and the filled symbols the calculation with the new method.

The effect of the surface potential on the adsorbed amount is shown in fig 4.15. With increasing surface potential the adsorbed amount increases, due to the increase in electrostatic attraction. First we see (for both the old calculation method and the new calculation method) at  $I = 0.1$  mol/L a large increase in the adsorption with increasing surface potential followed by a smaller increase. For the low salt concentration, a steadily increasing adsorption is seen in fig 4.15. According to Andelman and Joanny,<sup>80</sup> this increase in the adsorbed amount should scale as  $\psi^{3/2}$  for low ionic strength and as  $\psi$  for the high ionic strength. We see in fig 4.15 that the slope is increasing with decreasing salt concentration. The slope at  $I = 0.001$  mol/L and for the new calculation method it is closer to 1 than to  $3/2$ .

The critical salt concentration, below which the polyelectrolyte adsorbs, has been studied by Muthukumar.<sup>77</sup> He has evaluated this critical salt concentration for adsorption on a surface with a constant charge:

$$(\kappa^3 l_1 T)_c = \frac{48\pi|\sigma_s/m|}{2.4048\epsilon l k_B} \quad (4.5)$$

## Adsorption of a quenched polyelectrolyte: SF–SCF model

in which  $\kappa$  is the inverse Debye length,  $l_1$  an “electrostatic Kuhn” length (which depends on  $m$ ),  $T$  the temperature,  $\sigma_s$  the surface charge density,  $\varepsilon$  the permittivity of the solution,  $l$  the Kuhn length, and  $k_B$  the Boltzmann constant. The 2.4048 is the numerical value of the first positive zero of a Bessel function of the first kind. For a quenched surface with  $\sigma_s = 1.7 \cdot 10^{-2}$  C/m<sup>2</sup> and a polyelectrolyte with  $m = 10$  the critical salt concentration is calculated to be 0.9 mol/L. In our SF–SCF calculations, we find critical salt concentrations for the new method is around 2 mol/L and for the old method 0.3 mol/L. Both values are of the same order as that predicted by eq 4.5. Eq 4.5 does not contain the polymer concentration, as can be seen in fig 4.3, a different critical salt concentration can be assigned for different concentrations of polyelectrolyte where the polymer starts to adsorb, but this is a small difference which is ignored in the scaling analysis.

Muthukumar<sup>77</sup> also analyzes the layer thickness  $D_e$ , which is defined as the maximum in the endpoint distribution, as function of the salt concentration and derives the following relation:  $D_e \sim \kappa^{-1}$ . This relation should be valid according to Muthukumar<sup>77</sup> if the system is far from the critical adsorption temperature or salt concentration. In our calculations a maximum in the endpoint distribution function is only found for polyelectrolytes with high amount of charges, i.e.  $m = 2$  and not for  $m = 10$ .

For these comparisons with scaling laws it can be concluded that if the scaling laws fit the data of the new method, in most cases also the data from the old method will have the same scaling exponents, see as an example the open and filled symbols in fig 4.14. This means that the new method, although different, it does not show on a logarithmic scale.

## 4.5 Conclusions

A new way to calculate polyelectrolyte adsorption has been explored. The effect of the new calculation method was compared to the old method and only electrostatic interactions were taken into account. Due to the new calculation method

- The adsorbed amount found is higher
- Polyelectrolyte adsorption occurs at the pzc of a surface with annealed charges
- The surface charge can be overcompensated by the polyelectrolyte charge
- The volume fraction profiles of the new method are wider and higher
- The volume fraction profiles show minima

The differences between the old and the new method of calculating the equilibrium adsorption of polyelectrolytes seem small but are remarkable.

In the new method the amount adsorbed for a branched polyelectrolyte (a higher charge density in the bulk) is larger than for a linear polyelectrolyte. Calculations with the old method showed no differences in adsorbed amount between these cases.

## 4.5 Conclusions

With increasing salt concentration the adsorbed amount of polyelectrolyte decreases as long as the surface charge is not overcompensated by the charge of the adsorbed polyelectrolyte.

More charges on the chain (decreasing  $m$ ) will increase the adsorbed charge density  $\sigma_p$ . The competition with salt ions is smaller for polyelectrolytes with higher charge density. Furthermore, overcompensation of the surface charge is easier for the more highly charged polymer, especially in a solution with a high ionic strength. As a last feature, more strongly charged molecules adsorb flatter on the surface, but they can have in considerable thickness due to a “plateau”, see fig 4.13b.

The adsorbed amount on a surface with annealed surface groups is relatively large compared to  $\theta_{\text{exc}}$  on a quenched surface. This is due to induction of extra charges on the surface by the adsorbing polyelectrolyte. On an annealed surface it is more difficult to overcompensate the surface charge than on a quenched surface. The reason is that the surface charge of an annealed surface will increase with the adsorbed amount. These annealed surfaces will “follow” the adsorbed charges, in a way that the surface charge is just overcompensated. Only for high salt and high fractional charges on the polyelectrolyte, a large overcompensation can be expected.

# Chapter 5

## Charge adaptation of a hematite surface upon poly(styrene sulfonate) adsorption

Theoretical calculations and experimental results

### Abstract

The charge regulation of the iron oxide hematite upon adsorption of the strong polyelectrolyte poly(styrene sulfonate) (PSS) is studied both theoretically and experimentally.

Self-Consistent-Field calculations were done to evaluate the charge characteristics of a model hematite, i.e. the point of zero charge and the surface charge at different ionic strength, in the absence and presence of a linear strong polyelectrolyte. The calculations show high affinity adsorption isotherms. The adsorption is increasing with decreasing  $pH$  and at its plateau the surface charge is overcompensated by the charge of the adsorbed polyelectrolyte. The charge adaptation of the model surface is large, it can become of similar magnitude as the surface charge of a bare hematite at a  $pH$  which is lower by three units.

In contrast with the calculated results, the measured adsorption isotherm of PSS on hematite does not show a high affinity character. However, the adsorption of PSS does increase the surface charge and bringing it to a level which is comparable to the surface charge of a bare hematite in a solution in which the  $pH$  is three  $pH$ -units smaller, similarly as in the calculations. The total increase of the surface charge depends only on the amount of PSS present but not on the  $pH$ . At the adsorption plateau the surface charge is overcompensated by the adsorbed charge. Before the adsorption plateau is reached the surface charge increases linearly with the adsorbed amount.

## 5.1 Introduction

### 5.1 Introduction

In soil chemistry mineral oxides are regarded as highly reactive for the adsorption of oxy-anions and natural organic matter. In general the adsorption is determined by specific and electrostatic interactions.<sup>104–106</sup> In this article, we will mainly focus on the charge regulation upon adsorption, which has not been studied a lot. Using measurements and model calculations,<sup>107,108</sup> it has been shown that due to the adsorption of charged species the primary charge of the oxide surface adapts to the new situation by taking up or releasing protons. This has been well established for inorganic ions.<sup>96,109</sup> In the adsorption models of metal ions or oxyanions it is taken into account that the adsorbing ions compete with the ions that determine the primary charge on the oxide, i.e.  $H^+$  and  $OH^-$ . In that case charge adaptation is obvious. However, Fokkink et al.<sup>110</sup> have shown that also in the absence of competition strong charge adaptation may occur due to only electrostatic interactions.

In the study on the adsorption of small organic acids by Barja et al.<sup>111</sup> the emphasis was not on the quantitative assessment of the charge adaptation of the surface, but on binding mechanisms. Filius et al.<sup>112</sup> measured and modelled the adsorption of small organic acid to goethite (an iron-oxide surface). They took the competition for surface sites with  $H^+$  and  $OH^-$ , and with that the surface charge adaptation, into account in the modelling the adsorption. However, to be able to model the  $pH$ -dependency of the adsorption, charge distribution of the adsorbed molecules over the surface was also needed.<sup>113</sup> For surfactant adsorption the prime charge of the oxide surface is affected too, as is clearly demonstrated both experimentally and theoretically by Koopal et al..<sup>114,115</sup>

For even larger molecules, such as polymers and polyelectrolytes, the adsorption and surface charge adaptation have been studied less systematically. The early work on surface charge regulation concerned colloidal AgI particles upon adsorption of poly(vinyl alcohol)<sup>116,117</sup> and of polylysines.<sup>118</sup> Bonekamp et al.<sup>119,120</sup> studied the adsorption of polylysines on different substrates among which mineral oxides. More work on the adsorption on silica has been done by Siderova et al.,<sup>121</sup> they found that poly(ethylene imine) induces extra charge on a silicon-oxide surface. The adsorption of different polyelectrolytes on oxides surfaces has also been studied by Vermöhlen et al.<sup>122</sup> and by Gebhardt and Fuerstenau.<sup>123</sup> Furthermore, the influence of proteins on the charge adjustment has been studied by Fukuzaki et al.<sup>124</sup> and the charge regulation of goethite upon adsorption of sulfate by Rietra et al.<sup>125</sup> and of fulvic acids by Filius et al.<sup>126</sup> The adsorption of polyelectrolytes with a  $pH$ -dependent charge and their influence on the surface charge has been investigated theoretically by Vermeer et al..<sup>91,127</sup> In this case the calculations were used to gain insight in the adsorption of a natural organic material to mineral particles. The adsorption of a polyelectrolyte with a  $pH$ -dependent charge on a surface, which has also a  $pH$ -dependent charge, has also been studied by Shin et al..<sup>128,129</sup>

In order to examine the surface charge adaptation upon polyelectrolyte adsorption more systematically, the system metal oxide and a strong polyelec-



## Adsorption of poly(styrene sulfonate) onto hematite

trolyte is chosen. Such a system has the advantage that only the surface can adjust its charge. The calculations are based on the well known self-consistent-field theory originally developed by Scheutjens and Fler<sup>13,16</sup> for homopolymer adsorption and later extended to polyelectrolyte adsorption.<sup>43,67,90</sup> Experimentally, the strong polyelectrolyte poly(styrene sulfonate) is used to adsorb on the mineral oxide hematite; the change in the  $pH$  in the solution upon adsorption reflects only the change of the surface charge.

The article is organized as follow. In section 5.2 we will present results from numerical calculations. We do this to model our experimental system and obtain insight in what may happen when a strong polyelectrolyte adsorbs to a surface with a  $pH$ -dependent charge. In section 5.3 the materials and methods are denoted and in section 5.4 the experimental results. Finally, a comparison is made between the numerical calculations and the experimental results and a further discussion is given of the latter.

## 5.2 Theoretical model and results

### 5.2.1 SF–SCF model and choice of the parameters

The self-consistent-mean-field model of Scheutjens and Fler<sup>13</sup> (SF–SCF), extended to adsorption of polyelectrolytes,<sup>43,67</sup> is used for the calculations. For the theoretical background of the model we refer to the cited articles; below the choice of parameters is briefly discussed. The calculations were done with the software package `sfbox`.<sup>17</sup>

The SF–SCF model for the adsorption of charged adsorbates is a mean-field multi-Stern-layer model, see fig 5.1. In the model the thickness of each layer is taken to be 0.3 nm. This corresponds to the edge of cube with the volume of a water molecule. Furthermore, we use a cubic lattice, i.e. in a flat geometry the interactions of a monomer in layer  $z$  with its surroundings is for 1/6 determined by layer  $z - 1$ , for 4/6 by layer  $z$ , and also 1/6 by layer  $z + 1$ .

The hematite surface is mimicked in a crude way by grafting one type of monomers,  $S$ , to a surface. The grafting density of 99.9% is taken to avoid free spaces between the sites. i.e. the site density is  $0.999/(0.3 \text{ nm})^2 = 11.1 \text{ sites/nm}^2$ . This value is too high compared to literature available. Venema et al.<sup>130</sup> consider two different faces, with 5 sites/nm<sup>2</sup> and 10 sites/nm<sup>2</sup>, respectively, to describe the measured titration curves of hematite. Hiemstra and van Riemsdijk<sup>131</sup> show that on hematite large amount of surface groups do not contribute to the surface charge.

The simple one- $pK$  model<sup>98,132</sup> is used in our calculations to describe the reaction of the model surface sites  $S$  with protons, according to the reaction:



$SH$  is a surface site which dissociates,  $K_{\text{diss}}$  is the dimensionless value for the dissociation constant, i.e. the concentrations of  $H_2O$  and  $H_3O^+$  are denoted as

## 5.2 Theoretical model and results

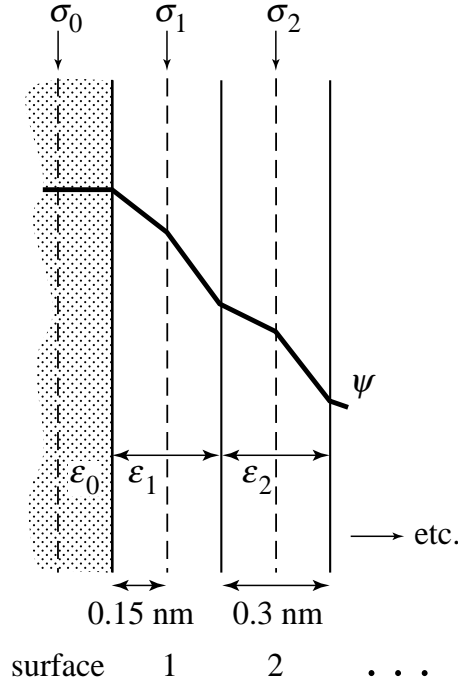


Figure 5.1: The layers, the placing of the charges and the distances in the numerical model

volume or mole fractions. The value of  $K_{\text{diss}}$  given here corresponds to a point of zero charge (pzc) at  $\text{pH}$  9.8. This value equals the measured value. A further simplification is made with respect to the interaction of the surface with salt ions. Although chemical interaction of salt ions with oxide surfaces is in general needed to fit experimental data, we have taken the interaction of the salt ions with the surface to be zero.<sup>133,134</sup> The relative permittivity  $\epsilon_{r,S}$  of the surface site  $S$  was taken to be 40. This value was chosen to ensure that the calculated titration curves of the bare hematite at different salt concentrations resembled the measured curves. Choosing a value for  $\epsilon_{r,S}$  is equivalent to introducing a Stern-layer capacitance in the usual site binding models.

The poly(styrene sulfonate) is mimicked in the calculations by a linear flexible polyelectrolyte with 681 monomers, in which every other monomer has a negative charge. The number of monomers is about twice as large as the experimental value because the size of a monomer in the model is small. This implies that the model polyelectrolyte will overestimate the flexibility of poly(styrene sulfonate). The segmental interactions between the different components are characterized by the Flory-Huggins  $\chi$ -parameters.<sup>135</sup> Every polyelectrolyte segment  $P$ , charged or uncharged, has a strong attraction to the surface. The  $\chi$  value is put equal to  $-8$ . The  $\chi$  for water-surface interaction is set equal to 0. This means that if water is replaced from the surface by a polymer segment,  $8/6 k_B T$  of energy is gained by the system. These  $\chi$ -values are chosen in order to give a good agreement between the measured and the

## Adsorption of poly(styrene sulfonate) onto hematite

calculated surface charges at  $pH$  10, in the presence of  $1.62 \cdot 10^{-5}$  mol  $PSS^-$ /L in the bulk solution with an ionic strength of  $10^{-2}$  mol/L.

The interaction of the polymer segments  $P$  with water molecules and salt ions is the same as for a  $\theta$ -solvent, i.e.  $\chi_{P-\text{solvent}} = 0.5$ . The relative permittivity of a polymer segment  $P$  is in most cases taken as  $\varepsilon_{r,P} = 80$ , the same as that of the water molecules and the salt ions. In some calculations  $\varepsilon_{r,P} = 10$ , because a polymer with a benzene entity may have a low permittivity. The  $\chi$ -value between salt ions and water molecules is put to zero.

The equilibrium adsorption of the linear polyelectrolyte to the model hematite surface is calculated. The condition for equilibrium is that the chemical potential, according to Flory and Huggins,<sup>136</sup> of the polyelectrolyte in bulk solution is equal to that in the adsorbed layer (cf Van Male et al.<sup>67</sup>).

### 5.2.2 Results of the SF–SCF calculations

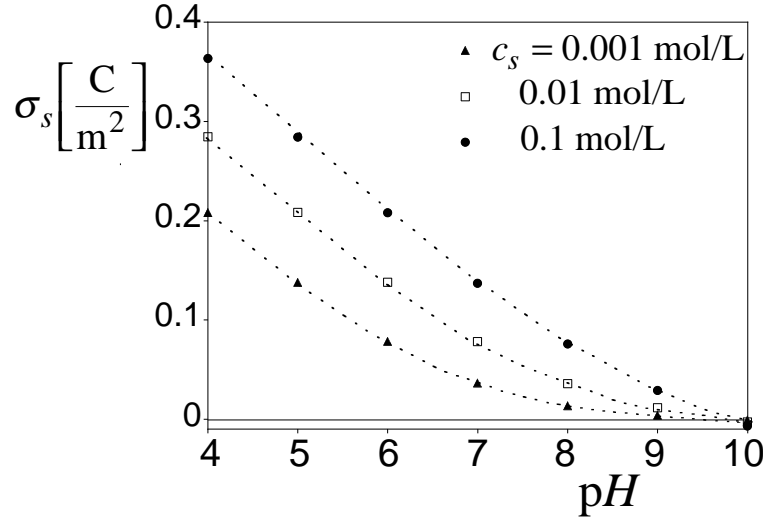


Figure 5.2: The surface charge density  $\sigma_s$  of the model hematite as a function of the  $pH$  for different salt concentrations. The dotted lines are guides to the eye.

**Bare model surface** In fig 5.2 we show the surface charge density  $\sigma_s$  of the bare model surface as a function of the  $pH$  and salt concentration. We see that with increasing the  $pH$  the surface charge decreases and that for  $pH$ 's smaller than the point of zero charge (pzc),  $\sigma_s$  increases with increasing salt concentrations. The maximal charge of the model hematite, i.e.  $0.5e0.999/(0.3 \text{ nm})^2 = 0.888 \text{ C/m}^2$ , is not reached within the  $pH$ -window studied.

The surface potential does not depend on the salt concentration and behaves pseudo-Nernstian from  $pH$  4 up to 10, i.e.  $pH \sim \psi_s$  (results not shown).

From the value of the capacitance as a function of the salt concentration, it can be derived whether the surface charge  $\sigma_s$  is compensated predominantly by the ions very close to the surface or by the diffuse ions. If it is assumed

## 5.2 Theoretical model and results

that the double layer can be modelled as two plate capacitors in series, one corresponding with a charge-free Stern layer and the other with the diffuse double layer, it follows that the total capacitance  $C_t$  is related to the Stern layer capacitance  $C_S$  and the diffuse double layer capacitance  $C_d$ :

$$\frac{1}{C_t} = \frac{1}{C_S} + \frac{1}{C_d} = \left( \frac{d_S}{\varepsilon_0 \varepsilon_S} + \frac{1}{\varepsilon_0 \varepsilon_{\text{water}} \kappa} \right) \Big|_{\text{pzc}} \quad (5.2)$$

where  $\varepsilon_0$  is the permittivity of vacuum,  $\varepsilon_S$  and  $\varepsilon_{\text{water}}$  are the relative permittivities of the Stern layer and the solvent, respectively and  $d_S$  and  $\kappa^{-1}$  (Debye length) are the thicknesses of the Stern layer and the diffuse layer. The equality of  $C_d = \varepsilon_0 \varepsilon_{\text{water}} \kappa$  only applies at low potentials, i.e. around the pzc.

The total capacitance  $C_t$  is related to the surface charge  $\sigma_s$  and the potential  $\psi_s$  via

$$\frac{\delta \sigma_s}{\delta \psi_0} = C_t \quad (5.3)$$

Due to the Nerstian behaviour of the surface, eq 5.3 can be rewritten into

$$\frac{\delta \sigma_s}{\delta \text{pH}} \sim C_t \quad (5.4)$$

This means that the slope in fig 5.2 is directly proportional to the total electrostatic capacitance  $C_t$

From eqs 5.2 and 5.4 it follows that if the ratio of the slopes for two different salt concentrations is inversely proportional to the ratio of the corresponding Debye screening lengths then the  $\sigma_s$  is mostly compensated by the diffuse part of the double layer, if this ratio between the slopes is close to one, then the charge at the Stern plane mostly compensates the charge.

Table 5.1: The ratio of the slopes around the pzc for different salt concentrations.

The two salt concentrations in mol/L	Ratio of the slope around the pzc	
	from the calculated model hematite	$\frac{\kappa_{\text{low salt}}}{\kappa_{\text{high salt}}}$
$10^{-2} : 10^{-1}$	0.40	0.316
$10^{-3} : 10^{-2}$	0.35	0.316
$10^{-3} : 10^{-1}$	0.14	0.100

The calculated ratios are shown in table 5.1. From the values presented in table 5.1, it can be concluded that in our model the compensation of the charge occurs in the diffuse layer. This is not surprising because we had assumed that there were no chemical interactions between the surface and the salt ions, therefore the salt ions spread and compensate the surface charge mostly in the diffuse part of the double layer.

## Adsorption of poly(styrene sulfonate) onto hematite

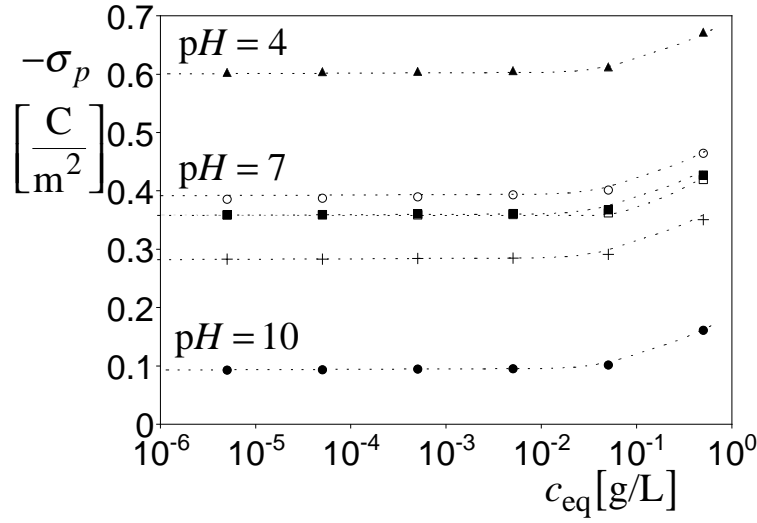


Figure 5.3: Calculated charge of the adsorbed polyelectrolyte  $\sigma_p$  as a function of the concentration of the polyelectrolyte in the bulk  $c_{eq}$  at  $pH$  4, 7, and 10 and 0.01 mol/L salt. At  $pH$  7 the salt concentration was also varied, open circles 0.1 mol/L salt, filled triangles 0.01 mol/L salt, and open squares 0.001 mol/L salt. The crosses are calculations for  $pH$  7, 0.01 mol/L salt, and the  $\varepsilon_{r,monomer} = 10$ .

**Polyelectrolyte adsorption** In fig 5.3 adsorption isotherms are shown for three  $pH$ -values. The concentrations of the polymer are plotted on a log-scale. The adsorbed amount of polymer is expressed as the number of adsorbed charges of the polymer. The charge of the adsorbed polyelectrolyte  $\sigma_p$  is calculated from the excess amount,  $\sigma_p = -0.5\theta_{exc}e/a^2$  in which  $e$  is the elementary charge,  $a$  the lattice size, the factor of 0.5 is due to the fact that only half of the monomers of the polymer has a charge, and the minus sign is needed because the polymer is negatively charged.  $\theta_{exc}$  is the excess adsorbed amount and defined as  $\sum_z(\varphi(z) - \varphi_b(z))$ . From fig 5.3 it is clear that the adsorption isotherms are of the high affinity type. With increasing  $pH$  the adsorbed amount in the plateau is decreased. This is due to less attraction with decreasing surface charge (with increasing  $pH$ ). The observed increase of the adsorbed amount at  $\varphi_b$  of  $10^{-4}$  is due to an increase in the ionic strength by the counterions of the polyelectrolyte.

The differences in adsorption at different salt concentrations are small, as is shown for  $pH$  7. The difference between 0.01 mol/L and 0.001 mol/L is graphically not visible. The somewhat higher adsorbed amount at 0.1 mol/L salt is due to screening of the electrostatic repulsion between the polyelectrolyte monomers in the adsorbed layer.

The adsorption isotherm of a polyelectrolyte with a relative permittivity of 10 instead of 80, has a substantially lower plateau value but the shape of the isotherm is also high affinity, compare the filled triangles with the crosses in fig 5.3.

## 5.2 Theoretical model and results

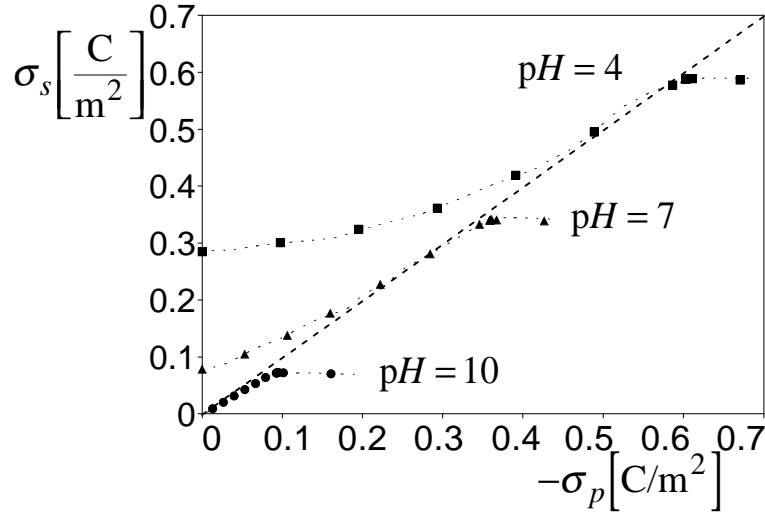


Figure 5.4: The surface charge  $\sigma_s$  as a function of charge of the adsorbed polyelectrolyte  $\sigma_p$ . The pH is denoted in the graph and the salt concentration is 0.01 mol/L. The dashed line denotes charge compensation.

To see the effect of adsorption on the surface charge of hematite,  $\sigma_s$  is plotted as a function of charge of the adsorbed polyelectrolyte  $\sigma_p$  in fig 5.4, for various pH's and at a salt concentration of 0.01 mol/L. To obtain information in the rising part of the adsorption isotherm, calculations are performed under “starved” conditions, i.e. the amount of added polyelectrolyte in the system is lower than the amount needed to reach the plateau value (the equilibrium bulk concentration of polyelectrolyte is practically zero). The dashed line in fig 5.4 represents the equality of the surface charge and the charge of the adsorbed polyelectrolyte.

We found that the surface charge initially increases with increasing polymer adsorption. In the adsorption plateau the surface charge is overcompensated by the charge of the adsorbed polyelectrolyte. At the salt concentration of 0.01 mol/L, the surface charge increases upon adsorption, from 0 to 0.1 C/m² for pH 10, from 0.1 to 0.35 C/m² for pH 7, and from 0.3 to 0.6 C/m² for pH 4.

In fig 5.5 the slope of fig 5.4 as a function of the overcompensation of the surface charge by the charge of the adsorbed polyelectrolyte is shown,  $\sigma_p/\sigma_s = 1$  denotes charge compensation. A slope of one,  $\frac{\partial \sigma_s}{\partial \sigma_p} = 1$ , means that the surface charge increases with the same amount as the adsorbed charges of the polyelectrolyte. In fig 5.5 it is seen that when reaching charge compensation the slope is increasing, this means that with increasing amount of adsorbed polymer the surface charge adopts its charge more than when hardly any polyelectrolyte is adsorbed. The slope is lower at pH 4 than at pH 7, this means that the surface charge at pH 7 adopts more easily to the adsorbed charges than at pH 4. This is due to the fact that the surface charge at pH 4 is higher (see fig 5.2) and can therefore not so easy adjust. For the different pH's, the slope comes to a maximum of 0.85 at the point where the polyelectrolytes starts to

## Adsorption of poly(styrene sulfonate) onto hematite

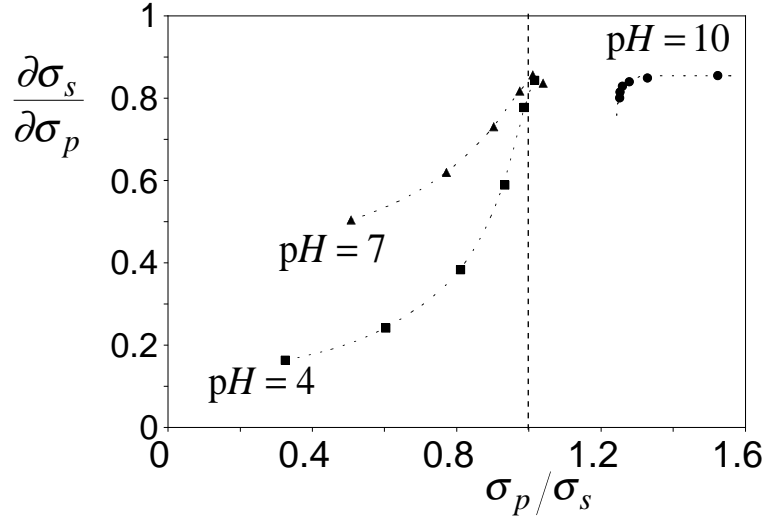


Figure 5.5: The increase in the surface charge due to adsorption  $\partial\sigma_s/\partial\sigma_p$  as a function of fraction of overcompensation  $\sigma_p/\sigma_s$ . The parameters are the same as in fig 5.4. The dashed line denotes charge compensation.

overcompensate the surface charge. At pH 10 the surface charge is in all cases overcompensated by the charge of the adsorbed polyelectrolyte and the slope is approximately constant at 0.85.

In fig 5.6 the slope of the surface-charge increase due to the adsorbed charges as a function of the ratio of the adsorbed charges and the surface charge at pH 7 is shown. As in fig 5.5 we find that the slope  $\partial\sigma_s/\partial\sigma_p$  increases with increasing fraction of overcompensation, and also the maximum is found when the charge of the adsorbed polymer just overcompensates the surface charge. This maximum decreases with increasing salt concentration. This is due to the fact that at low salt concentration the polyelectrolyte is more effectively in screening the surface charge. All polyelectrolyte segments within the Debye screening length  $\kappa^{-1}$  screen the surface charge, at low salt concentration  $\kappa^{-1}$  is larger than at high salt concentration and therefore more polymer segments help to screen the surface charge. The polymer with monomers with a low permittivity, i.e. the crosses in fig 5.6, is less effective in screening of the surface charge. Furthermore the initial slope is the lowest for the system with the highest surface charge without adsorption  $\sigma_{s,0}$ , as was seen in fig 5.5. The surface charge for the lower salt concentrations or higher pH is relatively low and therefore it can increase more easily than at high salt concentration or lower pH.

In figs 5.3 and 5.6 it is also shown that the maximum adsorbed amount and the maximum induced surface charge are both influenced by a lower permittivity of the adsorbing polyelectrolyte, see the crosses.

In calculations it is easy to obtain the slopes of the induced surface charge as a function of the polymer charge, but in experiments this is more difficult due to scatter of the measured points. As an alternative the co-adsorption of

## 5.2 Theoretical model and results

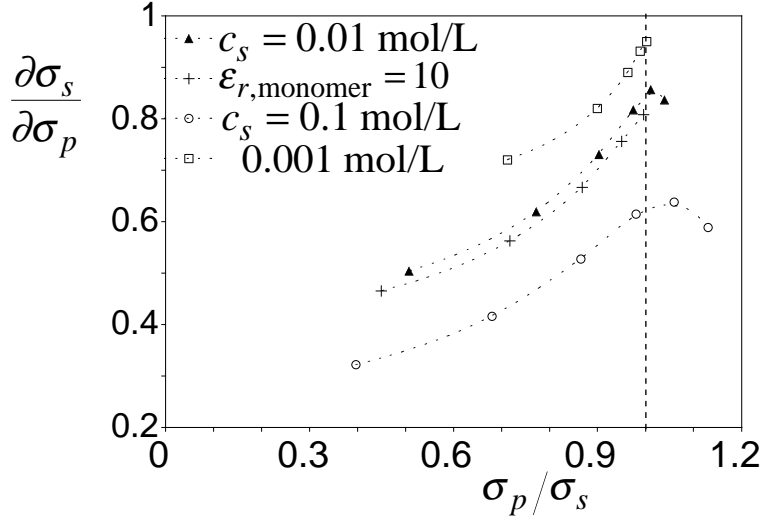


Figure 5.6: The increase in the surface charge due to adsorption  $\partial\sigma_s/\partial\sigma_p$  as a function of fraction of overcompensation  $\sigma_p/\sigma_s$  at pH 7, and three salt concentrations: open circles 0.001 mol/L, filled triangles 0.01 mol/L, and open squares 0.1 mol/L. Results denoted by the crosses apply to pH 7, 0.01 mol/L and the  $\epsilon_{r, \text{monomer}} = 10$ . The dashed line denotes charge compensation.

protons with the adsorbed polymer is used, the co-adsorption is defined as

$$\text{Co-ads } H^+ = \frac{\sigma_s - \sigma_{s,0}}{\sigma_p} \quad (5.5)$$

In fig 5.7 the co-adsorption of the protons for the different calculated systems is shown. The initial slope is the same as in figs 5.5 and 5.6 because the definition is then the same. The trends are also the same, but it cannot be seen anymore that the maximum in the slope is the same for one salt concentration, this is due to the fact that also the initial slope plays a role in the calculation of the co-adsorption of  $H^+$ .

The conclusions from the calculations are as follows. The adsorption isotherm of the polyelectrolyte is high affinity. The effect of pH on the adsorbed amount is large and the effect of the salt concentration small. The surface charge changes strongly upon adsorption.

The slope of the surface charge increase with the adsorbed charges,  $\partial\sigma_s/\partial\sigma_p$  has a maximum where the surface charge is just overcompensated by the charge of the adsorbing polyelectrolyte. This maximum does not depend on the pH but it does depend on the salt concentration. The maximum decreases with increasing salt concentration.

The co-adsorption of protons with the adsorption of the polyelectrolyte depends on the pH and salt concentration. A higher initial surface charge without adsorption  $\sigma_{s,0}$  leads to a lower co-adsorption of protons, i.e. the surface charge can not as easily adapt to the adsorbed polyelectrolytes as when  $\sigma_{s,0}$  is low. Just as for the slope  $\partial\sigma_s/\partial\sigma_p$ , a maximum in the co-adsorption of protons



## Adsorption of poly(styrene sulfonate) onto hematite

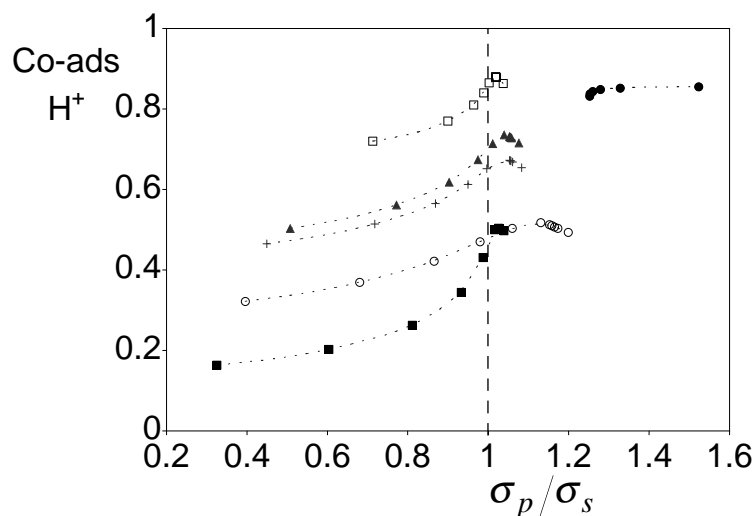


Figure 5.7: The co-adsorption of  $H^+$  with the adsorption of polyelectrolyte as a function of fraction of overcompensation of the surface charge by the charge of the adsorbed polyelectrolyte. The symbols are explained in the legends of figs 5.5 and 5.6.

with the adsorption of the polyelectrolyte is reached when the charge of the polyelectrolyte just overcompensates the surface charge.

## 5.3 Materials and Methods

### 5.3.1 Materials

The hematite used was prepared according to the method of Penners.<sup>137</sup> After preparation it was washed with pure water to remove excess salt and attain a stable solution. The  $pH$  was then around 3 and the conductivity of the suspension was mainly determined by the  $pH$ . The washed suspension at  $pH$  3 was autoclaved (aged) for 8 hours at  $120^\circ\text{C}$  at a pressure of 1.2 atm, to reduce surface asperities, irregularities, and to decrease the time required to reach equilibrium in the proton titrations. The aged hematite suspension was washed with pure water until the  $pH$  of the suspension was above  $pH$  4 and stored.

Sodium poly(styrene sulfonate) (NaPSS) salt, with a molecular mass  $M$  of 70 kg/mol, i.e. degree of polymerization  $N = 340$ , was obtained from Biochem Inc.. The molecular mass of the polymer was checked by viscosimetry in a salt solution of 0.5 mol/L NaCl. The Mark-Houwink coefficients  $K$  and  $a$  for NaPSS in this medium are 1.087 and 0.764,<sup>138</sup> respectively, when the intrinsic viscosity is denoted in g NaPSS per g solution and the molecular mass as kg/mol. A stock solution of about 3 g NaPSS/L and a  $pH$  around 10 was made. To this end the polymer was dissolved in water and KOH was added to reach a  $pH$  of 10. The high  $pH$  prevents degradation of the poly(styrene sulfonate).

## 5.3 Materials and Methods

Ultrapure water from Branstead EASYpure UV (demineralization followed by percolation through an activated carbon column, UV-light treatment to prevent bacterial contamination, and filtration over a 0.2  $\mu\text{m}$  microfilter) was used in all measurements, the conductivity was 18.3  $\text{M}\Omega/\text{cm}$ . All other chemicals were analytical grade.

For the titration the Wallingford titrator in combination with “Titration Program Version T047” was used.<sup>139</sup> Potentiometric titrations were done under  $\text{N}_2$  atmosphere with at least 30 ml of a suspension containing about 0.8 g of hematite, a given concentration of  $\text{KNO}_3$  or  $\text{KCl}$ , and a fixed amount of  $\text{NaPSS}$ . Acid (0.1 mol/L  $\text{HNO}_3$  or  $\text{HCl}$ ) and base (0.1 mol/L  $\text{KOH}$ ) titrants obtained from Merck or Bernd Kraft GmbH were added with Metrohm Dosimat 665 burettes. The EMF measurements in the cell were made with two electrode systems at the same time. One electrode set was a combined  $\text{pH}$ -electrode from Metrohm and the other set was a glass electrode from Ingold, combined with a  $\text{KCl}$ -reference electrode from Mettler Toledo (InLab 301). In this case the reference electrode was placed in a salt bridge of 0.01 mol/L  $\text{KNO}_3$ . The two electrode systems were used as two independent measurements of the  $\text{pH}$ . The electrodes were standardized with buffers also from Merck or Bernd Kraft GmbH.

A Hitachi U2010 UV/VIS spectrophotometer was used to measure the concentration of  $\text{PSS}^-$  in solution.

### 5.3.2 Methods

**Titration** Titrations started after equilibrating the suspension at  $\text{pH}$  4 for half an hour. The next dose is given when the drift of both electrode sets is smaller than 0.5 mV/min over a two-minute time interval. Titrations, that are also used to measure the  $\text{PSS}^-$  adsorption, were carried out with  $\text{KCl}$  and  $\text{HCl}$  because  $\text{NO}_3^-$  interferes with the signal of  $\text{PSS}^-$  in the UV/VIS spectrophotometer.

To measure the surface charge adjustment upon adsorption of  $\text{PSS}^-$  a  $\text{pH}$ -stat measurement is done. A  $\text{pH}$ -stat measurement means in this case that first the hematite is titrated to a desired  $\text{pH}$ , then  $\text{NaPSS}^-$ -solution is added. Subsequently the amount of acid to restore the initial  $\text{pH}$  is recorded.  $\text{KCl}$  or  $\text{KNO}_3$  is used to keep the salt concentration constant (in most cases at 0.01 mol/L). After this titration the last small  $\text{pH}$  adjustments are made by using either an acid or a base titrant to keep the  $\text{pH}$  at the initial  $\text{pH}$  for 20 min. From the total amount of acid and base added, the surface charge adjustment upon adsorption of  $\text{PSS}^-$  is obtained.

**$\text{PSS}^-$ -adsorption** Adsorption isotherms of  $\text{PSS}^-$  onto hematite are measured by depletion experiments.  $\text{HCl}$  and  $\text{KOH}$  are used to bring the solution to the desired  $\text{pH}$ . The ionic strength is 0.01 mol/L  $\text{KCl}$ . For each adsorption experiment about 0.5 gram hematite in 20 ml electrolyte solution with a certain concentration of  $\text{PSS}^-$ , contained in a closed test tube, is used. The

## Adsorption of poly(styrene sulfonate) onto hematite

adsorption is allowed to equilibrate for at least 20 hours, while shaking the tube end over end in a rotating wheel. The concentration of PSS<sup>-</sup> left in solution is measured by means of UV absorption after filtration (Aerodisc 0.2  $\mu\text{m}$  from GelmanSciences) of the suspension. The wavelength used is 263 nm. The molar extinction coefficient, measured by Papenhuijzen<sup>140</sup> for a molecular weight sample of 88,000,  $\epsilon_{263}$  equals 427.7 L mol<sup>-1</sup> monomers cm<sup>-1</sup> in the absence of salt. Using a concentration series of our PSS<sup>-</sup> with no added salt results in a value of 368 L mol<sup>-1</sup> monomers cm<sup>-1</sup> for  $\epsilon_{263}$ . This low value shows that our NaPSS sample contained hydration water.

**Determination of dissolved iron** To be sure that our hematite is not dissolving upon adsorption, the concentration of iron in solution after adsorption is, in some cases, measured. The method used, is the reaction of Fe(II) with 2,2'-dipyridyl,<sup>141</sup> which gives a colored product with an absorption peak at 522 nm. For the determination of iron, 2 mL of a sodium acetate/acetic acid buffer solution of pH 5 and 1 mL of a reducing agent (1% by weight hydroxylamine hydrochloride solution) were added to 6 mL supernatant of the adsorption studies. Finally 1 mL of dipyridyl solution (0.1% by weight) is added. The solution is then shaken and left standing for 10 min. The presence of PSS<sup>-</sup> in solution presents no problem with this method, (in fact it rather enhances the signal which becomes 5 times as strong as that without PSS<sup>-</sup> in solution, but exploration of this phenomenon is beyond the scope of this study).

## 5.4 Results

**Hematite surface** The shape and size of the hematite particles was examined by AFM: the particles remained approximately spherical upon autoclaving and had a radius of  $30 \pm 5$  nm. Dynamic Light Scattering gave a radius of 25 nm for these particles. The specific surface area as determined by N<sub>2</sub>-BET adsorption for the two hematite batches is denoted in table 5.2. The radius calculated from the specific surface area\* is also denoted in this table. The result is comparable to the radii determined with the AFM and DLS, which indicates that the particles are non-porous.

Table 5.2: The measured specific surface area of the two hematite batches used in this study.

System	Specific surface area in m <sup>2</sup> /g	Radius in nm
Hematite I	22.0	26
Hematite II	19.7	29

---

\* $r = \frac{3}{S\rho}$  in which  $r$  is the radius of a spherical hematite particle,  $S$  the specific surface area and  $\rho$  the density of hematite, i.e. 5.24 kg/l.<sup>142</sup>

## 5.4 Results

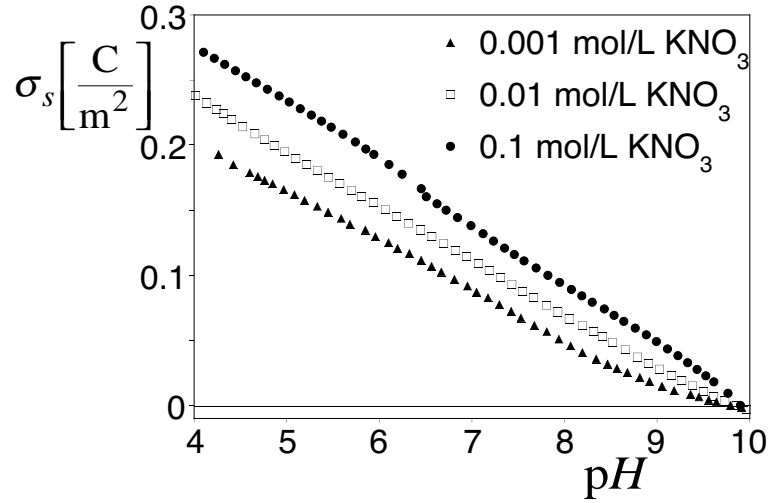


Figure 5.8: The surface charge  $\sigma_s$  of hematite as a function of the  $pH$  and the ionic strength.

In fig 5.8 the surface charge  $\sigma_s$  of hematite is shown as a function of the  $pH$  and salt concentration. We see that with increasing the  $pH$  the surface charge decreases. As expected, for  $pH$ 's smaller than the point of zero charge (pzc)  $\sigma_s$  increases with increasing salt concentrations. The pzc of the hematite is 9.8 which is in good agreement with Penners.<sup>95</sup> For the present sample the charge density at  $pH$  4 is lower than for the hematite prepared in the same way, but not autoclaved.<sup>95</sup> However, the charge density at  $pH$  4 is still higher than that of the hematite prepared by Breeuwsma and Lyklema<sup>143</sup> which is heated after preparation. The small kink in the 0.1 mol/L curve is a measurement artifact.

The time to reach equilibrium after a dose of acid or base is similar for the whole  $pH$ -range and equals about 4 min. This is much shorter than the times observed by Penners<sup>144</sup> for similar hematite that was not aged.

The results for the slope around the pzc give information about the way the surface charge is compensated, see eqs 5.2 and 5.4. The ratio of the slopes determined from fig 5.8 are given in table 5.3.

Table 5.3: Ratio of the slopes for different salt concentrations around the pzc.

The two salt concentrations	Ratio of the slope around the pzc
in mol/L	measured (theoretical values)
$10^{-2}:10^{-1}$	0.67 (0.316)
$10^{-3}:10^{-2}$	0.66 (0.316)
$10^{-3}:10^{-1}$	0.45 (0.1)

By comparing table 5.3 with the values denoted in table 5.1, it follows that the surface charge is partly compensated by the diffuse part of the double layer. The difference between the salt concentrations is smaller than predicted on the basis of screening by diffuse charges only. We conclude from this result that

## Adsorption of poly(styrene sulfonate) onto hematite

the surface charge is not only governed by the diffuse layer capacitance but also by the Stern plane capacitance and/or specific adsorption. The fact that the slope of the curves is not changing much with  $pH$  is also an indication that Stern layer effects are important.

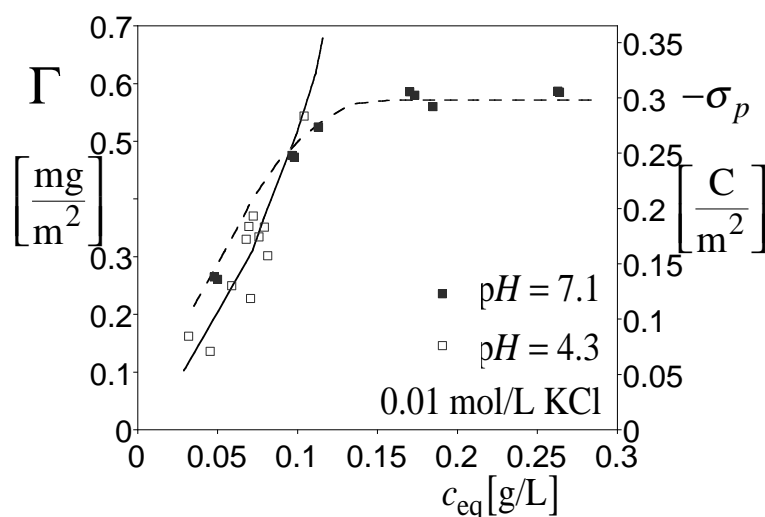


Figure 5.9: The adsorption isotherm of PSS onto hematite at  $pH\ 7.1 \pm 0.1$  and  $4.3 \pm 0.3$  at 0.01 mol/L KCl. The dashed and solid lines are guides to the eye.

**Adsorption of PSS** In fig 5.9 the adsorption isotherms of PSS onto hematite are shown at two different  $pH$ 's and 0.01 mol/L KCl. Two observations can be made. Firstly, the equilibrium concentrations of PSS  $c_{eq}$  in the rising part of the isotherm are *not* very low, i.e. the isotherms are *not* of the high affinity type. Secondly, for  $c_{eq} < 0.1$ g/L there is hardly any difference between the adsorption isotherms of  $pH\ 4$  and  $7$ . It seems that the surface charge is not the dominating factor in the initial adsorption of PSS onto hematite. At  $pH\ 4$  and  $c_{eq} > 0.1$ g/L, experimental data are not available. We return to the measured adsorption isotherms in the discussion section.

**Surface charge and adsorption** A typical result of a  $pH$ -stat titration is shown in fig 5.10, where the  $pH$  during the measurements is plotted as a function of the change in surface charge  $\sigma_s$ . The first big jump is due to the  $PSS^-$  addition. The subsequent points are due to acid addition. The total amount of acid needed to restore the initial  $pH$  corresponds to the charge adjustment of the surface.

The charge adaptation of the hematite surface as a function of the charge of the adsorbed polyelectrolyte, gives information about the point of over-compensation. This is shown in fig 5.11, the data is obtained from different experiments: batch-experiments (open symbols), points on titration curves of

## 5.4 Results

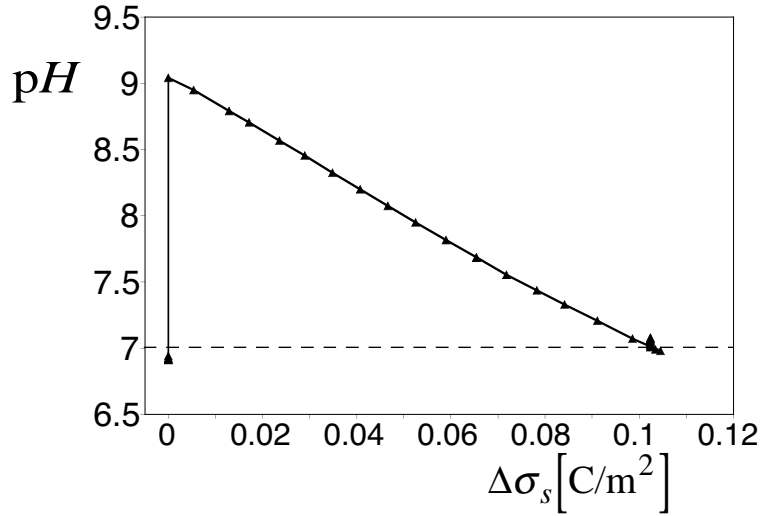


Figure 5.10: The pH as a function of the change in the surface charge for a typical pH-stat measurement.

hematite with PSS<sup>-</sup> (filled symbols), and pH-stat experiments (crosses), see also appendix 5.A.

Let us first discuss the results at pH 7. The measurements indicate that the surface charge increases linearly with the adsorbed PSS<sup>-</sup> charge ( $\sim$  the amount of PSS<sup>-</sup> adsorbed) until the equivalence point is reached. Beyond the equivalence point the surface charge is roughly constant. At pH 4 we only see a linear increase of the charge, because the equivalence point is not reached. At pH 10 only one point is available and therefore the course of the charge adjustment can not be seen.

For the calculated results we saw that the co-adsorption of protons is different for different pH's and a maximum was obtained around the equivalence point of the surface charge and the charge of the adsorbed polymer. In fig 5.12 the co-adsorption of protons is shown as a function of the overcompensation of the surface charge by the adsorbed polyelectrolyte at 0.01 mol/L salt and for pH 4 and 7. A large scatter of points below the overcompensation of the surface charge is seen. Approximately 0.6 protons adsorb to the surface if one charged group of the polyelectrolyte is adsorbing. There is no difference found between high and low amount of adsorbed polyelectrolyte before the surface charge is overcompensated. Furthermore there is no difference in the co-adsorption of protons between the two different pH's, i.e. pH 4 and 7. When the surface charge is overcompensated, i.e.  $\sigma_p/\sigma_s > 1$ , the co-adsorption decreases, just as in the calculated results in fig 5.7.

**Titration in the presence of PSS** The hematite is titrated in the presence of a given amount of PSS ( $c_{\text{tot}} = 0.60$  g PSS<sup>-</sup>/m<sup>2</sup>). During the titration both the amount PSS<sup>-</sup> adsorbed and the surface charge can change. At this amount of total PSS<sup>-</sup> in solution, the amount adsorbed at pH 7 just overcom-

## Adsorption of poly(styrene sulfonate) onto hematite

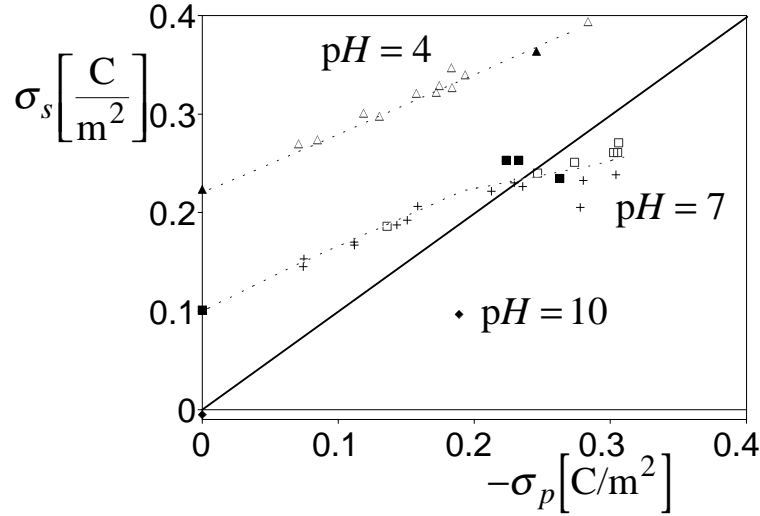


Figure 5.11: Charge density  $\sigma_s$  of hematite as a function of the adsorbed amount  $\Gamma$  of PSS at pH 4.3, 7.1, and 10. The ionic strength is  $10^{-2}$  mol/L. The filled symbols give the results from the titration experiments where also the  $c_{\text{eq}}$  of  $\text{PSS}^-$  is measured, the open symbols give the results from the depletion experiment and the crosses at pH 7 give the results of titrations where the adsorbed amount is calculated from the adsorption isotherm. The solid line denotes charge compensation.

pensates the surface charge. In fig 5.13 the PSS-solution is added at pH 7 (see the arrow) and the surface charge adjustment is calculated from a pH-stat measurement. Subsequently the sample is titrated to pH 4, the titration is continued with base to pH 10 and then back to pH 4 again. There is no hysteresis in the titrations. The fact that the curves in the absence and presence of  $\text{PSS}^-$  run about parallel indicates that the amount of extra surface charge is approximately the same for all the pH's. Furthermore, there is no sign of flattening of the  $\sigma_s$  at low pH, so probably the maximum surface charge of hematite is not reached. Extrapolation of the curve to  $\sigma_s = 0$  C/m<sup>2</sup> gives a pzc in the presence of  $\text{PSS}^-$  of about 12.

## 5.5 Discussion

**Experimental adsorption isotherm** The most unexpected feature of the adsorption isotherm of PSS on hematite is that it is not a high affinity curve, which is theoretically expected for an adsorption isotherm of a polymer or a polyelectrolyte, see fig 5.3. In the following we discuss four possible reasons for this unexpected behaviour:

- Blocking of part of the surface area due to fast flocculation
- Polydispersity of the PSS sample
- Incomplete equilibration of PSS adsorption

## 5.5 Discussion

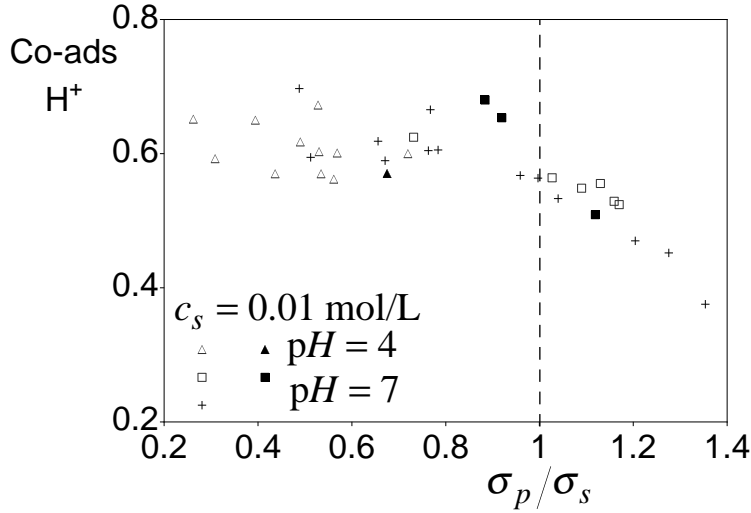


Figure 5.12: The co-adsorption of  $H^+$  with the adsorption of polyelectrolyte as a function of fraction of overcompensation of the surface charge by the charge of the adsorbed polyelectrolyte. The symbols are explained in fig 5.11.

- Spreading of the polyelectrolyte is kinetically blocked

Flocculation of hematite is observed for samples as soon as PSS in low concentration is added. While preparing samples for the depletion measurements, a marked difference between the plateau values and the other points can be observed by the eye: Upon adding PSS for the lower concentrations, the hematite suspension flocculates immediately, whereas at the plateau values the hematite is stable. Hence, in the initial part of the isotherm it is possible that surface area is lost for PSS adsorption. In that case our reported initial adsorbed amount per  $\text{m}^2$  is wrong because we use a too large surface area. Because this flocculation is only seen at small amounts of added PSS, the first guess is that this is flocculation due to bridging. But this way of flocculation should only occur if there is enough surface area available for the polymer. In this case, commonly, the polymer concentration tends to zero. Alternatively, the flocculation is induced due to charge reduction and a loss of electrostatic repulsion. Using electroacoustics it has been reported that flocculation of bare hematite can already start at a  $pH$  of 7.<sup>145,146</sup>

For polydisperse polyelectrolyte samples the adsorption isotherm can give also a non-high affinity part. But there are two reasons to think that the sample is hardly polydisperse. PSS has a very narrow molecular mass distribution and viscosimetric measurements show that the present sample gave the same molecular weight as specified by the manufacturer. This rules out degradation of the polymer. The second reason is that the titration curves did not show any hysteresis upon titrating from  $pH$  4 to  $pH$  10 and back. Some titrations, carried out with a polydisperse sample of PSS adsorbed onto hematite, showed large hysteresis in the titration curve. Furthermore, in literature high affinity adsorption isotherms even for polydisperse samples have been reported.<sup>147,148</sup>



## Adsorption of poly(styrene sulfonate) onto hematite

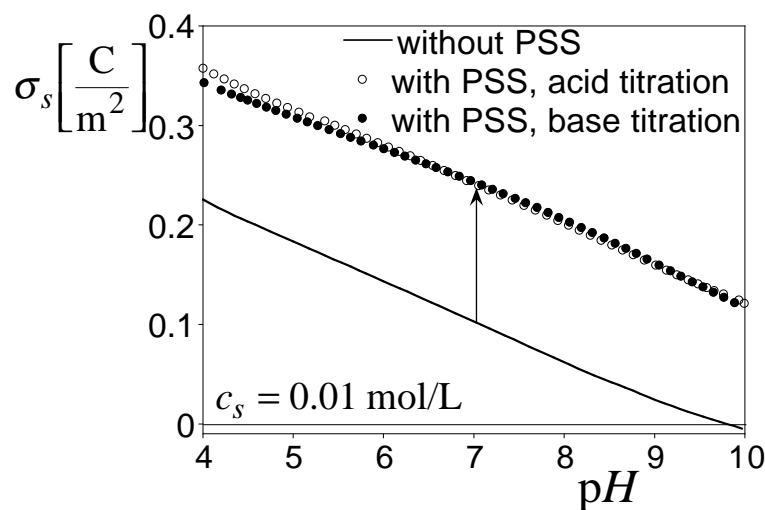


Figure 5.13: The surface charge  $\sigma_s$  of hematite as a function of the  $pH$ . The amount of PSS is  $0.60 \text{ mg PSS}^-/\text{m}^2$  hematite and the ionic strength is  $0.01 \text{ mol/L KNO}_3$ . Open symbols denote the titration with acid and the filled symbols the titration with base. The solid line is the reference titration of the bare hematite surface, derived from fig 5.8.

Samples of natural organic matter, taken from soils, which are known to be highly polydisperse, gave a high affinity isotherm on goethite.<sup>149</sup>

The third possibility is that the equilibrium has not been reached despite 20 hours of shaking. Calculations done by Cohen Stuart et al.<sup>107</sup> indicate that equilibrium for polyelectrolyte adsorption can take days. Adsorption of poly(acrylic acid) on aluminum oxide showed a difference between the zeta potential measured after one day or after 40 days.<sup>150</sup> Furthermore, the calculations are equilibrium calculations and they do not show adsorption lower than the plateau value, even for very low concentrations in the bulk solution of polymer.

Yet, in the titration experiments we did not find any time effects. The  $pH$  stayed constant while waiting for over 14 hours at  $pH$  7 and the response of the  $pH$  upon adding acid or base happens for different samples in the same time span. The solutions, that are compared, consisted of bare hematite, hematite with PSS, that just is adsorbed, and hematite on which PSS is already adsorbed for over 14 hours.

The fourth possible explanation is a kinetically frozen situation of the adsorbed polyelectrolyte. The polyelectrolytes adsorbing from a dilute solution have time to spread over the surface and adsorb as thin layers. However, when the polyelectrolytes adsorb from a solution of higher concentration, next to an adsorbed polymer, another polyelectrolyte is adsorbed. The possibility of spreading is low because a neighbouring polyelectrolyte must be removed. This means that the adsorbed amount for the low concentrations can be the equilibrium value but for the high polyelectrolyte concentrations, the adsorption

## 5.5 Discussion

is too high. The kinetics to remove a polyelectrolyte is so slow that  $\Gamma$  stays constant.

This last possibility would also explain another feature of the experimental adsorption isotherm. The plateau value is relatively high for polyelectrolyte adsorption. If a flat conformation of the adsorbed polyelectrolyte is assumed, it follows that for every styrene sulfonate monomer an area of  $0.44 \text{ nm}^2$  is available for  $\Gamma = 0.6 \text{ mg/m}^2$ . This value is rather small compared to the estimated area of a monomer ( $\approx 1.5\text{--}2.4 \text{ nm}^2$ ). This means that a part of the polyelectrolyte should be adsorbed in loops and tails. The adsorption of PSS on hematite measured by Papenhuijzen<sup>138</sup> shows a lower adsorbed amount, i.e. of  $0.4 \text{ mg/m}^2$  for  $\text{pH } 6$  and at a salt concentration of  $0.01 \text{ mol/L}$ . Van der Schee and Lyklema found a plateau in the adsorbed amount of  $0.6\text{--}1 \text{ mg/m}^2$  for neutral polymers but for adsorbed polyelectrolytes the lower value of  $0.3 \text{ mg/m}^2$  was measured.<sup>118</sup> Yim et al.<sup>151,152</sup> found adsorbed amounts of  $1 \text{ mg/m}^2$  but they used a higher salt concentration; for the lowest salt concentration ( $0.12 \text{ mol/L}$ ) used an adsorbed amount of  $0.8 \text{ mg/m}^2$  was found.<sup>151</sup> Dalhgren et al.<sup>153</sup> found for the adsorption of PCMA on mica an adsorbed amount of  $0.7 \text{ mg/m}^2$  at low salt concentrations, the surface charge of mica is at the plateau value just overcompensated by the charge of the adsorbed PCMA.

**Surface charge change due to PSS adsorption** The surface charge density of hematite changes a lot due to the adsorption of PSS. The increase of the surface charge density is approximately the same for different  $\text{pH}$ 's. A similar trend is also found for surfactant adsorption.<sup>114,115,154</sup>

Before the charge of PSS overcompensates the surface charge of hematite, the surface charge density increases with increasing adsorption. This increase of the surface charge density with adsorption seems to be linear.

**Comparison between the calculations and the measurements** The amount adsorbed in  $\text{C/m}^2$  in the adsorption plateau in the calculations is a bit larger than that in the experiments and also the calculated surface charge density is larger than the measured surface charge density. The ratio of overcompensation,  $\sigma_{p,\text{max}}/\sigma_{s,\text{max}}$ , is comparable between the measurements and the calculations. That the amount adsorbed and the surface charge density are too high in the calculations is probably due to the fact that the surface charge density in the calculations is more easily increased than on real hematite, as was also the case for the bare hematite, compare figs 5.2 and 5.8. This discrepancy can be reduced by choosing a low permittivity for the surface species, i.e.  $\varepsilon_{r,\text{surface}} < 40$ .

Shubin and Linse<sup>94</sup> compared the experimental adsorption of polyelectrolytes of acryl amide and ((3-methacrylamido)propyl)trimethylammonium chloride on silica with self-consistent-field calculations. They found that if the surface charge is fitted correctly by the theory, the calculated adsorbed amount is lower than the experimentally observed amount. The predicted overcompen-

## Adsorption of poly(styrene sulfonate) onto hematite

sation of the surface charge density is a factor of 2 to 4 lower than the results of the experiment. They used the same kind of calculation as we did, but in this case the polyelectrolyte in the bulk behaves like an ideal coil, because the electrostatic potential in the bulk is zero. In our calculations we took into account the intramolecular interactions in the bulk, and this results in better comparison of the numerical data with the experimental data.

Comparing the co-adsorption of the experiments and the calculated results two main differences are seen. Firstly the maximum in the co-adsorption of protons in the calculations is not found in the experiments. Secondly in the model calculations the initial co-adsorption at  $pH$  4 and 7 are different but in the experiments they are the same. The maximum in the co-adsorption is seen in all the systems calculated just when the surface charge is overcompensated. In the measurements we find a “plateau” in the co-adsorption, this might mean that the experimental system is in all cases at the point of overcompensation. This in turn would mean that the amount of available surface area is lower than the amount of surface which was put in. This can be due to flocculation and would also be able to explain the non-high-affinity adsorption isotherms.

In general we see that, except for the shape of the adsorption isotherm, the main features of the measurements are captured by the calculations with a minimum of parameters.

## 5.6 Acknowledgements

Mr W. Threels is acknowledged for preparing the hematite and the technical assistance. Mr A. Korteweg is acknowledged for the BET-measurements of the hematite samples. Mr R. Fokkink is thanked for the DLS-measurements and dr.ir. J. H. Maas for the help with the AFM.

## 5.A Calculation of the surface charge from different experiments

### 5.A Calculation of the surface charge from different experiments

**Depletion experiments** The extra charge on the surface is calculated from the amount of acid and base added to get the desired  $pH$ , corrected for the initial amount needed for a solution without  $PSS^-$  added (blank). These points are denoted as open symbols in fig 5.11.

**Titration experiments with KCl as salt** From a  $pH$ -stat measurement the surface charge increase is measured. After the  $pH$ -stat measurements a sample was taken and the concentration of  $PSS^-$  in solution was measured. The charge densities obtained in this way are plotted in fig 5.11 as filled symbols.

**Titration experiments with  $KNO_3$  as salt** From a  $pH$ -stat measurements the surface charge density in the presence of  $PSS^-$  is measured. However, we can not measure the  $PSS^-$  left in solution, due to interference of  $NO_3$  in the determination of  $PSS^-$  with UV-adsorption. Therefore the adsorbed amount is calculated from a linear extrapolation between two points from the adsorption isotherm which have a ratio of  $PSS^-$  added per  $m^2$  of hematite closest to the titration experiment. These points have only been obtained at  $pH$  7 and are denoted by crosses in fig 5.11.

# Chapter 6

## Evaluation of the mastercurve procedure

### Abstract

A self-consistent-field (SCF) model is used to calculate the dissociation of acidic polyelectrolyte stars and dendrimers. The numerical results are transformed into mastercurves using two simple electrostatic models: the Donnan model and a hard-sphere model. For both models, it is checked whether the calculated charge- $pH$  curves of a given molecular architecture result in a good mastercurve. The dissociation constant  $K$  obtained from the mastercurve procedure is compared to the intrinsic dissociation constant  $K_{\text{int}}$ . Furthermore, the Donnan potential and the hard-sphere potential are compared to the electrostatic potential profile, which results from the SCF-model.

In the mastercurve procedure a size is assigned to the Donnan or hard sphere volume. This size can be obtained from the SCF calculations for each  $pH$ . However, it is also of interest to use sizes which do not depend on the  $pH$ , so several estimates for the size based on the chain architecture and salt concentration have been used.

For the case of a  $pH$ -dependent size, the Donnan model gives a good estimate of the  $pK_{\text{int}}$ -value. However, the mastercurve is in most cases diffuse: the points of a charge- $pH$  curve for different salt concentration do not merge completely. Only for large molecules and molecules with a large number of branches a good mastercurve is found. In contrast, the hard-sphere model always results in a good mastercurve. However, in this case the resulting  $pK$ -value deviates more from the  $pK_{\text{int}}$ -value. Upon increasing the number of branches in the molecules this deviation increases.

When using estimates of the Donnan or hard sphere volume which do not depend on  $pH$ , the resulting mastercurves are generally less good. We have compared five different estimates. Surprisingly, the size resulting from a maximal stretching of the arms (without any ionic strength dependence) gives the best mastercurves and estimates of  $pK_{\text{int}}$  both for the Donnan and hard-sphere

model. The mastercurves become better when the monomer density in the stars and dendrimers increases. However, the  $pK$ -values obtained from the mastercurve procedure will always be overestimated.

These results may be useful as a guideline for obtaining mastercurves when titrating humic substances.

## 6.1 Introduction

Modelling of metal ion binding to humic acid is a difficult task. This is due to their intrinsic heterogeneity and due to the competition for binding sites between a given metal ion and protons or other metal ions. The idea is that from adsorption isotherms of different metal ions to humics also the competition between different metal ions can be predicted. Almost a decade ago several models to describe the proton binding to humic substances came up.<sup>155–159</sup> Two of these models, Model VI<sup>160</sup> and the NICA–Donnan model,<sup>161</sup> are most promising. They have been tested extensively with data collected on purified humic substances.<sup>160,161</sup> With the parameters obtained in these studies the behaviour of metal ions in natural systems can be predicted reasonably well.<sup>162</sup>

In these models the metal ion adsorption to humics is determined by electrostatic and chemical interactions. To be able to distinguish between these two types of interaction, the so-called mastercurve procedure is developed as part of the NICA model.<sup>163</sup>

The idea behind a mastercurve is that a set of charge- $pH$  curves of a polyelectrolyte or a humic substance at different salt concentrations can be transformed into one single charge- $pH_{\text{site}}$  curve, the mastercurve, where  $pH_{\text{site}}$  is the  $pH$  in the solution in the direct vicinity of the dissociating sites.

In order to obtain the relation between the  $pH$  and the  $pH_{\text{site}}$  the electrostatic potentials at the location of the sites should be known. Under the assumption that this potential is the same for all sites, it can be calculated from the degree of dissociation using an electrostatic model that links the charge density to the site potential. The  $pH_{\text{site}}$  incorporates all electrostatic effects and the resulting mastercurve reflects the intrinsic or chemical properties of the polyelectrolyte or humic substances, i.e. the intrinsic dissociation constants.

With the NICA model mainly two approaches have been used to model the electrostatics: the hard-sphere model (HS)<sup>159,164,165</sup> and the Donnan model (D).<sup>165,166</sup> Both models require an extra parameter, for the HS-model this is the particle area and for the Donnan model the Donnan volume of the particles. The transformation of the measurable charge- $pH$  curves into charge- $pH_{\text{site}}$  curves can be done with both models. In order to achieve that the different charge- $pH_{\text{site}}$  curves really merge into one mastercurve, the common practice has been to make either the area (HS) or the volume (D) in the electrostatic models somewhat dependent on the salt concentration (and/or  $pH$ ).

As humic substances are quite complex in nature, the assumption that the electrostatics at a given  $pH$  and ionic strength can be described with just one site potential clearly is a simplification. In order to assess the quality of this type of approximation, we will apply the mastercurve procedure to the calculated charge- $pH$  curves of a series of simple polyelectrolytes with well defined and different architectures. We have investigated how closely the true intrinsic dissociation constants and true site potentials can be matched by

## 6.2 Electrostatic models

the dissociation constants and the site potentials that are derived from the mastercurve procedure.

The calculation of the charge-pH curves of the different polyelectrolytes will be based on the SF-SCF theory described in the previous chapters. These calculations also provide a measure of the size of the polyelectrolyte molecules under the given conditions. This size depends on the salt concentration and pH, in practice, the dependence of the size on the solution conditions is not always known. Therefore, we will use five other sizes to investigate the effect of the size on the results of the mastercurves.

This chapter is organized as follows, first the two electrostatic models, the Donnan model and the hard-sphere model will be explained. This is followed by a description of the polyelectrolyte molecules used in the SF-SCF calculations. Then the results of the mastercurve procedure applied to the charge-pH curves are given, followed by a discussion. At the end conclusions in relation to the use of the mastercurve procedure for humic substances are drawn.

## 6.2 Electrostatic models

**Donnan model** In the Donnan model, the polyelectrolyte is envisioned as a penetrable sphere. The charge of the polyelectrolyte is compensated within the Donnan volume  $V_D$  by co- and counterions. Within in the Donnan volume the electrostatic potential  $\psi_D$  is constant and outside the Donnan volume the potential is zero, as schematically shown in fig 6.1. In the presence of only a simple  $\nu$ - $\nu$  electrolyte the Donnan model leads to the following relation between the charge density and the Donnan potential:<sup>167</sup>

$$\frac{Q_{\text{im}}}{V_D} = c_s e^{-\nu e \psi_D / k_B T} \quad (6.1)$$

in which  $Q_{\text{im}}$  is the number of univalent immobile charges on the polyelectrolyte,  $V_D$  the Donnan volume of the polyelectrolyte molecule,  $c_s$  the concentration of salt ions in the bulk,  $\nu$  the valency (with sign) of the counter ions,  $e$  the elementary charge,  $\psi_D$  the Donnan potential, and  $k_B T$  Boltzmann's constant times the temperature. In eq 6.1 only the counterions are taken into account, as is usually done. In practice  $Q_{\text{im}}$  is more conveniently expressed in eq/g, the corresponding  $V_D$  is then expressed in  $\text{m}^3/\text{g}$ .

**Hard-sphere model** In the hard-sphere model the polyelectrolyte is seen as a hard sphere, all the charges are located at the surface of a sphere and are compensated outside the hard sphere in the diffuse double layer, see fig 6.2.

In order to obtain the relation between the surface charge density  $\sigma_s$  and the surface potential  $\psi_s$  the Poisson-Boltzmann equation can be used.<sup>168</sup> For spherical geometry the Poisson-Boltzmann equation cannot be solved analytically.



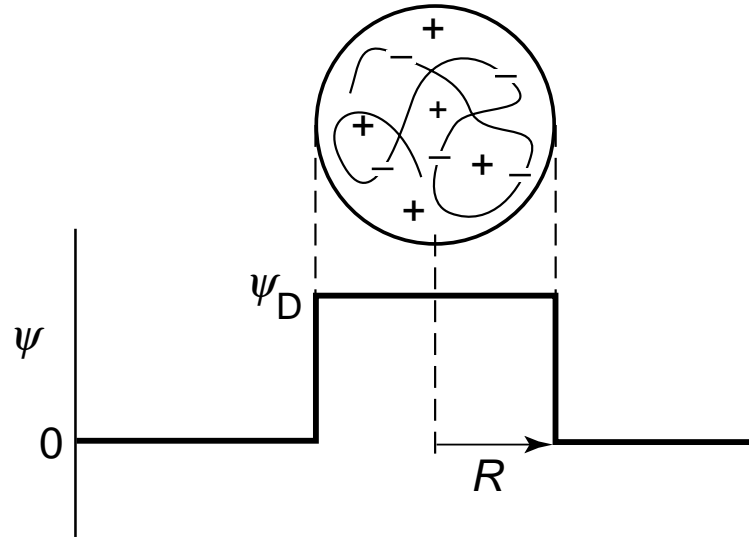


Figure 6.1: Schematic representation of the Donnan model.

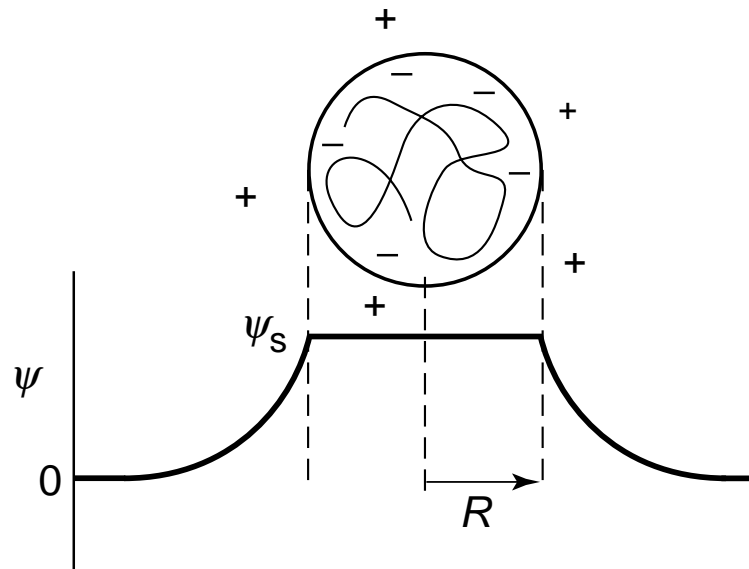


Figure 6.2: Schematic representation of the hard-sphere model.

### 6.3 Method

ically, so we use an approximate expression for a symmetrical electrolyte<sup>168</sup>

$$\frac{Q_{\text{im}}}{4\pi R^2} = \frac{-2Fc_s\nu}{\kappa} \left[ 2 \sinh \left( \frac{\nu e \psi_s}{2k_B T} \right) + \frac{4 \tanh(\nu e \psi_s / 4k_B T)}{\kappa R} \right] \quad (6.2)$$

where  $Q_{\text{im}}$ ,  $c_s$ ,  $\nu$ ,  $e$ , and  $k_B T$  have the same meaning as in eq 6.1. The radius of the hard sphere is denoted by  $R$ ,  $F$  is Faraday's constant,  $\psi_s$  the electric potential at the surface of the hard sphere, and  $\kappa$  the inverse Debye length. For a symmetrical electrolyte the Debye length is given by  $\kappa^2 = \frac{2Fec_s\nu^2}{k_B T \varepsilon_0 \varepsilon_r}$ , in which  $\varepsilon_0$  is the permittivity of vacuum and  $\varepsilon_r$  the relative permittivity of the solvent. In practice  $Q_{\text{im}}$  will in this case be expressed in C/g and the particle area,  $4\pi R^2$ , is replaced by the specific area in  $\text{m}^2/\text{g}$ .

### 6.3 Method

The numerical self-consistent-field model (SCF), that is used to calculate the charge-pH curves has been developed by Böhmer et al.,<sup>90</sup> Israëls et al.,<sup>43</sup> and Van Male.<sup>67</sup> It basically is an extension of the polymer adsorption model developed originally by Scheutjens and Fleer.<sup>13</sup> An outline of the theory for calculating annealed polyelectrolytes is partially presented in chapter 3.

In the present study polyelectrolytes with a  $pK_{\text{int}}$  of 5, different architectures, and different number of monomers (or molecular mass) are used. The interaction with the solvent is chosen such that if the polyelectrolyte is uncharged the solvent is a  $\theta$ -solvent. The pH is varied between 3 and 11 and three different salt concentrations are used, i.e. 0.55 mmol/L, 55 mmol/L, and 5.5 mol/L. From the calculations we obtain the average degree of dissociation  $\alpha$ , the electrostatic potential profiles  $\psi(z)$ , and the size  $R_e$  of the molecules as a function of the salt concentration and the pH. The size  $R_e$  is the first moment over de endpoint profiles. This size is for star shaped molecules comparable to a hydrodynamic radius. The equations for  $\alpha$ ,  $R_e$ , and  $\psi(z)$  are given in section 3.3 of chapter 3.

The different polyelectrolyte molecules used, can be grouped into five different structures. Each structure consists of 5 or 6 different molecules, that differ in the number of arms  $f$  the structure has. The five structures are explained in fig 6.3. In this figure the minimal density is introduced as a way to represent each of the different molecules by one number. The minimal density  $\varphi_{\text{min}}$  is the average density of the molecule when it is totally stretched and defined as

$$\varphi_{\text{min}} = \frac{N}{4/3\pi R_{\text{max}}^3} \quad (6.3)$$

in which  $N$  is the total number of monomers per molecule and  $R_{\text{max}}$  the length of an arm when it is totally stretched.

In fig 6.3 only the architectures with four arms are drawn. For each of these structures also architectures with different numbers of arms  $f$  are used, as denoted in table 6.1. The number of chargeable groups in a molecule equals  $N/3$ , where  $N$  is the total number of monomers.

## Evaluation of the mastercurve procedure

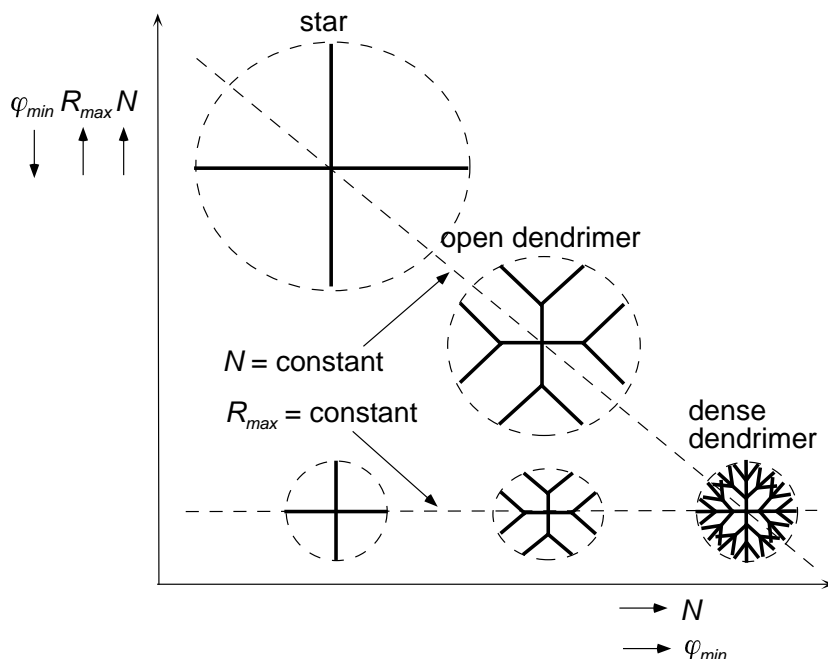


Figure 6.3: Shapes of the five different structures all with four arms.  $\varphi_{\min}$  denotes the minimal density,  $R_{\max}$  the length of an arm if this is totally stretched and  $N$  the total number of segments per molecule.

## 6.4 Mastercurve procedure

The mastercurves are compared to the intrinsic charge-pH curves. To decide if a mastercurve is good, two criteria are used

- The extent to which the data points of charge-pH curves for the different salt concentrations merge into a mastercurve
- The agreement between the true intrinsic (chemical) dissociation constant  $pK_{\text{int}}$  and the dissociation constant obtained from the mastercurve procedure

In order to work out these criteria in practice, it is convenient to use the logarithm of the apparent dissociation constant as a parameter

$$pK_p(H_p, \alpha) = pH_p - \log \frac{\alpha}{1 - \alpha} \quad (6.4)$$

where  $\alpha$  is the degree of dissociation and  $pH_p$  is the negative logarithm of the proton concentration changed by the electrostatic potential of interest. For  $p = 0$ , the potential is zero and  $pH_p$  is the bulk pH. For  $p = D$  or HS the  $pH_p$  is the  $pH_{\text{site}}$  for Donnan model and the hard-sphere model, respectively. To denote both the models, we will use  $p = \text{model}$ . Due to the electrostatic interactions the values of  $pK_0$  differ from the intrinsic  $pK$ -value,  $pK_{\text{int}}$ . The values of  $pK_{\text{model}}$  will also differ from  $pK_{\text{int}}$  if the electrostatic model is incorrect. However,  $pK_{\text{int}} - pK_{\text{model}}$  will be much smaller than  $pK_{\text{int}} - pK_0$

## 6.4 Mastercurve procedure

Table 6.1: Definition of the molecules used in the calculation

	large star		large open dendrimer		dense dendrimer		small open dendrimer		small star	
$R_{\max}$	40.2 [nm]		27 [nm]		4.8 [nm]		4.5 [nm]		4.5 [nm]	
$f$	$N$	$\varphi_{\min}$	$N$	$\varphi_{\min}$	$N$	$\varphi_{\min}$	$N$	$\varphi_{\min}$	$N$	$\varphi_{\min}$
2			268	$8.8 \cdot 10^{-5}$	268	$1.6 \cdot 10^{-2}$	46	$3.1 \cdot 10^{-3}$	30	$2.1 \cdot 10^{-3}$
4	536	$5.3 \cdot 10^{-5}$	536	$1.8 \cdot 10^{-4}$	536	$3.1 \cdot 10^{-2}$	92	$6.2 \cdot 10^{-3}$	60	$4.2 \cdot 10^{-3}$
8	1072	$1.0 \cdot 10^{-4}$	1072	$3.4 \cdot 10^{-4}$	1072	$5.2 \cdot 10^{-2}$	184	$1.0 \cdot 10^{-2}$	120	$7.0 \cdot 10^{-3}$
16	2144	$2.1 \cdot 10^{-4}$	2144	$6.8 \cdot 10^{-4}$	2144	0.10	368	$2.1 \cdot 10^{-2}$	240	$1.3 \cdot 10^{-2}$
32	4288	$4.1 \cdot 10^{-4}$	4288	$1.3 \cdot 10^{-3}$	4288	0.18	736	$3.4 \cdot 10^{-2}$	480	$2.3 \cdot 10^{-2}$
53	7102	$6.7 \cdot 10^{-4}$	7102	$2.2 \cdot 10^{-3}$	7102	0.29	1219	$5.7 \cdot 10^{-2}$	795	$3.9 \cdot 10^{-2}$

if the electrostatic model to calculate the mastercurves is a reasonably good approximation.

Hence, in general the quality of the mastercurve procedure can be judged by converting the  $(\alpha, \text{p}H_{\text{site}})$ -data into a  $\text{p}K_{\text{model}}$ -data. However, instead of using the difference  $\text{p}K_{\text{int}} - \text{p}K_{\text{model}}$  to judge the mastercurve, we prefer to separate this condition in two conditions that meet the two criteria formulated above.

The first criterion can be investigated by using a variance  $\sigma_p$ , defined as

$$\sigma_p^2 = \frac{\sum_{c_s} (\text{p}K_{p,c_s} - \text{p}K_{p,av})^2}{n - 1} \quad (6.5)$$

where the summation runs over all salt concentrations and  $n$  is the number of salt concentrations. The  $\text{p}K_{p,c_s}$  is the average  $\text{p}K$  when using the  $(\alpha, \text{p}H_p)$  points for one salt concentration  $c_s$  and  $\text{p}K_{p,av}$  is the average calculated using all data points for one molecular structure. The quality of the mastercurve can now be derived from the ratio  $\Upsilon$

$$\Upsilon = \frac{\sigma_{\text{model}}}{\sigma_0} \quad (6.6)$$

denotes the ratio between the variance found for a mastercurve with an electrostatic model  $\sigma_{\text{model}}$  and the variance found for the original data  $\sigma_0$ . In the ideal case that the electrostatic model used to calculate the mastercurve is correct, then  $\sigma_{\text{model}} \rightarrow 0$  and  $\Upsilon \rightarrow 0$ . In practice this extreme will not be reached, but  $\Upsilon$  should at least be considerably smaller than unity, otherwise no improvement is achieved with respect to the original “experimental” data. In order to satisfy our first criterion, we will use the condition  $\Upsilon < 0.3$ . This criterion tells us that the merging of the  $(\alpha, \text{p}H_{\text{site}})$  curves derived from the  $(\alpha, \text{p}H)$  curves at different salt concentrations is satisfactory.

Secondly, the quality of the obtained mastercurve is also depending on the difference  $\delta_{\text{p}K}$ .

$$\delta_{\text{p}K} = \text{p}K_{\text{int}} - \text{p}K_{\text{model},av} \quad (6.7)$$

## Evaluation of the mastercurve procedure

The smaller this difference is the more closely the mastercurve represents the true intrinsic (chemical) properties of the polyelectrolyte. If  $\delta_{pK} < 0$  the  $pK_{\text{int}}$  is overestimated and if  $\delta_{pK} > 0$  the  $pK_{\text{int}}$  is underestimated. We will use for the quantification of the second criterion the value of  $-1 < \delta_{pK} < +1$ .

## 6.5 Results

In this section we will show how well the mastercurve procedure works for the different molecular structures and investigate conditions that may allow us to select the most appropriate model (Donnan or hard-sphere) if some information on the molecular structure is available.

**$R_e$  as the characteristic size** In fig 6.4 the different molecules used in the calculations are plotted in a  $\varphi_{\text{min}}(f)$  plot. The solid lines connect the points of a given architecture, ranging from large stars, with the lowest density, to the dense dendrimer, with the highest density. In fig 6.4a the results with the Donnan model are shown. As a criterion of a good mastercurve the value of  $\Upsilon < 0.3$  is used. The dense dendrimer with  $f \geq 16$  and the large open dendrimer and the large star both with  $f = 53$  give good mastercurves. If the criterion is extended to  $\Upsilon \leq 0.6$  pH-units then 26 out of the 35 structures do give mastercurves that qualify.

In fig 6.4b it can be seen that the hard-sphere model gives in almost all cases a good mastercurve, only for the small number of arms the  $\Upsilon$  is larger than 0.3. The hard-sphere model gives either a good mastercurve *or* a bad one, there are hardly any intermediate cases as for the Donnan model where  $\Upsilon$  changes more gradually.

The second criterion for a good mastercurve is that the chemical and electrostatic interactions are correctly separated. For the present situation the  $pK_{\text{int}}$  of 5 should recover from the mastercurve, or  $\delta_{pK} \rightarrow 0$ . In fig 6.5 the calculated  $pK_{\text{model},av}$  values for the two electrostatic models are shown. In fig 6.5a the results with the Donnan model are given; for the large molecules, i.e. the large star and the large open dendrimer, a  $pK_{D,av}$  of  $4.75 \pm 0.1$  is found which is quite reasonable in comparison with the true  $pK_{\text{int}}$ -value of 5. The smaller molecules give a lower  $pK_{D,av}$ -value, i.e.  $4.35 \pm 0.15$ . In general, we may say that the  $pK_{D,av}$ -value is underestimated by the Donnan model but it is not far from the true value of the  $pK_{\text{int}}$ .

The results for the HS-model, as shown in fig 6.5b, agree less well with the intrinsic  $pK_{\text{int}}$  than the  $pK_{\text{HS},av}$ 's found with the Donnan model. The  $pK_{\text{HS},av}$ -value is in most cases too low (shaded area). In fig 6.5b a clear trend in the  $pK_{\text{HS},av}$ -value can be seen: with increasing density  $pK_{\text{HS},av}$  decreases. This implies that for molecules with a high density, it is not reasonable to put all the charges on the surface of that particle.

## 6.5 Results

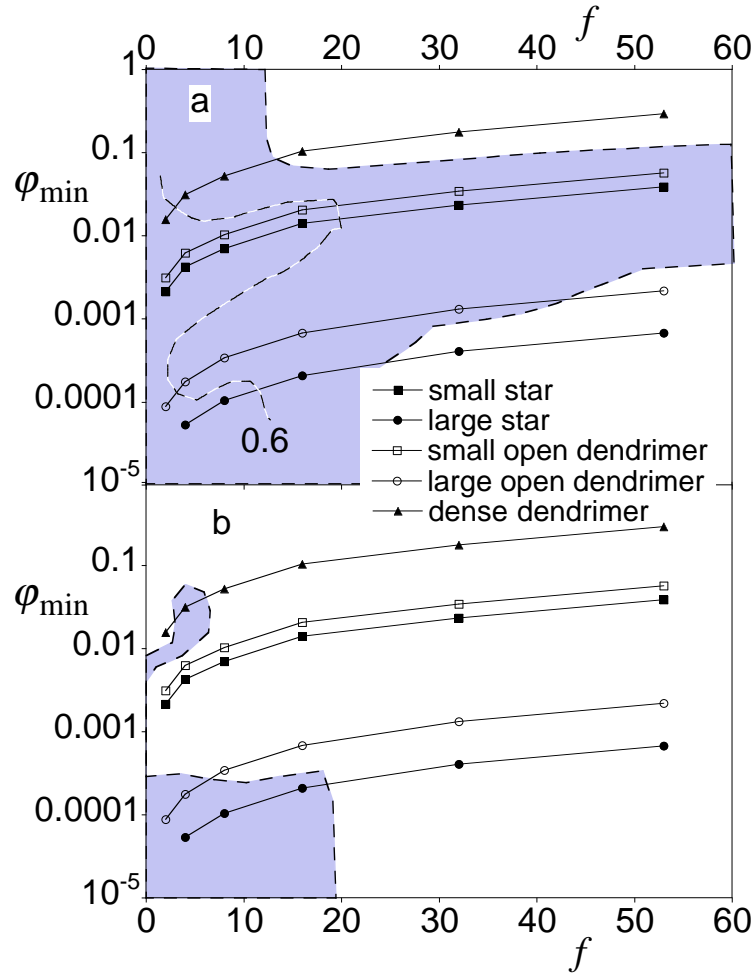


Figure 6.4: Minimal density of the molecules as a function of the number of arms, for different structures as denoted by the symbols in the graph. The size used for the mastercurve is  $R_e$ . The dashed line denotes the relative variance  $\Upsilon \leq 0.3$  and the grey area indicates which structures do not give a reasonable mastercurve. In fig (a) the relative variance is denoted for the Donnan model, the second dashed line denotes  $\Upsilon \leq 0.6$  and in fig (b) for the hard-sphere model.

## Evaluation of the mastercurve procedure

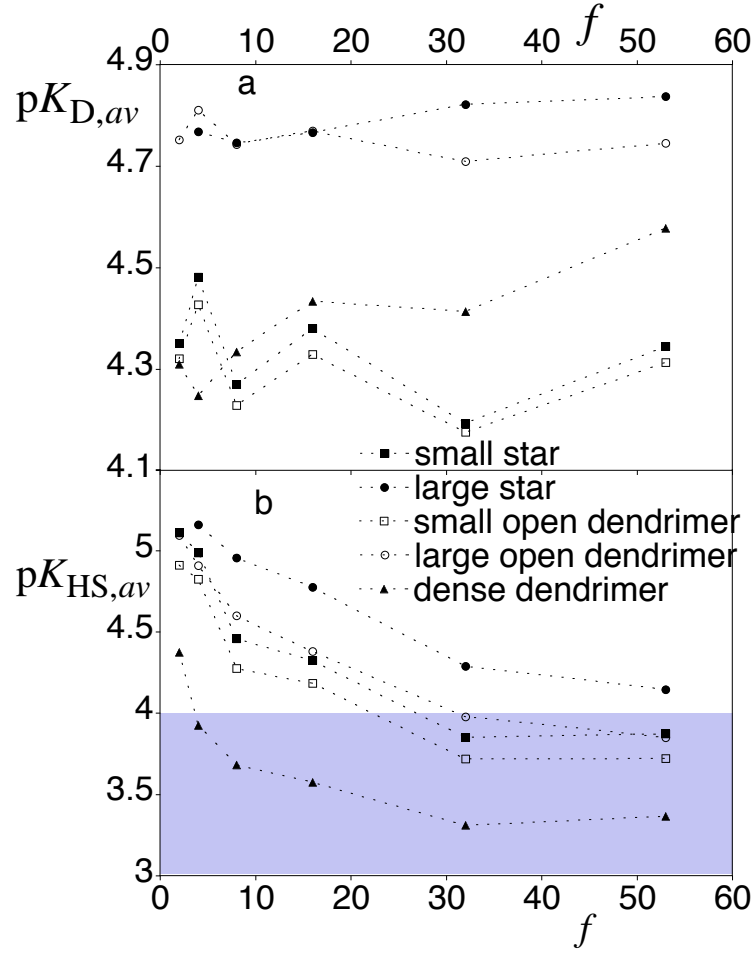


Figure 6.5: The average  $pK_{\text{model},av}$  found for a structure as a function of the number of arms  $f$ , the size used for the mastercurve is  $R_e$ . (a) with the Donnan model and (b) with the hard sphere model. The grey area denotes a too small  $pK_{\text{model},av}$  values.

## 6.5 Results

**Effect of the size** In the above calculations of the mastercurve we used the first moment of the endpoint distribution function as a measure of the size of the molecules. However, in view of the fact that the electrostatic potentials used in the mastercurve procedure are just an approximation of reality, it is possible that a different size parameter gives a better result. Furthermore, in practical application of the mastercurve procedure to humic substances the size is often taken to be indepent of the  $pH$ .<sup>160,166</sup> In general this is an approximation also for humic substances: increasing the  $pH$  and therefore increasing the number of charges will lead to swelling.<sup>165</sup> Indeed the sizes evaluated in the previous paragraph, were  $pH$  dependent. For instance, the size increase,  $R_{e,high\ pH}/R_{e,low\ pH}$  at one salt concentration, varied from 1.12 for the dense star with  $f = 53$  and high salt concentration to 4.36 for the large star with  $f = 16$  at low salt concentration. For the dense dendrimer the increase in size due to a decreasing salt concentration is 1.6 and this increase has the maximal value of 3.6 for the the large star.

In view of the practice with humic substances where often a  $pH$ -independent size is used, we will continue our investigation by neglecting the  $pH$ -effect on the size. The crucial question is what an appropriate choice for this size is, and how it is related to the molecular architecture. Five formulas for the size, specified in table 6.2, will be studied.

Table 6.2: Definition of used sizes

Name	Definition
$R_{small}$	$\kappa^{-1}$
$R_{medium1}$	$R_{filled\ sphere} + \kappa^{-1}$
$R_{medium2}$	$R_{filled\ sphere} * \left[\frac{c_s}{5.5}\right]^{-1/5}$
$R_{max}$	$R_{max}$
$R_{ext}$	$R_{max} + \kappa^{-1}$

$R_{small}$  is taken as independent of the molecular size/mass and it depends solely on the salt concentration through the Debye-length  $\kappa^{-1}$ . The  $R_{medium1}$  and  $R_{medium2}$  do depend on both the molecular mass and the salt concentration. The molecular mass is incorporated through  $R_{filled\ sphere}$  defined as  $(3N/(4\pi))^{-1/3}$ , i.e. a sphere totally filled with all the monomers. The salt concentration is taken into account in two different ways, for  $R_{medium1}$  with the Debye length, for  $R_{medium2}$  a different way is used, justified as follows. In analytical theory the effect of the salt concentration on the size of a polyelectrolyte is taken into account by an effective volume interaction  $v$  which depends on the salt concentration  $v \sim c_s^{-1}$ . This leads to a size which depends on the salt concentration as  $R \sim c_s^{-1/5}$ . For  $R_{medium2}$  we used the highest salt concentration, where  $c_s = 5.5$  mol/L as the starting point, with a size  $R_{filled\ sphere}$ , and calculated from there the sizes for the other salt concentrations.  $R_{max}$  is the maximal extension of the arms and given in table 6.1. We should point out that  $R_{max}$  is not always larger than  $R_{small}$  because the Debye length for 0.55



## Evaluation of the mastercurve procedure

mmol/L is quite large (13 nm) whereas  $R_{\max}$  for the small molecules is 4.5 nm, but for the other salt concentrations  $R_{\text{small}} < R_{\max}$ . The final radius  $R_{\text{ext}}$  is obtained by extending  $R_{\max}$  with the Debye length  $\kappa^{-1}$ .

The results of the mastercurves generated with each of these different sizes as denoted in table 6.2 will now be discussed. The use of  $R_{\text{small}}$  has a devastating effect: in all cases  $\Upsilon > 1$ , i.e. a mastercurve on which the different salt concentrations come together is not found. Moreover, the low salt concentration resulted in an approximately correct  $pK$ -value but for the two higher salt concentrations much too low  $\delta_{pK}$ -values are found.

The mastercurve procedure with  $R_{\text{medium1}}$  does not give a good mastercurve:  $\Upsilon > 0.3$ . The HS-models are worse than the Donnan model. For the small molecules the electrostatic interaction is underestimated for the lowest salt concentration, i.e.  $\delta_{pK} > 0$ . For the largest molecule, the large star, the intermediate salt concentration leads to a negative  $\delta_{pK}$ .

The mastercurves generated with  $R_{\text{medium2}}$  and the Donnan model are reasonable for low number of arms and low densities. Values of  $\Upsilon < 0.3$  and the  $pK_{D,av}$  is between 4.5 and 5 were obtained. The calculated  $pK_{D,av}$  is increasing with increasing  $f$  and higher for the more dense molecules. The HS model does not satisfy the criteria.

The mastercurves generated with  $R_{\max}$ , which is not only independent of the  $pH$  but also of the salt concentration, appear satisfactory for the small star and the dense dendrimer. Both criteria for a good mastercurve for both the Donnan and the HS-model, see figs 6.6 and 6.7, are met. For small  $f$  or low densities the mastercurves are not good, see fig 6.6.

The  $pK$ -values, calculated with  $R_{\max}$  are shown in fig 6.7. In most cases the  $pK$ 's are larger than 5, i.e. the electrostatic interactions are underestimated. However, they all satisfy the criterion of  $-1 < \delta_{pK} < 1$ . In contrast to fig 6.5 the Donnan model now gives positive values of  $\delta_{pK}$ , and  $\delta_{pK}$  increases with the number of arms. For the HS-model the differences in a series of the same structure but different number of arms are small, except for the dense dendrimer. This latter molecule shows a considerable decay in the  $pK$  as a function of  $f$ . Qualitatively, this behaviour is similar to that in fig 6.5, and probably due to the fact that the  $pH$ - and salt dependency of the size for the dense dendrimer is small. This is not the case for the small and the large star.

The mastercurves generated with  $R_{\text{large}}$  do not meet the criterion  $\Upsilon \leq 0.3$ . As was the case for  $R_{\text{medium1}}$ , the shift for the lowest salt concentration is too small.

**Electrostatic potential** For some selected cases which gave a good mastercurve with a reasonable  $pK$ , the SCF-electrostatic potential profile  $\psi(z)$  will be compared to the Donnan potential  $\psi_D$  and to the hard-sphere surface potential  $\psi_s$ . The electrostatic decay from the HS-surface potential is taken as a simple Debye-Hückel decay:

$$\psi(z) = \psi_s \frac{Re^{-\kappa(z-R)}}{z} \quad (6.8)$$

## 6.5 Results

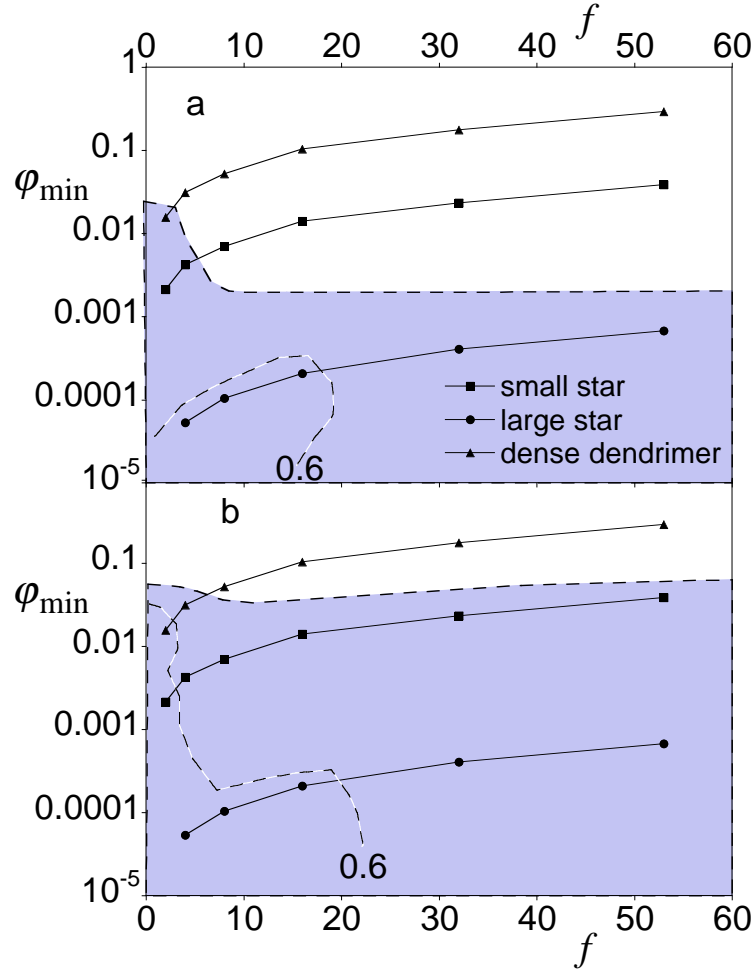


Figure 6.6: Minimal density of the molecules as a function of the number of arms, for different structures as denoted by the symbols in the graph. The size used for the mastercurve is  $R_{\max}$ . The dashed line denotes the relative variance  $\Upsilon \leq 0.3$  as denoted eq 6.6 and the grey area indicates which structures do not give a reasonable mastercurve. In fig (a) the relative variance is denoted for the Donnan model and in fig (b) for the hard-sphere model. The dashed line within the grey area denote  $\Upsilon \leq 0.6$ .

## Evaluation of the mastercurve procedure

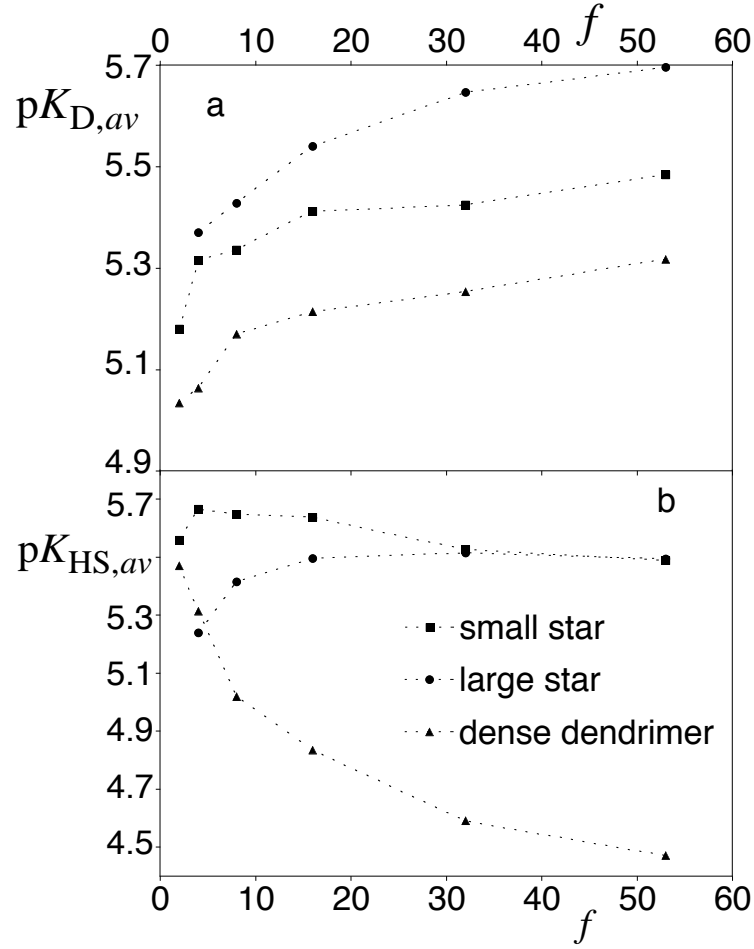


Figure 6.7: The average  $pK_{\text{model},av}$  found for a structure with  $R_{\text{max}}$  taken as the size in the mastercurve procedure as a function of the number of arms  $f$ , (a) with the Donnan model and (b) with the hard sphere model.

## 6.5 Results

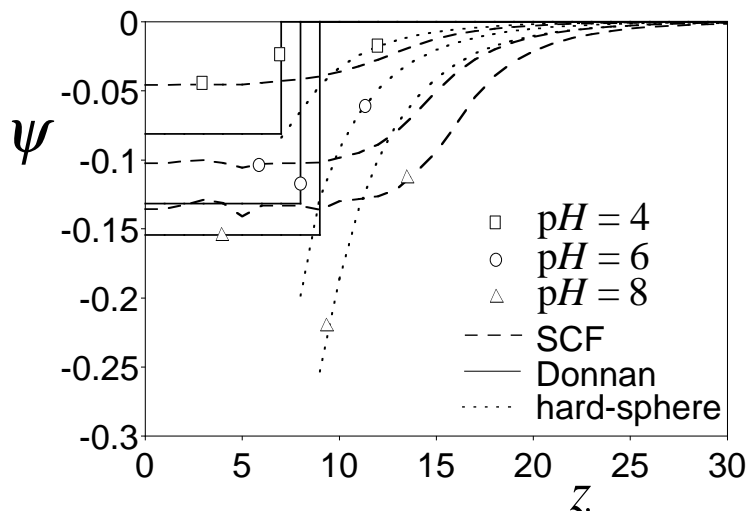


Figure 6.8: Electrostatic potential profile from the numerical calculations compared with the simple electrostatic decay from the Donnan model and from the hard-sphere model and  $R = R_e$ . For the dense dendrimer with  $N = 4288$  at 55 mmol/L and the  $pH$  as denoted in the graph.

First we will show some results obtained with  $R = R_e$ , i.e. the size which depends both on the  $pH$  and on the salt concentration. For the dense dendrimer, see fig 6.8, the SCF-potential profile shows a plateau in the centre, followed by a gradual decrease. Such a gradually decreasing potential is also obtained with the HS-model, but the surface potential is higher than the SCF-potentials. The Donnan model has a step profile, and the Donnan potential is higher than the SCF-potential. Yet, the Donnan potential is lower than the hard-sphere potential. The fact that the Donnan potential is higher than the SCF-potential and lower than the HS-potential corresponds to the  $pK$ -values in fig 6.5. i.e.  $pK_{HS,av} < pK_{D,av} < pK_{int}$ . The Donnan potential is close to the real potential if the  $pH$  is high.

The large star is a large molecule with a low density. This object can be regarded to be the opposite of the dense dendrimer, yet the criteria to obtain a good mastercurve are satisfied for both the Donnan and the hard-sphere model. The potential profiles for the large star are presented in fig 6.9. The SCF electrostatic potential profile for the large star is more complex than that for the dense dendrimer. Close to the centre of the molecule a maximum occurs in the profiles at  $pH$  5 and 8, but most of the profile is characterized by a gradual decrease. For  $pH$  3 the Donnan potential and the surface potential both equal the SCF-potential at the centre of the molecule. For  $pH$  5 and 8 the Donnan model gives awkward results: for  $pH$  8  $\psi_D$  is lower than that for  $pH$  5. This is due to the larger size of the molecule at  $pH$  8. The hard-sphere potential behaves more reasonably and is always an increasing function of the  $pH$ . For most  $pH$ 's the  $\psi_s$  is smaller than the SCF-potential in the centre of the molecule, and the potential decay faster than that of the SCF-potential.

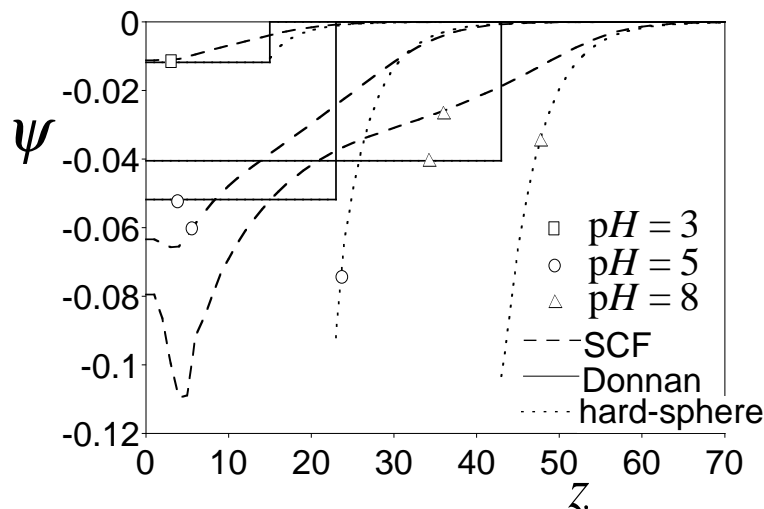


Figure 6.9: Electrostatic potential profile from the numerical calculations compared with the simple electrostatic decay from the Donnan model and from the hard-sphere model and  $R = R_e$ . For the large star with  $N = 4288$  at 55 mmol/L and the pH as denoted in the graph.

This is due to the fact that the surface potential is located at a large distance from the centre.

Also with  $R_{\max}$  reasonable mastercurves have been obtained for the large star. In fig 6.10 the SCF-potentials are compared to those of the two simple electrostatic models when  $R_{\max}$  is used to describe the size of the molecules. Due to the large size the potentials from the simple electrostatic models are now much smaller than the SCF-potential.

Finally, the electrostatic potential profiles of a small star with small number of arms are shown in fig 6.11. The size used for the Donnan and the HS-model is  $R_e$ . In this case, the HS-model gives a good mastercurve and the Donnan model does not. This is obvious from fig 6.11: the Donnan model completely fails to describe the potential. The Donnan potential  $\psi_D$  is far too large for pH 4 and 6, therefore the differences between the different pH's are too small. Moreover, we find  $\psi_{D, \text{pH}=9} < \psi_{D, \text{pH}=6}$ . The HS-potentials give a much better description. Due to the small size of this molecule the potential decay starts at a reasonable distance from the centre. The correspondence between the SCF- and HS-potential profiles indicates that the decay of the potential is determined by the counterions and not by charges of the polyelectrolyte.

## 6.6 Discussion

For the molecular architectures considered in this work, the Donnan model gives a reasonable mastercurve when the density is high or the size of the molecule is large. Furthermore, it gives a good indication about the  $\text{p}K_{\text{int}}$ -value, especially for large molecules. The mastercurve from the HS-model

## 6.6 Discussion

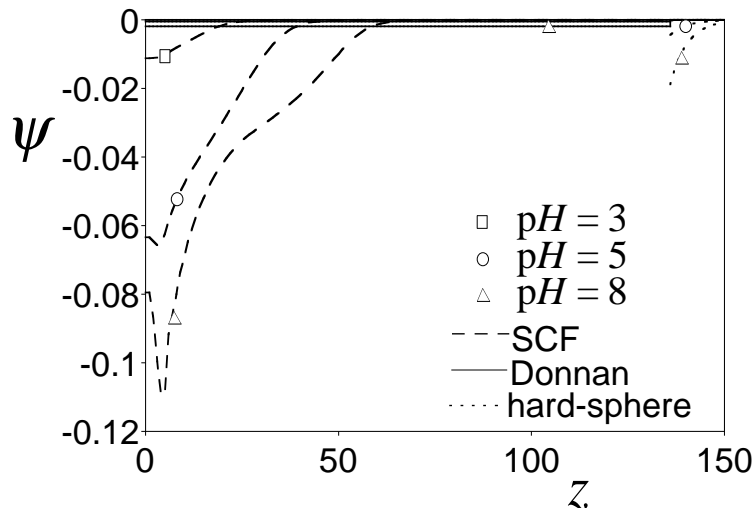


Figure 6.10: Electrostatic potential profile from the numerical calculations compared with the simple electrostatic decay from the Donnan model and from the hard-sphere model. The system is the same as in fig 6.9 only  $R = R_{\max}$  instead of  $R_e$ .

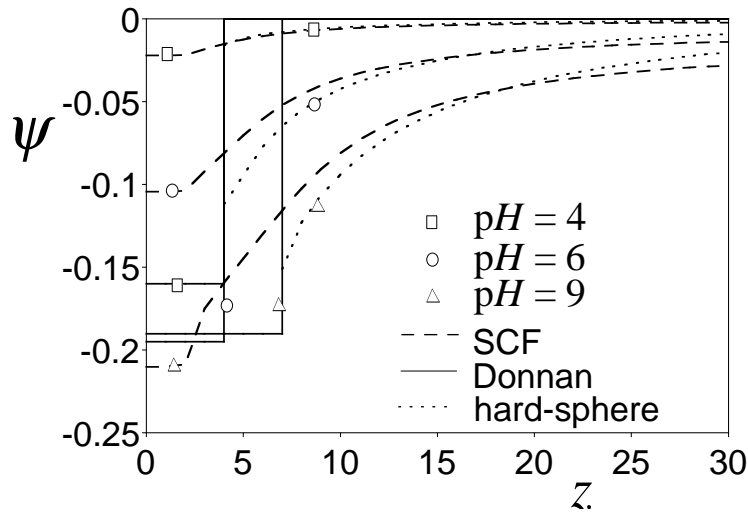


Figure 6.11: Electrostatic potential profile from the numerical calculations compared with the simple electrostatic decay from the Donnan model and from the hard-sphere model and  $R = R_e$ . For the small star with  $f = 4$  at 0.55 mmol/L and the pH as denoted in the graph.

## Evaluation of the mastercurve procedure

is either good or very bad. However, even if the mastercurve is good, this does not mean that the correct  $pK_{\text{int}}$ -value is observed. For molecules with large densities, the obtained  $pK$ -value deviates more from the  $pK_{\text{int}}$  than for molecules with a small density.

The electrostatic potential profile can of course not be fully described by the simple Donnan potential or the HS-potential profile. At best, the models give an indicative value. Dense structures with a high potential can be captured by both the Donnan and the HS-model. Small structures with a low potential are poorly described by the Donnan model but well by the HS-model. Large, open structures give good mastercurves with both the Donnan and HS-model, but the values of  $\psi_D$  or  $\psi_s$  depend much on what kind of measure for the size of the molecules is used. Larger sizes lead to a small electrostatic potential and in general to too large  $pK$ 's, compare figs 6.5 and 6.7.

The average endpoint size  $R_e$  is defined as the first moment over de endpoint profiles, resulting from the SCF calculations. When using  $R_e$ , which depends on the  $pH$  and salt concentration, as a measure of the size of the molecule reasonable mastercurves were obtained for all considered molecular architectures. The other tested measures of the size were independent of  $pH$  and are listed in tabel 6.2. For these size definitions, the mastercurves were always worse. In particular, modelling the effect of salt concentration on the size by using the Debye length  $\kappa^{-1}$  turned out to yield rather poor results.

If sizes are taken to be independent of the  $pH$ , it is better to use the large sizes from table 6.2. A large size can give reasonable mastercurves, but the actual electrostatic potential can be 4 to 10 times bigger than the calculated potential from the hard-sphere or the Donnan model, respectively. The calculated  $pK$  from such an analysis is of course substantially larger than the true  $pK_{\text{int}}$ . The Donnan model gives a reasonable  $pK$ -value whenever the density of the structure is high.

## 6.7 Humic substances

From the previous discussion it follows that one certainly may not assume that the mastercurve procedure works well in all cases. The results depend on the molecular architecture which is titrated. In this paragraph we discuss the implications of this conclusion for titrations of humic substances. The questions are whether one may expect the mastercurve procedure to work for humic substances and how accurate the results will be. In order to be able to answer these questions the density of the humic substances and their size have to be analysed. Our above analysis has shown that the best chances for success are obtained when a radius is chosen close to the hydrodynamic radius and a dense structure can be assumed. Let us first discuss the density.

**Density of humic substances** The molecules in table 6.1 and the results in figs 6.4 and 6.6 are shown as a function of  $\varphi_{\text{min}}$ , the minimum volume

## 6.7 Humic substances

fraction, as defined by eq 6.3. This volume fraction can be converted to a density in kg/L by assigning a mass to a polymer volume. If it is assumed that the model polyelectrolytes consist mainly of carbon and oxygen an estimate can be made of the densities. The volume of an oxygen or of a CH<sub>2</sub>-group is about (0.3 nm)<sup>3</sup>.<sup>142</sup> Furthermore, if carbon and oxygen are equally available then the average density of such a dry polyelectrolyte is in the order of  $\frac{1}{2}(16 + 14)10^{-3}/(N_{\text{Av}}(0.3 \cdot 10^{-8})^3)$  kg/L  $\approx 1$  kg/L. Hence, the densities denoted as volume fraction in table 6.1 may also be interpreted as densities in kg/L. This is only because the dry density of the polymer is  $\approx 1$  kg/L, but in general the conversion from volume fractions to wet densities is given by

$$\rho_{\text{wet}} = \varphi \rho_{\text{dry}}$$

A dry density of 1 kg/L for the polyelectrolyte is small compared to the range of 1.4–1.7 kg/L for dry humic acids which has been commonly used in literature.<sup>165,166</sup> Therefore, it may be better to multiply the volume fraction as denoted in table 6.1 with 1.6 kg/L to be able to compare the calculated results with wet densities of humic substances. The wet densities found for humic substances in literature range between 0.013 and 1.16 for fulvic acids and 0.11 to 1.16 kg/L for humic acids.<sup>165,166,169</sup> From the model molecules, the small star, the small open dendrimer and the dense dendrimer have comparable densities, especially the dense dendrimer.

This means that if a size is used which depends on the pH and salt concentration, the HS-model is expected to give a good mastercurve but the present results suggest that for large densities the p*K* obtained from the HS-model will be much too low. The Donnan model will give good results for very high densities, with respect to both the mastercurve and the p*K*-value. For the less dense ( $\varphi_{\text{min}} < 0.07$  or  $\rho_{\text{wet}} < 0.1$  kg/L) and small molecules, it will be hard to find a mastercurve that has physical reality.

On the other hand, if a size comparable to  $R_{\text{max}}$  is used for the fulvic and humic acids both the Donnan and the HS-model are appropriate. However, the calculated p*K*'s will be larger than the intrinsic p*K*, i.e.  $\delta_{\text{p}K} > 1$ .

**Size of humic substances** When trying to map the results of the mastercurves obtained from the calculations to humic acids not only the density is a parameter but also the size, see for instance the results of the Donnan model in fig 6.4a. A good mastercurve is consistently obtained for high densities and sometimes for low densities, namely in the case of large sizes. Furthermore, we have seen that the quality of the results of the mastercurve depends on the size used. Therefore, we will analyse which sizes are found for humic substances in literature, and what the effect of salt concentration and pH is on the size.

In humic acid literature, a lot of sizes can be found for humic acid molecules. Partly, this may be due to the large polydispersity of humic substances. Due to the polydispersity, different averages are measured with different techniques. For instance, dynamic light scattering (DLS) is very sensitive to the presence



## Evaluation of the mastercurve procedure

of large particles (because the scattering intensity scales as  $\sim R^6$ ). This means that always large sizes for humic acids are found.<sup>170</sup> Viscosimetry measures the volume fraction, but is insensitive to the particle size.

In practice, we have to distinguish between the small sized humic acids (in the order of 1 nm)<sup>171–173</sup> and the larger ones (in the order of 300 nm).<sup>174</sup> Most probably, the larger ones are aggregates of the smaller ones.<sup>175</sup> The “primary particles” are generally 1–2 nm in radius, and the aggregates about 300 nm.<sup>175</sup> Different techniques have been used by Lead et al.<sup>171</sup> to measure the size of a fulvic acid. The radius, calculated from the diffusion coefficient with the Stokes–Einstein relationship for spherical particles, was in the order of 0.7–1 nm. Using membranes, the diffusion coefficient was measured by Cornel et al.<sup>172</sup> and Wang et al.<sup>173</sup> Cornel et al.<sup>172</sup> first fractionated the samples and found a diffusivity of  $1 \cdot 10^{-9} \text{ m}^2/\text{s}$  for the sample with the lowest molecular mass and  $2.5 \cdot 10^{-10} \text{ m}^2/\text{s}$  for the sample with the highest molecular mass. These diffusivities together with the (too simple) Stokes–Einstein relation for spheres lead to radii of 0.75 nm and 2.2 nm, respectively. The diffusion constants found by Wang et al.<sup>173</sup> were between 2 and  $5 \cdot 10^{-10} \text{ m}^2/\text{s}$ , and gave radii between 0.4 and 1 nm. However, also intermediate sizes and extremely large sizes have been measured. Pinheiro et al.<sup>176,177</sup> measured sizes which were about 50 nm. Ren et al.<sup>170</sup> also measured sizes with DLS in the order of 40–95 nm. Senesi and co-workers<sup>178,179</sup> analysed the fractal dimension of humics as a function of time, pH, and salt concentration. The average size they obtained was 3–80  $\mu\text{m}$ , which is very large compared to the values mentioned by other authors.

For comparison of the results derived from the SCF-model with humic substances, we should discuss only the primary humic acid particles, because these primary particles do not disaggregate upon increasing the charge. This means that the sizes are most likely in the order of 1–10 nm. The sizes  $R_e$  resulting from the SCF calculations ranged from 3.6 to 18.4 nm for the large star, from 1.0 to 2.0 nm for the small star, and from 1.4 to 3.0 nm for the dense dendrimer. The  $R_{\text{max}}$  is denoted in table 6.1. This means that the sizes of the dense dendrimer and the small star can be compared with the sizes of the primary humic acid particles.

**Size and salt concentration** The effect of the salt concentration on the size of polyelectrolytes has been analysed using analytical theories in several articles. For various different shapes of molecules, i.e. stars,<sup>34,35,55,180</sup> random polyelectrolytes,<sup>36</sup> and dendrimers<sup>181</sup> the result is always that  $R \sim I^{-1/5}$ . On the basis of these ideas some literature results about the size of humic acid as function of the size and/or the pH will be analysed.

When the mastercurve procedure is applied assuming a Donnan model, a Donnan volume at different salt concentrations is needed. Often the following empirical relation is used<sup>161,166,182</sup>

$$\log V_D = b(1 - \log I) - 1 \quad (6.9)$$

## 6.7 Humic substances

in which  $V_D$  is the Donnan volume,  $I$  the ionic strength, and  $b$  an adjustable parameter. For the purpose of comparison with the scaling results discussed above, this equation can be rewritten as  $R \sim I^{-b/3}$ . From the analytical polyelectrolyte theory a value of  $-1/5$  was predicted for this exponent, which implies  $b = 3/5$  for the  $b$  in eq 6.9.

The “standard”  $b$ -values used in the NICA-Donnan model to describe the swelling of the humic acid and fulvic acid as a function of the salt concentration are 0.49 and 0.57, respectively.<sup>161</sup> These results are based on an investigation of over 20 fulvic acids and 20 humic acids. Christl and Kretschmar<sup>182</sup> have analysed several fractions of a humic acid using eq 6.9. They found  $b$ -values ranging from 0.3 till 0.6. The lower values are for the higher molecular mass molecules. Both the results of Milne et al.<sup>161</sup> and Christl and Kretschmar<sup>182</sup> show that the adjusted Donnan volumes of the larger molecular mass molecules depend less on the salt concentration than the smaller molecular mass molecules. This may be due to a hydrophobic core of the large molecules. This core does not have charges and therefore does not respond to changes in the salt concentration. Comparing these results with the scaling arguments it means that in general the fulvic acids behave more like simple polyelectrolytes than the humic acids.

The before mentioned  $b$ -values can be compared reasonably well to the scaling predictions. However also larger  $b$ -values have been reported. Christensen et al.<sup>183</sup> reported of  $b$ -values of 0.8 to 0.9 for four fulvic acids. Ren et al.<sup>170</sup> measured that with increasing salt concentration the size decreases as a power law with an exponent of  $-0.23$ , i.e. a  $b$ -value of  $3 \cdot 0.23 = 0.7$ , which is large. The exponent is based on only three points, the first decrease is smaller, but the decrease from 0.05 to 0.1 mol/L is larger. A larger decrease can be due to the effect that increasing salt concentration can also change the solvent quality, i.e. salting-out effect.

A very systematic study of the size of humic acids as a function of the salt concentration and  $pH$  was performed by Avena et al.<sup>165</sup> who used viscosimetry. For low  $pH$  ( $pH$  3 or 4) the salt concentration has hardly any influence. This may indicate that

- some humic acid molecules aggregate and form flocs
- the humic acids are hardly charged

For  $pH$ 's, 7 and 10 or 11, the decrease of the size with increasing salt concentration is always lower than that predicted by the analytical theory. The experimental range of  $\tau$  in the dependency of  $R \sim I^{-\tau}$  is 0.03-0.15 and the predicted decrease was  $1/5$ , i.e. 0.2. For two out of the nine humic acid samples\* at  $pH$  11 the decrease between 0.001 and 0.01 mol/L was lower than the decrease between 0.01 and 0.1 mol/L, this can be due to an osmotic effect in the humic acid.

The effect of  $pH$  measured by Avena et al.<sup>165</sup> was always an increase in size with increasing  $pH$ . For the salt dominance regime, i.e. where the relation  $R \sim$

---

\*The two samples were the Kinbosan F humic acid and the Kinbosan OH humic acid. These were obtained from Y.-H. Yang.<sup>184</sup>

## Evaluation of the mastercurve procedure

$c_s^{-1/5}$  holds, the size scales as  $\alpha_b^{2/5}$ , see eq 3.23. At smaller salt concentrations the relations are more complex, around the  $pK$ -value  $R \sim \frac{\alpha_b}{1-\alpha_b}$  and when  $pH \gg pK$  then  $R \sim \alpha_b^{1/2}$ , see eq 3.19. These relations seem simple but they can not be straight forwardly compared to humic acid because the intrinsic  $pK$  is not known, and therefore  $\alpha_b$  is not known. To be able to do this, intrinsic  $pK$ 's and the amount of sites per group of  $pK$ 's have to be chosen. This is too arbitrary and therefore it is concluded that the effect of  $pH$  on the size of humics cannot be compared to the results of analytical theory.

# Appendix A

## Dependence of a reaction constant on the discretisation

The reaction constant  $K$  used in the SCF-calculation is dimensionless. So in principle it should not depend on the lattice, and in particular not on the thickness of the layers. For systems with only uncharged species it is indeed independent. For systems with charges, this is not the case because the thickness of the layer is determining the electrical capacitance of a layer, and with that the electrostatic potential decay.

Let us take the simple reaction of the dissociation of water:



The dissociation constant  $K_w$ , used in practice is  $10^{-14} \text{ mol}^2\text{L}^{-2}$  at room temperature and defined as

$$K_w \equiv [H_3O^+][OH^-] = 10^{-14} \text{ mol}^2\text{L}^{-2} \quad (A.2)$$

where the square brackets denote the concentration in solution. In order to make  $K_w$  dimensionless, it has to be divided by the concentration of water squared,  $[H_2O]^2$ . The concentration of water in water is  $55 \text{ mol L}^{-1}$ , the value of the dissociation constant then becomes  $3.3 \cdot 10^{-18}$ . This value is correct if one uses a lattice based on the size of water, i.e. for a cubical lattice with the distance between two layers is 0.3 nm:

$$\begin{aligned} 55 \text{ mol/L} &= 55 * N_{av} * 10^3 \text{ molecules/m}^3 \\ &= 33 \text{ molecules/nm}^3 \\ a &= \sqrt[3]{\frac{1}{33}} \text{ nm} = 0.3 \text{ nm} \end{aligned}$$

The conversion factor  $A$  in eq 3.38 is in this case  $55 \text{ mol/L}$ .

But instead of taking the distance between two layers equal to 0.3 nm, another value can be taken, for instance, the Bjerrum length or the Kuhn length of the polymer studied. In this case the dissociation constant should

## Dependence of a reaction constant on the discretisation

be normalized differently. The general idea is that the number of charges per volume should remain the same, because the Debye screening length should be indifferent to the distance between two layers. But due to different distances between the layers the number of solvent molecules in a liter changes and therefore the  $K_w$  (actually any reaction constant which includes the solvent molecules in the reaction).

As an example we calculate the dissociation constant of water if the lattice size is take to be the Bjerrum length  $l_B$ . The number of solvent molecules per liter decreases with a factor of  $\left(\frac{l_B}{0.3\text{ nm}}\right)^3$ , with  $l_B$  in nm, so instead of 55 mol/L, there are  $55/\left(\frac{l_B}{0.3\text{ nm}}\right)^3$  mol solvent molecules per liter. The dissociation constant for water becomes then:

$$K_w = \frac{10^{-14}}{\left(55/\left(\frac{l_B}{0.3\text{ nm}}\right)^3\right)^2} \quad (\text{A.3a})$$

$$= \frac{10^{-14} \left(\frac{l_B}{0.3\text{ nm}}\right)^6}{55^2} \quad (\text{A.3b})$$

So the conversion factor  $A$  from volume fractions to mol/L is in this case  $55/\left(\frac{l_B}{0.3\text{ nm}}\right)^3$  mol/L.

# Appendix B

## The calculation of the charge distribution fraction

The distribution function for the number  $n$  of dissociated segments in one branch is calculated by employing a modified propagator to the field given by the SCF solution. The end-segment weighting factor in eq 3.29 is split up according to the number of dissociated segments in the chain

$$G_n(z, s|1) = \alpha_{b,k=0}(s)G_{k=0}(z, s)\langle G_n(z, s+1|1) \rangle \quad (\text{B.1a})$$

$$G_{n+1}(z, s|1) = \alpha_{b,k=-}(s)G_{k=-}(z, s)\langle G_n(z, s+1|1) \rangle \quad (\text{B.1b})$$

where the subscript  $k = 0$  denotes the neutral state of the segment and  $k = -$  the charged state. The starting conditions of the new propagator read

$$G_0(z, 1|1) = \alpha_{b,k=0}(1)G_{k=0}(z, 1) \quad (\text{B.2a})$$

$$G_1(z, 1|1) = \alpha_{b,k=-}(1)G_{k=-}(z, 1) \quad (\text{B.2b})$$

To check if the above given equations are calculated in the right way, the following equation must be true. The sum over all possible number of dissociated segments yields the total end-segment weighting factor:

$$\sum_n G_n(z, s|1) = G(z, s|1) \quad (\text{B.3})$$

The distribution function  $J(n)$  for the number  $n$  of dissociated segments can now be computed as:

$$J(n) = \frac{\sum_z G_n(z, N|1)}{\sum_z G(z, N|1)} \quad (\text{B.4})$$

# Bibliography

1. A. Piccolo. The supramolecular structure of humic substances. *Soil Sci.*, 166:810–832, 2001.
2. C. E. Clapp and M. H. B. Hayes. Sizes and shapes of humic substances. *Soil Sci.*, 164:777–789, 1999.
3. R. L. Wershaw. Molecular aggregation of humic substances. *Soil Sci.*, 164:803–813, 1999.
4. E Tombácz. Colloidal properties of humic acids and spontaneous changes of their colloidal state under variable solution conditions. *Soil Sci.*, 164: 814–824, 1999.
5. J. Lyklema. *Fundamentals of interface and colloid science, Fundamentals*, volume I. Academic Press, London, 1991.
6. J. Skolnick and M. Fixman. Electrostatic persistence length of a wormlike polyelectrolyte. *Macromolecules*, 10:944–948, 1977.
7. T. Odijk. Polyelectrolytes near the rod limit. *J. Polm. Sci, Polym. Phys. Ed.*, 14:477–483, 1977.
8. F. Oosawa. *Polyelectrolytes*. Marcel Dekker Inc. New York, 1971.
9. D. F. Hodgson and E. J. Amis. Polyelectrolyte dynamics. In M. Hara, editor, *Polyelectrolytes, science and technology*, chapter 3. Marcel Dekker Inc. New York, 1993.
10. E. B. Zhulina, T. M. Birshtein, and O. V. Borisov. Theory of ionizable polymer brushes. *Macromolecules*, 28:1491–1499, 1995.
11. E. B. Zhulina and O. V. Borisov. Structure and interaction of weakly charged polyelectrolyte brushes: Self-consistent-field theory. *J. Chem. Phys.*, 107:5952–5967, 1997.
12. R. R. Netz and D. Andelman. Neutral and charged polymers at interfaces. *to be published in Physical Reports*, pages 1–132, 2003.

## BIBLIOGRAPHY

13. J. M. H. M. Scheutjens and G. J. Fleer. Statistical theory of the adsorption of interacting chain molecules. I. Partition function, segment density distribution and adsorption isotherms. *J. Phys. Chem.*, 83:1619–1635, 1979.
14. S. F. Edwards. The statistical mechanics of polymers with excluded volume. *Proc. Phys. Soc.*, 85:613–624, 1965.
15. E. Helfand and Y. Tagami. Theory of the interface between immiscible polymers. II. *J. Chem. Phys.*, 56:3592–3601, 1972.
16. G. J. Fleer, M. A. Cohen Stuart, J. M. H. M. Scheutjens, T. Cosgrove, and B. Vincent. *Polymers at Interfaces*. Chapman & Hall, London, UK, 1993.
17. J. van Male. `sfbox`, 2001. A Computer Program.
18. J.-L. Barrat and J.-F. Joanny. Theory of polyelectrolyte solutions. In I. Prigogine and S.A. Rice, editors, *Polymeric systems*, Advances in Chemical Physics, pages 1–66. John Wiley, New York, USA, 94th edition, 1996.
19. D. H. Napper. *Polymeric Stabilization of Colloidal Dispersions*. Academic Press, London, UK, 1985.
20. J. F. Marko and Y. Rabin. Microphase separation of charged diblock copolymers - melts and solutions. *Macromolecules*, 25:1503–1509, 1992.
21. J. Wittmer and J.-F. Joanny. Charged diblock copolymers at interfaces. *Macromolecules*, 26:2691–2697, 1993.
22. P. Guenoun, S. Lipsky, J. W. Mays, and Tirrel M. Fluorescence study of hydrophobically modified polyelectrolytes in aqueous solution: Effect of micellization. *Langmuir*, 12:1425–1427, 1996.
23. P. Guenoun, M. Delsanti, D. Gazeau, J.W. Mays, D.C. Cook, M. Tirrell, and L. Auvray. Structural properties of charged diblock copolymer solutions. *Eur. Phys. J. B*, 1:77–86, 1998.
24. P. Guenoun, H. T. Davis, M. Tirrell, and J. W. Mays. Aqueous micellar solutions of hydrophobically modified polyelectrolytes. *Macromolecules*, 29:3965–3969, 1996.
25. M. H. B. Hayes, P. MacCarthy, R. L. Malcolm, and R. S. Swift, editors. *Humic Substances II, in search of structure*. Wiley Interscience, Chichester, UK, 1989.
26. G. S. Manning. Limiting laws and counterion condensation in polyelectrolyte solutions I, II, and III. *J. Chem. Phys.*, 51:924–933, 934–938, 3249–3252, 1969.



## BIBLIOGRAPHY

27. P. Pfeuty. Conformation of ordered polyelectrolytes insolution of polyelectrolytes. *J. Phys. (France)*, 39:149–160, 1978.
28. A. R. Khokhlov and K. A. Khachaturian. On the theory of weakly charged polyelectrolytes. *Polymer*, 23:1742–1750, 1982.
29. A. V. Dobrynin, R. H. Colby, and M. Rubinstein. Scaling theory of polyelectrolyte solutions. *Macromolecules*, 28:1859–1871, 1995.
30. M. Daoud. Self similarity in polyelectrolyte solution. preprint, 2002.
31. M. J. Stevens and K. Kremer. Structure of salt-free linear polyelectrolytes. *Phys. Rev. Lett.*, 71:2228–2231, 1993.
32. M. J. Stevens and K. Kremer. Form-factor of salt-free linear polyelectrolytes. *Macromolecules*, 26:4717–4719, 1993.
33. M. J. Stevens and K. Kremer. The nature of flexible linear polyelectrolytes in salt-free solution - a molecular-dynamics study. *J. Chem. Phys.*, 103:1669–1690, 1995.
34. O. V. Borisov. The conformation of star-branched polyelectrolytes. *J. Phys. II*, 6:1–19, 1996.
35. O. V. Borisov and E. B. Zhulina. The effects of ionic strength and charge annealing on the conformation of star-branched polyelectrolytes. *Eur. Phys. J. B*, 4:205–217, 1998.
36. O. V. Borisov and M. Daoud. Scaling theory of branched polyelectrolytes. *Macromolecules*, 34:8286–8293, 2001.
37. J. M. Ziman. *Models of Disorder*. Cambridge University Press, Cambridge, UK, 1979.
38. E. Yu. Kramarenko, A. R. Khokhlov, and K. Yoshikawa. Collapse of polyelectrolyte macromolecules revisited. *Macromolecules*, 30:3383–3388, 1997.
39. M. Daoud and J. P. Cotton. Star-shaped polymers: a model for the conformation and its concentration dependence. *J. Phys. (France)*, 43:531–538, 1982.
40. E. B. Zhulina. Phase diagram for semirigid macromolecules grafted to solid spherical surfaces. *Polymer Sci. USSR A*, 26:794–798, 1984. Vysokomol. Soedin., Ser. A.
41. T. M. Birshtein and E. B. Zhulina. Conformations of star-branched macromolecules. *Polymer*, 25:1453–1461, 1984.

## BIBLIOGRAPHY

42. T. M. Birshtein, E. B. Zhulina, and O. V. Borisov. Temperature-concentration diagram for a solution of star-branched macromolecules. *Polymer*, 27:1078–1086, 1986.
43. R. Israëls, F. A. M. Leermakers, and G. J. Fleer. On the theory of grafted weak polyacids. *Macromolecules*, 27:3087–3093, 1994.
44. S. Alexander, P. M. Chaikin, P. Grant, G. J. Morales, P. Pincus, and D. Hone. Charge renormalisation, osmotic pressure, and bulk modulus of colloidal crystals: theory. *J. Chem. Phys.*, 80:5776–5781, 1984.
45. P. Pincus. Colloid stabilization with grafted polyelectrolytes. *Macromolecules*, 24:2912–2919, 1991.
46. R. S. Ross and P. Pincus. The polyelectrolyte brush - poor solvent. *Macromolecules*, 25:2177–2183, 1992.
47. E. B. Zhulina, O. V. Borisov, and T. M. Birshtein. Structure of grafted polyelectrolyte layer. *J. Phys. II*, 2:63–74, 1992.
48. C. M. Wijmans and E. B. Zhulina. Polymer brushes at curved surfaces. *Macromolecules*, 26:7214–7224, 1993.
49. P.-G. de Gennes. *Scaling Concepts in Polymer Physics*. Cornell University Press, Ithaca, USA, 1979.
50. J. W. Mays. Synthesis of model branched polyelectrolytes. *Polymer Comm.*, 31:170–172, 1990.
51. W. Kördel, M. Dassenakis, J. Lintelmann, and S. Padberg. The importance of natural organic material for environmental processes in waters and soils. *Pure Appl. Chem.*, 69:1571–1600, 1997.
52. V. P. Torchilin. Structure and design of polymeric surfactant-based drug delivery systems. *J. Contr. Release*, 73:137–172, 2001.
53. H. Ohshima. On the general expression for the electrophoretic mobility of a soft particle. *J. Colloid Interface Sci.*, 228:190–193, 2000.
54. M. Heinrich, M. Rawiso, J. G. Zilliox, P. Lesieur, and J. P. Simon. Small angle X-ray scattering from salt free solutions of star branched polyelectrolytes. *Eur. Phys. J. E*, 4:131–142, 2001.
55. 2003. This thesis, chapter 2.
56. D. Kiserow, K. Prochazka, C. Ramireddy, Z. Tuzar, P. Munk, and S. E. Webber. Fluorometric and quasi-elastic light-scattering study of the solubilization of nonpolar low-molar mass compounds into water-soluble block-copolymer micelles. *Macromolecules*, 25:461–469, 1992.

## BIBLIOGRAPHY

57. K. Khougaz, I. Astafieva, and A. Eisenberg. Micellization in block polyelectrolyte solutions .3. Static light-scattering characterization. *Macromolecules*, 28:7135–7147, 1995.
58. P. Guenoun, F. Muller, M. Delsanti, L. Auvray, Y. J. Chen, J. W. Mays, and M. Tirrell. Rodlike behavior of polyelectrolyte brushes. *Phys. Rev. Lett.*, 81:3872–3875, 1998.
59. S. Förster, N. Hemsdorf, W. Leube, H. Schnablegger, M. Regenbrecht, S. Akari, P. Lindner, and C. Böttcher. Fusion of charged block copolymer micelles into toroid networks. *J. Phys. Chem. B*, 103:6657–6668, 1999.
60. F. Muller, M. Delsanti, L. Auvray, J. Yang, Y. J. Chen, J. W. Mays, B. Demé, M. Tirrell, and P. Guenoun. Ordering of urchin-like charged copolymer micelles: Electrostatic packing and polyelectrolyte correlations. *Eur. Phys. J. E*, 3:45–53, 2000.
61. W. Groenewegen, S. U. Egelhaaf, A. Lapp, and J. R. C. van der Maarel. Neutron scattering estimates of the effect of charge on the micelle structure in aqueous polyelectrolyte diblock copolymer solutions. *Macromolecules*, 33:3283–3293, 2000.
62. W. Groenewegen, A. Lapp, S. U. Egelhaaf, and J. R. C. van der Maarel. Counterion distribution in the coronal layer of polyelectrolyte diblock copolymer micelles. *Macromolecules*, 33:4080–4086, 2000.
63. P. W. Atkins. *Physical chemistry*. Oxford University, Oxford, UK, sixth edition, 1998.
64. E. P. K. Currie, A. B. Sieval, G. J. Fleer, and M. A. Cohen Stuart. Polyacrylic acid brushes: surface pressure and salt-induced swelling. *Langmuir*, 16:8324–8333, 2000.
65. Yu. V. Lyatskaya, F. A. M. Leermakers, G. J. Fleer, E. B. Zhulina, and T. M. Birshtein. Analytical self-consistent-field model of weak polyacid brushes. *Macromolecules*, 28:3562–3569, 1995.
66. E. B. Zhulina and O. V. Borisov. Polyelectrolytes grafted to curved surfaces. *Macromolecules*, 29:2618–2626, 1996.
67. J. van Male. *Self-consistent-field theory for chain molecules: extensions, computational aspects, and applications*. PhD thesis, Wageningen University, Wageningen, the Netherlands, 2003.
68. J. S. Higgins and H. C. Benoît. *Polymers and Neutron Scattering*, volume 8 of *Oxford Series on Neutron Scattering in Condensed Matter*. Oxford University Press, Inc, Oxford, UK, 1994.

## BIBLIOGRAPHY

69. W. H. Press, S. A. Teukolsky, W. T. Vetterling, and B. P. Flannery. *Numerical Recipes in C, the art of scientific computing*. Cambridge University Press, Cambridge, UK, second edition, 1992.
70. E. B. Zhulina, J. Klein Wolterink, and O. V. Borisov. Screening effects in a polyelectrolyte brush: Self-consistent-field theory. *Macromolecules*, 33: 4945–4953, 2000.
71. O. V. Borisov, F. A. M. Leermakers, G. J. Fleer, and E. B. Zhulina. Polyelectrolytes tethered to a similarly charged surface. *J. Chem. Phys.*, 114:7700–7712, 2001.
72. X. Guo and M. Ballauff. Spherical polyelectrolytes: A comparison between annealed and quenched brushes. *Phys. Rev. E*, 64:015406, 2001.
73. X. Guo. *Synthesis and Study of the Colloidal Polyelectrolyte Brushes prepared by Photo-emulsion Polymerization*. PhD thesis, University of Karlsruhe, Karlsruhe, Germany, 2001.
74. H. A. van der Schee and J. Lyklema. A lattice theory of polyelectrolyte adsorption. *J. Phys. Chem.*, 88:6661–6667, 1984.
75. I. Borukhov, D. Andelman, and H. Orland. Polyelectrolyte solutions between charged surfaces. *Europhys. Lett.*, 6:499–504, 1995.
76. I. Borukhov, D. Andelman, and H. Orland. Scaling laws of polyelectrolyte adsorption. *Macromolecules*, 31:1665–1671, 1998.
77. M. Muthukumar. Adsorption of a polyelectrolyte chain to a charged surface. *J. Chem. Phys.*, 86:7230–7235, 1987.
78. C.Y. Kong and M. Muthukumar. Monte Carlo study of adsorption of a polyelectrolyte onto charged surfaces. *J. Chem. Phys.*, 109:1522–1527, 1998.
79. M. A. G. Dahlgren, A. Waltermo, E. Blomberg, P. M. Claesson, L. Sjöström, T. Åkesson, and B. Jonsson. Salt effects on the interaction between adsorbed cationic polyelectrolyte layers – theory and experiment. *J. Phys. Chem.*, 97:11769–11775, 1993.
80. D. Andelman and J.-F. Joanny. Polyelectrolyte adsorption. *Compt. Rend. l'Académie SciIV*, 1:1153–1162, 2000.
81. I. Borukhov, D. Andelman, and H. Orland. Effect of polyelectrolyte adsorption on intercolloidal forces. *J. Phys. Chem. B*, 103:5042–5057, 1999.
82. G. Busca. Infrared studies of the reactive adsorption of organic molecules over metal oxides and of the mechanisms of their heterogeneously-catalyzed oxidation. *Catalysis Today*, 27:457–496, 1996.

## BIBLIOGRAPHY

83. M. J. Avena and L. K. Koopal. Desorption of humic acid from iron oxide surface. *Environmental Sci. Tech.*, 32:2572–2577, 1998.
84. G. E. Brown. Spectroscopic studies of chemisorption reaction mechanisms at oxide-water interfaces. *Rev. Mineral.*, 23:309–363, 1990.
85. G. W. Bryan and W. J. Langston. Bioavailability, accumulation and effects of heavy metals in sediments with special reference to United Kingdom estuaries: a review. *Environ. Pollut.*, 76:89–131, 1992.
86. L. S. Johansson. Static SIMS studies of coated TiO<sub>2</sub> pigments. *Surf. Interface Anal.*, 20:304–309, 1993.
87. I. Langmuir. . *J. Am. Chem. Soc.*, 40:1361, 1918.
88. T. Hiemstra, W. H. van Riemsdijk, and G. H. Bolt. Multisite proton adsorption modelin at the solid/solution interface of (hydr)oxides: A new approach. *J. Colloid Interface Sci.*, 133:91–104 and 488–508, 1989. 179:488–508, 1996; 184:680–692, 1996.
89. M. Borkovec. Origin of 1-pK and 2-pK models for ionizable water-solid interfaces. *Langmuir*, 13:2608–2613, 1997.
90. M. R. Böhmer, O. A. Evers, and J. M. H. M. Scheutjens. Weak polyelectrolytes between two surfaces: adsorption and stabilization. *Macromolecules*, 23:2288–2301, 1990.
91. A. W. P. Vermeer, F. A. M. Leermakers, and L. K. Koopal. Adsorption of weak polyelectrolytes on surfaces with a variable charge. self-consistent-field calculations. *Langmuir*, 13:4413–4421, 1993.
92. F. A. M. Leermakers, J. M. P. van den Oever, and E. B. Zhulina. On the charge overcompensation of quenched polyelectrolyte stars electrostaticly adsorbed onto a quenched oppositely charged planar surface. *J. Chem. Phys.*, 118:969–980, 2003.
93. H. G. M. van de Steeg, M. A. Cohen Stuart, A. de Keizer, and B. H. Bijsterbosch. Polyelectrolyte adsorption: A subtle balance of forces. *Langmuir*, 8:2538–2546, 1992.
94. V. Shubin and P. Linse. Self-consistent-field modeling of polyelectrolyte adsorption on charge-regulating surfaces. *Macromolecules*, 30:5944–5952, 1997.
95. N. H. G. Penners, L. K. Koopal, and J. Lyklema. Interfacial electrochemistry of haematite ( $\alpha$ -Fe<sub>2</sub>O<sub>3</sub>): Homodisperse and heterodisperse sols. *Colloids Surfaces*, 21:457–468, 1986.

## BIBLIOGRAPHY

96. P. Venema, T. Hiemstra, and W. H. van Riemsdijk. Multi site adsorption of cadmium on goethite. *J. Colloid Interface Sci.*, 183:515–527, 1996.
97. 2003. This thesis, chapter 5.
98. G. H. Bolt and W. H. van Riemsdijk. Ion adsorption on inorganic variable charge constituents. In G. H. Bolt, editor, *Soil chemistry*, volume 5 B of *Developments in soil science*, chapter 13. Elsevier, Amsterdam, The Netherlands, second edition, 1982.
99. A. Breeuwsma. *Adsorption of ions on hematite ( $\alpha$ -Fe<sub>2</sub>O<sub>3</sub>). A colloid-chemistry study*. PhD thesis, Landbouwhogeschool Wageningen, Wageningen, The Netherlands, 1973.
100. N. G. Hoogeveen, M. A. Cohen Stuart, and G. J. Fleer. Polyelectrolyte adsorption on oxides. II. Reversibility and exchange. *J. Colloid Interface Sci.*, 182:146–157, 1996.
101. N. G. Hoogeveen, M. A. Cohen Stuart, and G. J. Fleer. Adsorption of charged block copolymers with two adsorbing blocks. *Farad. Discuss. Chem. Soc.*, 98:161–172, 1994.
102. A. V. Dobrynin. Effect of solvent quality on polyelectrolyte adsorption at an oppositely charged surface. *J. Chem. Phys.*, 114:8145–8153, 2001.
103. A. Broukhno, M. O. Khan, T. Akesson, and B. Jonsson. Polyampholyte-induced repulsion between charged surfaces: Monte Carlo simulation studies. *Langmuir*, 18:6429–6436, 2002.
104. E. Pefferkorn. The role of polyelectrolytes in the stabilization and destabilization of colloids. *Adv. Colloid Interface Sci.*, 56:33–104, 1995.
105. B. Alince, A. Vanerek, and T. G. M. van de Ven. Effects of surface topography, pH and salt on the adsorption of polydisperse polyethylenimine onto pulp fibers. *Ber. Bunsen-Ges. Phys. Chem. Chem. Phys.*, 100:954–962, 1996.
106. J. B. Schlenoff and M. Li. Kinetics and multilayering in the adsorption of polyelectrolytes to a charged surface. *Ber. Bunsen-Ges. Phys. Chem. Chem. Phys.*, 100:943–947, 1996.
107. M. A. Cohen Stuart, C. W. Hoogendam, and A. de Keizer. Kinetics of polyelectrolyte adsorption. *J. Phys. Condensed Matter*, 9:7767–7783, 1997.
108. 2003. This thesis, chapter 4.
109. R. P. J. J. Rietra, T. Hiemstra, and W. H. van Riemsdijk. The relationship between molecular structure and ion adsorption on variable charge. *Geochim. Cosmochim. Acta*, 63:3009–3015, 1999.

## BIBLIOGRAPHY

110. L. G. J. Fokkink, A. de Keizer, and J. Lyklema. Specific ion adsorption on oxides: surface charge adjustment and proton stoichiometry. *J. Colloid Interface Sci.*, 118:454–462, 1987.
111. B. C. Barja, M. I. Tejedor-Tejedor, and M. A. Anderson. Complexation of methylphosphonic acid with the surface of goethite particles in aqueous solution. *Langmuir*, 15:2316–2321, 1999.
112. J. D. Filius, T. Hiemstra, and W. H. van Riemsdijk. Adsorption of small weak organic acids on goethite: Modeling of mechanisms. *J. Colloid Interface Sci.*, 195:368–380, 1997.
113. T. Hiemstra and W. H. van Riemsdijk. A surface structural approach to ion adsorption: The charge distribution (cd) model. *J. Colloid Interface Sci.*, 179:488–508, 1996.
114. E. M. Lee and L. K. Koopal. Adsorption of cationic and anionic surfactants on metal oxide surfaces: surface charge adjustment and competition effects. *J. Colloid Interface Sci.*, 177:478–489, 1996.
115. L. K. Koopal and T. Goloub. Self-assembly of ionic surfactants adsorbed on mineral oxides. In R. Sharma, editor, *Surfactant adsorption and surface solubilization*, volume 615 of *ACS Symposium series*, chapter 6. American Chemical Society, Washington DC, USA, 1995.
116. L. K. Koopal and J. Lyklema. Characterization of polymers in the adsorbed state by double layer measurements. the AgI-PVA system. *Farad. Discuss. Chem. Soc.*, 59:230–241, 1975.
117. L. K. Koopal and J. Lyklema. Characterization of adsorbed polymers from double layer experiments. the effect of acetate groups in polyvinyl alcohol on its adsorption on silver iodide. *J. Electroanalytical Chem.*, 100: 895–912, 1979.
118. H. A. van der Schee and J. Lyklema. Adsorption of oligo- and polypeptides on agi, their effects on double layer and colloid stability. In Th. F. Tadros, editor, *The Effect of Polymers on Dispersion Properties*, pages 81–100. Academic Press, London, UK, 1982.
119. B. C. Bonekamp and J. Lyklema. Conductometric and potentiometric monitoring of polyelectrolyte adsorption on charged surfaces. *J. Colloid Interface Sci.*, 113:67–75, 1986.
120. B. C. Bonekamp. *Adsorption of polylysines at solid-liquid interfaces*. PhD thesis, Landbouwhogeschool Wageningen, Wageningen, The Netherlands, 1984.

## BIBLIOGRAPHY

121. M. P. Siderova, T. P. Goloub, and K. B. Musabekev. Electokinetic and adsorption properties of SiO<sub>2</sub> in polymer and surfactant solutions. *Adv. Colloid Interface Sci.*, 43:1–15, 1993.
122. K. Vermöhlen, H. Lewandowski, H. D. Narres, and M. J. Schwuger. Adsorption of polyelectrolytes onto oxides — the influence of ionic strength, molar mass, and Ca<sup>2+</sup> ions. *Colloids Surfaces A*, 163:45–53, 2000.
123. J. E. Gebhardt and D. W. Fuerstenau. Adsorption of polyacrylic acid at oxide/water interfaces. *Colloids Surfaces*, 7:221–231, 1983.
124. S. Fukuzaki, H. Urano, and K. Nagata. Adsorption of bovine serum albumin onto metal oxide surfaces. *J. Ferment. Bioeng.*, 81:163–167, 1996.
125. R. P. J. J. Rietra, T. Hiemstra, and W. H. van Riemsdijk. Sulfate adsorption on goethite. *J. Colloid Interface Sci.*, 218:511–521, 1999.
126. J. D. Filius. *Modeling the adsorption of weak organic acids on goethite. The ligand and charge distribution model*. PhD thesis, Wageningen Universiteit, The Netherlands, 2001.
127. A. W. P. Vermeer, W. H. van Riemsdijk, and L. K. Koopal. Adsorption of humic acid to mineral particles. 1. Specific and electrostatic interactions. *Langmuir*, 14:2810–2819, 1998.
128. Y. Shin, J. E. Roberts, and M. M. Santore. Influence of charge density and coverage on bound fraction for a weakly cationic polyelectrolyte adsorbing onto silica. *Macromolecules*, 35:4090–4095, 2002.
129. Y. Shin, J. E. Roberts, and M. M. Santore. The relationship between polymer/substrate charge density and charge overcompensation by adsorbed polyelectrolyte layers. *J. Colloid Interface Sci.*, 247:220–230, 2002.
130. P. Venema, T. Hiemstra, P. G. Weidler, and W. H. van Riemsdijk. Intrinsic proton affinity of reactive surface groups of metal (hydr)oxides: Application to iron (hydr)oxides. *J. Colloid Interface Sci.*, 198:282–295, 1998.
131. T. Hiemstra and W. H. van Riemsdijk. Effect of different crystal faces on experimental interaction force and aggregation of hematite. *Langmuir*, 15:8045–8051, 1999.
132. L. K. Koopal. Mineral hydroxides: from homogeneous to heterogeneous modelling. *Electrochim. Acta*, 41:2293–2305, 1996.
133. T. Hiemstra, H. Yong, and W. H. van Riemsdijk. Interfacial charging phenomena of aluminum (hydr)oxides. *Langmuir*, 15:5942–5955, 1999.



## BIBLIOGRAPHY

134. K. Bourikas, T. Hiemstra, and W. H. van Riemsdijk. Ion pair formation and primary charging behavior of titanium oxide (anatase and rutile). *Langmuir*, 17:749–756, 2001.
135. P. J. Flory. *Principles of polymer chemistry*. Cornell University Press, Ithaca , USA, 1964.
136. P. J. Flory. *Statistical mechanics of chain molecules*. Interscience Publishers, New York, USA, 1969.
137. N. H. G. Penners and L. K. Koopal. Preparation and optical properties of homodisperse haematite hydrosols. *Colloids Surfaces*, 19:337–349, 1986.
138. J. Papenhuijzen, G. J. Fleer, and B. H. Bijsterbosch. Adsorption of polystyrene sulfonate on polyoxymethylene single crystals at high ionic strength. *J. Colloid Interface Sci.*, 104:530–539, 1985.
139. D. G. Kinniburgh and C. J. Milne. *Guide to the Wallingford Titrator*, volume WE/93/23 of *Technical report*. British Geological Survey, Wallingford, UK, 1993. version T047, march 1998.
140. J. Papenhuijzen. *Adsorption of Flexible Polyelectrolytes*  
*A theoretical and experimental study of polystyrene sulfonate adsorption on polyoxymethylene single crystals*. PhD thesis, Landbouwhogeschool Wageningen, Wageningen, The Netherlands, 1985.
141. G. Charlot. *Colorimetric determination of elements : principles and methods*. Elsevier, Amsterdam, The Netherlands, 1964. Part II and references therein.
142. D. R. Lide. *CRC handbook of chemistry and physics : a ready-reference book of chemical and physical data*. CRC Press, Boca Raton, USA, 82nd edition, 2001–2002.
143. A. Breeuwsma and J. Lyklema. Interfacial electrochemistry of haematite ( $\alpha\text{Fe}_2\text{O}_3$ ). *Discuss. Farad. Soc.*, 52:324–333, 1971.
144. N. H. G. Penners. *The Preparation and Stability of Homodisperse Colloidal Haematite ( $\alpha\text{-Fe}_2\text{O}_3$ )*. PhD thesis, Landbouwhogeschool Wageningen, Wageningen, The Netherlands, 1985.
145. M. Schudel, S. H. Behrens, R. Kretzschmar, and M. Borkovec. Absolute aggregation rate constants of hematite particles in aqueous suspensions: a compersion of two different surface morphologies. *J. Colloid Interface Sci.*, 196:241–253, 1997.
146. M. Gunnarsson, M. Rasmusson, S. Wall, E. Ahlberg, and J. Ennis. Electroacoustic and potentiometric studies of the hematite/water interface. *J. Colloid Interface Sci.*, 240:448–458, 2001.

## BIBLIOGRAPHY

147. Ronald Rhemet and E. Killmann. Adsorption of cationic poly(diallyl-dimethyl-ammoniumchloride), poly(diallyl-dimethyl-ammoniumchloride-co-n-methyl-n-vinylactamide) and poly(n-methyl-n-vinylactamide) on polystyrene latex. *Colloids Surfaces A*, 149:323–328, 1999.
148. T. Sennerfors and F. Tiberg. Adsorption of polyelectrolyte and nanoparticles at the silica- aqueous solution interface: Influence of the history of additions of the two components. *J. Colloid Interface Sci.*, 238:129–135, 2001.
149. J. D. Filius, D. G. Lumsdon, J. C. L. Meeussen, T. Hiemstra, and W. H. van Riemsdijk. Adsorption of fulvic acid on goethite. *Geochim. Cosmochem. Acta*, 64:51–60, 2000.
150. E. Pfefferkorn, E. Ringenbach, and F. Elfarissi. Aluminium ions at polyelectrolyte interfaces. III. Role in polyacrylic acid/aluminium oxide and humic acid/kaolinite aggregate cohesion. *Colloid Polymer Sci.*, 279:498–505, 2001.
151. H. Yim, M. Kent, A. Matheson, R. Ivkov, S. Satija, J. Majewski, and G. S. Smith. Adsorption of poly(styrenesulfonate) to the air surface of water by neutron reflectivity. *Macromolecules*, 33:6126–6133, 2000.
152. H. Yim, M. Kent, A. Matheson, M. J. Stevens, R. Ivkov, S. Satija, J. Majewski, and G. S. Smith. Adsorption of sodium poly(styrenesulfonate) to the air surface of water by neutron and x-ray reflectivity and surface tension measurements: Polymer concentration dependence. *Macromolecules*, 35:9737–9747, 2002.
153. M. A. G. Dahlgren, P. M. Claesson, and R. Audebert. Highly-charged cationic polyelectrolytes on mica – influence of polyelectrolyte concentration on surface forces. *J. Colloid Interface Sci.*, 166:343–349, 1994.
154. T. P. Goloub, L. K. Koopal, B. H. Bijsterbosch, and M. P. Sidorova. Adsorption of cationic surfactants on silica. surface charge effects. *Langmuir*, 12:3188–3194, 1996.
155. J. A. Marinsky. *Ion Exchange and Solvent Extraction*, volume 11. Marcel Dekker Inc. New York, 1993.
156. E. Tipping and M. A. Hurley. A unifying model of cation binding by humic substances. *Geochim. Cosmochem. Acta*, 56:3627–3641, 1992.
157. B. M. Bartschat, S. E. Cabaniss, and F. M. M. Morel. Oligoelectrolyte model for cation binding by humic substances. *Environmental Sci. Tech.*, 26:284–294, 1992.
158. P. Barak and Y. N. Chen. Equivalent radii of humic macromolecules from acid-base titration. *Soil Sci.*, 154:184–000, 1992.

## BIBLIOGRAPHY

159. C. J. Milne, D. G. Kinniburgh, J. C. M. de Wit, W. H. van Riemsdijk, and L. K. Koopal. Analysis of proton binding by a peat humic acid using a simple electrostatic model. *Geochim. Cosmochem. Acta*, 59:1101–1112, 1995.
160. E. Tipping. Humic ion-binding model VI: An improved description of the interactions of protons and metal ions with humic substances. *Aquat. Chem.*, 4:3–48, 1998.
161. C. J. Milne, D. G. Kinniburgh, and E. Tipping. Generic NICA-Donnan model parameters for proton binding by humic substances. *Environmental Sci. Tech.*, 35:2049–2059, 2001.
162. L. P. Weng, E. J. M. Temminghoff, S. Lofts, E. Tipping, and W. H. van Riemsdijk. Complexation with dissolved organic matter and solubility control of heavy metals in a sandy soil. *Environmental Sci. Tech.*, 36:4804–4810, 2002.
163. J. C. M. de Wit, W. H. van Riemsdijk, L. K. Nederhof, D. G. Kinniburgh, and L. K. Koopal. Analysis of ion binding on humic substances and the determination of intrinsic affinity distributions. *Anal. Chim. Acta*, 232:189–207, 1990.
164. J. C. M. de Wit, W. H. van Riemsdijk, and L. K. Koopal. Proton binding to humic substances. 1. electrostatic effects. *Environmental Sci. Tech.*, 27:2005–2014, 1993.
165. M. J. Avena, A. W. P. Vermeer, and L. K. Koopal. Volume and structure of humic acids studied by viscosimetry, *ph* and electrolyte concentration effects. *Colloids Surfaces A*, 151:201–212, 1999.
166. M. Benedetti, W. H. van Riemsdijk, and L. K. Koopal. Humic substances considered as a heterogeneous Donnan gel phase. *Environmental Sci. Tech.*, 30:1805–1813, 1996.
167. L. K. Koopal. Adsorption. In J. S. Laskowski and J. Ralston, editors, *Colloid Chemistry in Mineral Processing*, chapter 2. Elsevier Science Publishers, Amsterdam, 1991.
168. J. Lyklema. *Fundamentals of interface and colloid science, Solid-liquid interfaces*, volume II. Academic Press, London, 1995.
169. E. Tipping. Modeling ion-binding by humic acids. *Colloids Surfaces A*, 73:117–000, 1993.
170. S. Z. Ren, E. Tombácz, and J. A. Rice. Dynamic light scattering from power-law polydisperse fractals: Applications of dynamic scaling to humic acid. *Phys. Rev. E*, 53:2980–2983, 1996.

## BIBLIOGRAPHY

171. J. R. Lead, K. J. Wilkinson, E. Balnois, B. J. Cutak, C. K. Larive, S. Assemi, and R. Beckett. Diffusion coefficient and polydispersities of Suwannee river fulvic acid: Comparison of fluorescence correlation spectroscopy, pulsed-field gradient nuclear magnetic resonance, and flow field-flow fractionation. *Environmental Sci. Tech.*, 34:3508–3513, 2000.
172. P. K. Cornel, R. S. Summers, and P. V. Roberts. Diffusion of humic acid in dilute aqueous solution. *J. Colloid Interface Sci.*, 110:149–164, 1986.
173. Y. Wang, C. Combe, and M. M. Clarke. The effects of  $pH$  and calcium on the diffusion coefficient of humic acid. *J. Membrane Sci.*, 183:49–60, 2001.
174. M. N. Jones and N. D. Bryan. Colloidal properties of humic substances. *Adv. Colloid Interface Sci.*, 78:1–48, 1998.
175. M. J. Avena and K. J. Wilkinson. Disaggregation kinetics of a peat humic acid: Mechanism and  $pH$  effects. *Environmental Sci. Tech.*, 000:000, 2002. DOI 10.1021/es025582u.
176. J. P. Pinheiro, A. M. Mota, J. M. R. d'Oliveir, and J. M. G. Martinho. Dynamic properties of humic matter by dynamic light scattering and voltammetry. *Anal. Chim. Acta*, 329:15–24, 1996.
177. J. P. Pinheiro, A. M. Mota, M. L. S. Simoes Goncalves, and H. P. van Leeuwen. The  $pH$  effect in the diffusion coefficient of humic matter: Influence in speciation studies using voltammetric techniques. *Colloids Surfaces A*, 137:165–170, 1998.
178. N. Senesi, F. R. Rizzi, P. Dellino, and P. Acquafredda. Fractal dimension of humic acids in aqueous suspensions a function of  $pH$  and time. *Soil Sci. Soc. Am. J.*, 60:1773–1780, 1996.
179. N. Senesi, F. R. Rizzi, P. Dellino, and P. Acquafredda. Fractal humic acids in aqueous suspensions at various concentrations, ionic strengths, and  $pH$  values. *Colloids Surfaces A*, 127:57–68, 1997.
180. 2003. This thesis, chapter 3.
181. J. Klein Wolterink, M. Daoud, and O. V. Borisov. Scaling theory of branched polyelectrolytes. in preparation, 2003.
182. I. Christl and R. Kretzschmar. Relating ion binding by fulvic and humic acids to chemical composition and molecular size. 1. Proton binding. *Environmental Sci. Tech.*, 35:2505–2511, 2001.
183. J. B. Christensen, E. Tipping, D. G. Kinniburgh, C. Grøn, and T. H. Christensen. Proton binding by groundwater fulvic acids, and structure modeled with the model V and NICA–Donnan model. *Environmental Sci. Tech.*, 32:3346–3355, 1998.

## BIBLIOGRAPHY

184. Y.-H. Yang and D.-H. Zhang. Concentration effect on the fluorescence spectra of humic substances. *Commun. Soil Sci. Plant Anal.*, 26:2333–2349, 1995.

# Summary

In chapter 1 the motivation and outline of the present study is presented. Apart from trying to get a better qualitative insight in the behaviour of synthetic polyelectrolytes, the study is also intended to get a better qualitative insight in the behaviour of natural organic matter such as humic acids.

## Polyelectrolytes in solution

Chapters 2 and 3 study the equilibrium conformations of star-branched polyelectrolytes in dilute solution on the basis of a numerical Self-Consistent-Field (SF-SCF) approach, originally developed by Scheutjens and Fleer. The results are compared to existing analytical theories. Two types of star-branched polyelectrolytes are considered: quenched and annealed stars. Chapter 2 deals with quenched stars, which have a constant charge per monomer. Chapter 3 deals with annealed stars, which have a  $pH$ -dependent charge.

The size of an individual star molecule results from a balance of forces. As the arms stretch, their conformational entropy is reduced, which results in a net contractive force. This contractive force is balanced by three forces which cause swelling. Firstly, the charges on the monomers are of the same sign, which results in a Coulombic repulsion. Secondly, the charges on the monomers attract counterions and (if present) salt ions. Therefore, the concentration of ions inside the stars may be higher than the concentration of ions outside the star. This results in a net osmotic pressure difference, which also leads to swelling. Finally, each monomer occupies a certain volume, which leads to excluded volume swelling due to steric repulsion.

For quenched stars (chapter 2) the molecular parameters of the polyelectrolyte star are the amount of arms in a star  $f$ , the number of monomers in each arm  $N$ , and the fraction of charged monomers  $m^{-1}$ . Here,  $m - 1$  is the number of uncharged monomers in between two neighbouring charges along the chain. Depending on these three molecular parameters ( $f$ ,  $m$ , and  $N$ ) three regimes are commonly distinguished in analytical theory. Furthermore, a distinction is made between salt free solutions and solutions with added salt. In *salt free solutions* of stars three regimes can be distinguished:

1. **The polyelectrolyte regime** occurs for a low number of arms. Most counterions are released in the bulk solution, therefore the Coulombic repulsion between the monomers of the star is dominant.

2. **The osmotic regime** occurs for a higher number of arms. Most counterions are retained in the star so that the Coulombic repulsion is largely screened by counterions and, consequently, the osmotic pressure is the dominant contribution to the swelling.
3. **The quasi-neutral regime** occurs when the amount of arms becomes very large. Here, the excluded volume interactions are dominant.

*Addition of salt* results in a better screening of the Coulombic repulsion, which leads to a reduced star size  $R$ . This corresponds to a fourth regime:

4. **The salt dominance regime** occurs when the amount of salt becomes high. The repulsion between the monomers is largely screened and the star behaves as a neutral star with a monomer size which is determined by the Debye screening length.

For stars in the polyelectrolyte regime the addition of salt results always in a reduction of the size. In the osmotic regime, this reduction in  $R$  only becomes significant if the concentration of added salt  $c_s$  exceeds that of the counterions in the star itself. For stars in the quasi-neutral regime, the addition of salt has no consequences because the swelling was not due to Coulombic repulsion between the charges on the polyelectrolyte chains.

For each of these regimes, the analytical theory predicts scaling relations of the star size depending on the number of arms, the charge density on each arm, and the length of the arms. The results from the numerical SCF theory agree well with these scaling laws. For instance, in the salt dominance regime the scaling prediction is  $R \sim c_s^{-1/5}$  and this significant reduction is confirmed by the SF-SCF calculations.

Furthermore, the SF-SCF calculations predict various internal details of the star like the counterion distribution, the monomer volume fractions, and the position of the end-points of the arms. At low salt concentration, the volume fraction profiles  $\varphi(r)$  show a power law decay with an exponent of  $-2$ , i.e.  $\varphi(r) \sim r^{-2}$ . At a high salt concentration the decay is slower,  $\varphi(r) \sim r^{-4/3}$ .

The SF-SCF theory also shows that the boundaries between the various regimes are not sharp but diffuse. The internal molecular details of the star, as calculated by the SF-SCF theory, elucidate one of the reasons behind the diffuse boundaries between the different regimes. A star without added salt, for example, may show all three regimes at the same time. Going from the interior to the exterior of the star, the density drops significantly and one may subsequently encounter a quasi-neutral region, an osmotic region, and a polyelectrolyte region within the same star polyelectrolyte.

The results discussed so far dealt with an individual star in solution. This is a good model for a very dilute solution of stars. As the concentration of stars increases, the star size will eventually decrease due to overlap of the stars. However, in the absence of salt a significant contraction of the stars is observed well before the stars physically overlap. This effect is most pronounced for stars in the polyelectrolyte regime, since most counterions are then outside the stars.

Increasing the concentration of stars leads to an overlap of the counterion clouds around the star. This forces more counterions inside the stars, which leads to an enhanced screening of the monomer charges. This effect is largely absent in the osmotic regime (stars with more arms) since then most counterions reside inside the stars. In the dilute regime, the star size  $R$  is more sensitive to an increase in salt concentration than to an increase in the concentration of stars.

Chapter 3 deals with annealed polyelectrolyte stars in solution, i.e. stars with a  $pH$ -dependent monomer charge. The monomers of the stars are weak acids, which may release a proton as a counterion, depending on the local electrochemical environment of the star monomer. Therefore, the total charge of the polyelectrolytes depends on the  $pH$ , the salt concentration  $c_s$ , the number of arms  $f$ , the length of the arms  $N$ , and the fraction of monomers with an acidic group  $m^{-1}$ . As in chapter 2, the results from the numerical SCF theory are compared with analytical predictions.

The degree of dissociation  $\alpha$  of the monomers need not be constant within the star. Generally, the dissociation of monomers will be lower in centre of the star, compared to the outer region of the star. The dissociating monomers generate a local electrostatic potential which will prevent neighbouring monomers from dissociating. This effect is more pronounced in the centre of the star since at the centre the density of monomers is higher. However, for three regimes, the polyelectrolyte, the quasi-neutral and the salt dominance regime, discussed in chapter 2, this difference in dissociation is small or unimportant. Obviously, for the quasi-neutral regime, the repulsion of the chains is still governed by the steric interactions. For the salt dominance regime, most electrostatic repulsion is screened, and the dissociation is assumed constant within the star. In the polyelectrolyte regime, the  $pH$ -dependent monomers on a polyelectrolyte are assumed to dissociate in the same way as small molecules and so that the degree of dissociation is uniform in the star. Therefore, the behaviour of the star with quenched and annealed charges will be the same in this regime.

The most significant differences are found in the osmotic regime. For a  $pH$  such that almost all monomers are dissociated, the osmotic regime of quenched stars is recovered. Likewise, a  $pH$  such that almost no monomer is dissociated leads to a neutral star. However, we can distinguish an additional regime:

**5. The osmotic annealing regime** occurs for polyelectrolytes with a number of branches which is high enough to have an osmotic regime in the quenched case. For such annealed stars at a  $pH \approx pK$ , the degree of dissociation of monomers varies strongly within the star.

It is this regime which yields results which are significantly different from those found for a quenched star. Two rather surprising maxima were predicted earlier by analytical theory: upon increasing either the number of arms  $f$  or the salt concentration  $c_s$ , the size of the star shows a maximum. Both maxima are confirmed by numerical SCF calculations. The volume fraction profiles of the star-shaped polyelectrolyte  $\varphi(r)$  are expected to show a powerlaw decay with an exponent of  $-8/3$ , i.e. the local stretching of a branch of a star increases



when going further from the centre. In the numerical results the exponent of  $-\frac{8}{3}$  can only be found for a small range of  $pH$ 's and number of arms. Although a fast decrease of the polymer density with a power law exponent, which is more negative than -2, and a huge increase of the charge on the star with distance from the centre are seen, there does not seem to be a single scaling exponent for the osmotic annealing regime.

Furthermore, our calculations show that at the periphery of the star corona, the effect of curvature on the conformations of the star branches is less important, i.e. the outermost regions of the star corona behave just like a planar annealed polyelectrolyte brush. This conclusion is supported by (i) a bimodal distribution of the end-segments and (ii) a quasi-linear dependence of  $\log(1 - \alpha)$  on  $z^2$ .

## Polyelectrolytes adsorbing on a surface

The adsorption of polyelectrolytes on charged surfaces was studied both numerically and experimentally. Chapter 4 comprises a theoretical study, and in chapter 5 theoretical and experimental results are compared. In the calculations a new method of calculating the adsorbed amount is compared to an older method. Furthermore, the effect of the type of surface charge (quenched charges or annealed charges) is studied as well as the influence of the molecular architecture of the polyelectrolyte, all for different salt concentrations and  $pH$ 's. In the experiments a quenched linear polyelectrolyte (poly(styrene sulfonate)) on an annealed surface (hematite,  $\alpha\text{Fe}_2\text{O}_3$ ) was measured.

The calculations were done with a numerical SCF model. In the calculations presented in chapter 4 only electrostatic interactions between the polyelectrolyte and the surface are taken into account.

In the new way of calculating, the charging and swelling of the polyelectrolytes in bulk solution is explicitly taken into account. In the older SCF model this effect has been neglected. Comparison with the classical method shows that the adsorbed amount calculated with the new SCF model is higher, the adsorbed layers are more extended, and the surface charge can be overcompensated by the adsorbed charges. At low salt concentration the polyelectrolyte profile shows a minimum when overcompensation of the surface charge occurs, i.e. the polyelectrolyte is depleted from the surface by the adsorbed polyelectrolytes.

A surface with annealed charges is almost a constant-potential surface if the total number of chargeable sites is high. The amount of adsorbed polyelectrolytes on a quenched surface is lower than on an annealed surface, if the initial surface charge is the same. On an annealed surface, the adsorption of a polyelectrolyte induces extra charges and this increases the adsorption. For the same reason it is harder to overcompensate the charge on an annealed surface than on a quenched surface.

The effect of molecular architecture on the adsorption was studied by com-

paring the adsorption of a linear, a star-shaped and a dendrimeric polyelectrolyte. The adsorbed amount increases with increasing density of the polyelectrolyte. However, the differences in adsorbed amount between the different molecular architecture were small.

The adsorbed amount and the change in surface charge are studied as a function of the salt concentration. The adsorbed amount decreases with increasing salt concentration, as long as the surface charge is not overcompensated by the charges of the adsorbed polyelectrolyte. The reason is that salt ions compete with the polyelectrolyte for adsorption. At low salt concentration the surface charge is just overcompensated and the surface charge of an annealed surface follows the adsorbed amount. This is due to the much better screening of the surface charge by the charges on the polyelectrolyte than by the salt ions at low salt concentration. At high salt concentration it is difficult to overcompensate the surface charge, and the effect of the adsorbed charges on the surface charge is relatively small, i.e. the surface charge does not increase with the same amount as the adsorbed charges in contrast to what happens for low salt concentration. At the high salt concentration not only the charges on the polyelectrolyte screen the surface charge but also the salt ions screen the surface charge.

The last result from the calculations is the influence of charge density on the polyelectrolyte chain on the adsorption. Upon increasing the charge density of the chains the adsorbed amount, counted as the number of adsorbed charges, is increasing. The salt ions can compete less well with a highly charged polyelectrolyte than with one which has a lower charge density. The volume fraction profiles of the highly charged polyelectrolytes show a plateau region somewhat further away from the surface. The adsorbed polyelectrolytes are extended due to an electrostatic repulsion between the adsorbed molecules.

In chapter 5 the adsorption of poly(styrene sulfonate) (PSS) on hematite ( $\alpha\text{Fe}_2\text{O}_3$ ) is studied both theoretically and experimentally. PSS is a linear polyelectrolyte with a constant charge; hematite is an iron oxide surface, which has annealed charges.

The experimental adsorption isotherm of PSS on hematite does not show a high-affinity character at  $pH$  4 and 7 and 0.01 mol/L salt. The adsorption plateau at  $pH$  7 is 0.6 mg/m<sup>2</sup>. At  $pH$  4 the adsorbed amount is comparable to that at  $pH$  7, but the true plateau has not been measured. From the theoretical calculations it was unexpected that the adsorption of PSS on hematite was not high affinity. The adsorption of PSS increases the hematite surface charge, bringing it to a level which is comparable to the surface charge of a bare hematite in a solution in which the  $pH$  is three  $pH$ -units smaller than the actual  $pH$ . The total increase of the surface charge depends only on the amount of PSS present and not on the  $pH$ . At the adsorption plateau the surface charge is overcompensated by the adsorbed charges. Before the adsorption plateau is reached the surface charge increases linearly with the adsorbed amount.

Numerical calculations were done to mimic the PSS adsorption onto hematite. In these calculations not only electrostatic interactions but also a

specific affinity of the polyelectrolyte for the model surface was taken into account. The calculated adsorption isotherm was high affinity. The surface charge adjustment upon the adsorption of the quenched polyelectrolyte was large. This adjustment can also be expressed as the co-adsorption of protons, which is experimentally measureable. The proton co-adsorption increases with increasing amount of adsorbed polyelectrolyte, decreasing salt concentration, and decreasing surface charge of the bare surface.

## Polyelectrolytes and the mastercurve procedure

At the end of the thesis, we come back to annealed polyelectrolytes in solution. One of the methods to characterize humic substances is to titrate them and to analyse the results to obtain the distribution of dissociation constants. This is done with a so-called mastercurve procedure. From a set of charge- $pH$  curves at different salt concentrations one single charge- $pH_{\text{site}}$  curve is obtained by accounting for the electrostatic interactions in the  $pH_{\text{site}}$ : the mastercurve. The electrostatic interactions are calculated with an electrostatic model based on the charge of the humics under the assumption that all chargeable groups experience the same electrostatic potential. As a result, only the chemical interactions of the protons with the polyelectrolyte are captured in the mastercurve. In chapter 6 we test how well the mastercurve procedure works for different molecular architectures. From the results we can estimate under which conditions it may be assumed that the mastercurve procedure works reasonably.

The SF-SCF model is used to calculate the dissociation of various star-shaped and dendrimeric polyelectrolytes. The numerical results are transformed into mastercurves using the Donnan model (fixed potential inside a particle) and a hard-sphere model (fixed surface potential). For both models, it is checked whether for a given molecular architecture the charge- $pH$  curves calculated at different salt concentrations merge in a mastercurve. The  $pK$ -values obtained after the mastercurve procedure are compared to the true  $pK_{\text{int}}$  to judge the quality of the mastercurve.

In the mastercurve procedure a size is assigned to the Donnan or hard-sphere volume. This size can be obtained from the SCF calculations for each  $pH$ . However, it is also of interest to use a size which does not depend on the  $pH$ . Therefore, several estimates for the size based on the chain architecture and salt concentration have been used.

For the case of the size which is both  $pH$  and salt concentration dependent, the Donnan model gives a good estimate of the  $pK_{\text{int}}$ -value. However, the mastercurve is in most cases “diffuse”: the points of the charge- $pH_{\text{sites}}$  curves for different salt concentration do not merge. Only for large molecules and molecules with a large number of branches a good mastercurve is found. In contrast, the hard-sphere model results in general in a good mastercurve. However, in this case the resulting  $pK$ -value is considerably smaller than the true

intrinsic  $pK_{\text{int}}$ -value. Upon increasing the number of branches in the molecules this deviation increases.

When using estimates of the Donnan or hard-sphere volume which do not depend on  $pH$ , the resulting mastercurves are in general less good. We have compared five of these estimates. Surprisingly, the size resulting from a maximal stretching of the arms (without any ionic strength dependence) gives the best mastercurves and estimates of  $pK_{\text{int}}$  both for the Donnan and hard-sphere model. The mastercurves becomes better when the monomer density in the stars and dendrimers is larger. However, the  $pK$ -values obtained from the mastercurve procedure will always overestimate the intrinsic  $pK$ -value.

# Samenvatting

Dit proefschrift gaat over polyelektrolieten in de oplossing en in de nabijheid van een oppervlak. Polyelektrolieten zijn grote geladen molekulen. Ze bestaan uit segmenten (ook wel monomeren genoemd) die onderling verbonden zijn zoals kralen in een ketting. Deze ketting kan ook vertakkingen bevatten. Doordat meerdere van de segmenten geladen zijn lossen polyelektrolieten over het algemeen goed op in water, we spreken dan van een oplossing van polyelektrolieten. Verder kunnen polyelektrolieten zich ophopen aan oppervlakken, die in contact staan met de polyelektrolietoplossing. Dit wordt adsorptie genoemd.

Dit onderzoek is gedaan om het gedrag van polyelektrolieten beter te begrijpen. Hierbij is ook gedacht aan natuurlijke polyelektrolieten zoals humuszuren. Humuszuren komen voor in natuurlijke wateren en in de bodem. Zij geven het water de bruine kleur en kunnen adsorberen (ophopen) aan de zand- en kleideeltjes in de bodem. Humuszuren zijn oplosbare afbraakproducten van dode planten en dieren. Hun grootte en samenstelling hangen sterk af van de lokale omstandigheden waarin ze gevormd zijn. Een gedetailleerde beschrijving van humuszuren is daarom moeilijk te geven. Toch hebben ze gemeen dat ze in oplossing geladen zijn en dat ze door het opladen zwellen. Eenvoudige polyelektrolieten vertonen dit gedrag ook. In dit proefschrift worden alleen goed definiëerde polyelektrolieten bestudeerd om duidelijke conclusies te kunnen trekken.

Polyelektrolyten kunnen verschillende vormen aannemen. Een voorbeeld daarvan is in de eerste plaats *lineaire* ketens, vergelijkbaar met spaghetti, in de tweede plaats een *stervormig* polyelektroliet, waarbij verschillende lineaire ketens samenkomen in één knooppunt. Elk van deze lineaire ketens in een stervormig polyelektroliet wordt een arm van de ster genoemd. Een laatste voorbeeld is een dendrimeer, dit is een ster waarbij de eindpunten allen weer splitsen in meerdere ketens. De drie genoemde vormen zijn afgebeeld in figuur 1.1 op pagina 3. Een sterk vertakte ster of een dendrimeer is op te vatten als een vereenvoudigd model van een humuszuur. Echter, humuszuren hebben een veel onregelmatigere vertakkingsstructuur.

Naast een indeling in vorm, kunnen polyelektrolieten in twee groepen worden onderverdeeld naar de aard van de lading op de monomeren. In de eerste groep hebben de monomeren een constante of vaste lading, in de tweede groep hebben de monomeren een zwak zure of zwak basische groep. Beide groepen worden in dit proefschrift behandeld.

De zwak zure monomeren kunnen een proton ( $H^+$ ) afstaan aan de omgeving, waardoor de monomeren negatief geladen worden. De zwakke basische monomeren kunnen een proton opnemen en krijgen een positieve lading. In dit proefschrift worden alleen polyelektrolieten met zure monomeren bestudeerd en daar zal dan ook nu de aandacht op worden gericht. Basische polyelektrolieten gedragen zich geheel analoog. Het gemak waarmee een monomeer een proton kan afstaan wordt weergegeven door de dissociatieconstante  $K$ . Omdat er een groot gebied van dissociatieconstanten is, wordt de waarde meestal uitgedrukt op een logaritmische schaal en spreken we van de  $pK = -\log K$ . Een kleine  $pK$  geeft aan dat een proton makkelijk wordt afgestaan, een grote  $pK$  dat dat moeilijk is. De fractie monomeren, die een proton heeft afgestaan (gedissocieerd is), wordt de dissociatiegraad genoemd. Of een  $H^+$  daadwerkelijk wordt afgesplitst hangt bij een gegeven  $pK$  af van de zuurgraad  $pH$  en van de zoutconcentratie  $c_s$  van de oplossing.

Een groot deel van dit onderzoek bestaat uit model-berekeningen aan polyelektrolieten. De meeste berekeningen zijn gedaan met de gemiddeld-veld theorie van Scheutjens en Fler. Deze theorie gebruikt onder andere de volgende vereenvoudingen:

- De ketenmolekulen worden beschreven als gewogen 'dronkenmans wandelingen'. Dit betekent dat twee segmenten van het polyelektroliet in principe op dezelfde plaats in de ruimte kunnen zijn, wat uiteraard in het echt niet kan. Wel wordt er een maximum gesteld aan de totale hoeveelheid monomeren die op een bepaalde plaats kan zijn.
- Er wordt gebruik gemaakt van de gemiddeld-veld benadering. Dit betekent dat een gegeven molekuul niet alle afzonderlijke afstotende en aantrekkende krachten van zijn burens voelt. Omdat die burens steeds bewegen veranderen die krachten steeds. In de gemiddeld-veld benadering worden deze fluctuerende krachten vervangen door een gemiddelde.

De berekeningen met de gemiddeld-veld theorie zijn uitgevoerd met een speciaal computer programma: **sfbx**. Deze berekeningen worden door de computer opgelost en zullen hierna de numerieke berekeningen of numerieke resultaten genoemd worden.

De numerieke resultaten voor polyelektrolieten in oplossing worden vergeleken met reeds bestaande analytische theorieën. Deze theorieën gaan ook uit van de bovenstaande vereenvoudingen. Door nog verdere vereenvoudingen te gebruiken resulteren deze theorieën in vergelijkingen die aangeven hoe verschillende grootheden samenhangen. In hoofdstuk 2 en 3 wordt getest in hoeverre deze verdere vereenvoudingen gerechtvaardigd zijn.

In hoofdstuk 4 wordt het adsorberen van polyelektrolieten vanuit de oplossing aan een vast oppervlak theoretisch bestudeerd. Het is bekend dat de klassieke numerieke theorie van Scheutjens en Fler hierin minder goede benaderingen maakt. Daarom worden de resultaten van deze theorie vergeleken met die verkregen zijn met een nieuwe methode. Vervolgens wordt in hoofdstuk 5 de adsorptie van polyelektrolieten experimenteel bepaald, waarna een

vergelijking met de theoretische resultaten volgt. In hoofdstuk 6, tenslotte, wordt van een aantal simpele modellen getest of die de lading van zure polyelektrolieten als functie van de  $pH$  goed kunnen benaderen en in hoeverre dit afhankelijk is van de structuur van het polyelektroliet.

## Ster-polyelektrolieten in oplossing

In hoofdstuk 2 wordt de grootte van stervormige polyelektrolieten berekend met behulp van de numerieke gemiddeld-veld theorie. De uitkomsten van de numerieke theorie worden vergeleken met een bestaande analytische theorie. De grootte van een gegeven ster hangt uiteraard af van de lengte van de armen in de ster. Een gegeven arm is geen rechte staaf maar vormt een kluwen, zoals bij een ontrolde bol wol op een losse hoop: de losse hoop is groter dan de bol maar niet zo groot als de hele lengte van de draad. In dit hoofdstuk wordt de grootte van de kluwen berekend. Die grootte is ook afhankelijk van het aantal armen, omdat de armen allemaal een bepaalde ruimte innemen.

De sterren in hoofdstuk 2 bevatten een bepaald aantal geladen monomeren. De lading op die monomeren wordt verondersteld *niet* afhankelijk van de zuurgraad te zijn, dit effect wordt in hoofdstuk 3 bestudeerd. De hoeveelheid lading op de ster is van invloed op de grootte omdat gelijk geladen segmenten in de keten elkaar afstoten, wat tot zwelling van de kluwen leidt. Verder heeft de zout concentratie een invloed op de grootte van de ster.

De grootte van de stervormige polyelektrolieten wordt bepaald door verschillende krachten die op het molecuul werken. De balans van deze krachten bepaalt of de kluwen gezwollen of ineengekrompen is. Als een arm van een stervormig polyelektroliet wordt uitgerekt dan gedraagt deze arm zich als een kleine veer. De arm is een zogenaamde *entropieveer*, de analogie met het uitrekken van een veer gaat goed op. Een tegengesteld effect komt van de ladingen op de arm. Deze ladingen hebben hetzelfde teken en stoten elkaar daarom af, wat leidt tot strekking van de armen en daarmee tot zwelling van de keten. Dit heet *Coulombse* repulsie. De ladingen op de arm trekken tegenionen aan. Tegenionen zijn kleine moleculen met een lading tegengesteld aan de lading op het polyelektroliet. De aantrekking van tegenionen heeft twee effecten. Enerzijds wordt de onderlinge afstoting tussen de monomeren minder omdat de tegengesteld geladen ionen in de kluwen fungeren als een soort lijm. Dit wordt ook wel *afscherming* van lading genoemd. Anderzijds zorgt de ophoping van tegenionen voor de aantrekking van watermolekules, hierdoor zwelt de kluwen om ruimte te maken voor het aangetrokken water. Dit wordt *osmotische* repulsie genoemd. Tenslotte is er nog een kracht die voor zwelling zorgt: de *volume-repulsie*. Twee monomeren kunnen simpelweg niet op dezelfde plaats in de ruimte zitten. Dus, als het aantal armen toeneemt strekken ze zichzelf om ruimte te maken.

De numerieke theorie neemt dit hele complex van zwel- en krimpkrachten allemaal tegelijkertijd mee. In de analytische theorie wordt gebruik gemaakt

van het feit dat deze krachten niet allemaal op ieder moment even belangrijk zijn. Men onderscheidt aparte gevallen (regimes) waarin telkens slechts één van de drie zwelkrachten in rekening wordt gebracht. Als aan de oplossing *geen* zout is toegevoegd, dan onderscheidt de analytische theorie drie regimes:

1. **Polyelektroliet regime** Als een stervormig molecuul weinig armen heeft, dan verspreiden de tegenionen zich over de gehele oplossing. Dit zorgt ervoor dat de repulsieve Coulombse interactie dominant is.
2. **Osmotisch regime** Als de hoeveelheid armen groter is worden de tegenionen sterker aangetrokken. Dit kan zo'n sterk effect zijn dat vrijwel alle tegenionen in de kluwen worden vast gehouden. In dit geval is de osmotische repulsie dominant.
3. **Quasi-neutraal regime** Dit komt voor als het stervormige polyelektroliet heel veel armen heeft, waardoor ze dicht opeengepakt zijn. Dan heeft de ster hetzelfde zwelgedrag als een ongeladen (neutrale) ster, de lading op de ster doet er niet meer toe.

Als er *wel* zout is toegevoegd dan is de ster in het algemeen kleiner. Net zoals hierboven beschreven voor de tegenionen heeft zout een soort 'lijm' functie in de kluwen en leidt tot krimp. Als er voldoende zout is toegevoegd resulteert dit in een vierde regime:

4. **Zout gedomineerd regime** Door het toevoegen van zout wordt de repulsie verkleind en lijkt te bestaan uit een volume repulsie. Het is echter niet het eigen volume van de monomeren die de repulsie bepaalt maar een groter, *effectief* volume van de monomeren dat afhankelijk is van de hoeveelheid toegevoegd zout.

Voor elk van deze regimes zijn in de analytische theorie relaties afgeleid die de grootte van de kluwen voorspellen als functie van de lengte van de armen, het aantal armen en de hoeveelheid lading op het polyelektroliet. Deze relaties worden bevestigd door de numerieke berekeningen. Dit betekent dat de indeling in regimes en de bijbehorende aannames in de analytische theorie bevestigd worden.

De numerieke theorie laat zien dat de overgangen tussen de regimes niet scherp zijn: er zijn duidelijk overgangssituaties waar de analytische theorie niet goed mee uit de voeten kan. Verder geeft de numerieke theorie voorspellingen over de interne structuur in de kluwen, zoals bijvoorbeeld de verdeling van de tegenionen over de ruimte en de positie van de eindpunten van de armen.

Tot nu toe hebben we de resultaten besproken van individuele polyelektrolieten. Dit is een goed model voor verdunde oplossingen van deze polyelektrolieten. Als de concentratie polyelektrolieten wordt verhoogd dan beïnvloeden de polyelektrolietmoleculen ook elkaar. Ongeladen polymeren beïnvloeden elkaar pas als de concentratie zo hoog is dat ze elkaar raken, de ketens krimpen dan over het algemeen wat. Bij polyelektrolieten is dit beeld genuanceerder. In het osmotische regime zitten alle tegenionen binnen in de kluwen, zodat de kluwen als geheel neutraal is. Daardoor gedragen de sterren zich als ongeladen ketens:



er is pas krimp van de kluwen als de ketens elkaar raken. In het polyelektroliet regime zitten vrijwel alle tegenionen buiten de kluwen. De kluwens merken elkaar nu veel eerder op en er ontstaat veel eerder krimp. Dit effect is in dit proefschrift voor het eerst berekend.

Hoofdstuk 3 gaat ook over stervormige polyelektrolieten maar nu hebben de monomeren zwak zure groepen. Deze zure groepen kunnen een protonen afstaan aan de omgeving, waardoor het monomeer negatief geladen wordt. Zoals eerder opgemerkt hangt de mate waarin protonen worden afgestaan (dissociëren) af van de dissociatieconstante  $pK$ . Als de zuurgraad  $pH$  veel groter is dan de  $pK$  dan zijn alle monomeren gedissocieerd. Er is dan geen verschil tussen de polyelektrolieten met constante lading en die met zwak zure groepen. Als de  $pH$  veel kleiner is dan de  $pK$ , zal geen van de monomeren gedissocieerd zijn. Dan gedraagt het stervormige polyelektroliet zich als een ongeladen ster. De meest interessante waarden voor de  $pH$  liggen dus in de buurt van de  $pK$ .

Voor deels gedissocieerde polyelektrolieten is de fractie gedissocieerde monomeren binnen de kluwen niet overal hetzelfde. In het centrum van de kluwen is de dissociatie kleiner dan aan de buitenkant. In de numerieke theorie wordt dit effect altijd meegenomen. In de analytische theorie zorgt het voor een extra complicatie, die alleen beschouwd wordt in het osmotische regime, dus voor een redelijk aantal armen.

Polyelektrolieten met zwak zure groepen kunnen in alle regimes voorkomen die beschreven zijn in hoofdstuk 2. Maar als de  $pH$  ongeveer gelijk is aan de  $pK$  dan wordt in de analytische theorie nog een extra regime onderscheiden

**5. Osmotisch regime voor zwak zure groepen** In dit regime varieert de dissociatie binnenin het polyelektroliet sterk. Dit komt voor als de hoeveelheid armen hoog genoeg is om in het osmotisch regime te zitten en de  $pH$  in de buurt zit van de  $pK$  van de zure monomeren.

In dit regime worden resultaten gevonden voor polyelektrolieten met zure monomeren die duidelijk verschillen van die voor polyelektrolieten met een constante lading. Het opmerkelijkste verschil is dat de grootte van de kluwen door een *maximum* gaat met het toenemen van het aantal armen of van de zoutconcentratie. Beide maxima werden in de analytische theorie voorspeld en bevestigd door de numerieke berekeningen.

Een opmerkelijk resultaat van de numerieke berekeningen wordt gevonden voor de positie van de eindpunten in de kluwen. De verdeling van de eindpunten over de ruimte laat *twee* maxima zien, in tegenstelling tot *één* maximum, wat meestal wordt gevonden.

## Polyelektrolieten geadsorbeerd aan een wand

In hoofdstuk 4 wordt de adsorptie van polyelektrolieten aan een wand berekend met de numerieke gemiddeld-veld theorie. De klassieke numerieke theorie verwaarloost de zwelling van de ketens ver weg van de wand volledig. Aan de

wand zijn de ketens echter wel gezwollen. Dit is een inconsistente benadering. Daarom wordt een nieuwe variant van de theorie gebruikt waarbij de zwelling ver weg van de wand wel wordt verrekend. De resultaten van de nieuwe methode zijn beter in overeenstemming met experimenten dan de resultaten van de oude methode.

Uit de berekeningen volgt dat de geadsorbeerde hoeveelheid met de nieuwe berekeningsmethode hoger is, en de geadsorbeerde laag dikker. Een ander effect dat uit experimenten bekend is, is *overcompensatie*. Dit wil zeggen dat de lading op het geadsorbeerde polyelektroliet groter is dan de lading op de wand. Dit effect kan met de klassieke theorie niet gevonden worden als alleen ladingseffecten worden bekeken. De nieuwe methode vindt in dit geval wel overcompensatie van de wandlading.

In dit hoofdstuk wordt ook het effect bekeken van het soort wand waaraan de polyelektrolieten adsorberen. Een wand met een vaste lading wordt vergeleken met een wand met  $pH$ -afhankelijke, aanpasbare lading. Het polyelektroliet heeft een vaste lading. Als er geen polyelektrolieten adsorberen dan is de lading op beide wanden gelijk. De geadsorbeerde hoeveelheid polyelektroliet is op de wand met vaste lading lager dan op de wand met de aanpasbare lading. Dit komt doordat de dissociatie van de zwak zure groepen vergroot wordt door de geadsorbeerde polymeren. De wandlading gaat dus omhoog, zodat meer polyelektrolieten worden aangetrokken.

De adsorptie van verschillende polyelektroliet structuren heeft weinig effect op de geadsorbeerde hoeveelheid. Er is een klein verschil: de geadsorbeerde hoeveelheid neemt toe met toenemende vertaktingsgraad van het polyelektroliet, dus die is het laagst voor een lineaire keten en het hoogst voor een dendrimeer.

Ook de zoutconcentratie heeft twee effecten op de adsorptie van polyelektrolieten. Enerzijds kunnen de negatief geladen zoutionen ook adsorberen op het oppervlak. Ze gaan een competitie aan met de polyelektrolieten, zodat de geadsorbeerde hoeveelheid daalt. Anderzijds schermen de zoutionen de ladingen op de ketens af, waardoor de geadsorbeerde ketens elkaar minder afstoten. Dit effect zorgt voor een hogere adsorptie. De resultaten van de berekeningen laten zien dat het netto effect van zout afhangt van de overcompensatie van de wandlading door de polyelektrolieten. Als er geen overcompensatie is dan zorgt zout voor een daling van de adsorptie. Als er wel overcompensatie is dan stijgt de geadsorbeerde hoeveelheid met toenemende zoutconcentratie. Dit effect is gevonden voor zowel een wand met constante lading als voor een wand met zwak zure groepen.

In hoofdstuk 5 is de adsorptie van poly(styreen sulfonaat) ( $PSS^-$ ) aan hematiet ( $\alpha Fe_2O_3$ ), bestudeerd zowel experimenteel als met berekeningen.  $PSS^-$  is een lineaire keten met een vaste negatieve lading, hematiet is een ijzeroxide met op het oppervlak zwak zure groepen. Hematiet is positief geladen als de  $pH$  van de oplossing kleiner is dan 9.

Er zijn twee soorten experimenten gedaan: adsorptie-experimenten en proton-titraties. Met behulp van de adsorptie-experimenten wordt de hoeveelheid

PSS<sup>-</sup> aan het oppervlak gemeten. Omdat de hematiet deeltjes zo klein zijn, is er geen nauwkeurige methode om de hoeveelheid geadsorbeerde ketens direct te meten. Daarom wordt een indirecte methode gebruikt die als volgt werkt. Een oplossing met een bekende hoeveelheid PSS<sup>-</sup> en met een bekende hoeveelheid hematiet wordt een nacht geschud. Dan wordt de hematiet van de oplossing gescheiden en wordt de hoeveelheid PSS<sup>-</sup> in de oplossing bepaald. De geadsorbeerde hoeveelheid PSS<sup>-</sup> is het verschil tussen de toegevoegde hoeveelheid PSS<sup>-</sup> en de hoeveelheid PSS<sup>-</sup>, die in de oplossing gemeten is.

In titraties wordt de hoeveelheid protonen H<sup>+</sup> in de oplossing gemeten. De hoeveelheid protonen in de oplossing kan veranderen doordat ze door het oppervlak worden afgesplitst dan wel opgenomen. In titraties wordt een bekende hoeveelheid H<sup>+</sup> of OH<sup>-</sup> toegevoegd. Daarna wordt de nieuwe concentratie H<sup>+</sup> of OH<sup>-</sup> in de oplossing gemeten. Net als bij de adsorptie experimenten is het verschil tussen wat is toegevoegd en wat in oplossing wordt gevonden, opgenomen door het oppervlak. Ook PSS<sup>-</sup> is toegevoegd tijdens de titraties. Een deel van het PSS<sup>-</sup> dat wordt toegevoegd, adsorbeert aan het hematiet. Hierdoor worden extra protonen opgenomen door het oppervlak. Ook dit effect is gemeten.

De titratie-experimenten geven de volgende resultaten. De wandlading van het hematiet stijgt sterk door de adsorptie van PSS<sup>-</sup>. Bij pH 7 bijvoorbeeld verdubbelt de wandlading als gevolg van adsorptie. De absolute hoeveelheid extra lading op het hematiet als gevolg van adsorptie is niet gevoelig voor de pH. Overcompensatie van de wandlading door geadsorbeerd PSS<sup>-</sup> wordt ook gevonden. Zodra overcompensatie plaatsvindt neemt de adsorptie als functie van de concentratie van polyelektrolieten in oplossing nauwelijks nog toe.

Een aantal resultaten uit de experimenten zijn nog niet volledig begrepen. In de experimenten is de geadsorbeerde hoeveelheid bij pH 4 vergelijkbaar met die bij pH 7. Dit is vreemd omdat de lading van het hematiet bij pH 4 twee keer zo groot is als die bij pH 7. Verder wordt al een vrij hoge concentratie PSS<sup>-</sup> gemeten in de oplossing voordat de adsorptie maximaal is. Dit is niet normaal, in vergelijking met andere experimenten hoewel met andere stoffen wordt de maximale waarde van de adsorptie bereikt bij een hele lage concentratie polyelektroliet.

Er zijn numerieke berekeningen gedaan om de gemeten resultaten verder te analyseren. Net als in de experimenten neemt de wandlading in de berekeningen sterk toe als polyelektrolieten adsorberen. In de berekeningen wordt gevonden dat de maximale adsorptie wordt bereikt terwijl de concentratie PSS<sup>-</sup> in de oplossing bijna nul is. Dit is dus in tegenspraak met de experimentele resultaten. Het is niet duidelijk waar dit verschil tussen de metingen en de berekeningen vandaan komt.

Zowel in de berekeningen als in de experimenten zijn voorts nog een aantal andere effecten bekeken. De invloed van de zoutconcentratie op de adsorptie is bijvoorbeeld klein, zowel in de experimenten als in de berekeningen. Ook is preciezer gekeken naar de toename van de wandlading bij verschillende geadsorbeerde hoeveelheden. Hier worden wel verschillen gevonden tussen de

experimenten en de berekeningen.

De resultaten van de berekeningen en experimenten verschillen op een aantal punten. Dit zou kunnen komen omdat in de experimenten nog geen evenwicht is bereikt. In de berekeningen wordt altijd het evenwicht bereikt. Verder is het niet zeker dat het gebruikte model adequaat is. De benaderingen in de gemiddeld-veld theorie zouden ook een reden voor de verschillen kunnen zijn.

## Polyelektrolieten en de mastercurve procedure

Aan het einde van het proefschrift komen we weer terug op het gedrag van polyelektrolieten in oplossing. Als zwak zure polyelektrolieten in oplossing worden getitreerd met  $H^+$ , verandert hun lading en de  $pH$  van de oplossing. De resultaten van titraties bij verschillende zoutconcentraties zijn over het algemeen verschillend. De mastercurve procedure probeert de resultaten van experimenten bij verschillende zoutsterkte samen te vatten in één curve: de mastercurve.

Uit de mastercurve procedure wordt een zogenaamde *intrinsieke* dissociatieconstante van de zwak zure groepen berekend. Deze intrinsieke constante zou identiek moeten zijn voor verschillende zoutconcentraties en idealiter gelijk zijn aan de  $K$ -waarde van het polyelektroliet. Dit in tegenstelling tot de gemeten schijnbare dissociatieconstante die wel afhankelijk is van de zoutconcentratie.

Om de intrinsieke dissociatieconstante uit te rekenen, moeten de resultaten van de titraties worden doorgerekend met behulp van een model dat de invloed van de zoutconcentratie beschrijft. Er zijn verschillende van deze modellen in omloop. Het doel van dit hoofdstuk is om te kijken welk model het beste voldoet voor stervormige polyelektrolieten en dendrimeren (zie figuur 1.1 op pagina 3).

Over het algemeen worden twee simpele modellen gebruikt in de mastercurve procedure: het Donnan model en het harde bol model. In het Donnan model wordt het polyelektroliet beschouwd als een voor water en ionen doordringbaar gel. Alle ladingen op het polyelektroliet worden in de kluwen gecompenseerd: alle tegenionen zitten in het gel. Verder wordt aangenomen dat de dichtheid in de kluwen overal gelijk is (zie figuur 6.1 op pagina 129). Het harde bol model geeft een ander extreem geval weer. Hier wordt de kluwen opgevat als een harde bol, ondoordringbaar voor ionen. Alle ladingen op het polyelektroliet worden op het oppervlak van de bol geplaatst. De tegenionen zitten nu juist allemaal buiten de bol (zie figuur 6.2 op pagina 129). Beide modellen vatten het gedrag van een polyelektroliet samen in twee parameters. Voor het Donnan model zijn dat de Donnan-potentiaal en het Donnan-volume. Voor het harde bol model zijn dat de oppervlaktepotentiaal en de grootte van het oppervlak.

Voor het toekennen van een volume (Donnan model) of een oppervlak (harde bol model) is een maat voor de grootte van de polyelektrolietkluwen

nodig. De grootte van de kluwen kan berekend worden met de numerieke theorie of direct geschat uit de structuur van de sterren of dendrimeren. Er zijn verschillende schattingen getest. De resultaten van deze schattingen zijn vergeleken met de numerieke berekeningen.

Als de grootte van de kluwen numeriek wordt berekend worden de volgende resultaten gevonden. Het Donnan-model geeft over het algemeen geen mooie mastercurve: de resultaten voor verschillende zoutsterktes vallen niet over elkaar heen. De voorspelling van de intrinsieke dissociatieconstante is echter verrassend goed. Het harde bol model geeft juist wel een mooie mastercurve maar de voorspelling van de intrinsieke dissociatieconstante is een stuk slechter.

Zoals gezegd is de grootte van de kluwen ook direct geschat uit de structuur van de polyelektrolieten. Verschillende van deze modellen zijn gebruikt, waarbij ook de invloed van de zoutconcentratie op de grootte van de kluwen is geschat. Een verrassend resultaat is dat het meenemen van dit effect van de zoutconcentratie de mastercurves niet beter maar slechter maakt. Verder is een overschatting van de grootte van de kluwen minder ernstig dan een onderschatting. Deze conclusies kunnen dienen als een ruwe richtlijn voor het analyseren van titratie-experimenten aan humuszuren, zoals die in de bodem voorkomen.

# Dankwoord

Het heeft even geduurd maar het is dan nu af! En nu zou ik graag wat mensen willen bedanken. Allereerst: dank je wel Luuk. Voor het snelle becommentarëring van mijn schrijfsels (krabbels ?!). De prettige gesprekken en dat je af en toe de zorgzame vader was. Bedankt. Martien, bedankt voor het doordrukken en je prettige enthousiasme. Willem, de gesprekken die we hebben gehad over het werk waren prettig en verrassend. Je bleef vragen stellen en liet een andere invalshoek zien, waar ik veel van geleerd heb.

I would like to thank Oleg Borisov, for giving me an introduction in analytical theories. Also for sharing wisdom about life and science. The visits in St. Petersburg and in Pau were both remarkable and I hope we can keep in contact.

Bij het laatste aio-uitje was ik een beetje afscheid aan het nemen, eindelijk zullen mensen zeggen, maar ik heb het erg prettig gevonden op fysko. Prettige collega's en een goede sfeer, ik houd er wel van. Ik wil een paar mensen in het bijzonder noemen. Wil, bedankt voor de gesprekken. Ben, bedankt voor het wegwijs maken op fysko, voor alle gebietste shaggies en de prettige gesprekken. Wim, bedankt voor de hulp met het drie keer opbouwen van een titratie-opstelling en je adviezen. Peter, bedankt voor het stellen van vragen.

De oude aio-club en de nieuwe aio's, prettig om jullie te hebben ontmoet. Een paar wil ik graag even met name noemen: Joost (prettig nuchter en humuszuren is geen systeem), Jerome (misschien toch maar Frans gaan leren), Stefan (sterren zijn leuk, prettige kamergenoot en groots als brouwmeester) en René (bedankt dat ik mijn frustraties van het practicum kon wegpraten en nu zitten we beide op het trans).

Carla, thanks for all the coffee and sigarette breaks. Now that this thesis is finished I can come to visit you in Argentina!

Naast de mensen op het werk, zijn er gelukkig ook nog anderen. Het studentenpastoraat voor de broodnodige bezinning (??? zeilen, wandelen en kolonisten spelen). De club van Geloof en Wetenschap voor het samen lezen van boeken waar ik anders nooit aan zou beginnen maar die wel prettig zijn (Oke niet alle!). De reisjes naar Erfurt omdat Europa niet alleen iets is van de politiek maar ook van de mensen en omdat Erfurt een mooie stad is.

Voor de broodnodige ontspanning en het afblazen wil ik graag de volgende mensen bedanken: dank je Berend, Renate, Kim, Marijn, de dijkgraafafdeling, de dames van thuis-thuis en de hele Benedenclan.

## Dankwoord

Geraldine en Judith, bedankt voor het af en toe opvoeden van mij en ik vind het erg prettig dat jullie naast me staan op het podium. Pa en Ma, bedankt voor de stimulatie maar ook voor het leren omzien naar anderen. Ik ben blij dat jullie mijn ouders zijn. Jan, bedankt voor het helpen met de laatste, laatste loodjes, je programma maar voornamelijk dat je er bent.

Dag Wageningen, tot ziens in Leiden!

Joanne

# Levensloop

Joanne Klein Wolterink werd geboren op 16 december 1972 te Aalten. In 1991 behaalde zij het VWO diploma aan de Christelijke Scholengemeenschap Aalten. In datzelfde jaar begon ze aan de studie Moleculaire Wetenschappen aan de landbouwuniversiteit te Wageningen. In 1996 studeerde zij af met afstudeervakken in de Kolloïdchemie en Bodemscheikunde. In mei 1997 werd ze Assistent in Opleiding bij de leerstoelgroep Fysische Chemie en Kolloïdkunde. Hieruit is dit proefschrift voortgekomen.